# Synthesis and Size Control of Light Element and Its Alloy Nanoparticles by Pulsed Discharge and Their Applications

**NGUYEN DUY HIEU**

A thesis presented for the degree of
Doctor of Philosophy

Research Supervisor
**Professor HISAYUKI SUEMATSU**

長岡技術科学大学
Nagaoka University of Technology

**Department of Science of Technology Innovation**
**Graduate School of Engineering**
**Nagaoka University of Technology**
**August 2021**

# Acknowledgements

Firstly, I would like to express my sincere gratitude to my supervisor Prof. Hisayuki Suematsu for the continuous support of my Ph.D study and kind instruction of my study career, for his patience, motivation, and immense knowledge. His guidance helped me all the time in research and writing this thesis.

I would like to thank the rest of my thesis committee: Dr. Toshiyuki Nishimura, Prof. Tadachika Nakayama, Prof. Makoto Nanko, Prof. Toru Sasaki for their insightful comments and encouragement.

I am grateful to Prof. Tadachika Nakayama, Prof. Tsuneo Suzuki, Prof. Weihua Jiang, Prof. Toru Sasaki, Prof. Yoshinori Tokoi, Prof. Thi-Mai-Dung Do, Prof. Hyoung-Won Son, and Prof. Koichi Niihara for their assistance and discussion to accomplish this thesis and during my Ph.D.

I also thank Dr. Toshiyuki Nishimura and Dr. Yoshio Matsui at National Institute of Materials Science, Tsukuba for supporting me during my internship there.

I would like to thank Prof. Makoto Nanko for allowing me to use the spark plasma sintering in his laboratory.

I would like to thank all the technicians and staff in Extreme Density-Energy Research Institute of Nagaoka University of Technology: Mr. Shida, Mrs. Watanabe, Mr. Ishizaki, Ms. Araki, and Ms. Konishi at the office of Department of Science of Technology Innovation for their great help.

I would like to express my gratitude to Ministry of Education, Culture, Sports, Science, and Technology of Japan and Department of science of technology information for the financial support of Monbukagakusho Scholarship and Research Assistance, respectively, during my Ph.D.

I would like to thank Dr. Huy Dinh Vu for his support of using spark plasma sintering at Nanko laboratory.

I thank my friend-Dr. Ranjan Prem for fruitful discussion about life and research during my Ph.D.

I also would like to thank all the students, seniors and juniors, in Extreme Energy-Density Research Institute during my Ph.D. Especially, I would like to thank all the members of PWD team: Mr. Chu, Mr. Takami, Mr. Yamamoto, Mr. Rahul for their support, and Mr. Sugiyama, Mr. Trung, Mr. Okawa for their help with works related to ceramics.

I would like to thank all Vietnamese and international friends who shared with me joyful ( and sometimes stressful) moments in Ph.D life.

Finally, I deeply thank my parents and my fiancée Dieu Minh in Vietnam for their unconditional love for me during my Ph.D.

# Abstract

In the present study, by using methods of pulsed discharge of wire and powder, nanoparticles (NPs) of light elements such as Al, Mg, B, and transition metal borides (TMBs) have been synthesized. Among these, NPs of TMBs have been conventionally synthesized by thermal plasma methods such as plasma jet, plasma torch, etc. However, these methods have high power consumption (in order of kW), hence, achieve low energy conversion efficiency. Here, pulsed wire discharge (PWD) method is a one-step, cost-effective, high energy conversion efficiency and production rate method for NPs synthesis was employed in the present study. Due to the challenge of heating B wire, a modification of PWD-pulsed discharge of compacted powder was attempted for B powder. By pulsed discharge of compacted powder, for the first time, spherical crystalline B and TMBs NPs were synthesized by a pulsed discharge. The synthesis of each kind of NPs depends on the material of the electrodes: Cu for B, Ti for $TiB_2$, Mo for $MoB_2$, Zr for $ZrB_2$, and W for $WB_4$, which was confirmed by XRD and TEM results. Besides the main phases, minor phases were detected by XRD due to the uneven metal: B ratio in the process and are explainable by phase diagrams. A small amount of impurities like C, Fe/Cr are detected by EDS in B and TMBs NPs, however, these impurities can be suppressed by alternating the experimental setup. These NPs may be used as raw materials for sintering of TMBs pellet and are expected to be useful for lowering sintering temperature. A sub-study of sintering TMBs of monolithic $TiB_2$ and tungsten boride by spark plasma sintering (SPS) was done to investigate the effect of the size of starting powder on sintering behavior. In addition, by preparing NPs of light elements like Al and Mg, it was confirmed that these elements did not fit well with the particle size determining equation by PWD proposed by Tokoi et al., as a result, a complement to fulfill this inconsistency was suggested. First, by considering number density instead of the mass density of plasma/vapor during the PWD process, atomic mass was added. Then, besides Brownian coagulation, the nucleation process also plays an important role in particle formation and the critical size of the nucleus must contribute to the size of NPs. Therefore, considering the time the plasma/vapor expansion attains its largest volume (i.e. pressure of metal plasma/vapor is equal to ambient gas pressure), by a combination of experiment and simulation using hydrodynamic behavior calculation, it was found that the temperature of plasma/vapor was approximately 0.7 and 0.56 times of the normal boiling temperature of Mg and Cu, respectively. Furthermore, due to the correlation of nucleation temperature and latent heat of vaporization, the critical sizes of Mg, Al, Cu, Ag, Ni, Pd were calculated. Since the volume of nuclei is proportional to particle size, volumes of nuclei with calculated critical sizes of the above metals were added into the newly proposed parameter termed as relative nucleus number. It turned out that data of NPs of the above metals fell in a curve in the geometric mean diameter-relative nucleus number graph, which confirmed the validity of the newly proposed parameter. By this complement, the particle size determining equation can be applied for NPs of various light and heavy metals by PWD.

# Contents

# Chapter 1

# Introduction

## 1.1 General

In this chapter, there will be four sections in order: motivation for the present study, literature survey, problem statement, and composition of the present study. First of all, the first section-motivation for the present study gives a general outlook. Next, the literature survey provides a comprehensive background regarding this study including technical approaches for nanoparticles, then pulsed wire discharge as a method for nanoparticle preparation/synthesis, and finally, nanoparticles of light elements such as aluminium, magnesium, boron, and boron's alloys. After that, based on the background mentioned in the last section by the literature survey, the author addresses problems that this study is dealing with. Lastly, the composition of the present study gives brief summaries of each chapter so that readers can easily understand the scope of this study.

## 1.2 Motivation for the present study

Nanoparticles, which are involved in broader field-nanomaterials, started to be studied approximately two decades ago. Since then, the number of studies on nanoparticles has always been increasing year by year, which is demonstrated by the impressively continuous increment of the number of scientific reports concerning nanoparticles. This number of reports reached over 50 thousand in the single year of 2020 (surveyed by Scopus on March 2021). And yet interest in this area does not seem to cease. The reason is that nanoparticles with a range of sizes from few nanometers to less than 100 nm possess many distinctive properties which have never been observed in their bulk size counterparts. These fascinating properties include changes of melting point, bandgap, magnetic, optical, etc. and stemming from the fact that the specific surface area and surface electron number significantly enhances with decreasing particle size.

By taking advantage of these exceptional properties of nanomaterials, scientists around the world are solving present issues regarding to energy (e.g low-energy consumption, energy harvesting, energy storage, sustainable energy), pollution (waste and water solution), and health (cancer treatment, drug delivery), etc.

Inspired by the endless interesting properties of nanomaterials and nanoparticles in particular as well as their potential in solving human being's present issues, the author decided to conduct this study on synthesis and size control of nanoparticles of light metals and their applications. In this study, pulsed wire and powder discharge was being used as the main experimental methodology for synthesis and size control of nanoparticles. In addition, spark plasma sintering was also used as a supportive experimental methodology to synthesize tungsten borides pellet for the evaluation of mechanical properties of synthesized compounds.

According to *Light Alloys-Metallurgy of the Light Metals* (2017), the term "light metals" has traditionally been given to both aluminium and magnesium. Additionally, titanium and beryllium should also be included. Moreover, there are ten other elements that are lighter than titanium and are classified as metals. Except for boron in the form of strong fibers embedded in a suitable matrix, because of the fact that the alkali metals such as lithium, potassium, sodium, rubidium, and cesium, and the alkaline earth metals such as calcium and strontium are too reactive, while yttrium and scandium are quite rare, none of them can be used as a base material for structural purpose.

In this study, nanoparticles of aluminium, magnesium, boron, and its alloys were chosen to be synthesized by pulsed wire and powder discharge. Nanoparticles of aluminium and magnesium were prepared by pulsed wire discharge, nanoparticles of boron were prepared by pulsed discharge of compacted powder. Especially, in the first time, nanoparticles of transition metal borides were synthesized by a pulsed discharge. In addition to preparing nanoparticles of aluminium and magnesium by pulsed wire discharge, size control of particles was also discussed and a complement for particle size prediction equation was proposed. An in-depth discussion on these topics will be given in later sections.

## 1.3 Literature survey

First of all, this section provides information on synthesis methods for nanoparticles including top-down ad bottom-up approaches. In each kind of o approach, some representatives methods and their advantages, as well as disadvantages, are briefly reviewed. Then, pulsed wire discharge (PWD) as a method for nanoparticle preparation/synthesis is introduced. This introduction goes through the basic principles of PWD, the history of PWD, and particle size control by PWD. After that, nanoparticles of light elements and alloys that the present study deals with, namely aluminium, magnesium, boron, and its alloys prepared/synthesized by many different methods and their applications are discussed.

### 1.3.1 Synthesis methods for nanoparticles

Nanoparticle synthesis/preparation methods are usually classified into two large groups of approaches: top-down and bottom-up. Top-down approaches include methods that principally reduce materials from bulk size to nano-size. Representative methods of top-down approaches are mechanical milling, pulsed laser ablation, arc discharge. Next, bottom-up approaches include methods of generating particles with nano-size by assembling clusters. For example physical vapor deposition, chemical vapor deposition, sol-gel method, pyrolysis.

#### 1.3.1.1 Top-down approaches

Koch [1] reviewed comprehensively the synthesis and structure of nanocrystalline materials produced by mechanical attrition including mechanical milling and mechanical alloying. In this method, grain size decreases with increasing milling time[2, 3, 4]. Nanoparticles of a series of bcc and hcp structure elements with grain sizes as small as 9 and 13 nm were reported to be obtained after milling for 24h[5] . According to the review[1], nanocrystalline grains of metals with different crystal structures fcc, bcc, hcp were produced and the grain sizes of these groups of metals saturated to a minimum value which correlated with the melting point of corresponding metals. Yamada and Koch obtained the minimum grain size of TiNi intermetallic of 5 nm prior to amorphization[6]. Also, the grain size was able to be reduced further by increasing the ball: powder weight ratio[1]. Moreover, the effect of composition on the final grain size of Fe-Cu alloys was reported by Eckert[7]. The advantages and disadvantages of mechanical milling and mechanical alloying were discussed in the review paper of Koch[1] and Suryanarayana[8]. The advantages were the capability of mass production of nanocrystalline materials for potential applications. The disadvantages were the issues of powder contamination (from milling media and/or atmosphere) and powder consolidation.

Another example of the top-down approach is laser ablation/deposition. Laser ablation/ deposition employs laser as an energy source to produce nanoparticles or directly deposit nanoparticles onto a substrate for thin film deposition. In this method, the laser is radiated to a bulk-size target of the desired material. By irradiating the target, the particles are either directly ejected from the target surface due to photomechanical effect or nucleation in the vapor phase following by condensation and cooling during adiabatic expansion. While the former one is the nanoparticle synthesis formation mechanism of fs/ps ablation (ultrashort/short pulse), the latter one corresponds to that of ns ablation[9]. Nanoparticles obtained by laser ablation can be generated in a vacuum/gas atmosphere or in liquids. Control of nanoparticle size distribution has been studied extensively. Orii et al. reported the generation of ZnTe nanoparticles in the Argon atmosphere and the effect of annealing temperature on the particle size distribution [10]. Tsuji et al. generated Ag nanoparticles using Nd: YAG laser ablation and described the dependence of particle size distribution on wavelengths of the laser source[11]. The ablation time duration was also investigated as a factor affecting the size distribution[12]. In laser ablation in liquid, the concentration of solutions can be used to tune the particle size distribution. Mafune et al. reported the decrease in particle size when increasing the concentration of anionic surfactant sodium dodecyl sulfate from 0.003M to 0.05M[13]. One more commonly used way to control particle size is by post-irradiation of the formed colloidal solution due to the interaction of nanoparticles with the laser beam, especially stronger with a wavelength close to the plasmon resonance wavelength of the nanoparticles[9]. Mafune et al. reported about the reduction of Au nanoparticles by irradiating the produced colloidal by laser with 532nm wavelength which is close to the plasmon resonance of Au nanoparticles (520nm) due to more effective absorption of radiation[14]. Despite the significant capability of controlling the particle size and tuning size distribution, the laser ablation method suffers from the low efficiency of the laser which is inherent. This is considered to be the largest drawback of this method.

The arc discharge is another common nanoparticle synthesis method that belongs to the top-down approach. Basically, in this method, two electrodes made of desired materials are adopted as anode and cathode for arc discharge. The setup can be placed either in gas or liquid media. Usually, electrodes themselves are employed as raw materials. Sometimes, catalysts are used to promote the process. After a DC or AC supply voltage is applied to anode and cathode, a current goes through the electrodes and induces the breakdown of dielectric media between electrodes. The arc discharge is greatly used to synthesize carbon nanomaterials[15, 16, 17, 18]. In addition, there is a large number of studies reporting the synthesis of nanostructures of oxides [19, 20], metals[21, 22, 23, 24], and many other non-carbonaceous nanostructures [25, 26]. Particle size control of the arc discharge method can be done by adjusting the electric current, arc discharge medium, or using catalysts. Generally, arc discharge is a simple method for the synthesis of nanoparticles. However, arc discharge has some disadvantages: for small scale synthesis, the production rate is quite low, however, for larger scale, the continuous discharging make the electrodes and chamber get hotter and hotter quickly and must be cooled down by a separate cooling system which makes the process more costly and less efficient.

#### 1.3.1.2 Bottom-up approaches

Physical vapor deposition (PVD) is a vapor phase method and one of the most well-known methods for the synthesis of nanostructures basing on the bottom-up approaches. Basically, PVD employs physical factors such as thermal energy, electron bombardment energy to eject atoms of desired materials out of the target and deposit them onto the substrate[27]. Synthesis of ZnO nanowires was reported using physical vapor deposition by means of heating precursor[28, 29, 30]. Continuous ultra-thin $MoS_2$ films were reported to be grown by the PVD synthesis process based on magnetron sputtering[31]. Generally, with a long history of research, PVD methods are chosen for well-controlled nanostructures' required purposes. Additionally, in this technique, not only precursor ejection but also substrate preparation is important. The drawback of PVD is considered to be the low energy conversion efficiency due to the heat loss during the process.

Chemical vapor deposition (CVD) is principally similar to PVD, however, chemical reactions play a crucial role in the formation of nanostructures. Furthermore, the selection and preparation of substrates and catalysts also have an effect on the final products by this method. Nanostructures of $MoS_2$ were reported to be synthesized by sulfurization of $MoO_3$ powder supported by means of heating[32, 33, 34]. Nanostructures of carbon such as graphene[35] and single-wall carbon nanotubes[36] were reported to be generated by CVD. Additionally, there were many nanostructures of oxides, silicon, the compound was successfully synthesized by CVD[37, 38, 39]. Similar to PVD, CVD can be used to synthesize well-controlled nanostructures with a high capability of controlling size and morphology thanks to the adjustment of temperature, flow gases, catalysts, etc. The disadvantage of CVD is considered to be similar to that of PVD which is the low energy conversion efficiency.

The sol-gel method is one of the bottom-up approaches which has been investigated for a long time. It is also known as one of the liquid phase methods. According to a review by Hench et al.[40], sols are dispersions of colloidal particles in a liquid, in which colloids are solid particles with diameters of 1-100 nm and a gel is an interconnected, rigid network with pores of submicrometer dimensions and polymeric chains whose average length is greater than a micrometer. By sol-gel methods, a wide range of materials are synthesized, for example, ceramic oxide compositions[41, 42, 43, 44], silica[45], hydroxides, sulfides, and metals[46, 47]. The main advantages of this method are the high purity and homogeneity of synthesized products, along with the high capability of size, size distribution, and morphology control of nanoparticles. The drawback of this method is considered to be the complexity of the synthesis process and the production rate is not high.

Besides PVD, CVD, and sol-gel methods, pyrolysis is also a common method for the synthesis of nanoparticles by a bottom-up approach. Pyrolysis is classified into three categories: vapor-fed aerosol flame synthesis (VAFS) where the precursor is supplied as a form of metal vapor, flame-assisted spray pyrolysis (FASP) where the precursor is supplied in the state of low combustion enthalpy solution and usually in an aqueous solvent, and flame spray pyrolysis (FSP) where the precursor is also in liquid form, but with significantly higher combustion enthalpy[48]. In this method, the synthesis of oxides is quite facile via combustion of metal halides such as synthesis of $Al_2O_3$ from $AlCl_3$ or $TiO_2$ from $TiCl_4$[49] and many other oxides[50, 51, 52]. Furthermore, multicomponent systems such as $V_2O_5/TiO_2$[53, 54], $CuO/CeO_2$[55, 56] and oxides of two or more metals such as

$MgAl_2O_4$[57, 58], $LaCoO_3$[59, 60] were reported to be synthesized by pyrolysis. However, synthesis of metallic nanoparticles by pyrolysis is scarce, only synthesis of Cu[61, 62], Co[63, 64], and Bi[65] have been reported. The size distribution of nanoparticles synthesized by this method is governed by self-preserving size distribution, in which particles nucleate and grow by Brownian coagulation, this gives the geometric standard deviation 1.46[66]. In general, pyrolysis is appropriate for nanoparticle synthesis method for industrial purposes thanks to high production, however, this method also faces some challenges such as the selection of suitable precursors and their high cost.

In summary, every method as well as approach has its specific advantages and disadvantages. Some methods provide high purity and homogeneity of nanoparticles but the trade-off is their complicated synthesis process, production rate, and vice versa. As a result, herein we introduce pulsed wire discharge as a method for nanoparticle synthesis which possesses the advantages of simple, low-cost, high energy conversion efficiency, and high production rate but high purity nanoparticle yield, along with the capability of particle size control. Detailed information is going to be written in the next section.

### 1.3.2 Pulsed wire discharge method

Pulsed wire discharge (PWD) is a cost-effective, one-step, eco-friendly, high production rate and energy conversion efficiency method for nanoparticle synthesis. The principle of PWD originally came from the exploding wire phenomenon which has a long history of investigation. These studies were mainly regarding peculiar but reproducible voltage and current waveforms, properties of matters at extreme conditions, shock waves, etc. Although PWD is fundamentally similar to exploding wire phenomenon, the research target of PWD is nanoparticles coming from the phenomenon and was first reported by Jiang et al.[67]. In this section, first, a brief history of investigations concerning exploding wire is surveyed, then basic principle of PWD for nanoparticle synthesis is introduced and an overview of studies regarding nanoparticle synthesis by this method is reviewed, and finally, means of particle size control by PWD are discussed.

#### 1.3.2.1 History of PWD

The exploding wire itself was done at a very early time due to its simple electrical components including a wire and a battery. Back to the first time when the exploding wire has been experimentally done by E. Nairne in 1774, the experiment was actually not subjected to the purpose of exploding wire but to prove that current in all parts of a series circuit is the same[68].

Not until when Faraday et al. reported the results of exploding gold and other metals' wires using a Leyden battery and obtaining very small particles in 1857 that the exploding wire was first investigated for the purposes close to the exploding wire phenomenon. However, at that time, due to the limitation of the optical microscope, he could not come to any conclusion about the size of particles synthesized but the extremely small size of them[69].

After that, in the 1920s, attraction to the phenomenon was evoked by the work of Anderson et al. for describing the temperatures generating in the phenomenon that can attain those on the sun[70, 71, 72]. During the following four decades, a number of studies were done by many researchers around the world: Nagaoka[73, 74, 75], Kleen[76], Wrana[77], Eiseilt[78], Conn[79], Kvartskhava[80, 81], Lebedev[82], Chace[83]. The fundamental circuit of exploding wire is shown in Fig 1.1

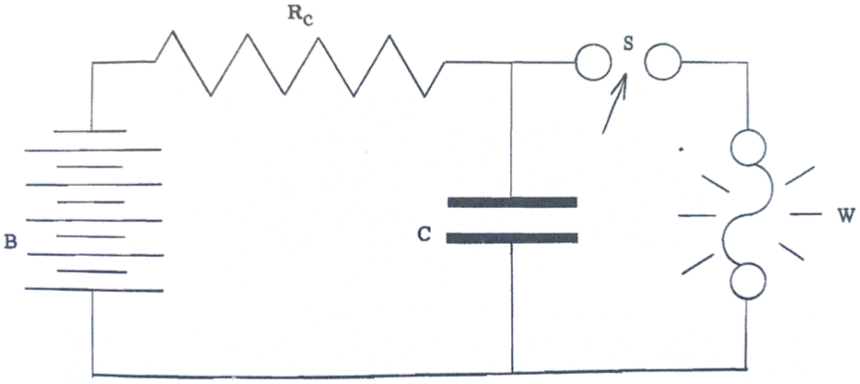

Figure 1.1: Fundamental circuit of exploding wire. B-charging source, C-storage condenser, S-switch, W-exploding wire, $R_c$-charging resistor[84].

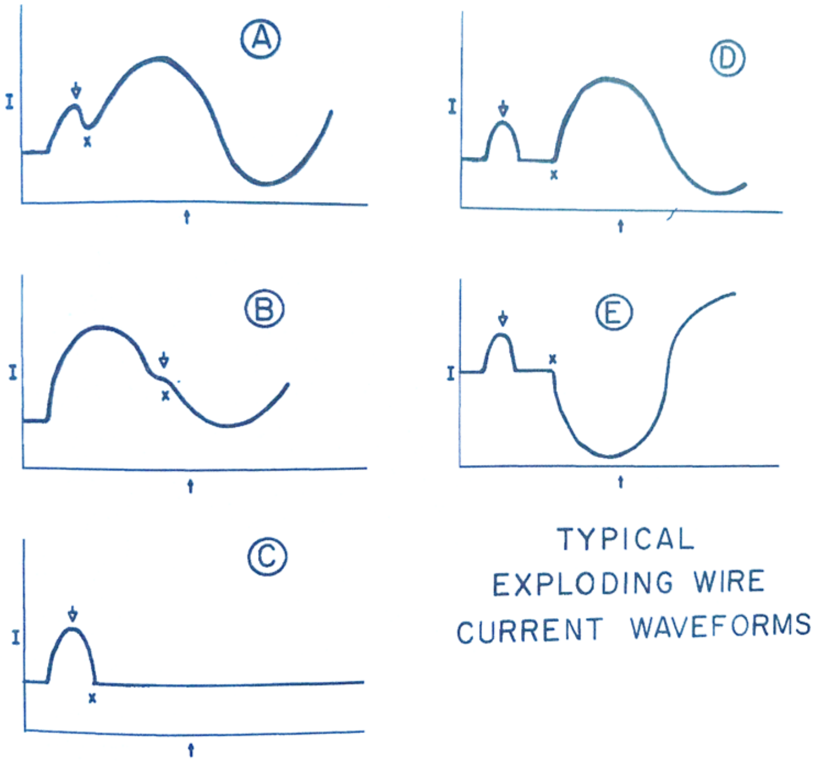

Figure 1.2: Typical current waveforms by exploding wire[84].

After the above studies, the number of investigations regarding the exploding wire phenomenon increased so drastically that a conference on this topic particularly was held in 1959, then later, the 2nd, 3rd, and 4th time of conference continued to be organized in 1961, 1964, and 1967, respectively. These conferences facilitated to gain knowledge greatly about the exploding wire phenomenon. The proceedings of these conferences were collected and published into 4 volumes of books, namely "Exploding wire" by W. G. Chace and H. K. Moore[85, 86, 87, 88]. Research issues in these conferences can be classified into the following categories: General researches on the phenomenon (Theoretical and Experimental), Shock waves, Applications, and Techniques.

What made the exploding wire phenomenon so special was the explosion of the wire in an extremely short time normally of the order of microseconds. Figure 1.2 shows the typical current waveforms described by Chace et al.[84]. If the wire had not been exploded i.e. by using a thicker wire, the current waveform with respect to time would be like Fig 1.2(C). However, because of the explosion of wire, the current waveforms were usually seen as Fig 1.2(D). Chace et al. gave an explanation basing on this current waveform as following. First, the wire is heated by the electric current and melts. The melted wire is further heated by the ever-increasing current. The physical shape of the wire is maintained by inertia and magnetic pressure. The temperature of the wire reaches the boiling point, however, the conditions are not appropriate for equilibrium boiling, which leads to the superheating of the liquid wire. Due to the lack of surface activation, the barrier for phase change is harder to reach and the temperature attaining is far above the normal boiling point of metal wire. When the barrier is surmounted, vaporization occurs along with the explosion. The vaporization of the wire leads to the decrease of current after reaching its peak due to the low electrical conductivity of the gas phase. After decreasing, the current keeps constant. This period is called "dwell time" or "dark time", in which the current flows at a constant, low rate carried by a limited supply of carriers-ions and/or electrons. Density at this time is still high and electrons do not receive enough energy by collisions to produce ionization, as a result, the number of carriers remains constant. This state exists for a very short time. The wire-shaped extremely hot metal vapor surpasses the pressure induced by inertia and ambient atmosphere and expands. Hence, the pressure drops, the mean free path increases, and ionization accompanying avalanche occurs. This is called "restrike" or "reignition". The current now rises again and is controlled by the RLC circuit.

General researches on the phenomenon include specific characteristic regarding the exploding wire such as electrical current, resistance/conductance, temperature, phase transition. "Current pause" or "dwell" were mentioned in the previous paragraph is one of the attractive topics of exploding wire. By using a composite system of an oscilloscope, a streak camera, and a time-resolving spectrogram, Reithel et al. compared and proposed the mechanisms of the explosions in the cases of the current pause and no current pause[89]. By means of sub-microsecond flash x-ray, Chace reported that the current during the dwell may be carried largely on thermionic electrons generated from the explosion fragments[90]. Due to the complicated phase transition during exploding wire, the variation of resistance/conductivity is apparently interesting. About this, by standard curving-fitting method, Good reported an expression of resistance with respect to time[91]. The temperature during the phenomenon was also studied extensively by both experimental and theoretical methods[92, 93]. In addition, the effects of external factors like ambient pressure and magnetic field were also examined[94, 95]. Regarding the plasma generation, Ross et al. suggested that since dense liquid core stabilizes the plasma against the evolution of instabilities and premature ejection from the circuit, moreover, delays the plasma formation until the peak of current, the use of exploding wire as a source of plasma is advantageous[96].

Some applications by exploding wire were described, for instance: in photochemistry[97], exploding wire plasma accelerator[98], metal-water reactions by exploding wire[99], pressure environments created by wires explosion in water[100], high power pulse steepening[101], a high voltage, quick-acting fuse to protect capacitor banks[102], hypervelocity projector[103], light source for plasma quantitative analysis[104].

#### 1.3.2.2 PWD for nanoparticle synthesis

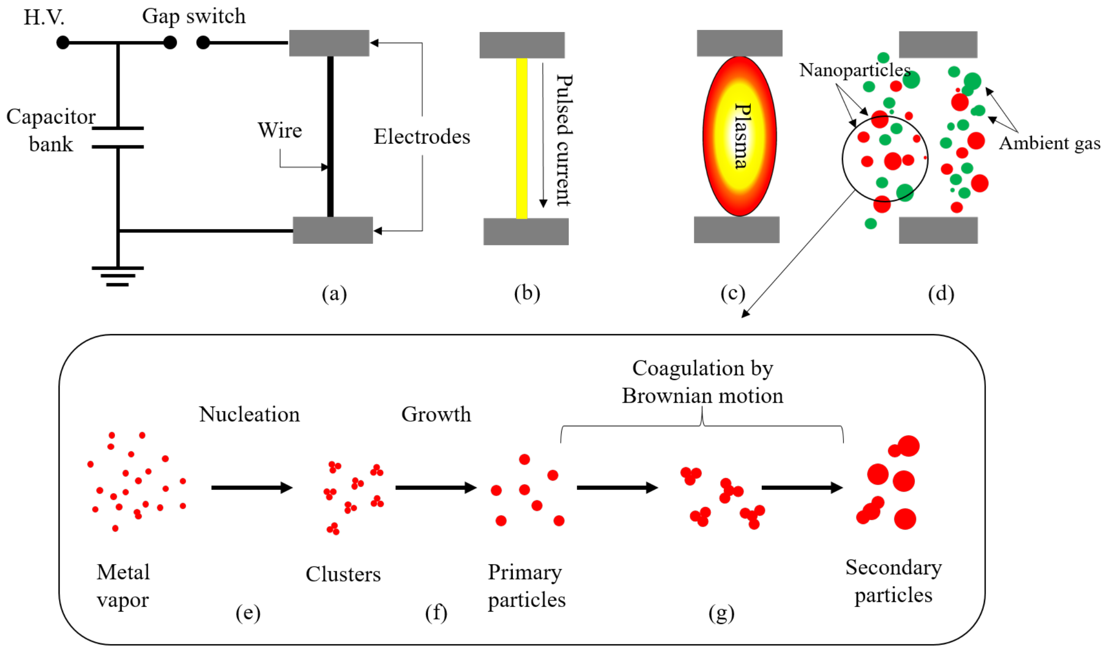

Figure 1.3: Schematic diagram of PWD for nanoparticle synthesis

Figure 1.3 shows a schematic diagram of PWD for nanoparticle synthesis. Since PWD is fundamentally similar to exploding wire phenomenon, the PWD experiment setup includes a simple RLC circuit similar to that shown in Fig. 1.1. A schematic diagram of PWD is shown in Fig. 1.3. This circuit comprises a high-voltage power supply, capacitor bank(s), a gap switch, and a thin metallic wire employed as starting material set between a pair of electrodes (Fig. 1.3(a)). By charging the capacitor bank(s) with a high voltage and discharging by closing the gap switch, a large pulsed current passes through and heats the thin metallic wire (Fig. 1.3(b)). Due to Joule heating, the wire melts, vaporized, partly ionized, and turns into a mixture of plasma/vapor (Fig. 1.3(c)). The mixture of plasma/vapor expands outwards and quenches by contacting with ambient medium (Fig. 1.3(d)). This plasma/vapor of metal quenches quickly from high temperatures and is supersaturated. The supersaturation of vapor of metal induces the homogeneous nucleation (Fig. 1.3(e)) and metal vapor turns into clusters. After nucleation, the clusters continue to grow to larger aggregates called primary particles (Fig. 1.3(e)). These primary particles move randomly, collide and stick together to become larger and larger, finally become secondary particles(final nanoparticles). This step is called coagulation by Brownian motion (Fig. 1.3(g)).

Nanoparticles of metals and oxides of U, Cu, Al, Pt, and Ag were reported to be synthesized using exploding wire in a very early age (1962). Obtained particles were almost in a spherical shape. With increasing charging voltage, particle size decreased and size distribution became narrower. The explosion of noble metals like Ag, Pt in air yielded metallic nanoparticles while other metals yielded a mixture of oxide and metallic nanoparticles [105].

The formation of other kinds of nanoparticles such as nitride, iodide, sulfide, carbide, fluoride was subsequently reported. Joncich et al. reported the formation of iodide, sulfide, carbide of Mg and Al in 1964[106]. After that, he and his colleagues reported the formation of Mg, Ti, Zn, Tn, Zn, and Al nitrides in 1966[107].

The understandings regarding the influence of explosion conditions on explosion results have been built generally after several decades of investigation.

- The overheating or ratio of charging energy/vaporization energy, $K$ is a crucial factor for characterization. The particle size decreases and the size distribution becomes narrower with increasing $K$. It can be explained by the rise of expansion rate and the degree of ionization of explosion products[108, 109]. This was also experimentally demonstrated by comparing particle size results obtained by transmission electron microscope (TEM) images and Brunauer Emmett Teller (BET) and concluded that with increasing $K$ the number of submicron-sized particles decreased, which also decreased the particle size[110].

- The characteristic of different metals affects the heating effectiveness of pulsed electric current on the wire. It is well known that metals in exploding wire are classified into two classes[111]:

    - Class 1: low boiling point and low heat of vaporization (Cu, Ag, Al, Au, Sn, Zn, Cd)

    - Class 2: high boiling point and high heat of vaporization (W, Mo, Pt, Ni, Fe, and Ti)

  For Class 1, heating energy is effectively deposited into the wire and the current waveform is usually like Fig 1.2(D). For Class 2, heating energy cannot deposit into the wire completely due to the breakdown on the surface of the wire caused by the extraction of thermal electrons. In this case, discharge occurs before the wire is vaporized, as a result, the current waveform is like Fig 1.2(A).

- The media surrounding the wire is very important for the formation of nanoparticles. Apparently, with different gas species, due to reactive or inert characteristics, products are different. With specific gas, the variation of gas pressure controls the particle size by controlling the expansion volume[112]. The thermal conductivity of different gases also affects the cooling rate, which affects particle size[113]. Dense media like liquids suppress the formation of discharge and may decrease the particle size.

- Particles obtained are usually in a spherical shape. Particle size distribution follows a log-normal distribution with geometric standard deviation varies from 1.4-1.8 depending on whether reaction happened or not[114].

Recently, the formation of nanoparticles by using exploding wire has been approached by analyses of thermodynamic models and numerical calculations. By thermodynamic modeling and characterization of Al nanoparticles, Kumar et al. explained the decrease in particle size with decreasing ambient gas pressure by the decrease in critical particle size[115]. Ranjan et al. employed a diffusion model and experimental results of the expansion of vapor cloud to explain the decrease in particle size with decreasing ambient gas pressure[116]. Bai et al. adopted a numerical method to calculate the size of atomic vapor clusters with respect to calculated temperature, then modelized and gave prediction on particle size distribution[117].

In recent researches, many papers are focusing on the applications and improve quality of nanoparticles synthesized by PWD for specific purposes. Intermetallic nanoparticles like Ti-Ag, Fe-Ag[118], Zn-Al, Zn-Ag, Zn-Cu, Zn-Ti-O[119] were synthesized for antibacterial purposes. Fe-$Fe_3O_4$ core-shell structure nanoparticles were produced for biomedical application[120]. $Fe_3O_4$ and $\gamma$-$Fe_2O_3$ nanoparticles for arsenic removal[121]. Multilayer graphene-coated Cu nanoparticles synthesized in isopropyl alcohol for stable dispersion for a long time[122]. Nanoparticles of Zn, Cu, Ni, Co, Fe, Mo, Nb, Ti, W, Zr, Hf, Ag, Pd, V were prepared in organic capping agents for air-stable purposes[123].

Table 1.1: Summary of studies on exploding wire for NPs synthesis

| Year | Kinds of NPs synthesized | Media | Point | Ref. |
|---|---|---|---|---|
| 1962 | $U_3O_8$, CuO, Al, Pt, Ag | Air, Ar | Synthesis and characterization | [105] |
| 1964 | Iodines, Sulfides, Carbides of Al and Mg | Nearly vacuum | Synthesis and characterization | [106] |
| 1966 | Nitrides of Mg, Ti, Zr, Ta, Zn, Al | $N_2$, $NH_3$ | Synthesis and characterization | [107] |
| 1993 | Diamond | Unknown | Diamond production | [124] |
| 1994 | Mo | Ar | Preparation Mo nanoparticles for $MoS_2$ synthesis | [125] |
| 1995 | $\gamma$+$\beta$-$Al_2O_3$, $TiO_2$, $ZrO_2$ | Ar+$O_2$ | Synthesis and characterization | [126] |
| 1996 | Al, $\gamma$-$Al_2O_3$, $Al_4C_3$, W, WC, $W_2C$ | Distilled water, Decane | Formation of chemical compounds in liquid | [127] |
| 1997 | Al, $Al_2O_3$ | Ar, Air | Synthesis and characterization | [128] |
| 1998 | Cu, Al, Ni, Fe, W, Pt, Ti | Ar, Air, $N_2$, $O_2$, $NH_3$ | Production and characterization | [129] |
| 1999 | Ni, Fe, W, Sn, Al, Cu, Zn, Ti, Ag, In | Ar | Preparation and characterization | [130] |
| 1999 | AlN | $N_2$, $N_2$+$NH_3$ | Synthesis and characterization | [131] |
| 2000 | Cu-Zn alloy | Ar | Synthesis and characterization | [132] |
| 2001 | $\gamma$-$Fe_2O_3$ | Dry air | Synthesis and characterization | [133] |
| 2002 | PZT | $O_2$ | Pb, Zr, Ti wire simultaneously discharged | [134] |
| 2002 | $NiFe_2O_4$ | $O_2$ | Investigation of magnetic properties | [135] |
| 2003 | $Al_2O_3$ | $O_2$ | Investigation of phase transition from activated alumina to $\alpha$-$Al_2O_3$ by adding $ZrO_2$ | [136] |
| 2003 | AlN | $N_2/NH_3$ | Achievement of AlN content at 97% | [137] |
| 2003 | Fullerene | $N_2$ | Discharge of carbon fibers | [138] |
| 2004 | W | Ar | Investigation of passivation, oxidation, and combustion of W NPs | [139] |
| 2004 | $SnO_2$ | $O_2$ | Synthesis of $SnO_2$ NPs and particle size distribution | [114] |
| 2005 | NiO | $N_2$ +$O_2$ | Synthesis and characterization | [140] |
| 2005 | Single-walled carbon nanotubes | $N_2$ | Discharge of carbon fibers | [141] |
| 2005 | Fe-N | $N_2/NH_3$ | Investigation of phase composition | [142] |
| 2005 | $ZnFe_2O_4$ | $O_2$ | Synthesis and characterization | [143] |
| 2006 | Al with passivated layers | Ar then stearic, oleic acid introduction | Passivation layer by non-inert coating | [144] |
| 2006 | $Al_2O_3$-$ZrO_2$ nanocomposite | $O_2$ | Simultaneous discharge of two wires | [145] |
| 2007 | Cu-Ni alloy | Ar | Explosion of Cu-plated Ni wire and characterization | [146] |
| 2008 | Cu-Sn alloy | Ar | Explosion of Sn-coated Cu wire and characterization | [147] |
| 2008 | Cu-Ni-P | $N_2$ | Explosion of Ni-P-plated Cu wire and characterization | [148] |
| 2008 | $TiO_2$ | $O_2$ | Control of rutile and anatase phase | [149] |
| 2008 | Ni-Cu | $N_2$ | Discharge stranded Ni and Cu wires and characterization | [150] |
| 2009 | Cu-Zn/CuO-ZnO | Ar | Nanoparticles for humidity sensors | [151] |
| 2009 | Al NPs with oxide shell | Ar with $O_2$ flow | Passivation layer for Al NPs and prevent agglomeration | [152] |
| 2009 | Ti-Cr alloy | Ar | Explosion of Cr-plated Ti wire and characterization | [153] |
| 2009 | TiN | $N_2$ | Synthesis and characterization | [154] |
| 2009 | Zn | Ethanol, Distilled water | Disperse in paints for anticorrosion purpose | [155] |
| 2010 | Al-$Al_4C_3$ | Ar + Butane | $Al_4C_3$ coated Al NPs for prevention of agglomeration | [156] |
| 2010 | organic-covered Ti | He | Discharge of Ti wire with oleic acid and vapor/mist. | [157] |
| 2010 | AlN | $N_2$ | AlN NPs with particle size less than 10 nm | [158] |
| 2011 | Ag nanofluid | Ethanol, Deionized water | Optimal synthesis of Ag nanofluid in liquids | [159] |
| 2011 | Fe-Ni | Ethanol, Deionized water | Investigation of magnetic properties | [160] |
| 2011 | Au colloid | Water, TW20 solution, Ascorbic acid | Preparation and stability characterization | [161] |
| 2011 | polymer-Cu composites | Polyaniline, Polyacrylic acid | Cu NPs dispersed in polymer mattrix | [162] |
| 2011 | Ti-Fe | Ar | Phase change with increasing content of Fe | [163] |
| 2012 | Carbides of W, Ti, Ta, Al | Ar, $C_2H_2$, $C_3H_8$, Benzene, Toluene, Decane | Synthesis and characterization | [164] |
| 2012 | Ni-Al | Ar/$N_2$ | Discharge of twisted-wire | [165] |
| 2013 | Pt, Ni | $Pt(NH_3)_2(NO_2)_2$ solution | Explosion of Ni wire in Pt solution | [166] |
| 2013 | $Fe_3O_4$, $\gamma$-$Fe_2O_3$ | Air | NPs for arsenic removal purpose | [121] |
| 2014 | Cu coated with oleic acid | Oleic acid | Oxidation prevention by oleic acid coating | [167] |
| 2014 | Fe-Ni | Ar+$N_2$+$O_2$ | Oxide shell Fe-Ni-core NPs | [168] |
| 2014 | BN nanosheet/nanotube-Fe nanocomposite | $N_2$ | Discharge of BNNS-coated Fe wires | [169] |
| 2015 | Organically- capped Zn NPs | Organic capping agents | Air-stable organically-capped ZNPs | [170] |
| 2015 | Zn, Cu, Ni, Co, Fe, Mo, Nb, Ti, W, Zr, Hf, Ag, Pd, V | Organic capping agents | Air-stable organically-capped NPs | [123] |
| 2015 | Oxidation-resistant Cu-based NPs | Ascorbic acid | Oxidation resistant NPs for conductive ink | [171] |
| 2015 | Pd | $N_2$, Ar, He | Pd NPs preparation and grain-size determining equation | [172] |
| 2016 | Cu-Ag, Cu-Pb, Al-Pb | Ar | Explosion of twisted wire for binary metallic | [173] |
| 2016 | Multilayer Graphene-coated Cu | Iso propyl alcohol | Synthesis of uniform and stable dispersions in common organic solvents | [122] |
| 2016 | Ag-Au alloys | Deionized water | Explosion of twisted-wire | [174] |
| 2016 | Mu metal | Poly(acrylamide-co-acrylic acid) | Preparation and characterization | [175] |
| 2016 | Mg, Al, Si, Ge, Sn | Toluene, 1,2-epoxydodecane, Tetrahydrofuran | Discharge of Si, Ge wafer, Mg ribbon | [176] |
| 2016 | AlN | Liquid $N_2$ | Discharge in liquid nitrogen | [177] |
| 2016 | ZrC | Ar, Ar/Oleic acid vapor, Oleic acid liquid | Synthesize and characterization | [178] |
| 2016 | Cu-Sn-58Bi | $N_2$ | Synthesis three-component NPs and characterization | [179] |
| 2017 | Fe, $Fe_3O_4$ and bimetallic Cu/Fe | $O_2$/Ar | Magnetic nanoparticles for biomedical applications | [180] |
| 2017 | Fe | Deionized water/Pre-prepared synthetic wastewater | NPs for removal of heavy metals | [181] |
| 2017 | Mg | Ar | Capability of prepare alkaline earth metal NPs by PWD. | [182] |
| 2017 | ZrN, $ZrO_2$ and $\beta$–$Zr_7O_{11}N_2$ | $N_2/O_2$ | Evidence to study on Zr alloys fuel cladding in nuclear accidents | [183] |
| 2018 | Ag-Al alloys | Ar | Twisted-wire explosion | [184] |
| 2018 | W, Ni, Fe | Unknown | W, Ni, Fe NPs as precursors for sintering | [185] |
| 2018 | Fe-FeO-graphene composite | Graphene oxide suspension | Discharge of Fe wire in graphene oxide suspension | [186] |
| 2019 | Cu-Nb, Pb-Cu, Ag-Ni, Ag-Fe | Ar | Explosion of twisted-wire | [187] |
| 2019 | W-Cu | Ar | Core-shell structured NPs and application in SPS | [188] |
| 2019 | Cu-Fe | Ar | Janus-like bimetallic NPs with high antibacterial activity | [189] |
| 2019 | Al | Ar, He, $N_2$ | Enhancement of hydrogen generation | [190] |
| 2019 | $(Cu_xZn_{1\text{-}x})O$ and $(Cu_xAg_{1\text{-}x})O$ | Ar+$O_2$ | NPs for antibacteria purpose | [191] |
| 2019 | Zn/Al, Zn/Ag, Zn/Cu. Zn/Ti-O composites | Ar+$O_2$ | Antimicrobial composite NPs synthesis | [119] |
| 2019 | Sn-0.75Cu | Ar | Synthesis and characterization | [192] |
| 2019 | MoC | Ar+Kerosene fume | High yield attraction of MoC | [193] |
| 2020 | Ti-Ag, Fe-Ag | Ar | Antibacterial bimetallic NPs synthesis | [118] |
| 2020 | Al-Mg alloy | Ar | Application for high-energy | [194] |
| 2020 | $\beta$-MoO3 | $O_2/N_2$ | Optimal condition for high yield content of $\beta$-$MoO_3$ | [195] |
| 2020 | Nanodiamond | Distilled water | Formation of nanodiamond | [196] |
| 2021 | $Fe/Fe_3O_4$ core-shell | Ar+$O_2$ | Magnetic nanoparticles for biomedical applications | [120] |

#### 1.3.2.3 Particle size control by PWD

Since particle size greatly influences the properties of nanoparticles, particle size control is one of the most concerns in any nanoparticle synthesis method. It was found that overheating $K$ and ambient gas pressure were two basic factors that can be used to manipulate the particle size. The effect of overheating $K$ on particle size was found early and reported [105]. Additionally, although the effect of ambient gas pressure on particle size was understood a long time ago, it was rather used for enhancing the degree of reactiveness of gas for synthesizing oxides or nitrides[108].

Jiang et al. first reported using gas pressure as a factor for controlling particle size in PWD[67]. For metallic nanoparticles prepared by PWD, it was known that particle size decreased with increasing overheating $K$ and decreasing ambient gas pressure. Many papers have reported this tendency. However, the conception of particle size control needs the combination of these two factors. Tokoi et al. proposed a particle size determining equation by PWD by suggesting a new parameter called plasma/vapor density[112]. There were theoretical plasma density, $D_{\mathrm{th}}$ and experimental plasma/vapor density, $D_{\mathrm{exp}}$. $D_{\mathrm{th}}$ was identified as follows,

$$D_{\mathrm{th}} = \frac{mP}{E_{\mathrm{c}}}, \tag{1.1}$$

where $m$ is mass of wire in [g], $P$ is ambient gas pressure in [Pa], and $E_{\mathrm{c}}$ is charging energy into capacitor banks in [J].The dimension of $D_{\mathrm{th}}$ is [g/m$^3$]. $D_{\mathrm{exp}}$ was derived experimentally by the mass of starting wire and the volume expansion of plasma/vapor during PWD obtained by high-speed images. The relationship between $D_{\mathrm{exp}}$ and $D_{\mathrm{th}}$ was empirically determine as follows,

$$D_{\mathrm{exp}} = 106(D_{\mathrm{th}})^{0.6}. \tag{1.2}$$

After that, the relationship between geometric mean diameter, $D_1$ was also found by experiments as follows,

$$D_1 = 3.8(D_{\mathrm{exp}})^{0.4}. \tag{1.3}$$

From the Eqs. (1.1),(1.2), and (2.13), the particle size determining equation was proposed as follows,

$$D_1 = 3.8\left[106\left(\frac{mP}{E_{\mathrm{c}}}\right)^{0.6}\right]^{0.4}. \tag{1.4}$$

This particle size determining equation was verified by the experimental results of three metals Cu, Ag, and Ni[112, 197].

In 2015, Sato et al. reported the preparation of Pd nanoparticles by PWD and proposed the addition of a new factor in the particle size determining equation. The ratio of and the vaporization energy of the wire, $K_{\mathrm{p}} = \frac{E_{\mathrm{p}}}{E_{\mathrm{v}}}$ where $E_{\mathrm{p}}$ is the energy deposited into the wire up to the end of wire heating stage and $E_{\mathrm{v}}$ is the vaporization energy of the wire. Therefore, now $D_{\mathrm{th}}$ defined in Eq. (1.1) became

$$D_{\mathrm{th}} = \frac{mPK_{\mathrm{p}}}{E_{\mathrm{c}}} = \frac{mP}{E_{\mathrm{c}}}\frac{E_{\mathrm{p}}}{E_{\mathrm{v}}}. \tag{1.5}$$

This modification did not affect the previously proposed particle size determining equation by Tokoi et al. since all the experimental results indicated that $E_{\mathrm{p}}$ is at least equal to $E_{\mathrm{v}}$. As result, with these results, $K_{\mathrm{p}}$ was supposed as 1, which means the wire is completely vaporized. With $K_{\mathrm{p}} < 1$, the wire vaporization was not complete due to the discharge on the wire's surface. With the above modification, experimental results of Pd nanoparticle by PWD fitted with the particle size determining equation proposed by Tokoi et al[172].

#### 1.3.2.4 Theoretical foundation of particle size control by PWD

Like other physical vapor methods for the synthesis of nanoparticles, particle formation in PWD commences with the diffusion and quenching of the plasma/vapor of metals. The theoretical mechanism of this process was first reported by Smoluchowski in 1917. First, let us think about the dispersion of initially identical particles (or primary particles). Primary particles collide with each other to become large particles. The transport mechanism of these particles follows Brownian motion. Therefore, this process is well-known as Brownian coagulation or aggregation. After a period of aggregation, these particles contain aggregates of various sizes and concentrations, for example: $n_i$ particles with size $i$, $n_j$ with size $j$. Here, $n$ is number concentration and size is the number of primary particles comprising the aggregate. There is a fundamental assumption that aggregation is a second-order rate process, in which the rate of collision is proportional to the product of concentrations of two colliding species. As a result, the rate of collisions between particles $i$ and particles $j$ is defined by:

$$J_{ij} = k_{ij} n_i n_j, \tag{1.6}$$

where $k_{ij}$ is a second-order rate constant, which depends on particle size and transport mechanism. Assuming that the interparticle forces do not affect the effectiveness of aggregation due to the short-range nature of these forces. As a result, this assumption means that every collision is effective in forming an aggregate. Therefore, it is possible to the rate of change of concentration of aggregate $l$ where $l = i + j$:

$$\frac{\mathrm{d}n_l}{\mathrm{d}t} = \frac{1}{2} \sum_{i+j \to l, i=1}^{i=l-1} k_{ij} n_i n_j - n_l \sum_{l=1}^{\infty} k_{il} n_i, \tag{1.7}$$

The first term on the right-hand side expresses the rate of formation of aggregates $l$ by the collision of any pair of aggregates, $i$ and $j$, such that $i + j = l$. Because by counting in this way each collision will be counted twice, the factor 1/2 is added. The second term represents the loss of aggregates $l$ by aggregation with any other aggregates.

Equation (1.7) can be considered as the discrete form of particle size distribution equation. The continuous form of particle size distribution is as followings,

$$\frac{\partial n(i,t)}{\partial t} = \frac{1}{2} \int_0^i k(i-j,j) n(j,t) n(i-j,t) dj - n(i,t) \int_0^\infty k(i,j) n(j,t) dj, \tag{1.8}$$

where the left-hand side indicates the rate of change of concentration of particles of size $i$, the coefficients $k(i-j,j)$ are equivalent to the collision rate constant $k_{ij}$ in Eq.(1.7). In integral expressions, thay are known as collision kernels.

By identifying the solution of Eq.(1.8), it is possible to understand the particle size distribution in terms of time. Some theoretical solutions have been reported. Meesters and Ernst et al.[198] provided the solution of Eq.(1.8) in a simple exponential form by assuming collision kernels are constant and independent of the size of the colliding aggregates. This result is in good agreement with the Smoluchowski result for the discrete case because for long times, the Smoluchowski result approaches the exponential distribution[199]. One more solution was given by Swift and Friedlander et al[200]. Their approach was known as the "self-preserving" distribution. Basing on this approach, Friedlander and Wang et al. derived a numerical solution for Brownian aggregation. The self-preserving distribution obtained with consideration of the inclusion of the dependence on aggregate size appeared to be approximately exponential form[199].

In the most recently, another approach to Brownian coagulation was proposed by Lee et al.[201, 202] that a log-normal form was assumed for the aggregate size distribution to compute the parameters of the distribution using kernels with consideration of the dependence of aggregate size. The size distribution function for particles with volume $v$ for a log-normal distribution is written as,

$$n(v,t) = \frac{N}{3\sqrt{2\pi}v\ln\sigma}\exp\left[\frac{-\ln^2(v/v_\mathrm{g})}{18\ln^2\sigma}\right], \tag{1.9}$$

where $v_\mathrm{g}(t)$ is the geometric median particle volume, $\sigma(t)$ is the geometric standard deviation, $N$ is the total number concentration. Lee et al. also showed that the value of $\sigma$ reached the limit value of 1.32 after long times and the volume distribution in reduced form could be expressed as,

$$xf(x) = \frac{1}{\sqrt{2\pi\ln2}}\exp\left[\frac{-(\ln\sqrt{2}\mathrm{x})^2}{\ln4}\right]. \tag{1.10}$$

A comparison between the exponential distribution, self-preserving distribution, and log-normal distribution has been made[199] and shown in the following graph.

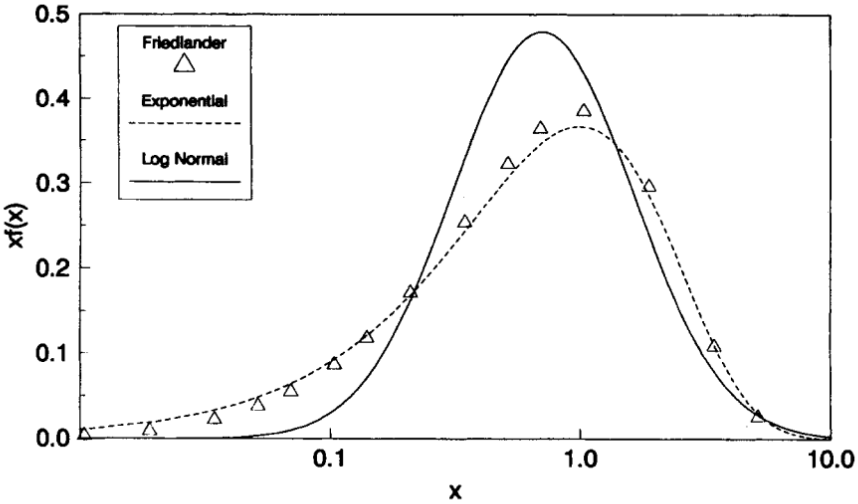

Figure 1.4: Comparison of "self-preserving" distributions, in terms of the reduced aggregate size, $x$, as $xf(x)$ versus $x$. The results are from the computations of Friedlander and Wang[203], the exponential form, and the log-normal distribution of Lee[202], Eq.(1.10).(cited of ref.[199])

Although the result of Lee has less fundamental justification than that of Friedlander, log-normal distribution is widely employed and has convenient mathematical properties[199]. Many studies of the synthesis of nanoparticles by PWD have adopted this model for the particle size distribution of the nanoparticles prepared by PWD. Experimental results have shown that log-normal distribution fits well with the particle size distribution of nanoparticles by PWD. Therefore, for the theoretical background of the particle size control proposed by Tokoi et al., an analytic solution for free molecular regime using log-normal distribution was used[204, 112]. The dependence of the geometric standard deviation ($\sigma_\mathrm{g}$) and the geometric mean particle volume ($v_\mathrm{g}$) on time ($t$) are expressed as follows,

$$\ln^2\sigma_\mathrm{g} = \frac{2}{15}\ln\left[2 + \frac{\exp\left(\frac{15}{2}Z_0 - 2\right)}{1 + \frac{5}{8}H\bar{t}}\right], \tag{1.11}$$

and

$$\frac{v_{\mathrm{g}}}{v_{\mathrm{g0}}} = \frac{\exp\left(\frac{9}{2}Z_0\right)\left[1+\frac{5}{8}H\bar{t}\right]^{6/5}}{\left[2+\frac{\exp\left(\frac{15}{2}Z_0-2\right)}{1+\frac{5}{8}H\bar{t}}\right]^{3/5}}, \tag{1.12}$$

where,

$$H = \exp\left(\frac{1}{8}Z_0\right) + 2\exp\left(\frac{5}{8}Z_0\right) + \exp\left(\frac{25}{8}Z_0\right), \tag{1.13}$$

$$\bar{t} = K{r_{\mathrm{g0}}}^{1/2}N_0 t = K{v_{\mathrm{g0}}}^{1/6}N_0 t, \tag{1.14}$$

$$K = \left(\frac{6kT}{\rho_{\mathrm{p}}}\right)^{1/2}, \tag{1.15}$$

$$Z_0 = \ln^2\sigma_{\mathrm{g0}}. \tag{1.16}$$

Here, $v_{\mathrm{g0}}$, $r_{\mathrm{g0}}$, $\sigma_{\mathrm{g0}}$, $N_0$, $t$, $k$, $T$, and $\rho_{\mathrm{p}}$ are the geometric mean of initial particle volume, the geometric mean of particle radius, the initial geometric standard deviation, the initial number concentration of particle, time, the Boltzmann constant, temperature, and the particle density, respectively. An assumption that $H\bar{t} \gg 1$, and $Z_0 \approx 0$ was made by Tokoi et al.[112]. With the same assumption, by substituting Eq.(1.14) to Eq.(1.12), we have the relation between $v_{\mathrm{g}}$ and $N_0$ and $v_{\mathrm{g0}}$ as follows,

$$v_{\mathrm{g}} \propto (v_{\mathrm{g0}}N_0 t)^{6/5}. \tag{1.17}$$

Therefore, because the geometric mean diameter ($D_1$) is proportional to cube root of geometric mean of particle volume, assuming $t$ to be constant, the relationship between $D_1$ and $N_0$ and $v_{\mathrm{g0}}$ can be written as,

$$D_1 \propto (v_{\mathrm{g0}}N_0)^{2/5}. \tag{1.18}$$

In PWD, it can be considered that $N_0$ corresponds to $D_{\mathrm{exp}}$. As a result, by comparing Eq.(1.18) and Eq.(2.13), it can be said that the experimental results obtained by Tokoi et al. in ref.[112] are in good agreement with the analytic solution of the equation of particle size distribution by a log-normal distribution.

### 1.3.3 Nanoparticles of light elements and alloys

Magnesium is one of the most abundant elements on the earth. Due to the advantages of lightweight (1.74 g/cm$^3$), high strength, and anti-corrosion, Mg is widely used for fabricating cover of electronic devices. Additionally, the high reactivity of Mg to $O_2$ made it useful for applying on the light sources. Recently, the use of Mg nanoparticles in Mg-air batteries was reported to improve the performance of Mg anode[205]. Mg nanoparticles also attracted much attention on their feasibility of hydrogen storage. The theoretical hydrogen absorption of Mg is nearly 7.7 wt%. There are many pieces of research working on hydrogen storage of Mg nanoparticles for enhancement of hydrogen absorption/desorption capacity, hydrogen absorption/desorption speed for the past decades. Wan et al. demonstrated hydrogen storage performance enhancement of Mg nanoparticles encapsulated in reduced graphene oxide[206]. Chen et al. reported the preparation of ultrathin carbon layer encapsulated Mg nanoparticles by methane plasma reaction method. At optimal condition, they obtained absorption of 4.8 wt% $H_2$ within 10 min at 573K and desorption of 5.0% $H_2$ within 20 min at 623K with an average 80 nm Mg nanoparticle covered with 3 nm ultrathin carbon shell[207]. By transition metal decoration (Ni, Ti, Pd), hydrogen storage capacity, absorption/desorption speed was improved[208, 209, 210, 211]. So far, localized surface plasmon resonance of Mg nanoparticles was also explored, besides the conventional metals (Au, Ag, Cu), which could be an alternative for expensive noble metals[212, 213]. Moreover, Mg nanoparticle was also employed in hydrogen generation[214] and light microwave absorber[215]. All of the above applications of Mg nanoparticles suggested an enormous potential of this material.

Amorphous boron has a large volumetric heat of combustion ($\sim$ 136 MJ/kg), which has the potential for use as a fuel additive. Additionally, $^{10}$B has a large thermal neutron capture cross-section (3840 barns), which is useful for neutron capture therapy[216]. Recently, several methods were used to prepare B nanoparticle[217, 218, 219], many of them aim for the application of fuel combustion. Nano-sized boron was reported to enhance 70% in the energy content and decrease the 15% boiling point of aviation turbine kerosene fuel[220]. Additionally, B nanoparticle was also reported to be used in textiles for antibacterial purpose[221]. So far, a boron-loaded polymeric sensor using boron nanoparticles for direct detection of the thermal neutron was reported[222]. Also for the application of neutron capture therapy, the production of boron nanoparticles by ultrasonication in an aqueous medium is described[223]. Beside elemental boron nanoparticle, nanoparticle of boron-containing compounds such as $B_4C$, BN, transition metal borides ($TiB_2$, $ZrB_2$, $WB_3$/$WB_4$). These compounds are especially well-known in the ceramic field. In general, these compounds has high melting temperature, high hardness, oxidation, and corrosion resistance, which are suitable for the use in harsh environment. Consolidation of these compounds is usually done by various sintering techniques: hot-press, spark plasma sintering, and pressureless sintering. Since their melting temperatures are quite high, sintering temperatures are also high, which may promote grain growth. By using starting materials as nano-sized powder, lower sintering temperature and smaller grain size are attributed. Synthesis of this nanosized powder normally requires high-temperature methods[224, 225, 226].

Besides magnesium, aluminium is also one of the lightest metals with a density of 2.7 g/cm$^3$. Similar to B, Al also has large volumetric heat of combustion ($\tilde{8}1$ MJ/kg). As a result, Al nanoparticle is especially potential for combustion applications such as rocket propellant[227, 228]. The combustion behavior of Al nanoparticles was also actively investigated [229, 230, 231, 232, 233, 234]. Additionally, plasmon resonance properties of Al nanoparticles in the ultraviolet range were also explored[235, 236, 237]. There are numerous ways to fabricate Al nanoparticle including solid, liquid, vapor phase[238, 239, 240, 241].

## 1.4 Problem statements and study purposes

First, in order to consolidate a ceramic pellet, it is widely known that the starting powder plays an important role in the sintering behavior of the product. The decrease of particle size of starting powder has the effect of reducing the sintering temperature, which saves energy consumption. However, for transition metal borides, the effects of different sizes of starting powder on the monolithic transition metal boride sintering and reactive transition boride sintering have not been discussed.

Second, for the sake of reducing the sintering temperature of transition metal boride, by which reducing power consumption and achieving desirable phase (metaphase) of transition metal boride pellets, using nano-sized powder as a starting material is considered to be a feasible solution. However, by conventional methods for synthesizing NPs of transition metal borides, considerably large power consumption is required, which may not improve the net power consumption for the whole process of synthesis of transition metal boride ceramics. As a result, it is necessary to adopt single-step, cost-effective, and high-energy conversion efficiency methods to synthesize NPs of transition metal borides. PWD is such a method, however, although various compounds of NPs have been synthesized by PWD, for example, oxides, nitrides, carbides by conducting PWD in the ambiance of $O_2$/air, $N_2$/$NH_3$, $CH_4$/organic vapor, respectively, NPs of borides have never been reported. Using PWD in boron-containing gas like diborane ($B_2H_6$), decaborane ($B_{10}H_{14}$) or boron trichloride ($BCl_3$) is an imaginable method. Nevertheless, due to the toxicity and/or flammability of those gases/vapors, appropriate treatments for safety are required and make the synthesis process more complicated and costly. This limitation is the barrier to synthesize NPs of transition metal borides by PWD.

Third, based on the literature survey in the section 1.3.2.2, it can be considered that a wide range of elements has been subjected to exploding wire as well as PWD for nanoparticle synthesis purposes. Most of them are transition metals or post-transition metals (Al, Sn, Pb), some of them are metalloids (Si, Ge). Mg is the only one belonging to alkaline earth metals which have been examined by PWD. On the other hand, metals are classified as class I (Cu, Ag, Al, Au, Sn, Zn, Cd) and class II (W, Mo, Pt, Ni, Fe, and Ti) for their different behavior in terms of exploding wire. This classification is also considered to be related to the characterization of nanoparticles synthesized by PWD due to the difference in heating effect. As a result, although Mg nano/submicron particles have been already prepared by PWD, due to large difference in atomic mass, boiling point, and heat of vaporization compared to metals classified in both class I and class II, whether and how Mg nanoparticle is different from other metal's ones has not been clarified yet.

Finally, the particle size determining equation proposed by Tokoi et al.[112] is considered to be significant progress on metallic nanoparticle synthesis by PWD. However, until now, this equation has been verified by only experimental results of Cu, Ag, Ni, and Pd nanoparticles. On the other hand, according to the aforementioned classification of metals in PWD, these metals are included in class I (Cu, Ag) and class II (Ni, Pd), hence, it is probably different for the case of Mg. When the particle size determining equation was proposed, the proposal of plasma/vapor density was given based on the theory of coagulation of particles by Brownian motion during the nanoparticle formation process. After that, by considering the different heating effects on different metals (class I or II), Sato et al. modified the equation by adding $K_{\mathrm{p}}$ factor without affecting previous results and provided experimental evidence of Pd nanoparticle. However, nucleation has not been considered yet. In particular, the important factors affecting the nucleation process including the critical size, the temperature, and the saturation at the time of nucleation for metals should be discussed to predict the particle size of various metal NPs.

Basing on the problem statements addressed above, there are four main topics of this research as follows,

1. Discussing the effects of different sizes of starting powder on the monolithic transition metal boride and reactive transition metal boride sintering.
2. Synthesis of NPs of transition metal boride by a one-step, cost-effective method.
3. Clarifying the particle formation of light elements (Mg and Al) by PWD.
4. By applying the case of Mg and Al in particle size determining equation by Tokoi et al. and considering a nucleation process in the particle size determining equation, confirming the validity of the equation and proposing a modification if necessary.

## 1.5 Composition of the present study

The present study composes of four chapters, namely, introduction, methodology, results and discussion, and conclusions.

First, chapter 1 including this section gave an introduction to the present study. This chapter began with general information and motivation for this study regarding nanoparticle synthesis of light elements. Subsequently, a literature survey including approaches for nanoparticle synthesis, PWD as a nanoparticle synthesis method accompanying with the history of its preceding exploding wire, particle size control by PWD, nanoparticles of light element-synthesis methods, and their application was carried out. This literature survey is a fundamental background to identify the objectives of the present study in the following section. Finally, problems that needed to be solved were pronounced and the objectives of the present studied were briefly described.

Second, chapter 2 provides information regarding the methodology necessarily used to accomplish this study. The methodology includes experimental setups for pulsed wire and powder discharge, spark plasma sintering for ceramic pellet formation. Next, information concerning raw materials and experimental conditions used in the study are listed. Subsequently, experimental procedures regarding experiments of pulsed wire discharge, pulse discharge of compacted powder, and spark plasma sintering are gone through. Finally, analytical methods adopted for characterizing nanoparticles and sintered bodies, and hydrodynamic behavior calculation for simulating temperature of plasma/vapor during the experiment of pulsed wire discharge are given in detail.

Third, chapter 3 shows results and discussion to fulfill the purposes of the present study. First, spark plasma sintering was used to fabricate ceramics pellets to discuss the effect of different sizes of starting powder on the monolithic transition metal boride and reactive transition metal boride sintering. Then, synthesis of NPs of B and transition metal borides by PWD and pulsed discharge of compacted powder are described and carefully characterized by using a combination of XRD, TEM images, EDS, and Raman spectroscopy. Subsequently, the preparation of NPs of light elements (Mg and Al) by PWD are described and discussed on aspects of particle formation (discharge waveforms, deposition energy) and material evaluation (phase, morphology, particle size distribution by XRD, TEM). Then, the introduction of prepared Mg nanoparticles to the particle size prediction equation proposed by Tokoi et al. and the inconsistency is expressed. Finally, calculation of the critical radius of metals and the appropriateness are discussed using experimental and simulated results, along with the new equation for particle size prediction by PWD is proposed.

Eventually, chapter 4 gives a summary of the results obtained in chapter 3 and combining with the objectives described in chapter 1. An assessment is provided and future plans need to be done with the present study are discussed.

# Chapter 2

# Methodology

## 2.1 General

This section describes experimental setups and electrical circuits adopted in pulsed wire and powder discharge for nanoparticle synthesis and spark plasma sintering for fabricating ceramic pellets. Additionally, calculations of energy deposition into the wire are presented. Information about raw material as well as experimental conditions is listed. Finally, analytical methods for characterization of nanoparticle and ceramic pellets such as X-ray diffraction, SEM, TEM, high-speed camera, Raman spectroscopy, Vickers hardness are described in detail.

## 2.2 Experimental setups for pulse wire and powder discharge

Experimental setups and electrical circuits for pulse wire and powder discharge, following with measurement of inductance, current, and voltage measurement, and energy deposition into the wire are described as following.

### 2.2.1 Experimental setups and electrical circuit

Experimental setups and electrical circuit of the present study are shown in Fig. 2.1. In Fig. 2.1(a), the experimental setup includes an airtight stainless steel (SUS304) chamber (V=23 l) with a stainless steel lid opened from the top, a simple RLC circuit shown in Fig.2.1 consisting of a high voltage DC power supply (Kikusui, PHS 35K-3), 3 capacitors (each has a capacity of 10 µF) in parallel which could be added or removed to adjust the capacity, a gap switch with a controller. Additionally, the chamber could be vacumed through 2 gas outlets, one was used for sucking the air inside the chamber prior to experiments and could be opened or closed by a rotating valve, the other was used for collecting synthesized powder via a membrane filter (Omnipore, pore size 0.1 µm and 0.2 µm). There was one more port to inlet ambient gas and air with Swagelok valves. Voltage was measured by using 2 voltage probes (Tektronix P6015A). Current was measured by a current transformer (Pearson 101). The voltage probes and the current transformer were connected to a digital oscilloscope (Yokogawa DLM2024) to monitor voltage and current waveforms during the experiments. A high-speed camera (Photron FASTCAM SA4) with shutter speed up to 500,000 fps was set in front of the viewport and around 4 meters away from the wire as shown in Fig. 2.1(a). An optical lens (Nikon 135mm f/2.8) was mounted on the high-speed camera and a neutral density filter (Kenko PRO-ND500) was set on the

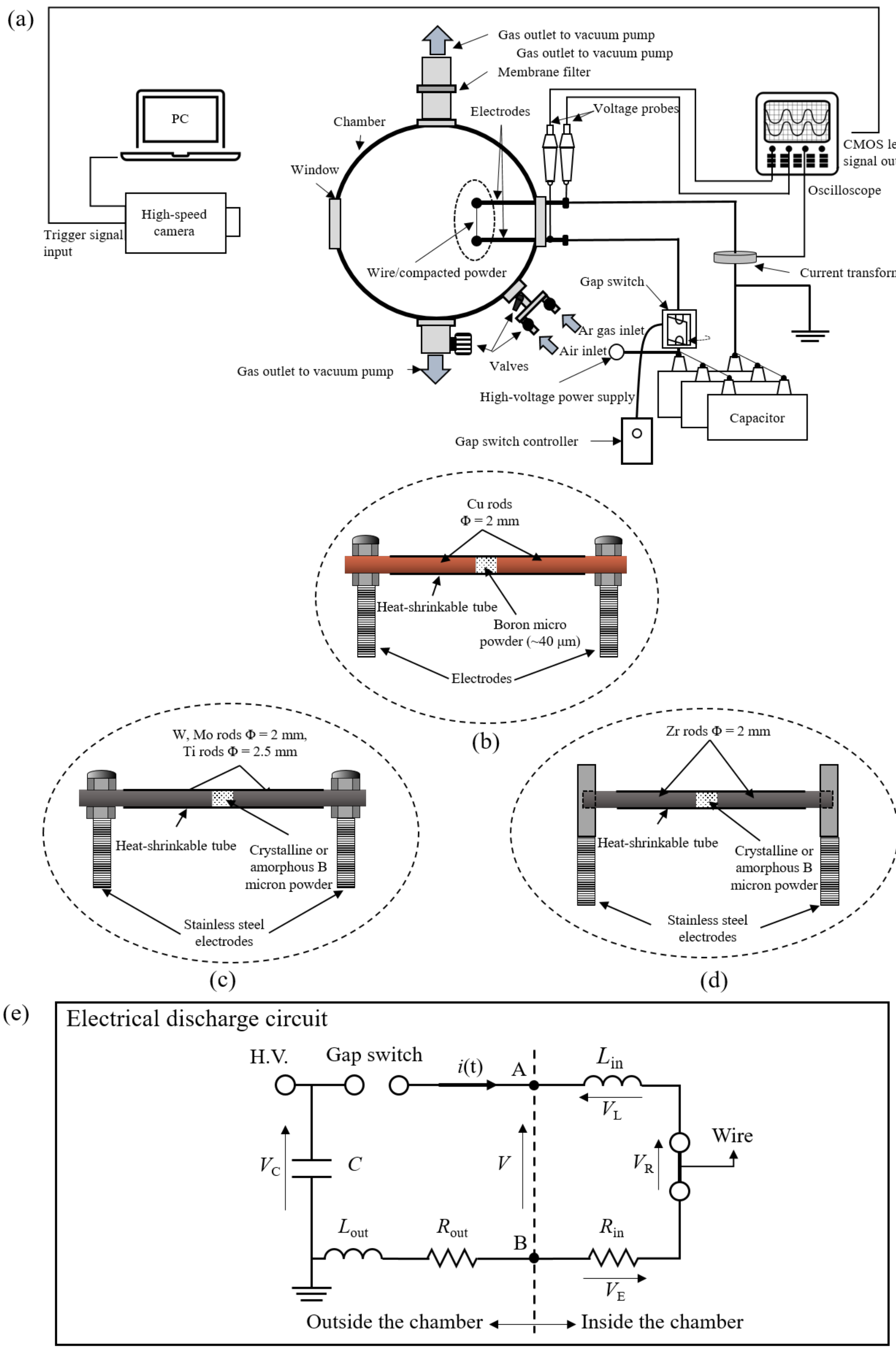

Figure 2.1: (a)Experimental setup used for pulsed discharge of wire and compacted powder for nanoparticle synthesis. For pulsed discharge of compacted powder, experimental setup at the position of electrodes circled by dash line was changed by (b) for B nanoparticle, (c) for nanoparticle of Ti, Mo, W borides, (d) for nanoparticle of Zr boride(improved setup for suppressing of impurity). (e) Electrical discharge circuit commonly used for both pulsed discharge of wire and compacted powder

lens to cut off highly intensive light from the pulsed wire discharge for better observation. Depending on the intensity of emitted light from different pulsed discharge experiments, the aperture of the lens was adjusted appropriately. To assure the pulsed discharge was recorded properly, the high-speed camera was triggered by using a CMOS level signal output from the oscilloscope. Whenever the oscilloscope received a signal of voltage, the oscilloscope outputted a 3.3V CMOS level signal to trigger the high-speed camera. For pulsed discharge of compacted powder, crystalline/amorphous B powder was compacted inside a carbon-made heat-shrinkable tube with 2 rods of Ti, Mo, W, or Zr from 2 sides so that the compacted powder was well-contacted with metal rods. These setups were clamped on the electrodes inside the chamber for pulsed discharge. With the case of using Zr rods, for the purpose of suppressing impurity of Fe which could be caused by the poor contact between metal rods and SUS nuts and electrodes, a pair of different electrodes was prepared by drilling through the electrodes. By this setup, contact between metal rods and stainless electrodes was improved and problems of Fe impurity could be solved.

Electrical circuit adopted in PWD experiment is a simple RLC circuit and is shown in Fig. 2.1(e). When the gap switch is closed and electrical current starts to discharge through the circuit ($t = 0$), equation of current in terms of time is shown as follows,

$$L\frac{d^2i}{dt^2} + R\frac{di}{dt} + \frac{1}{C}i = V_\mathrm{c}, \tag{2.1}$$

where

$$R = R_\mathrm{out} + R_\mathrm{in} + R_\mathrm{wire} = R_\mathrm{const.} + R_\mathrm{wire}, \tag{2.2}$$

$$L = L_\mathrm{out} + L_\mathrm{in} + L_\mathrm{wire} = L_\mathrm{const.} + L_\mathrm{wire}, \tag{2.3}$$

$$V_\mathrm{c} = Q_0/C, \tag{2.4}$$

Here, $R$ is the total resistance, $R_\mathrm{const.}$ is the resistance of the circuit including resistance of inside and outside of the chamber, $R_\mathrm{wire}$ and $L_\mathrm{wire}$ is the resistance and inductance of wire, respectively, which may change during PWD, $L$ is the total inductance including inductance of inside $L_\mathrm{in}$, outside $L_\mathrm{out}$ of the chamber, and inductance of wire $L_\mathrm{wire}$. The solution of Eq. (2.1) is shown as follows,

- $R^2 < 4L/C$

$$i(t) = \frac{Q_0}{LC\beta}e^{-\alpha t}\sin(\beta t), \alpha = \frac{R}{2L}, \beta = \sqrt{\frac{1}{LC} - \left(\frac{R}{2L}\right)^2}, \tag{2.5}$$

- $R^2 > 4L/C$

$$i(t) = \frac{Q_0}{LC\beta}e^{-\alpha t}\sinh(\beta t), \alpha = \frac{R}{2L}, \beta = \sqrt{\left(\frac{R}{2L}\right)^2 - \frac{1}{LC}}, \tag{2.6}$$

- $R^2 = 4L/C$

$$i(t) = \frac{Q_0}{LC\beta}te^{-\alpha t}, \alpha = \frac{R}{2L}. \tag{2.7}$$

Three types of the above equations are classified as underdamped, overdamped, and critically damped oscillation, respectively.

### 2.2.2 Measurement of inductance

Inductance was measured by shorting the circuit with a 3 mm diameter Cu rod with a voltage of 1000 V. This charging voltage $V_\mathrm{c}$ provided insufficient energy for the wire to vaporize. With unexploding wire, inductance is negligibly small, hence $L_\mathrm{wire} = 0$. As a result, the value of each element in the circuit of PWD is shown in Table 2.1

Table 2.1: Values of elements in the PWD circuit

| | |
|---|---|
| $\mathrm{L_{in}}$ | 250 nH |
| $\mathrm{L_{out}}$ | 1020 nH at C=10 µF, 900 nH at C=20 µF, 850 nH at C=30 µF |
| $\mathrm{R_{const.}}$ | 0.07 Ω |
| $\mathrm{R_{in}}$ | 1 mΩ |

### 2.2.3 Current, voltage measurement and energy calculation

In order to calculate deposition energy, it is necessary to calculate voltage dropping on the wire and current passing through the wire during the PWD experiment. First of all, measured voltage ($V(t)$) obtained by subtracting voltages monitored by the voltage probes at A and B in Fig. 2.1(e). From Fig. 2.1(e), $V(t)$ is defined by,

$$V(t) = V_\mathrm{R}(t) + V_\mathrm{E}(t) + V_\mathrm{L}(t), \tag{2.8}$$

where $V_\mathrm{R}(t)$, $V_\mathrm{L}(t)$, and $V_\mathrm{E}(t)$ are the voltage dropping on the wire, the inductance, and the resistance inside the chamber, respectively. From Eq. (2.8), $V_\mathrm{R}(t)$ can be expressed as,

$$V_\mathrm{R}(t) = V(t) - \left(R_\mathrm{in} i(t) + L_\mathrm{in}\frac{di(t)}{dt}\right). \tag{2.9}$$

By obtaining $V(t)$ and $i(t)$ from the experiments, $V_\mathrm{R}(t)$ in Eq. (2.9) can be calculated. The deposition energy ($E(t)$) during PWD is defined as follows,

$$E(t) = \int_0^t V_\mathrm{R}(t) \times i(t)dt. \tag{2.10}$$

A typical voltage-current waveform of PWD is shown in Fig. 2.2. The process of PWD can be divided into two stages: wire heating and arc discharge. At the wire heating stage, current increases with the phase transformation of the wire solid-liquid then decrease when the wire is vaporized. At the end of the wire heating stage, the voltage waveform attains its peak, then drops remarkably and oscillating due to the appearance of the arc discharge (plasma). At the arc discharge, the current also oscillates and is controlled by the parameters R, L, C of the circuit. The energy deposited into the wire up to the end of the wire heating stage is defined as $E_\mathrm{p}$. The energy deposited into the arc discharge (plasma) is defined as $E_\mathrm{a}$. Previously calculated deposition energy ($E(t)$) up to the end of the process is the total of $E_\mathrm{p}$ and $E_\mathrm{a}$, and is defined as $E_\mathrm{t}$. Besides, $E_\mathrm{v}$ is defined as vaporization energy of the wire. $K_\mathrm{p}$ is the ratio of $E_\mathrm{p}$ and $E_\mathrm{v}$, which indicates whether the wire has been completely vaporized or not, i.e. if the wire has been already completely vaporized, $K_\mathrm{p}$ should be equal or larger than 1. For the case $K_\mathrm{p}$ is larger than 1, the exceeded energy is considered to be dissipated in the surrounding environment.

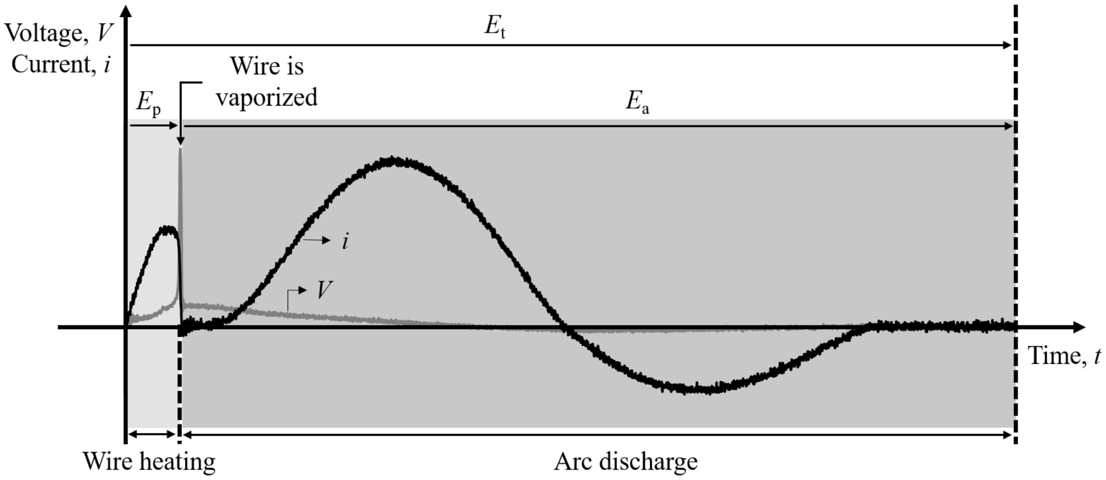

Figure 2.2: Typical voltage-current waveform by PWD and related parameters

## 2.3 Spark Plasma Sintering for fabricating ceramic pellets

Spark plasma sintering (SPS) experiments were carried out at Nanko Laboratory, Nagaoka University of Technology (NUT) and Structural Non-oxide Ceramics Group, National Institute for Materials Science (NIMS), Tsukuba. At NUT, commercial $TiB_2$ powders with different particle sizes were used to fabricate $TiB_2$ ceramic pellets. At NIMS, commercial W and B powders were employed to fabricate tungsten borides ceramic pellet under various conditions. Information on SPS instruments is shown in Table2.2. Conditions regarding experiments are described in section 3.2 for convenience.

Table 2.2: Information about SPS instruments

| | **Nanko Lab, NUT** | **Structural Non-oxide Group, NIMS** |
|---|---|---|
| **Manufacturer** | Sinterland Inc. | Sumitomo Coal Mining Co. Ltd |
| **Model No.** | LABOX$^{TM}$-1550i75S | Dr. Sinter SPS-1030 |

## 2.4 Raw materials

This section provides information on wires, rods, and powders used as raw materials in the present study.

### 2.4.1 Wires

Al wires ($\phi$=0.1 mm, 99.9%), Mg wires ($\phi$=0.1, 0.3, 0.5 mm, 99.95%), Cu wire ($\phi$=0.1 mm, 99.9%) were purchased from The Nilaco Corporation. Boron wire ($\phi$=0.1 mm) was purchased from Goodfellow Japan.

### 2.4.2 Rods and powders

Micron-sized crystalline B powder ($\approx$ 40 µm) was purchased from Soekawa Co., Ltd. Micro-sized amorphous B powder ($\leq$ 1 µm, $\geq$ 95%) was purchased from Sigma-Aldrich as a raw material of pulsed discharge of compacted powder and SPS for tungsten borides ceramic pellets fabrication. Also as a raw material for SPS for tungsten borides ceramic pellets, W powder (0.45-0.58 µm, $\geq$ 99.9%) was purchased from Japan New Metal Co., Ltd.. Metallic rods employed as electrodes of pulsed discharge of compacted powder were purchased from Nilaco Corporation (Cu rods($\phi$=2 mm, 99.9%), Ti rods ($\phi$=2.5 mm, 99.9%), Mo rods ($\phi$=2 mm, 99.95%), W rods ($\phi$=2 mm, 99.95%), and Zr rods ($\phi$ =2 mm, 99.2%)).

## 2.5 Experimental procedures

Here, experimental procedures of pulsed wire discharge, pulsed discharge of compacted powder, and spark plasma sintering experiments are described.

### 2.5.1 Pulsed Wire Discharge

In the present study, PWD experiments were carried out using Al, Mg, B, and Cu wires. Prior to experiments, wires were cleaned by alcohol to avoid contaminants. The procedure of a typical PWD experiment is described below,

1. Wire was set between two electrodes by clamping it with SUS304 nuts inside the experiment chamber as shown in Fig. 2.1.
2. Lid was closed and the chamber was vacuumed by a rotary pump or an oil-free scroll pump to around 10 Pa. Then, Ar gas was introduced into the chamber at 50 kPa and one more time vacuumed to around 10 Pa. This process was repeated 3 times at each condition to purge vapor sticking on the chamber wall.
3. Ambient gas (Ar/$N_2$) was introduced to the chamber at the desired pressure.
4. High-voltage DC power supply was switched on and started to charge capacitors via a load resistor at the desired voltage. Charging was carefully done so that the charging voltage does not exceed the working voltage of the capacitors (6.5 kV).
5. By closing the gap switch with a controller, a large pulsed current underwent the wire. The process of pulsed wire discharge was described in detail in the section 1.3.2.2.
6. At the same time as PWD experiments, voltage-current waveforms and high-speed images were taken by a digital oscilloscope and a high-speed camera. Regarding these measurements, a description was provided in the section 2.2.1.
7. After the pulsed discharge, the powder was collected through a membrane filter by sucking the ambient gas in the chamber via another route rather than the route for primary vacuuming by changing the vacuum route.
8. The membrane filter was separated from the experiment chamber with a locking door. This locking door was closed whenever experiments are being done and opened for collecting powders.
9. After collecting powder, the locking door was closed, and the air was introduced into the chamber at atmospheric pressure to supply wire.
10. Experiments were repetitively done until the obtained powder was estimated to be sufficient for characterization.
11. After synthesizing sufficient powder, the membrane filter was ejected and powder was collected by shaving the membrane filter. The collected powder was stored inside a sample bin for further characterization.

12. Last but not least, remaining electrical charges at the capacitors were connected to the ground carefully for the sake of other people's safety.

### 2.5.2 Pulse Discharge of Compacted Powder

Basically, the pulsed discharge of compacted powder is similar to pulsed wire discharge. However, before discharging, powder has to be compacted in advance. To compact powder for experiments, the first powder was inserted into a carbon-made heat-shrinkable tube ($\phi$=2.1 mm for $\phi$=2 mm for Cu, Mo, W, Zr rods and $\phi$=2.6 mm for Ti rods). Then, metallic rods were used to compact powder from two ends. Metallic rods were stabilized for tight contact with powder by heating the heat-shrinkable tube from its outside surface with a soldering iron. The heat-shrinkable tube was heated, shrank, as a result, stabilized the powder and metallic rods. The subsequent procedure was identical to that of pulsed wire discharge described in the previous section.

### 2.5.3 Spark Plasma Sintering

For SPS experiments, first, starting powders were prepared, then, powders were subjected to SPS for sintering. The preparation of starting powders was done by either dry mixing or wet mixing. Dry mixing was applied for mixing $TiB_2$ powders with different particle sizes. Wet mixing was applied for mixing W powder and amorphous B powder. Procedures for dry mixing and wet mixing are described as following.

- Dry mixing procedure
    1. Weighting two components for desired relative ratio.
    2. Pouring powders of two components into a plastic bottle.
    3. An amount of $ZrO_2$ balls ($\phi$=5 mm) which was around 4 times of powder's weight was pouring into the plastic bottle together with the mixture of powders. Caps were closed tightly.
    4. The bottle was placed on a ball milling machine at a rotational speed of approximately 270 rpm for 24 hours.
    5. After 24 hours, the mixture of powders and $ZrO_2$ balls was separated by using a sieve with mesh size 300 µm.
    6. Mixture of powder was collected and $ZrO_2$ balls were cleaned by an ultrasonication equiptment.
- Wet mixing procedure
    1. Weighting two components for desired relative ratio.
    2. Pouring powders of two components into a plastic bottle.
    3. An amount of $ZrO_2$ balls ($\phi$=10 mm) which was around 4 times of powder's weight was pouring into the plastic bottle together with the mixture of powders.
    4. 60 ml methanol was poured into the bottle. Caps and tapes were used to seal tightly to avoid leaks during ball milling.
    5. The bottle was placed on a ball mill machine at a rotational speed of approxi-

mately 270 rpm for 24 hours.

6. After 24 hours, the mixture was taken out and poured into a beaker.
7. After that, the mixture was subjected to an evaporator to separate methanol from the mixture of powders. Subsequently, the mixture was kept inside a drying furnace overnight for the complete vaporization of liquid matters.
8. After-drying mixture was pulverized into fine powder for SPS.

Next, the procedure of SPS experiments is described. Basically, the procedure is identical at NUT and NIMS, hence, the different points are provided in brackets. The procedure of SPS is as following,

1. For the preparation steps, switching on the main breaker (only in NUT), opening a cooling water valve, switching on the power of the SPS machine, switching on the SPS machine control unit was done in order. Values of z-axis displacement, temperature, voltage, current were monitored by a computer (at NUT) or a data logger (at NIMS).
2. Since the unused status of the chamber of SPS was a vacuum, one needed to introduce air inside the chamber to open it. Usually while waiting for this step, preparing the sample was done.
3. Graphite foils were prepared to prevent the contact of powder and graphite die and punches.
4. Depending on the size of pellets, starting powder was weighed and poured into the die and punches settings, then, they were pressed axially by a manual hydraulic press at an appropriate pressure for the powder to get cylinder shape, subsequently subjected to SPS machine as shown in Fig. 2.3.
5. After the air fulfilled the chamber, the setting of punches, dies, and powder was placed on the bottom spacers in the chamber. Next, upper spacers were placed on the top of the setting. It was required that a small hole for temperature monitoring could be seen from the viewfinder of a thermal radiation camera placed at a viewport of the chamber.
6. The whole system was moved all the way up until the spacer at the top contact with the upper electrode of SPS.
7. The aforementioned small hole was necessarily confirmed one more time for the precise temperature monitoring.
8. The lid of the chamber was closed and the rotary pump was switching on to evacuate the chamber. At NUT, after about an hour, the pressure was approximately 6 Pa. At NIMS, after 15 min, it was approximately 10 Pa, then, an oil diffusion pump was connected to continuously vacuum the chamber up to approximately $5 \times 10^{-3}$ Pa.
9. While waiting for the vacuum, the sintering program (temperature, pressure, holding time) was set. When the pressure reached the desired value, the sintering process was started by switching on the sintering function.
10. When the temperature rose to around 800°C, it should be checked in the viewfinder

of the thermal radiation camera if the small hole was being viewed at the center or not.

11. During the SPS experiment, it was important to monitor the z-axis displacement, programmed temperature (PV), and obtained temperature (SV) to assure proper sintering process. A large difference of PV and SV may lead to failure of the process or even damage of the SPS machine.

12. After the program ended, the sintering function was switching off at the control panel. Subsequently, about 1 hour of waiting for the sample to cool was required. The setting was lowered for quicker cooling speed. At NIMS, $N_2$ gas was introduced for cooling the sample.

13. The sample was taken out of the setting. Graphite foils on the surface of the sample were shaved, then the sample was subjected to further characterization.

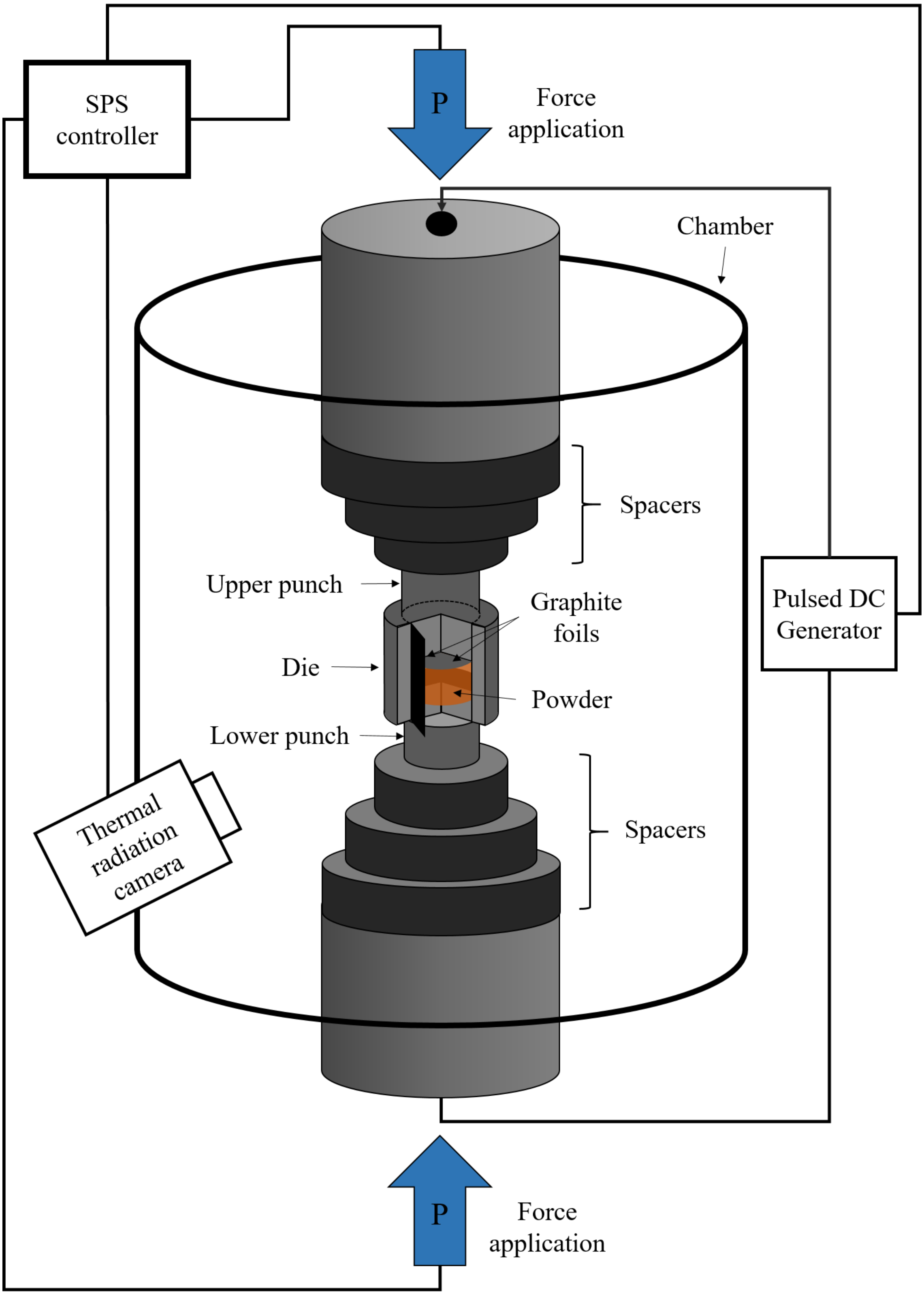

Figure 2.3: Spark plasma sintering experimental setup

## 2.6 Analytical methods for characterization of nanoparticles and sintered pellets

### 2.6.1 Powder X-ray diffraction

Powder X-ray diffraction (XRD) was employed in almost all the samples synthesized for phase composition analysis in the present study. There are 3 XRDs being used, two of them are located at NUT and the remaining is at NIMS. At NUT, they are Rigaku RINT2000, Cu-K$\alpha$ radiation of 0.15418 nm, 50 kV, 300 mA, and Rigaku Miniflex 600, 40 kV, 15 mA. At NIMS, the XRD instrument was similar to the Rigaku Miniflex 600 at NUT.

For the powder sample, the powder was placed in a small hole drilled on the surface of a zero diffraction Si crystalline holder. Then the powder was pressed to compact in the hole so that the pressed surface was smooth and matched with the surface of the holder.

For the ceramic pellet sample, the pellet was stabilized by an Al holder, a piece of glass, and clay so that the surface of the pellet was matched with the surface of the Al holder.

For quantification of the NPs purity, the reference intensity ratio (RIR) or a calibration-curve method was carried out. With the latter method, commercially available Cu and B powders were mixed at some compositions and XRD peak intensities were measured.

### 2.6.2 Scanning electron microscope

Scanning electron microscopes (SEM) adopted in the present study include a field emission scanning electron microscope (FE-SEM) (JEOL JSM-7500F) equipped with an energy dispersive X-ray Spectroscopy (EDS) detector and a desktop SEM (HITACHI TM3030). SEMs were used to observe nanoparticles prepared by PWD, micro-structure of pellet synthesized by SPS.

### 2.6.3 Transmission electron microscope

Transmission electron microscopes (TEM) used in the present study include a TEM (JEOL 2000FX) at an accelerated voltage of 200 kV and a field emission transmission electron microscope (FE-TEM) (JEOL JEM-2100F) at an accelerated voltage of 200 kV equipped with an EDS detector. In this study, TEMs were used for numerous analyses shown below.

#### 2.6.3.1 Bright Field Image

Bright-field image (BFI) was used in most of the samples prepared by PWD. By BFI, it was possible to identify the morphology and size of the particles. Then, BFI could be used to measurement of particle size distribution.

#### 2.6.3.2 Dark Field Image

Darkfield image (DFI) was used to identify the position of ultrafine MgO particles (several nanometers) together which the presence of Mg particles (several tens of nanometer). A DFI was obtained by moving objective aperture to the position of diffracted spots corresponding to diffraction of MgO in selected area diffraction (SAD) image.

#### 2.6.3.3 Selected Area Diffraction

Selected area diffraction (SAD) was used to identify the phase composition of the sample at the area of interest while observing using TEM.

#### 2.6.3.4 Energy Dispersive X-ray Spectroscopy

Energy-dispersive X-ray spectroscopy (EDS) was used to identify elements (from B to U) included in the sample at the area of interest while using TEM. Both qualitative and quantitative analyses could be done with EDS.

#### 2.6.3.5 Lattice image

Lattice images were used to identify the lattice fringes of the crystallites of the particles observed by TEM. By the images, it was possible to specify the phase composition of a single nanoparticle individually.

#### 2.6.3.6 Electron Energy Loss Spectroscopy

Electron Energy Loss Spectroscopy (EELS) is known as spectroscopy method for measuring atomic composition, chemical bonding, and valence and conduction band electronics properties by radiating a beam of electrons with a known, narrow range of kinetic energies into a sample, measuring the amount of energy loss via an electron spectrometer, and analyzing the causes of energy loss. In terms of atomic composition analysis, compared to EDS, EELS works best with relatively light elements. In the present study, EELS was used to investigate whether oxygen was present in the raw material of $\mathrm{TiB_2}$ or not.

### 2.6.4 Particle size distribution

Particle size distribution (PSD) was carried out as a inevitable characterization of nanoparticles prepared by pulsed discharge of wire and powder. PSD was obtained by doing a statistic of size of particle synthesized by PWD. Sizes of around 1000 particles were taken every condition to investigate the PSD. Then, the geometric mean diameter of particles are defined as following,

$$f(d) = \frac{1}{\sqrt{2\pi}d\mathrm{log}\sigma_\mathrm{g}}\mathrm{exp}\left(-\frac{(\mathrm{log}d-\mathrm{log}D_1)^2}{2\mathrm{log}^2\sigma_\mathrm{g}}\right), \tag{2.11}$$

where

$$\mathrm{log}\sigma_\mathrm{g} = \sqrt{\frac{\sum n_\mathrm{i}(\mathrm{log}d_\mathrm{i}-\mathrm{log}D_1)^2}{\sum n_\mathrm{i}}}, \tag{2.12}$$

$$\mathrm{log}D_1 = \frac{\sum n_\mathrm{i}\mathrm{log}d_\mathrm{i}}{\sum n_\mathrm{i}}. \tag{2.13}$$

Here, $d$ is particle size, $f(d)$ represents the lognormal distribution function, $D_1$ and $\sigma_\mathrm{g}$ are geometric mean diameter and geometric standard deviation, respectively, $n_\mathrm{i}$ and $d_\mathrm{i}$ are the number of particles with its diameter, respectively.

### 2.6.5 High-speed camera

A high-speed camera (Photron FASTCAM SA4) was used to record the time-evolution of plasma/vapor expansion during PWD experiments. The usage details of the high-speed camera were mentioned in the section 2.2.1.

### 2.6.6 Raman Spectroscopy

Raman spectroscopy instrument (Horiba Jobin Yvon, LabRAM HR-800) was adopted to identify the amorphous C in nanoparticles of borides synthesized by the pulsed discharge of compacted powder.

### 2.6.7 Archimedes density measurement

In order to measure the density of pellet fabricated by SPS, the Archimedes density measurement method was used. The procedure of measurements is described as follows,

1. A ceramic pellet after cleaning surfaces from graphite foils was weighted by electronic balance to obtain the mass of the pellet in dry condition $m_{\text{dry}}$.
2. The pellet was immersed inside a beaker of toluene for about 1 day so that toluene can infuse into the close pores of the pellet if they were present.
3. After 1 day, the pellet was picked out, slightly wiped by a piece of Kimwipe, and weighted to obtain the total mass of pellet and mass of toluene infusing into the close pore of the body $m_{\text{wet}}$.
4. Subsequently, the pellet was weighted inside toluene to obtain $m_{\text{in}}$.
5. At the same time, the temperature of toluene should be monitored.
6. Next, the volume of the pellet can be calculated as follows,

   $$V_{\text{pellet}} = \frac{m_{\text{wet}} - m_{\text{in}}}{\rho_{\text{toluene}}}, \tag{2.14}$$

   where

   $$\rho_{\text{toluene}} = 0.88412 - 9.2248 \times 10^{-4} \times T[^\circ\text{C}]. \tag{2.15}$$

7. Finally, density of the pellet can be calculated as follows,

   $$D_{\text{pellet}} = \frac{m_{\text{dry}}}{V_{\text{pellet}}}. \tag{2.16}$$

### 2.6.8 Vickers hardness

Before measuring hardness, the surfaces of the pellets were polished to a qualified roughness (nearly as gloss as a mirror). In order to test the hardness of ceramic pellets, a Vickers hardness testing equipment (Akashi MVK-H3) was used. A load of 2000, 1000, or 500 g was used in each SPS condition for testing Vicker hardness. For every load, 5 indentations were pressed for reproducibility of the measurement.

## 2.7 Hydrodynamic behavior calculation

To elucidate the temperature profile in terms of time during PWD experiments of different materials, an attempt to calculate the hydrodynamic behavior of the wire/plasma with a one-dimensional for the cylindrical geometry. The hydrodynamic motion of the PWD was solved using conventional hydrodynamic equations as the continuity, momentum, and energy conservation equations within the Lagrangian coordinate system, as follows,

$$\frac{\mathrm{d}\rho}{\mathrm{d}t} = -\rho(\nabla . \overrightarrow{u}), \tag{2.17}$$

$$\frac{\mathrm{d}\overrightarrow{u}}{\mathrm{d}t} = -\frac{\nabla p}{\rho}, \tag{2.18}$$

$$\frac{\mathrm{d}e}{\mathrm{d}t} = -\frac{p(\nabla . \overrightarrow{u})}{\rho} + E(t), \tag{2.19}$$

where $\rho$ is the mass density, $\overrightarrow{u}$ is the velocity, $p$ is the pressure, $e$ is the internal energy, and $E(t)$ is the experimentally obtained deposition energy. The thermal conduction and the radiation loss in the simulation were neglected since these effects were too small in the time range. The deposition energy was assumed to be a uniform distribution along with the radial direction. To enclose these equations, the equation of state model as QEOS was used[242]. The conditions of ambient gas species and gas pressures were set similar to those of experiments.

# Chapter 3

# Results and Discussion

## 3.1 General

This section includes four main sections which are presented in order: synthesis of ceramic pellet by spark plasma sintering, synthesis of NPs of B and transition metal borides by a pulsed discharge of compacted powder, preparation of NPs light elements (Al and Mg) by PWD, and a particle size determining equation. In each section, there are several subsections showing experimental results and corresponding discussion aiming to clarify and solve issues declared in section 1.4

## 3.2 Synthesis of ceramic pellets by spark plasma sintering

In the present study, spark plasma sintering was used as a supportive method to fabricate $TiB_2$ and tungsten boride pellets. For $TiB_2$ pellets, commercial micron-sized $TiB_2$ powder with different sizes was used as the starting powder and synthesized pellets were subjected to Vickers hardness measurements to discuss the effects of different sizes of starting powder on the monolithic transition metal boride. For tungsten boride pellets, commercial micron-sized W and amorphous B powder were used to synthesize boron-rich tungsten boride pellets and conditions of sintering to obtain single-phase along with the condition of the size of starting powder are discussed. This study is also the first step for the preparation of transition metal boride ceramic using NPs prepared by pulsed wire and powder discharge.

### 3.2.1 Titanium diboride sintering by SPS

Titanium diboride ($TiB_2$) is known as one of the ultra-high temperature ceramics (UHTC) due to its high melting temperature ($\sim$3200°), high hardness and strength at high temperatures, good thermal and electrical conductivity, high corrosion resistance and chemical stability[243, 244, 245]. These excellent properties of $TiB_2$ render $TiB_2$-based materials suitable for various applications such as wear-resistant components, cutting tools, armor, aluminum electrolysis cathodes[246]. However, the requirement of high temperature as high as 2000°C for binderless sintering monolithic $TiB_2$ has limited its feasibility for widespread applications[244, 247, 248]. Many methods for consolidation of $TiB_2$ were reported such as pressureless sintering[249, 250], hot press[247, 251, 252]. SPS[253, 254, 255]. Through various methods for consolidation of monolithic $TiB_2$, the particle size of starting powders plays an important role to obtain highly dense ceramic pellets. Khanra et al. reported the sintered body with a relative density of 97% and 86% of the synthesized nanosized powder and commercial micron-sized powder($\sim$ 10µm), respectively, at 1950°$C$ by pressureless sintering. Demirskyi et al. described the fabrication of a nearly fully dense body of 99.2% theoretical density and Vickers hardness of 23 GPa at 1700°C with nano-sized starting powder by microwave sintering[256]. Rabiezadeh et al. reported synthesis and sintering monolithic TiB$_2$ nanopowders by the hot press at 1700°C, which yielded the sintered body with a relative density attaining 92% and Vickers hardness of 25.9 GPa[250]. Recently, a study adopting SPS with submicron-sized starting powder was reported by Balci et al.[257]. They reported the densest body reached 96.7% theoretical density and Vickers hardness of 27.4 GPa at 1500°C, pressure 60 MPa, and keeping time 15 minutes. Without using nano-sized powders as starting material, the lowest sintering temperature for a dense body is 1400°C with relative density of 96.1% by SPS, however, due to the formation of secondary phase TiB, Vickers hardness decreased to as low as 17.4 GPa[258]. Hence, for a single-phase dense TiB$_2$ sintering body, at least 1800°C (SPS, 1-2µm starting powder, 97.6% theoretical density) is required[253]. With a larger particle size such as 5.68 µm[255] and $\sim$ 10 µm[249], relative density only attained 80% and 86% at 1800°C and 1950°C by SPS, respectively. In this section, an investigation on the relationship between the size of starting powder and the sintering behavior of monolithic TiB$_2$ is carried out. Commercial TiB$_2$ powder of two different sizes $\sim$10 µm and $\sim$ 1.87 µm were employed. First, the sintering behavior of each kind of powder at elevated temperatures was studied. Then, a small powder is mixed with a large powder to investigate the effect of mixing on attainable density and Vickers hardness. The table 3.1below shows the experimental conditions for sintering of TiB$_2$.

Table 3.1: Experimental conditions for sintering of TiB$_2$.

| | Experiment 1 | Experiment 2 | Experiment 3 |
|---|---|---|---|
| Size of TiB$_2$ powder | 10 µm | 1.87 µm | 1.87 µm:30%+10 µm:70%<br>1.87um:70%+10um:30% |
| Temperature [°C] | 1550, 1750, 1900 | 1600, 1700, 1900 | 1900 |
| Pressure [MPa] | 60 | | |
| Keeping time [min] | 10 | | |
| Sintering medium | Vacuum ($\sim$6 Pa) | | |
| Heating rate | 100 K/min | | |

#### 3.2.1.1 Sintering using ∼ 10 µm powder

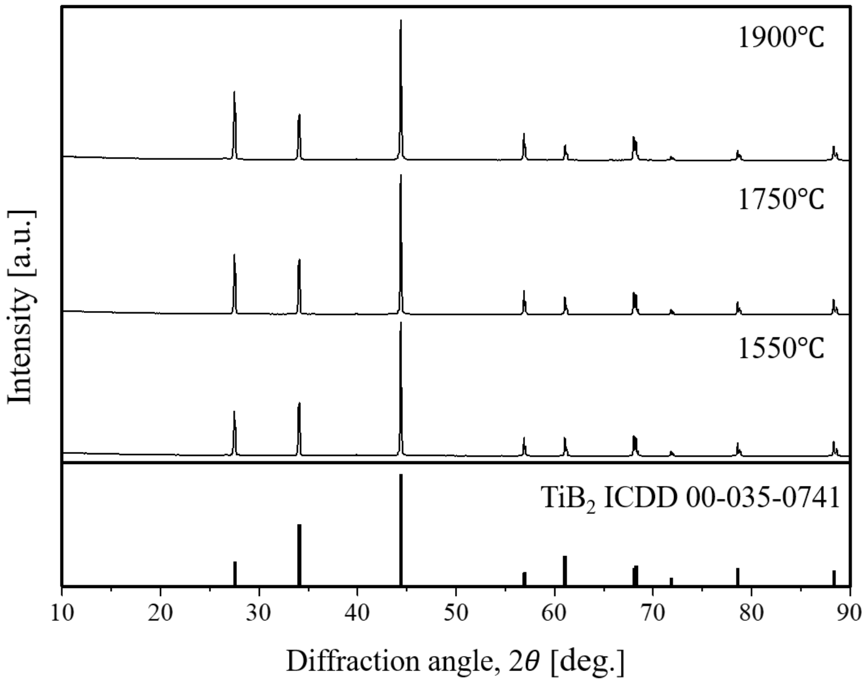

Figure 3.1: XRD patterns of as-prepared $TiB_2$ pellets sintered at various temperatures using ∼10 µm powder.

Figure 3.1 shows XRD patterns of as-prepared $TiB_2$ pellets at 1550, 1750, and 1900°C by SPS. It can be seen that at all temperatures, single-phase $TiB_2$ was obtained. The density of pellets was measured by the Archimedes method. Theoretical density of $TiB_2$ is 4.52 g/cm$^3$. Results of relative density are shown in Fig.3.2 below.

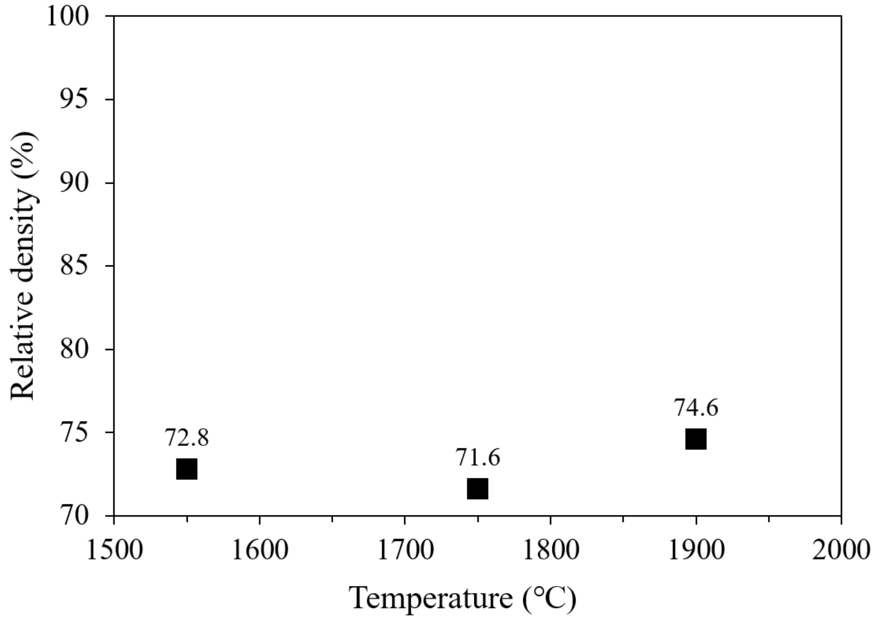

Figure 3.2: Relative density of as-prepared $TiB_2$ pellets sintered at various temperatures using ∼10 µm powder.

It is visible that relative density increased with increasing the temperature, however, even at 1900°C, it is not possible to obtain a dense sintered body of $TiB_2$ by using starting powder with size ∼10 µm.

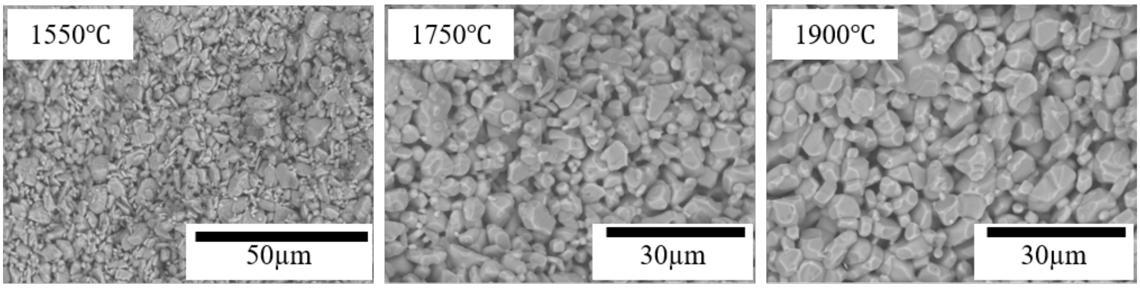

Figure 3.3: Fracture surfaces of as-prepared $TiB_2$ pellets sintered at various temperatures using ∼10 µm powder.

Figure 3.3 shows fracture surfaces of as-prepared $TiB_2$ pellets sintered at various temperatures using ∼10 µm powder. It can be seen that although grain growth was promoted with increasing the temperature, there were many intergranular voids, which may explain the low relative density.

#### 3.2.1.2 Sintering using ∼ 1.87 µm powder

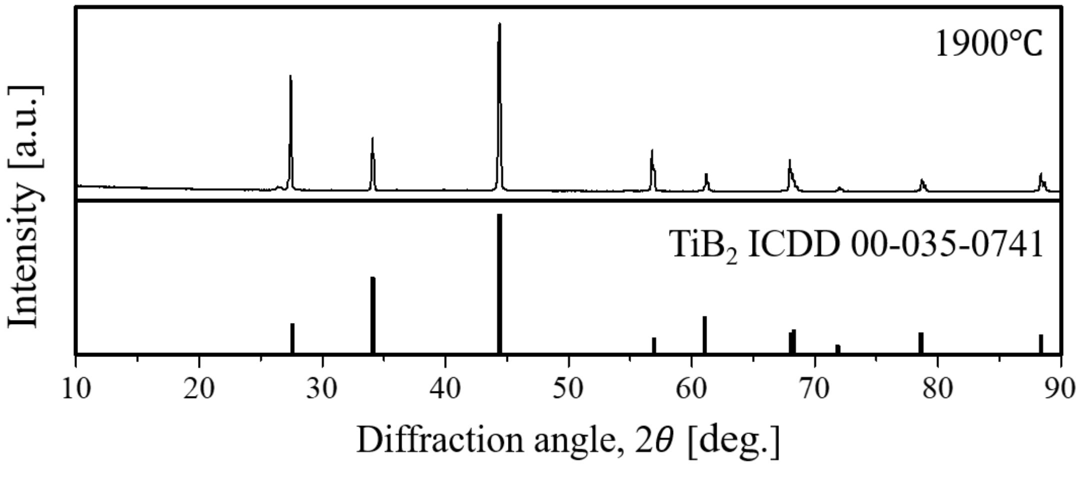

Figure 3.4: XRD pattern of as-prepared $TiB_2$ pellet sintered at 1900°C using ∼1.87 µm powder.

Figure 3.4 shows XRD pattern of as-prepared $TiB_2$ pellet sintered at 1900°C using ∼1.87 µm powder. Despite the small grain size and high sintering temperature, there was no secondary phase in the sample. Samples sintered at 1600 and 1700°C are considered to have similar single-phase $TiB_2$.

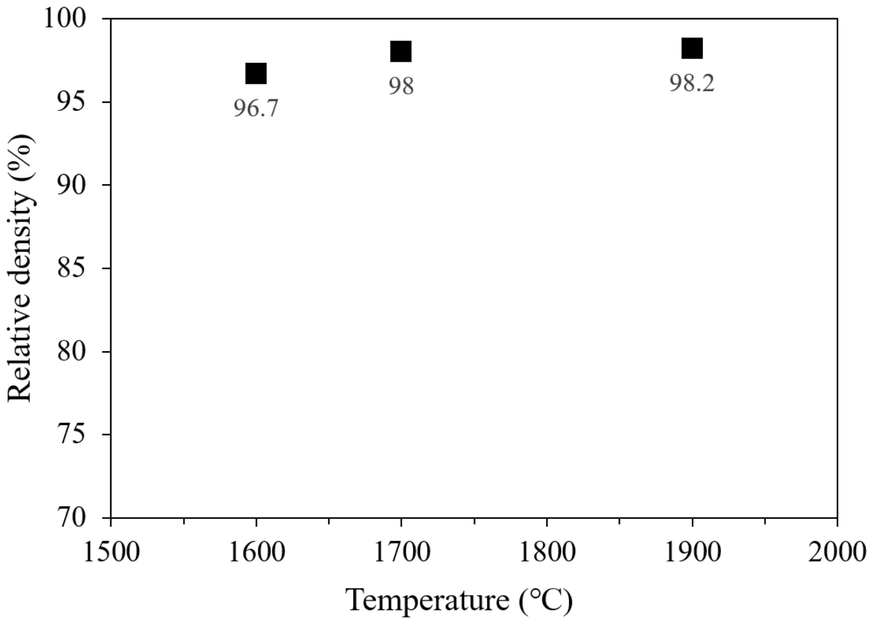

Figure 3.5: Relative density of as-prepared $TiB_2$ pellets sintered at various temperatures using ∼1.87 µm powder.

Figure 3.4 shows the relative density of as-prepared $TiB_2$ pellets sintered at various temperatures using ∼1.87 µm powder. It can be seen that with increasing sintering temperature, the relative density of pellets also increases. The high relative density indicates the dense sintered body. After measuring density, pellets were polished and subjected to Vickers hardness testing.

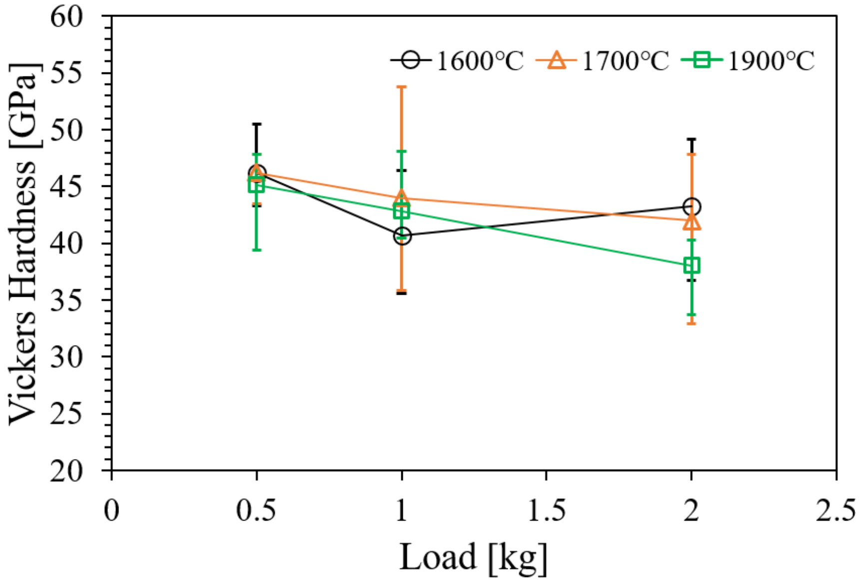

Figure 3.6: Vickers hardness of as-prepared $TiB_2$ pellets sintered at various temperatures using ∼1.87 µm powder.

Figure 3.6 shows Vickers hardness of as-prepared $TiB_2$ pellets sintered at various temperatures using ∼1.87 µm powder. At 0.5 kg load, Vickers hardness of pellets prepared at

1600 and 1700°C has an average value of approximately 46.2 GPa whereas pellet prepared at 1900°C has an average value of Vickers hardness of 45.1 GPa. Since the error bars are overlapped to each other at all 3 conditions, the values of Vickers hardness of pellets prepared at 3 conditions are possibly not much different from each other.

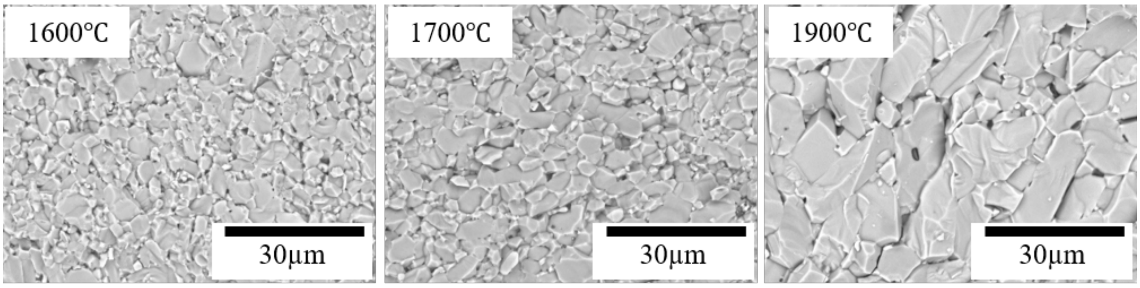

Figure 3.7: Fracture surfaces of as-prepared $TiB_2$ pellets sintered at various temperatures using ∼1.87 µm powder.

Figure 3.7 shows surfaces of as-prepared $TiB_2$ pellets sintered at various temperatures using ∼1.87 µm powder. It is clearly seen that with increasing temperature from 1600 to 1900°C, the grain growth was significantly promoted. Unlike the fracture surfaces of pellets prepared using ∼10 µm powder shown in Fig.3.3, the effect of using starting powder with size ∼1.87 µm is clearly seen, which may explain the increment of relative density. In addition, comparing to pellet prepared using ∼10 µm powder, the number of intergranular voids decreased significantly.

#### 3.2.1.3 Sintering using a mixture of ∼ 10 µm and ∼ 1.87 µm powders

By mixing ∼1.87 µm powder into ∼10 µm powder with a weight percentage of 30% and 70% and sintering by SPS at 1900°C, the effect of using starting powder with small grain size was investigated.

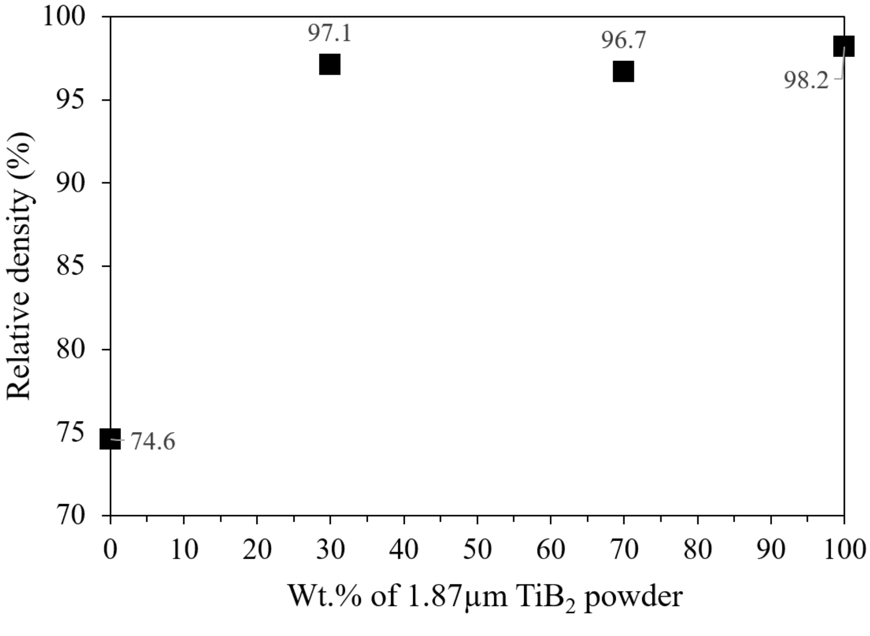

Figure 3.8: Relative density of as-prepared $TiB_2$ pellets sintered at various weight percentages of ∼1.87 µm powder at 1900°C.

Figure 3.8 shows relative density of as-prepared $TiB_2$ pellets sintered with various weight percentages of ∼1.87 µm powder at 1900°C. It can be seen that with the addition of 30 wt.% and 70 wt.% of ∼1.87 µm powder, the relative densities of pellets significantly increase and are close to that of pellet prepared using only ∼1.87 µm powder.

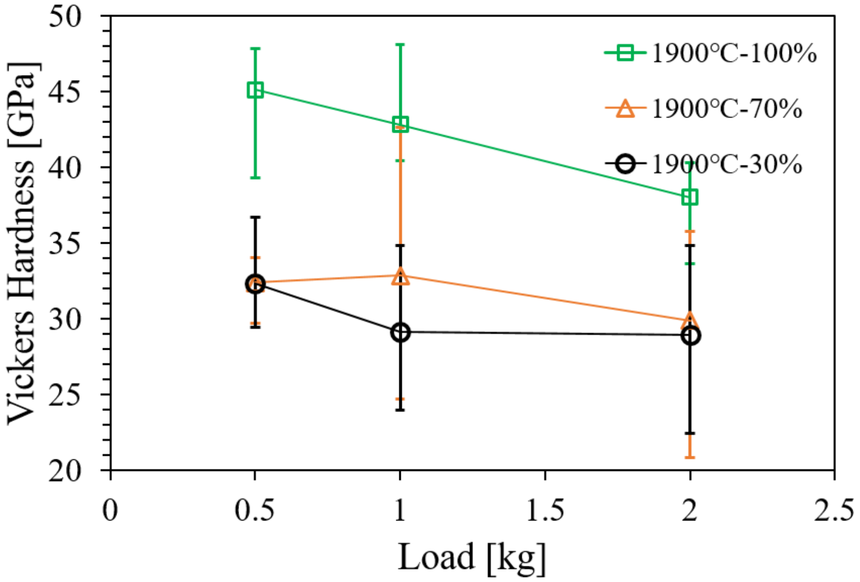

Figure 3.9: Vickers hardness of as-prepared $TiB_2$ pellets at various weight percentages of ∼1.87 µm powder at 1900°C.

Figure 3.9 shows Vickers hardness of as-prepared $TiB_2$ pellets sintered at various weight percentages of ∼1.87 µm powder at 1900°C. It can be seen that although the relative densities of pellets containing 30 wt.% and 70 wt.% of ∼1.87 µm powder are relatively high and comparable to pellets containing 100% ∼1.87 µm powder, the values of Vickers hardness are considerably low, which are approximately 32.4 GPa at both conditions with 0.5 kg load.

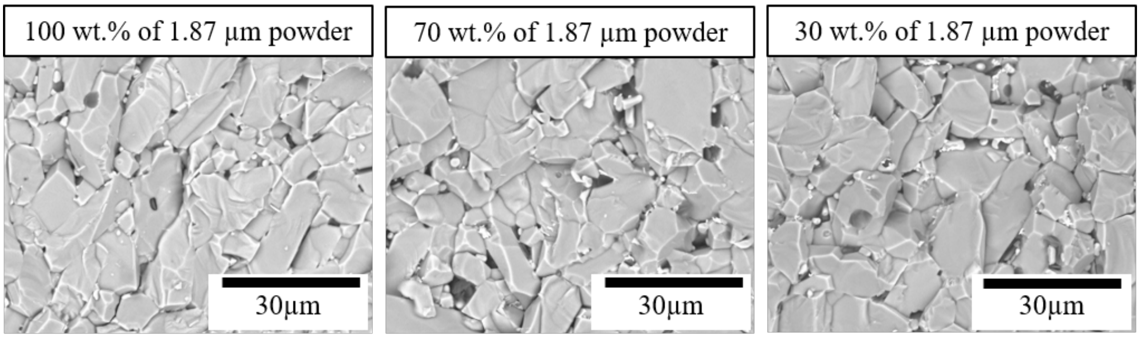

Figure 3.10: Fracture surfaces of as-prepared $TiB_2$ pellets sintered at various weight percentages of ∼1.87 µm powder at 1900°C.

Figure 3.10 shows fracture surfaces of as-prepared $TiB_2$ pellets sintered at various weight percentages of ∼1.87 µm powder at 1900°C. It can be seen that the 3 conditions are not much different from each other. At a sintering temperature of 1900°C, the addition of ∼1.87 µm powder from 30 wt.% greatly promotes the grain growth and consolidation of the pellet.

#### 3.2.1.4 Discussion on the result of Vickers hardness

By the results of Vickers hardness shown in Fig. 3.9 and the relative density shown in Fig. 3.8, it was found that although the relative density of samples fabricated with mixed powder was nearly as high as that of samples fabricated with small powder under similar conditions of temperature and pressure, which is necessary to be discussed. In order to elucidate this result, an XRD measurement was carried out with 3 pellets: 30 wt.% small powder, 70 wt.% small powder, and 100 wt.% small powder. The results are shown below figure.

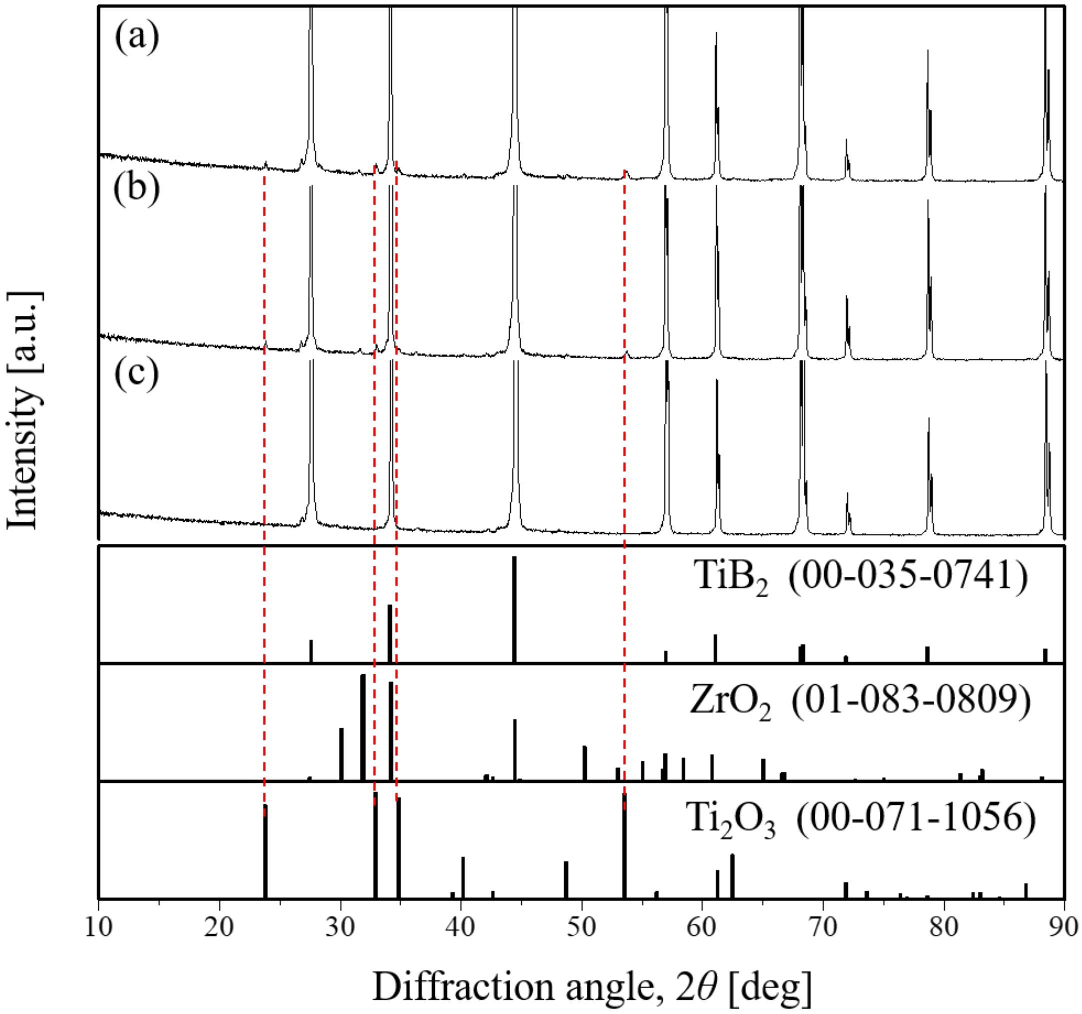

Figure 3.11: XRD patterns of pellets sintered under conditions of 1900°C with compositions of (a) 30 wt.% small powder, (b) 70 wt.% small powder, and (c) 100 wt.% small powder.

XRD results shown in Fig. 3.11 indicate that beside sharps peak of $TiB_2$, pellets sintered with compositions of 30 and 70 wt.% small powder exhibit small peaks at approximately 24, 33, 35, and 54°, which are corresponding to peaks of $Ti_2O_3$ phase. The presence of oxide phase in the sintered pellets may attribute to the decrease of Vickers hardness despite nearly similar relative density. However, pellet sintered with the composition of only small powder reveals only peaks of $TiB_2$ phase. The reason for the presence of $Ti_2O_3$ phase in pellets sintered with mixed powder will be discussed. There are two conceivable reasons: oxides were present in the raw material, and $ZrO_2$ phase was mixed into the powder during the mixing process using a zirconia ball mill. The former was investigated using X-ray diffraction analysis of raw materials of large, small, and mixed powder.

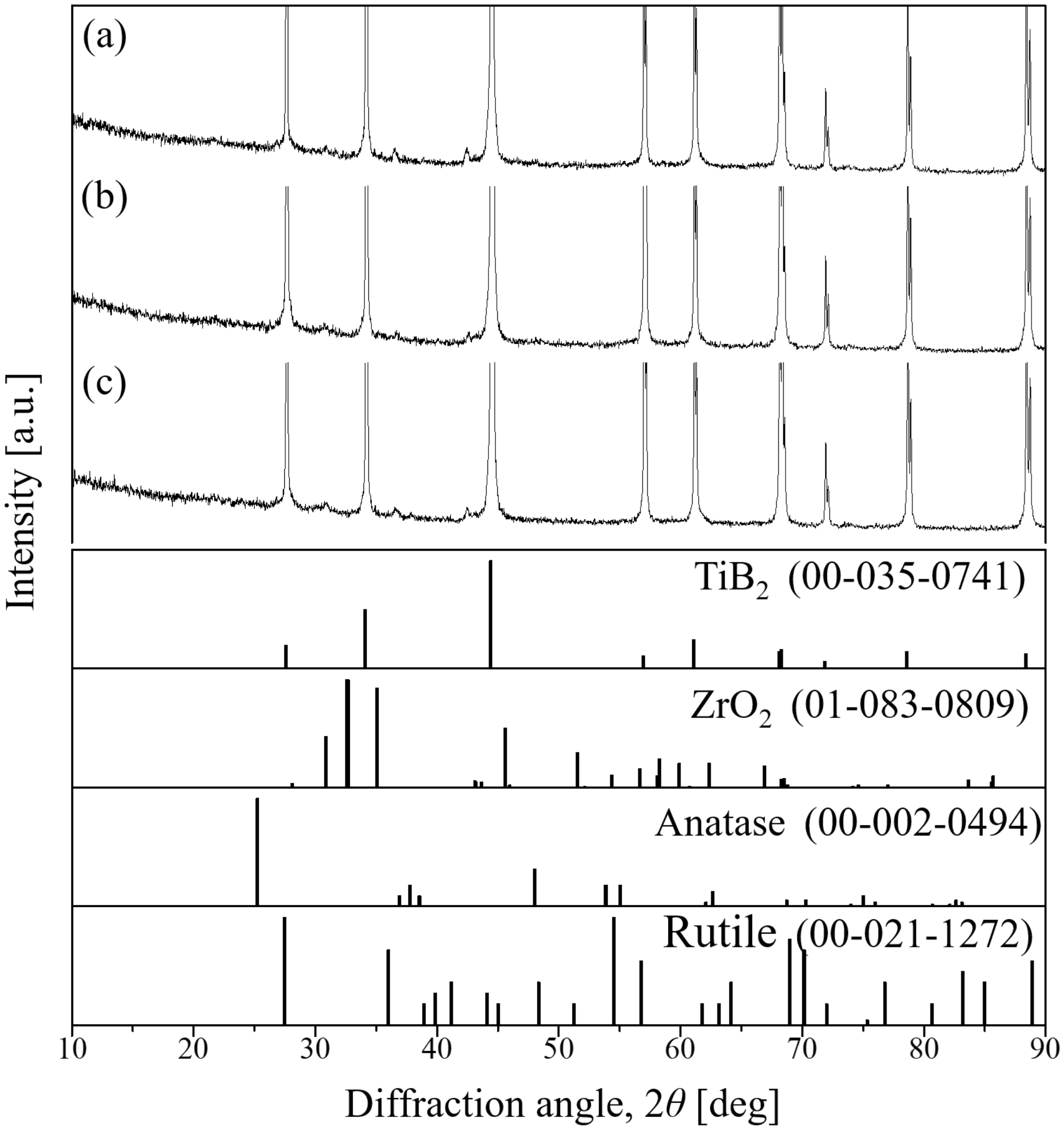

Figure 3.12: XRD patterns of raw materials of (a) large, (b) small, and (c) mixed powder with a composition of 30 wt.% small powder.

By looking at XRD patterns shown in Fig. 3.12, we can see that all three samples show nearly similar XRD patterns. Besides sharp peaks of $TiB_2$ as the main phase, which is obvious, there are some small peaks at approximately 30, 36, and 42°. These peaks are, however, not matched with any possible reason caused during experiments and processes such as $ZrO_2$, therefore, these peaks can be considered to belong to the original material. Additionally, $TiO_2$ phases (anatase and rutile) were not confirmed. Thus, it can be considered that probably the amount of $TiO_2$ phase was smaller than the detectable range of the XRD. For higher sensitivity of oxygen detection, the raw material of small powder was subjected to analysis of EELS equipped on an FE-TEM.

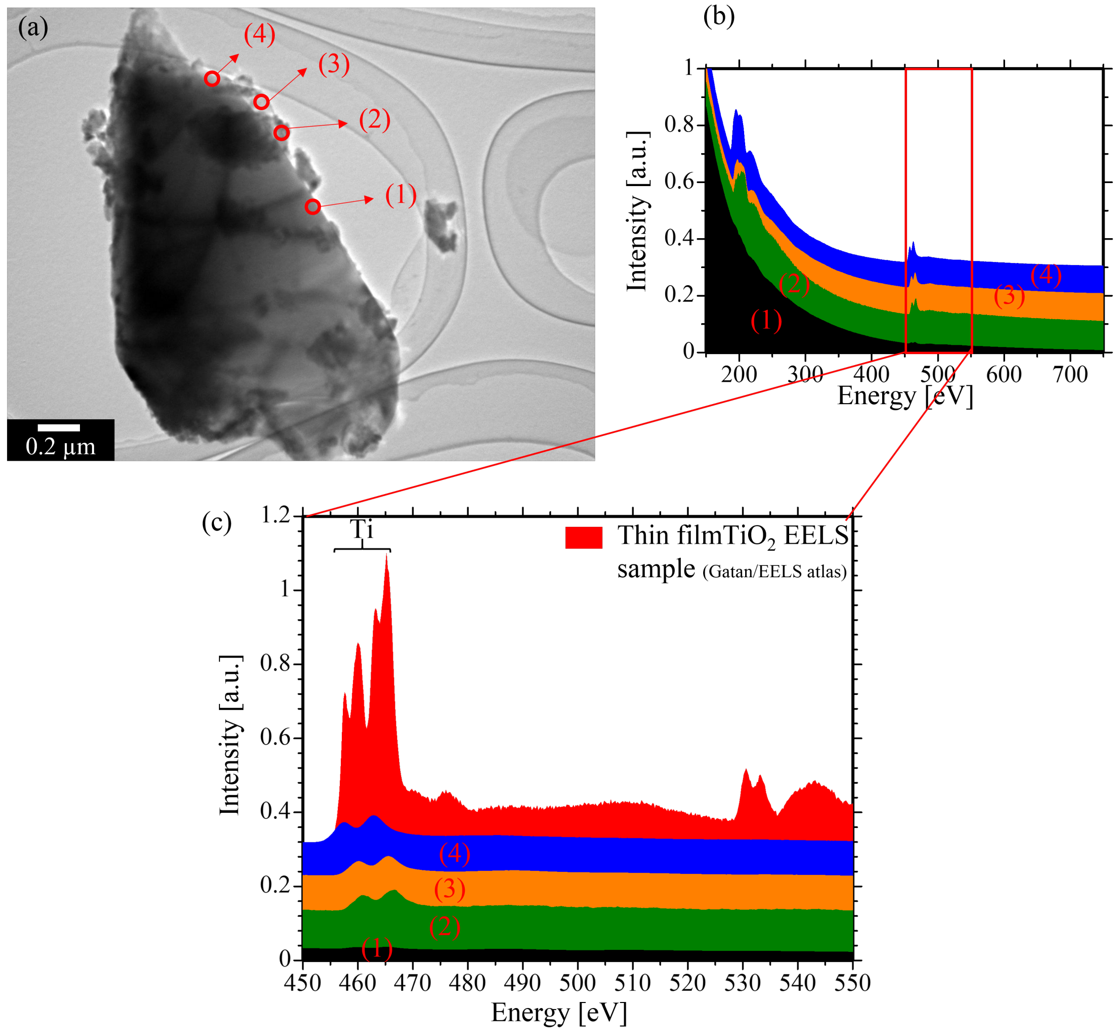

Figure 3.13: (a)Bright-field TEM image of a $TiB_2$ grain, (b) EELS spectra of marked positions (1) to (4) in (a) in the range 150-750 eV, and (c) enlargement of the range 450-550 eV of EELS spectra shown in (b).

Figure 3.13(a) shows a bright-field TEM image of a grain of raw material of small powder. EELS spectra were taken from positions (1)-(4) shown in this figure. The aperture of EELS analysis was set at 1 mm, which was corresponding to a region as small as approximately 20 nm with the magnification of 50k. Figure 3.13(b) shows the EELS spectra of positions (1)-(4). A sharp edge at approximately 200 eV of each spectrum reveals the presence of B with K-edge at 188 eV. Figure 3.13(c) shows the enlargement of Fig. 3.13(b) in the range 450-550 eV. A sample EELS spectrum of $TiO_2$ was also shown in Fig. 3.13(c). In this sample spectrum, it is apparent that sharp edges of Ti are seen at approximately 455-470 eV, which are consistent with EELS database of Ti's major edges $L_2$ and $L_3$ at 462 and 456 eV, respectively. Additionally, a sharp edge of O is clearly seen at approximately 530-535 eV, which is consistent with EELS database of O with K-edge at 532 eV. Because the energy values of Ti and O are quite close to each other that the energy resolution of EDS maybe not sufficiently fine, EELS was used. EELS spectra of a $TiB_2$ grain at (1)-(4) only reveal major edges of Ti at approximately 455-470 eV, while it was hardly detected any edges at approximately 530 eV. Therefore, it can be concluded that the amount of O in the sample is very small. Moreover, if only an amount of approximately 2-3 mol or vol.% of oxide phases were present in the raw material, there would be a steep increment of displacement at a certain temperature in the displacement-temperature when pellet was sintered due to liquid phase sintering (T. Nishimura, private communication, June 22, 2021). However, because the displacement-temperature graph shown in Fig. 3.14 does not exhibit any such abrupt increment of displacement of the piston of SPS, the amount of oxide phases in the raw material is less than 2-3 mol or vol.% and can be considered to be negligibly small. As a result, the first conceivable reason for the presence of $Ti_2O_3$ phase in the pellet that oxide phases were present in the raw material can be neglected.

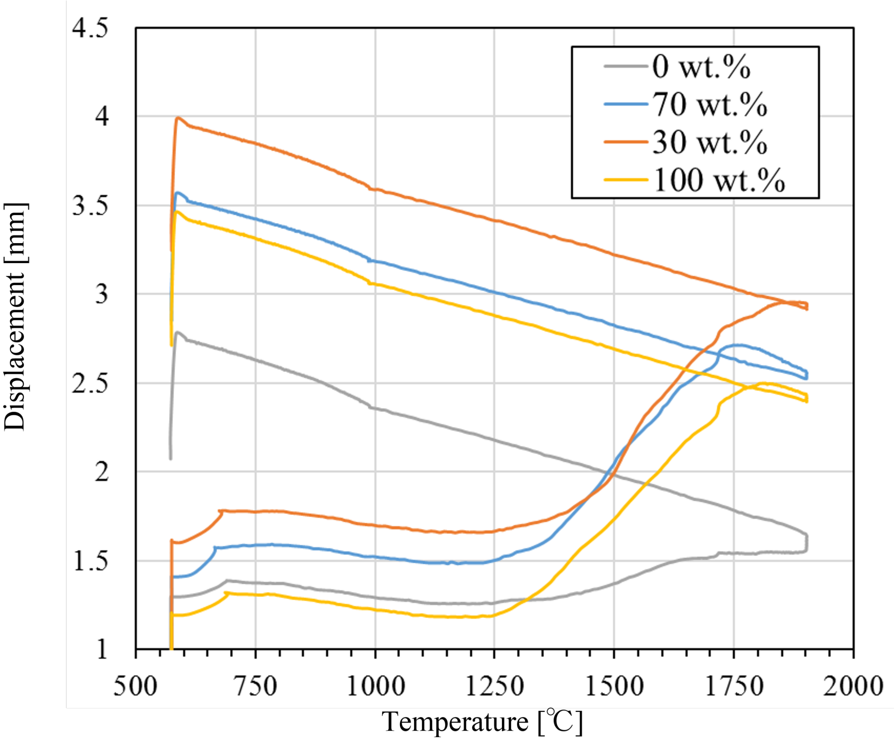

Figure 3.14: Displacement-temperature graph of sintering of $TiB_2$ pellets with compositions of only large powder, 70, 30 wt.% small powder, and only small powder.

For the second thinkable reason for the presence of $Ti_2O_3$ phase, $ZrO_2$ from zirconia milling ball was considered to mix into the raw material of mixed powders during the mixing process. This $ZrO_2$ phase was not able to be detected by XRD in Fig. 3.12 probably due to the small amount. At a sintering temperature of 1900 $[\circ]$C, although $ZrO_2$ was not melted, it can react with C in carbon foil wrapping around the sample to form ZrC and CO gas[259]. CO gas was thought to react with $TiB_2$ at high temperature to form $Ti_2O_3$ which is known as a high-temperature phase[260]. This thought was confirmed by using EDS equipped on the FE-TEM to detect the presence of Zr in the sintered pellet. A $TiB_2$ pellet sintered with the composition of 30 wt.% small powder was crushed by a set of mortar and pestle made of alumina and silica. EDS results are shown in the below figure.

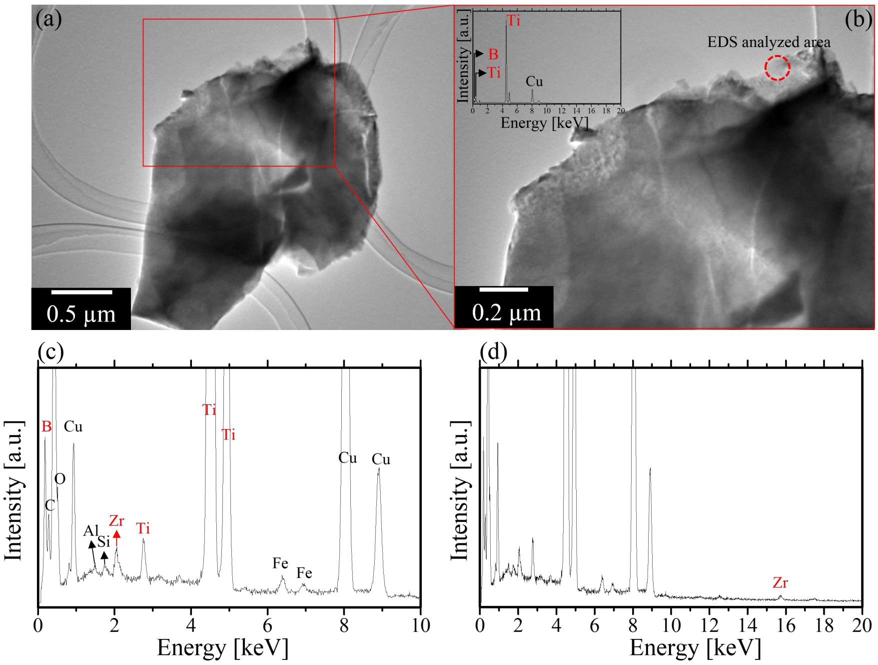

Figure 3.15: (a)Bright-field TEM image of a $TiB_2$ grain crushed from the pellet sintered with composition of 30 wt.% small powder, (b)Enlargement of (a), (c) EDS spectrum of an area shown in (b), and (d) similar EDS spectrum with range 0-20 keV.

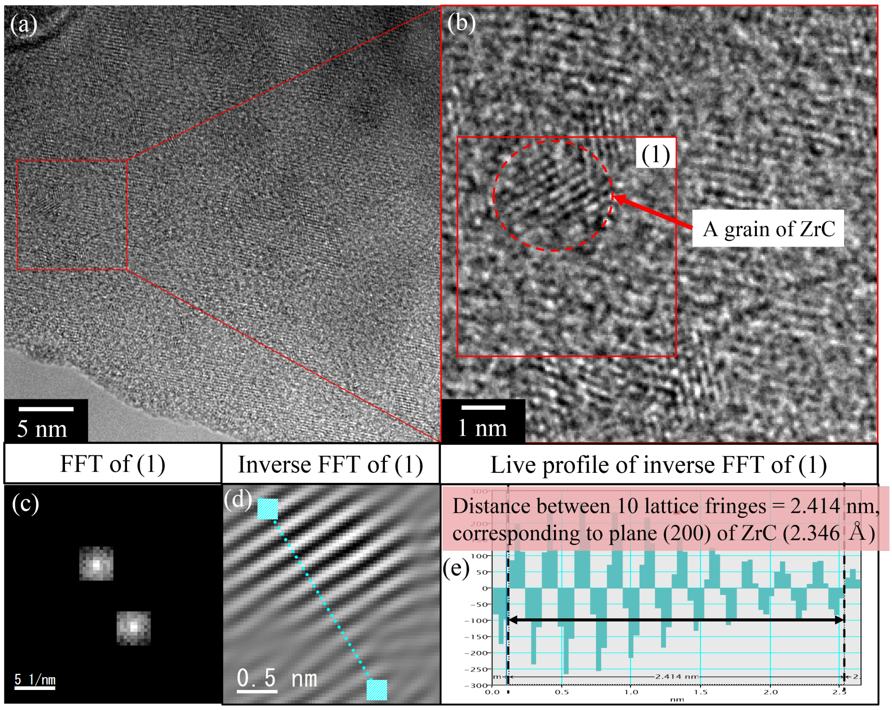

Figure 3.16: (a) A lattice image of the position that Zr was detected in Fig. 3.15, (b) Enlargement of (a) showing a small grain of ZrC in area (1), (c) FFT of area (1), (d) inverse FFT of area (1), and (e) live profile of inverse FFT of area (1).

By EDS spectrum shown in Figs. 3.15(c) and (d), it is seen that Zr was present in the sample. However, as mentioned before, the amount of Zr is considered to be very small, as a result, not all the positions that Zr could be detected. Peaks of Al and Si were also detected due to using the mortar and pestle of alumina and silica, thus, the intensity of the peak of O also increased. Peaks of Fe originated from an iron pole piece of the magnetic lens in the FE-TEM. At the place Zr was detected by EDS, an analysis of the lattice image was carried out. The result is shown in figure 3.16.

By Fig. 3.16, the presence of a small grain of ZrC was confirmed by identifying a distance of two continuous lattice fringes. The value of this distance is 0.2414 nm which is best matched with the plane (200) of ZrC with an interplanar distance of 0.2346 nm. Because there was no interplanar distance of any possible compound that could be confirmed with this distance, additionally, this grain was found to be distinguished with surrounding large grains which were easily confirmed $TiB_2$ phase. As a result, this grain must be ZrC and the thought that the presence of $Ti_2O_3$ phase was because of $ZrO_2$ from zirconia milling ball is reasonable. In particular, it should be noted that Vickers hardness is a property characterized at the surface of the pellet. For non-oxide ceramics like $TiB_2$, surface oxidation due to exposure to air containing water vapor is inevitable. Furthermore, if the oxides (e.g. $ZrO_2$) were present in amorphous, they could not be detected by XRD, which is probably correct with this case, hence, cannot be seen in Fig. 3.11.

#### 3.2.1.5 Summary of sintering of $TiB_2$ ceramics

In summary, there are some conclusions from the 3 experiments as follows,

1. By sintering starting powder with size ~10 µm by SPS, the highest value of relative density was 74.6% obtained at 1900°C and 60 MPa.

2. By sintering starting powder with size ~1.87 µm by SPS, a dense pellet was obtained at 1600°C with relative density attaining 96.7%. At 1900°C, a highly dense pellet with a relative density of 98% was obtained. Grain growth was observed clearly at elevated temperatures.

3. At 1600, 1700, and 1900°C, values of Vickers hardness were not much different and approximately 46 GPa at a load of 0.5 kg.

4. By mixing ~1.87 µm and ~10 µm powder with the ratio of 30 and 70 wt.%, it was possible to obtain dense pellets with the relative density of 97.1 and 96.7%, which was close to that of pellet prepared using only ~1.87 µm powder.

5. Despite the high relative density, values of Vickers hardness of pellets prepared by mixing ~1.87 µm and ~10 µm powder are equally approximately 32 GPa of 2 mixing conditions due to the formation of $Ti_2O_3$ phase. The reason was discussed as the mixture of $ZrO_2$ from zirconia ball of ball milling for the mixing process.

### 3.2.2 Tungsten borides synthesis and sintering by SPS

Tungsten borides include several stoichiometric formulas: $W_2B$, WB, $WB_2$, and "nominal $WB_4$". Among them, the highest boron-rich tungsten boride is attractive for much attention from the scientific community due to its fascinating mechanical properties[261] and is expected to be a potential inexpensive superhard material[262]. This compound was first proposed as $WB_4$ by Chretien and Helcorsky in 1961[263]. Since then, the correct composition has been long debated until nowadays. In 1966, Roman and Krug proposed a structural model of $WB_4$ with hexagonal symmetry $P6_3/mmc$[264]. Lundström and Rosenberg suggested the composition $W_{(1\text{-}x)}B_3$. By the computational method, Cheng et al. have predicted several stable structures of boron-rich W-B compounds and claimed that the extensively discussed $P6_3/mmc$ structure of $WB_4$ did not exist and should be altered to $WB_{(3+x)}$[265]. In 2015, by means of neutron diffraction, Lech et al. proposed the composition as $WB_{4.2}$[266]. Recently, by a combination of theoretical prediction and experimental synthesis, Kvashnin et al. has suggested the phase $WB_{(5\text{-}x)}$[267]. From experimental approaches, many studies have also been carried out adopting arc melting[262, 268, 269], high-pressure synthesis[270, 267], reactive hot press[271, 272], mechanochemical method[38, 273], and SPS[274, 275] methods. Despite the debate of finding the correct composition of the highest tungsten boride, the experimentalists obtained a nearly similar composition, which might be denoted as $WB_4$ or $WB_3$. This phase has been found metastable between 1200-1600°C depending on the ratio of B and W in the compound and method[271, 273]. With high—er ratio of B and W, $WB_4/WB_3$ is more stable. However, it was suggested that the ratio of B and W should be at least 8:1[276, 271],9:1[277] for the single-phase $WB_4/WB_3$. For the lower ratio of B and W, a third element must be added doped into the compound to maintain the phase $WB_4/WB_3$ such as Ni[272], Ta[278], or Zr[274]. However, the addition of metals might decrease the performance of ceramics at high-temperature applications. As a result, in this present study, an attempt to synthesize and consolidate boron-rich tungsten boride compound by means of SPS was carried out. In the present study, the first proposed stoichiometric formula-$WB_4$ is used. Table 3.2 shows the experimental conditions for sintering of tungsten boride.

Table 3.2: Experimental conditions of tungsten boride sintering by SPS

| | Experiment 1 | Experiment 2 |
|---|---|---|
| W:B ratio | 1:4.5, 1:8, 1:12 | 1:4.5, 1:8 , 1:12 |
| Temperature [°C] | 1300, 1400, 1500, 1600 | 1500 |
| Pressure [MPa] | 50 | 50, 70, 90 |
| Keeping time [min] | 5 | |
| Sintering medium | Vacuum ($10^{-3}$ Pa) | |
| Heating rate | 100 K/min | |

#### 3.2.2.1 Temperature and composition dependence

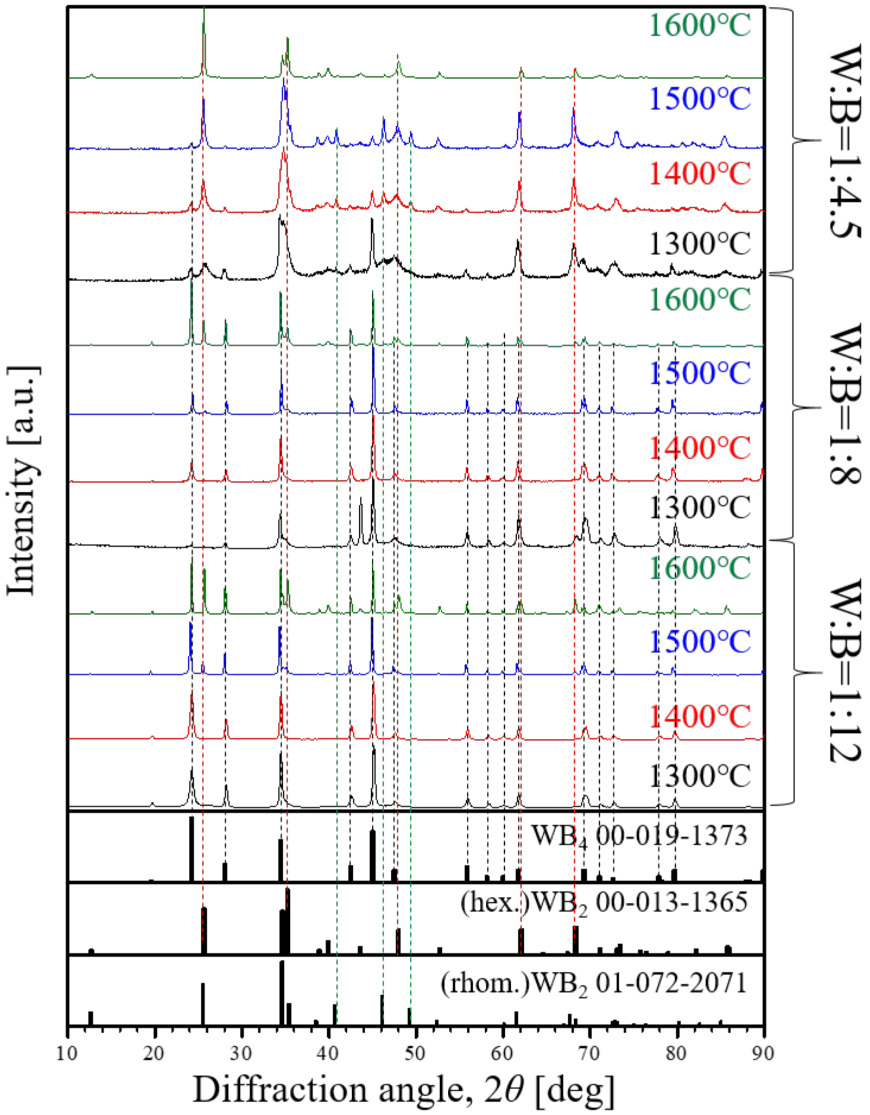

Figure 3.17: XRD patterns of as-fabricated tungsten boride pellets sintered at various temperatures and compositions under 50 MPa by SPS

Figure 3.17 shows XRD patterns of as-fabricated tungsten boride pellets sintered under various temperatures and composition by SPS. It is seen that at compositions of W:B=1:8 and 1:12, $WB_4$ was formed at all sintering temperatures. However, from 1500°C, phase hexagonal-$WB_2$ (hex-$WB_2$) was detected. At a composition of W:B=1:4.5, only a small amount of $WB_4$ was formed at 1300°C, however, with increasing temperature, only phase $WB_2$ was formed. Additionally, at a composition of W:B=1:4.5, both phase rhombohedral $WB_2$ (rhom-$WB_2$) and hexagonal $WB_2$ (hex-$WB_2$) were formed up to 1500°C, however, at 1600°C, only hex-$WB_2$ was detected.

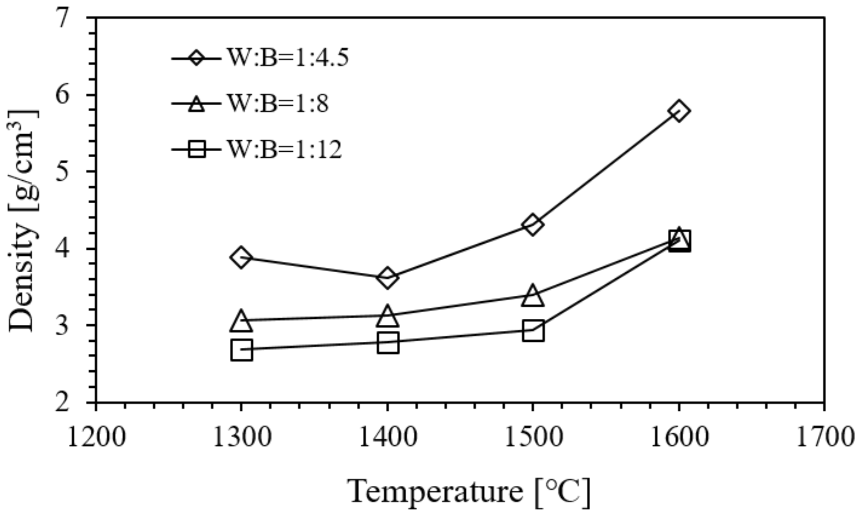

Figure 3.18: Densities of as-fabricated tungsten boride pellets sintered at various temperatures and compositions under 50 MPa by SPS

Figure 3.18 shows densities of as-fabricated tungsten boride pellets at various temperatures and compositions under 50 MPa by SPS. It can be seen in the graph that, in each composition of W and B, density increased with increasing temperature, however, between 1300°C and 1500°C, the increment of density is not clearly seen. Between 1500°C and 1600°C, this increment is clearly seen. Basing on the appearance of as-fabricated pellets, it was possible to recognize the difference of the surface of the pellets between samples fabricated at 1600°C and 1300−1500°C. Although crystallography data of phases hex-$WB_2$ and rhom-$WB_2$ were available and theoretical densities were also known, due to still being investigated, that information of $WB_4$ has not been officially specified. Therefore, it was not possible to calculate the relative densities of pellets. In addition, the composition of phases in the samples also must be considered.

### 3.2.2.2 Pressure dependence

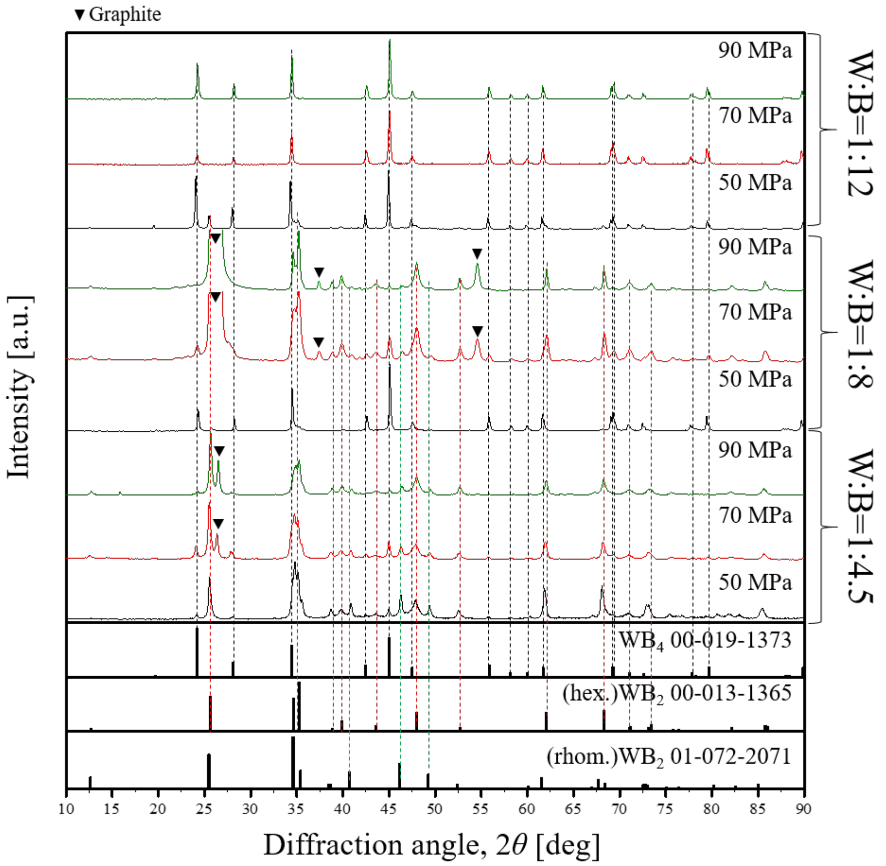

Figure 3.19: XRD patterns of as-fabricated tungsten boride pellets under various pressures and compositions at 1500°C by SPS

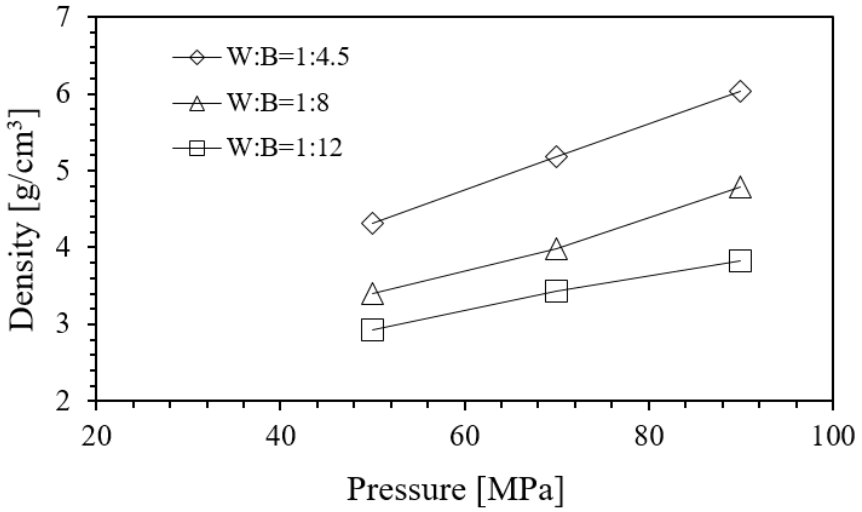

Figure 3.20: Densities of as-fabricated tungsten boride pellets under various pressures and compositions at 1500°C by SPS

Figure 3.19 shows XRD patterns of as-fabricated tungsten boride pellets sintered under various pressures and compositions at 1500°C. It can be seen that with a composition of W:B=1:12, $WB_4$ phase was maintained with increasing pressure. With a composition of W:B=1:8, phase $WB_4$ was decomposed into $WB_2$ with increasing pressure. In detail, at 70 and 90 MPa, mostly rhom-$WB_2$ and hex-$WB_2$ and only a small amount of $WB_4$ phase were simultaneously present. With a composition W:B=1:4.5, $WB_4$ phase was present but the concentration was low under all pressures.

Figure 3.20 shows densities of as-fabricated tungsten boride pellets under various pressures and compositions at 1500°C by SPS. It can be seen that at each composition of W and B, densities of tungsten boride pellets increased with increasing pressure at 1500°C. However, only with a composition of W:B=1:12 that $WB_4$ that $WB_4$ phase was maintained with increasing pressure, which reached the highest density of sintered $WB_4$ pellet as 3.82 g/cm$^3$.

#### 3.2.2.3 Summary of sintering of tungsten boride ceramics

In summary, there are some conclusions from 2 experiments as follows,

1. $WB_4$ phase is formed with excess boron and at least a component of W:B=1:8 was required.
2. With composition W: B=1:12, single-phase $WB_4$ was only obtained at temperatures no higher than 1500°C. At higher than 1500°C, $WB_4$ phase is decomposed into phase $WB_2$.
3. Pressure plays a crucial role to obtain dense tungsten boride pellets. At 1500°C, by increasing pressure, the density of pellets greatly increased.
4. Smaller starting powder (nano-sized) was expected to decrease sintering temperature to equal of less than 1500°C for a dense and high concentration of $WB_4$.

## 3.3 Synthesis of NPs of B and transition metal borides by the pulsed discharge of compacted powder

### 3.3.1 Boron nanoparticles

#### 3.3.1.1 Boron nanoparticles prepared by PWD

Boron is a metalloid element, which means, at room temperature, B is almost electrically non-conductive. The pulsed discharge of B was predicted to be a challenge. In the present study, attempts to discharge B wire in Ar and $N_2$ gas, and crystalline B micro-sized powder were carried out.

First, pulsed discharge of B wire in Ar and $N_2$ gas were carried out. Discharge conditions are shown in Table 3.3

Table 3.3: Experimental conditions of PWD of B wire

| | | | | | |
|---|---|---|---|---|---|
| | Material | B | | | |
| Wire | Diameter, $d$ [mm] | 0.1 | | | |
| | Length, $l$ [mm] | 25 | | | |
| Vaporization energy, $E_\mathrm{v}$ [J] | | 27.3 | | | |
| Charging voltage, $V_\mathrm{c}$ [kV] | | 6 | 2 | 4 | 6 |
| Capacitance, $C$ [µF] | | 30 | | | |
| Charging energy, $E_\mathrm{c}$ [J] | | 540 | 60 | 240 | 540 |
| Relative energy, $K$ | | 19.8 | 2.2 | 8.8 | 19.8 |
| Gas species | | Ar | $N_2$ | | |
| Pressure, $P$ [kPa] | | 100 | 10, 50, 100 | | |

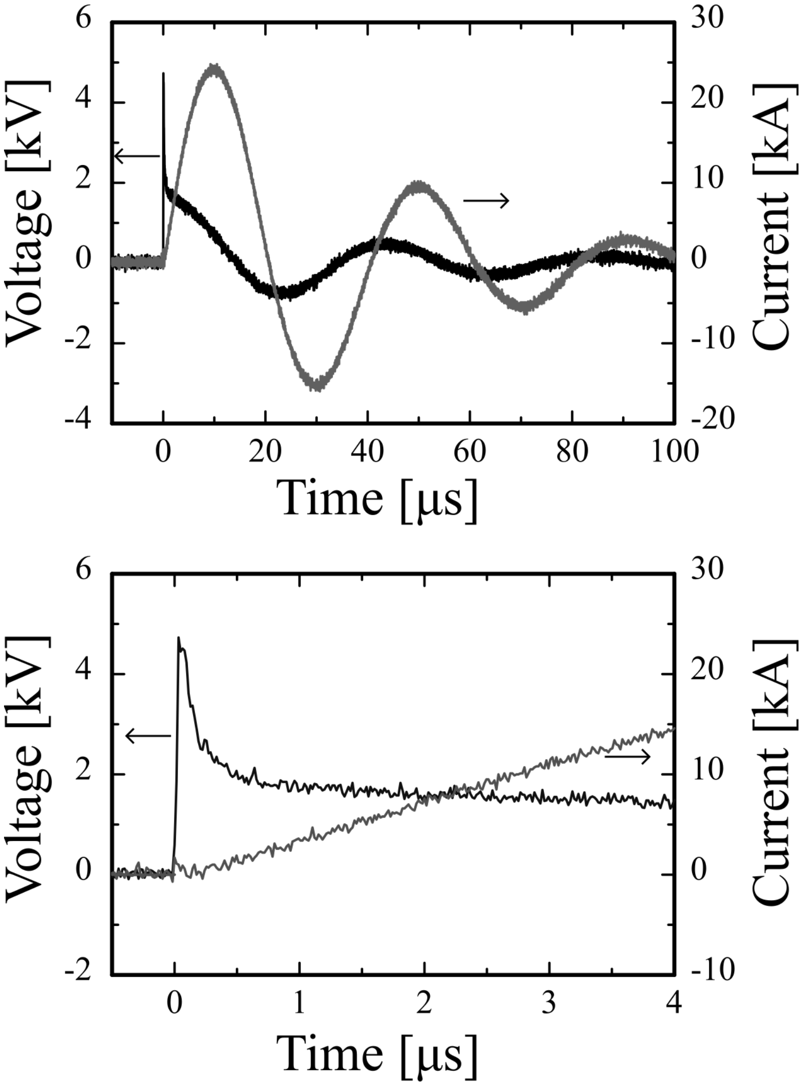

Figure 3.21: Waveforms of $V(t)$ and $I(t)$ of PWD of B wire at $P = 100kPa$ Ar, $K = 19.8$. Lower graph is enlargement of upper graph from 0 to 4 µs.

Figure 3.21 shows waveforms of $V(t)$ and $I(t)$ of PWD of B wire in Ar gas at 100 kPa. It can be seen that from the $V(t)$ waveform that, at the first peak, there were hardly any edges that could be used to detect the time when the wire was melted, which is very different from the typical V-I waveforms of PWD of metal wires (Fig. 2.2). After the peak of voltage, the waveform oscillated with an underdamped oscillation which might be induced from the arc discharge. The current waveform was also different from those of PWD of metal wires. Typically, first, when $t = 0$, the current waveform increases up to a maximum and decreases, which creating a small lump, along with underdamped oscillation controlled by the parameters of an RLC circuit. The small lump in the current waveform of PWD is the characteristic point for the wire heating stage of PWD. As a result, it was considered that there was no wire heating stage.

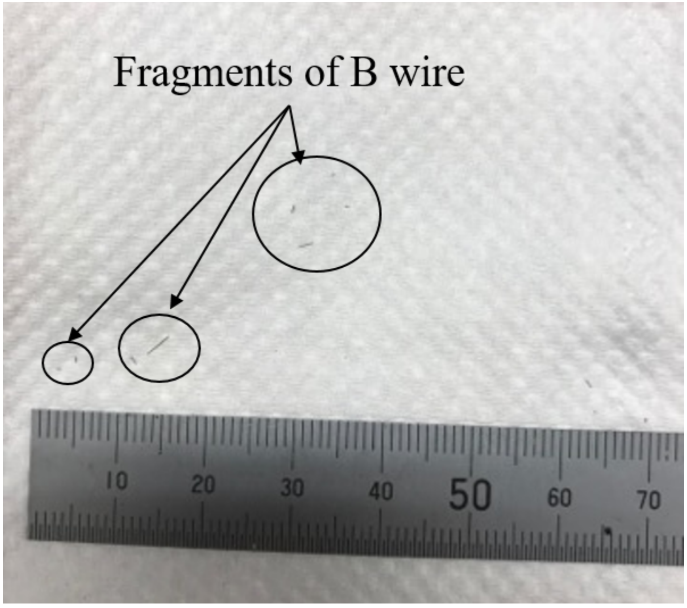

Figure 3.22: A photograph of fragments of B wire found on the bottom of the chamber after the experiment of pulsed discharge B wire in Ar gas

After several times of discharge, there was no powder collected. Using a piece of tissue to clean the bottom of the chamber, plenty of fragments of B wire were found. These fragments are shown in Fig. 3.22. These fragments of B wire indicated that B wire was broken into pieces rather than vaporized. The presence of these fragments of B wire also explained the unusual V-I waveforms mentioned above. In order to suppress the formation of arc discharge, $N_2$ gas was subsequently used as an ambient medium.

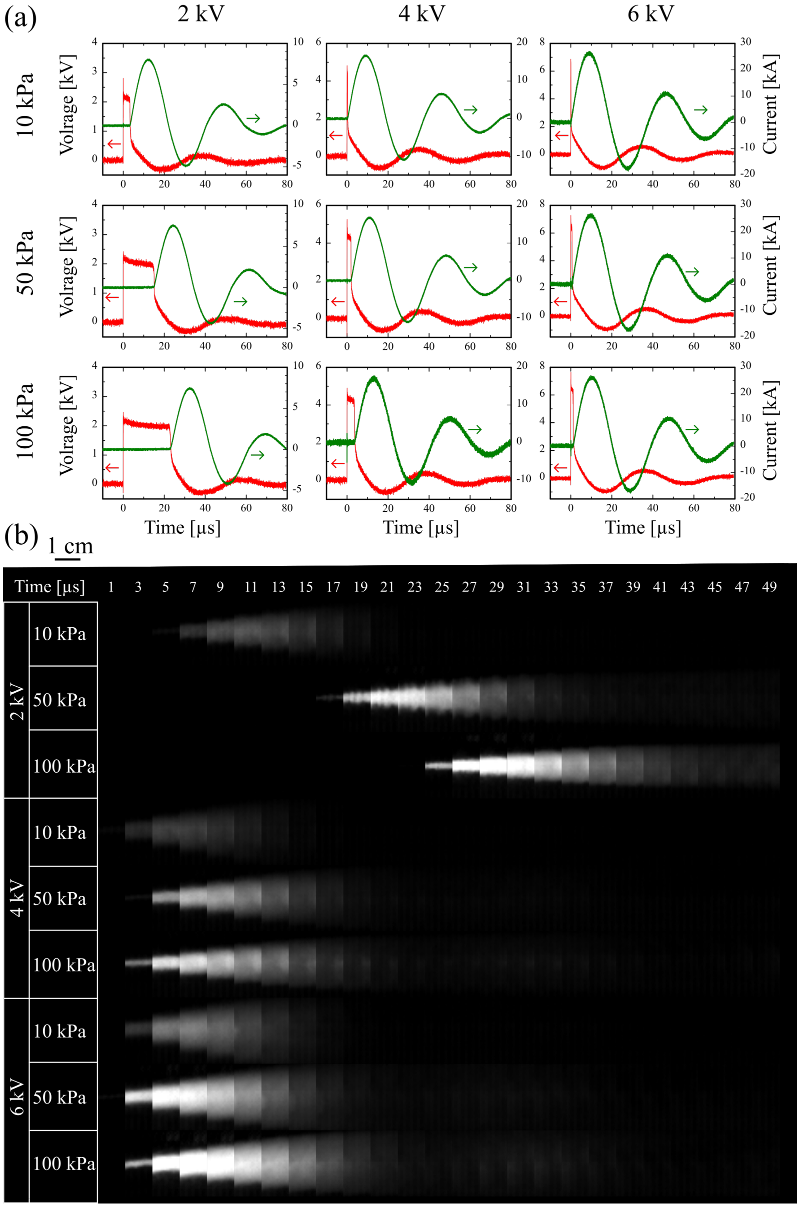

Figure 3.23: (a) Waveforms of $V(t)$ and $I(t)$ and (b) high-speed images during PWD of B wire at various values of $P$ of $N_2$ gas and $K$.

Figure 3.23(a) shows waveforms of $V(t)$ and $I(t)$ and (b) high-speed images during PWD of B wire at various values of $P$ of $N_2$ gas and $K$. From Fig. 3.23(a), it can be seen that with decreasing charging voltage 6 kV to 2 kV (K=19.8 to 2.2) and increasing $N_2$ pressure, the time for arc discharge to happen became longer. Time for arc discharge to happen was shortest with $V_{\mathrm{c}} = 6kV$ and $P = 10kPa$ at approximately 0.2 µs, and longest with $V_{\mathrm{c}} = 2kV$ and $P = 100kPa$ at approximately 23 µs. During this time, there was a small portion of charging voltage dropped on the wire and the current was nearly zero, which indicates that an unusual heating stage compared to typical ones observed in Fig. 1.2. Therefore, the heating effect of current on B wire was predicted to be very small or nearly zero which is reasonable due to the extremely high electrical resistance of B at room temperature. From Fig. 3.23(b), it is visible that during the time prior to arc discharge happened, there was no light emitted from the wire, which is consistent with the V-I waveforms. This period of time is particularly easy to see with a low charging voltage. The dropping of a small portion of charging voltage may be anticipated for the partial arc discharge on the surface of the wire before a sufficient amount of electrons was accumulated and induced an avalanche between two electrodes for the arc discharge. After several times of discharge, there was a very little amount of powder observed on the collecting membrane filter. A piece of tissue was used to clean the bottom of the chamber. Plenty of fragments of B wires were seen as in the case of using Ar gas. This means B wires were broken rather than vaporized during the pulsed discharge.

#### 3.3.1.2 Boron nanoparticles prepared by the pulsed discharge of compacted powder.

Despite adopting $N_2$ gas which has a larger dielectric breakdown voltage than Ar gas to suppress the formation of arc discharge, due to the extremely high resistance of B wire at room temperature, it was very difficult to prepare powders by discharging B wires. As a result, pulsed discharge of compacted powder was considered and tried. The experimental setup for pulsed discharge of compacted powder was shown in Fig. 2.1(b). The experimental conditions are shown in Table 3.4.

Table 3.4: Experimental conditions of pulsed discharge of B compacted powder.

| | |
|---|---|
| Raw material | Boron powder (∼40 µm) approx. 10 mg |
| Electrodes | Cu rod $\phi$=2 mm, 99.9% |
| Distance between Cu rods | Approx. 2.5 mm |
| Heat-shrinkable tube | Inner diameter=2.1 mm (before heating) |
| Charging voltage, $V_c$ | 6.2 kV |
| Capacity, $C$ | 30 µF |
| Charging energy, $E_c$ | 576.6 J |
| Ambient gas | Ar |
| Ambient gas pressure | 100 kPa |

Figure 3.24 shows the XRD patterns of the raw material B micron-sized powder and as-prepared B powder by the pulsed discharge of compacted powder. Card data of B, $B_2O_3$, Cu, and $B_4C$ referred from the ICDD are placed below the XRD patterns to determine phases including in the raw material and the as-prepared B powder. By comparing ICDD data and obtained XRD patterns, the raw material consisted of a B phase and a small amount of $B_2O_3$. Also, it can be seen that despite the high temperature of the pulsed discharge, there was no compound of Cu and B detected. This means that there was no reaction between Cu rods and micron-sized B powder raw material. Instead, the as-prepared powder was identified to include B as the main phase and an amount of Cu impurity phase. The broad peaks at $2\theta$=43.3° and $2\theta$=50.43° corresponding to Cu card data show the presence of Cu phase in the form of very small crystallites. Additionally, the intensity of the XRD pattern of the as-prepared powder was relatively lower than that of the raw material and the background of the pattern was higher than that of the raw material. Hence, it could be anticipated that a very small crystallite of B phase was present in the as-prepared powder. Also, there was also a small amount of $B_4C$ formed in the process of pulsed discharge of powder due to the reaction of vaporized B and C from the heat-shrinkable tube at high temperature of the pulsed discharge. A $B_2O_3$ phase was also detected in the as-prepared powder as in the raw material.

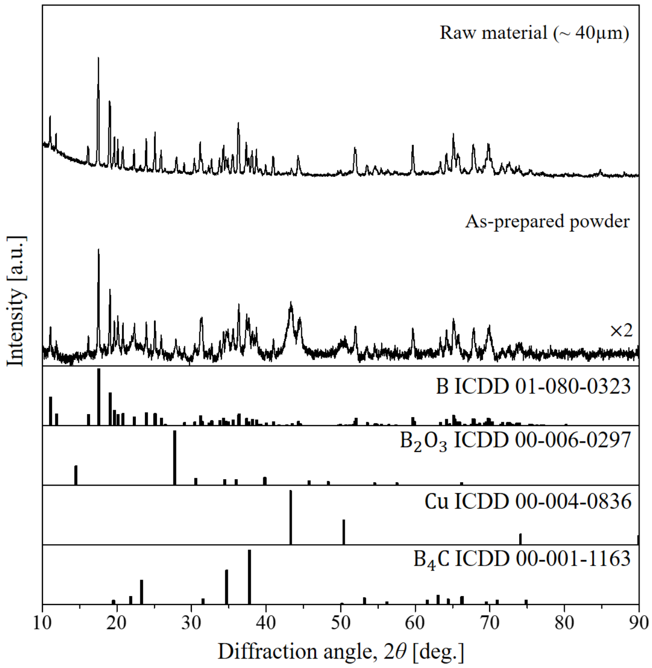

Figure 3.24: XRD patterns of raw material (B micron-sized powder) and as-prepared powder.

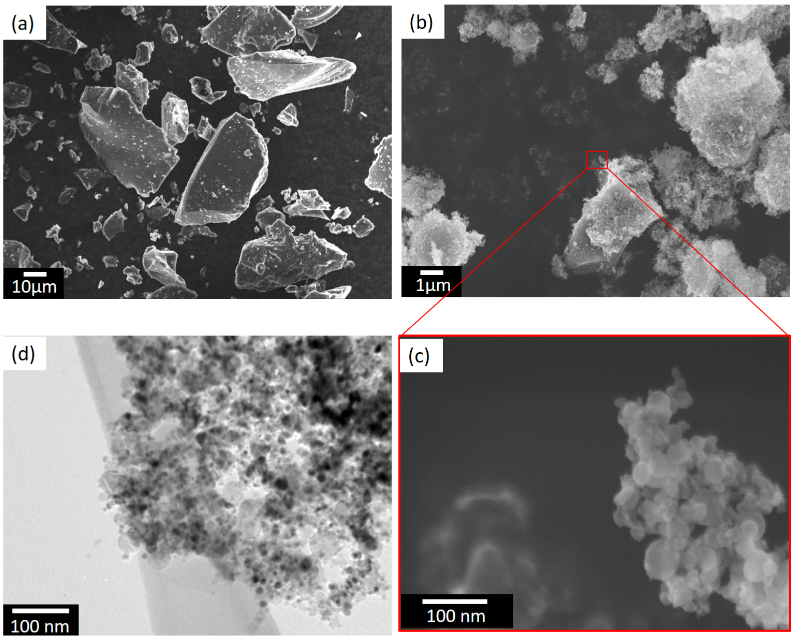

Figure 3.25: SEM images of (a) B micron-sized particles of raw material, (b) B powder after preparation, and (c) B nanoparticles with a size of less than 100 nm, (d) Bright-field TEM image of B nanoparticles with a size of less than 100 nm.

Figure 3.25 shows SEM images of B micron-sized powder used as raw material, B powder after preparation, and B nanoparticles. Basing on the size of particles shown in Figs. 3.25(a) and (b), it is apparent that there was a large difference between before and after the deposition of pulsed discharge. The sample of raw material contained a large number of micron-sized irregularly shaped particles. After the deposition of pulsed discharge, although there were still micron-sized particles observed, the particles became smaller, which can be estimated to be several micrometers. At higher magnification of SEM observations, a large number of spherical nanoparticles were distributed randomly in all observed areas. Some of them are shown in Fig. 3.25(c). Due to the high quenching rate, the morphology of B nanoparticles prepared in the present study was found to be generally spherical and similar to other kinds of nanoparticles prepared by PWD. Additionally, based on the observation of raw material, there were hardly particles with such nanoscale size, and spherical shape was found. Therefore, it is possible to conclude that these nanoparticles were a product of the preparation. By Figs. 3.25(c) and (d). Most of the nanoparticles were assessed to be smaller than 100 nm.

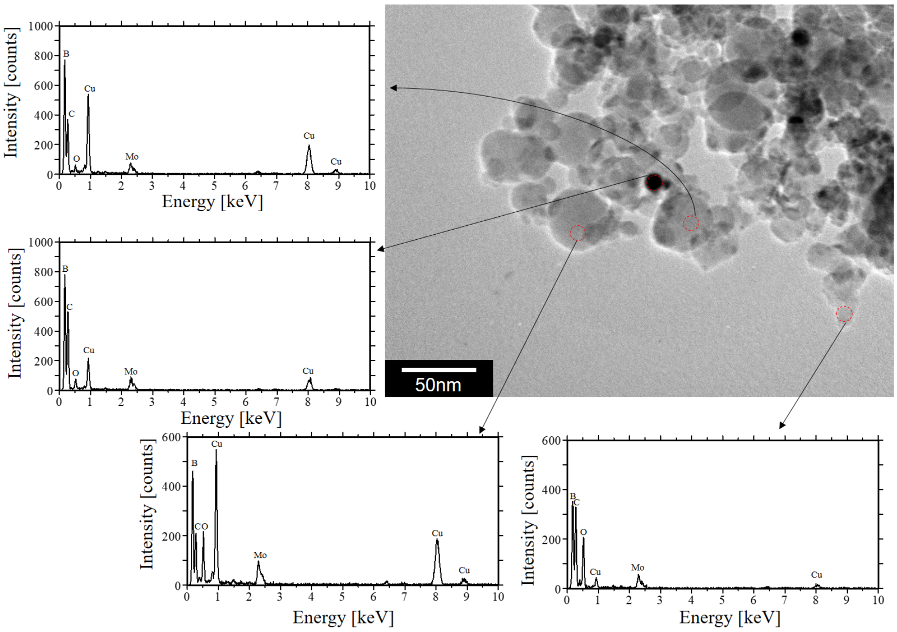

Figure 3.26: Bright-field TEM image of B nanoparticles and EDS spectra of some points in the observed area.

Figure 3.26 shows a bright-field TEM image of B nanoparticles and the EDS spectra of some points in the observed area. EDS was adopted to analyze the composition of small areas/particles observed by TEM. The electron beam was focused to approximately 10 nm in diameter to enhance the accuracy of the EDS analysis. The bright-field TEM image shows the presence of nanoparticles with a size less than 50 nm. Some of the areas/particles were chosen randomly to analyze by EDS. In the EDS spectra, it is seen that in all positions, the intensity of B peak was very high despite the limitation in detecting B which is the lightest element that can be detected with this EDS and emits a low intensity of characteristic X-ray upon electron radiation. With these data, it is possible to say that most of the particles have a high concentration of B compared to Cu and other impurities. Due to the detection of Cu in the XRD pattern, Cu was also carefully analyzed in each EDS spectrum. Basing on the EDS spectra, it is visible that Cu was detected in all positions but the intensity of Cu peaks was different in each position. Moreover, due to the large difference in the atomic mass between Cu and B, in the case that Cu is present in the grains as large as those of B, it must be clearly observed by the bright-field TEM images due to the large contrast. However, no such large contrast was seen in any bright-field TEM images. One of the positions with the largest contrast was analyzed by EDS showed only a small amount of Cu, as a result, it is not a Cu grain.

Therefore, it is considered that a small amount of Cu from the electrodes was melted into the solid solution and condensed on the quenching B vapor and formed nanoparticles. The presence of oxygen was confirmed in some positions, which is considered to be the oxide of B. Since oxide was detected previously by XRD in both raw material and as-prepared powder, the presence of oxide in EDS was understandable. Traces of C in the EDS spectra were attributed to the C of the melted heat-shrinkable tube during the discharge. Mo was from the Mo-made TEM mesh grid.

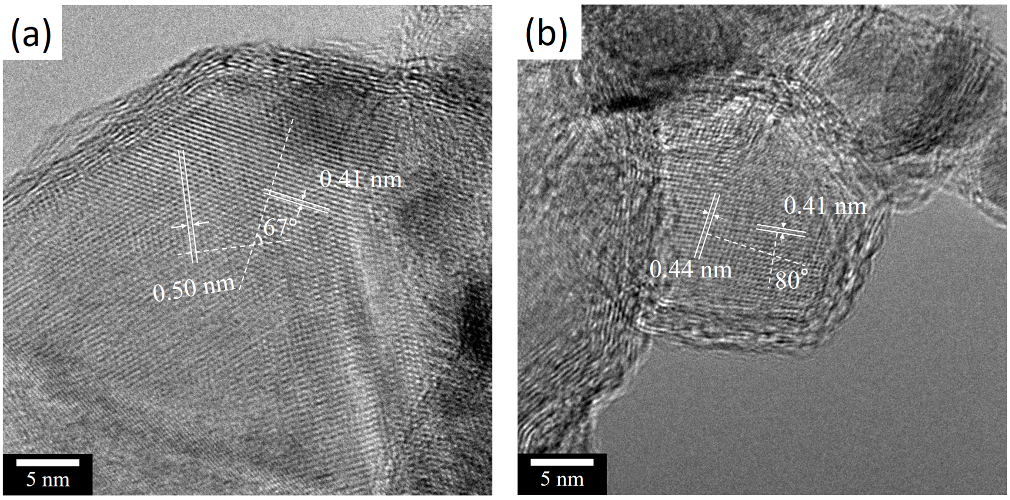

Figure 3.27: Lattice images of B nanoparticles: (a) an angle of 67° between interplanar distances of 0.5 nm and 0.41 nm corresponding to (110) and (105) of B, respectively; (b) an angle of 80° between interplanar distances of 0.44 nm and 0.41 nm corresponding to ($\bar{2}$13) and (105) of B, respectively.

In order to analyze further the nanoparticles of B formed by pulsed discharge of compacted powder, lattice images of them were taken. Figure 3.27 shows lattice images of as-prepared B nanoparticles. By analyzing the distances between two adjacent lattice fringes and the angles generating between those interplanar distances, it was possible to conclude the presence of B nanoparticles. In detail, in Fig 3.27(a), an angle of 67° between the interplanar distances of 0.50 nm and 0.41 nm corresponding to (110) (0.5465 nm) and (105) (0.4255 nm) of B, respectively, were confirmed. In Fig. 3.27, at another position, an angle of 80° between the interplanar distances of 0.44 nm and 0.41 nm corresponding to ($\bar{2}$13)(0.4501 nm) and (105)(0.4255 nm) of B, respectively, was also found.

In the present experiment, because Cu and/or Cu-B particles were mixed with B nanoparticles, a supportive test was done to quantitatively assess the amount of Cu impurity in the sample. By mixing B and Cu powders, with known compositions, standard samples were prepared. Then, XRD patterns of the standard samples were obtained. By comparing these results with the obtained XRD patterns of the prepared sample, it is possible to conclude that the mass of Cu impurity in the sample was approximately 4.8 wt.%. In addition, by SEM images, in the as-prepared powder, there were micron-sized particles remaining. The presence of these particles is considered to be caused by the insufficiency of the deposition energy. 10 mg of B powder needs 591 J to vaporize while only 576.6 J was deposited. Furthermore, the discharge of powder was not energetically as effective as the discharge of wire. A portion of raw material flew out of the arc discharge, hence, was not heated and dropped on the bottom of the chamber.

In summary, due to the extremely high resistance of B at room temperature, it is very difficult to discharge through B elements to generate B nanoparticles. Attempts to discharge B wires in Ar and $N_2$ gas were done, however, it was not possible to collect enough powder for characterization and apparently not suitable for the purpose of production of B nanoparticles. By discharging through B micron-sized powder using Cu rods to compact B powder inside a heat-shrinkable tube, it was possible to prepare crystalline B nanoparticles. However, there are some limitations such as impurity and low effectiveness. Further enhancement of charging voltage as well as improvement of the experimental setup is considered to be essential.

### 3.3.2 Transition metal boride nanoparticles prepared by the pulsed discharge of powder

As described in the previous section, the preparation of B nanoparticles by the pulsed discharge of compacted B micron-sized powder facilitated the synthesis of B-containing compounds, which has never been reported before. For the preparation of B nanoparticles by the pulsed discharge of compacted powder, Cu rods were used as electrodes since Cu did not react with B to form any compounds. However, if the electrodes were varied to other materials such as transition metals, it would be possible to synthesize borides of transition metals. Ti, Mo, W, and Zr were chosen to be the materials of electrodes. In addition, besides crystalline B micron-sized powder used as a starting material as in the previous experiment, amorphous B micron-sized powder was also used for cost-effectiveness and probably more reactive with transition metals than crystalline B was. The experiments were carried out using the experimental setups shown in Fig. 2.1(a), (c), and (d). Experimental conditions of this experiment are shown in Table 3.5.

Table 3.5: Experimental conditions for synthesis of transition metal boride nanoparticles by pulsed discharge of compacted powder

| | | |
|---|---|---|
| Raw material | Crystalline B micron-sized powder (~40 µm) ~5 mg/discharge | Amorphous B micron-sized powder (<1 µm) ~1.5 mg/discharge |
| Electrodes | W, Mo, and Zr rod $\phi$=2 mm, Ti rod $\phi$ =2.5 mm | |
| Sublimation energy | 296 J | 88 J |
| Heat-shrinkable tube | Inner diameter=2.1 mm (before heating) for $\phi = 2$ mm<br>Inner diameter=2.6 mm (before heating) for $\phi = 2.5$ mm | |
| Charging voltage, $V_c$ | 6.2 kV | 6 kV |
| Capacitance, $C$ | 30 µF | |
| Ambient gas | Ar | |
| Ambient gas pressure | 100 kPa | |

#### 3.3.2.1 Titanium boride nanoparticles

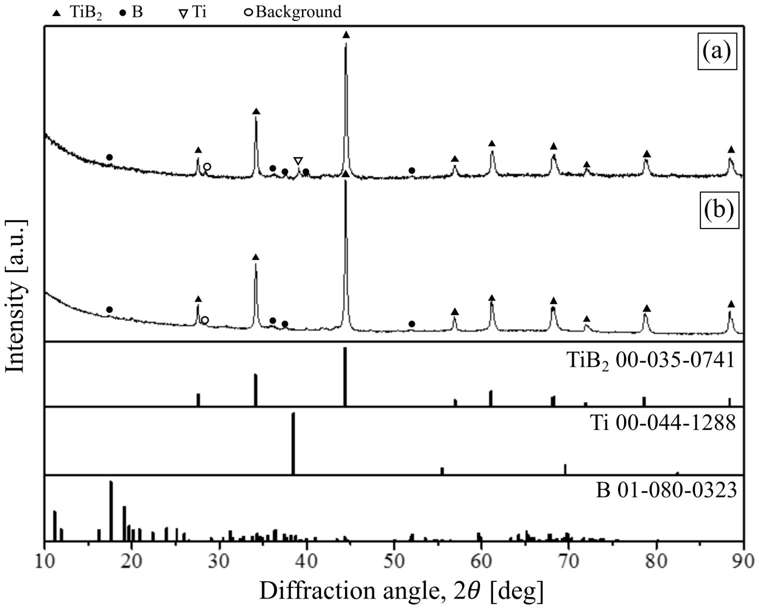

Figure 3.28: XRD patterns of as-prepared powder by the pulsed discharge of (a) crystalline B micron-sized powder and (b) amorphous B powder with Ti rods.

Figure 3.28 shows XRD patterns of the as-prepared powders obtained by the pulsed discharge of (a) crystalline and (b) amorphous B micron-sized powders between Ti rods. According to the XRD patterns, $TiB_2$ and B were detected in both (a) crystalline and (b) amorphous B powders. However, the peaks of $TiB_2$ show the highest intensity among detected phases, thus, $TiB_2$ is the main phase of the product in both (a) crystalline and (b) amorphous B powders. In the case of crystalline B powder used as the raw material, peaks of Ti phase were detected. This Ti phase is a high-temperature phase formed at T ¿ 1173 K[279] and was likely formed at a high electrical discharge temperature. These peaks of Ti were not detected in the XRD pattern of the powder synthesized from amorphous B. This difference can be explained by the higher specific surface area of the amorphous powder than the crystalline one. Considering the particle size of both raw materials, due to the smaller size of amorphous B powder than crystalline B powder ($\leq$ 1 µm vs $\sim$ 40 µm), the reactions between amorphous B and metals are considered to be faster than those between crystalline B and metals. Therefore, it is reasonable to consider that the high-temperature phase of Ti detected in the case of using crystalline B powder as a raw material originated from the melted Ti that did not react with B powder to form $TiB_2$. Furthermore, B peaks detected in the XRD patterns might come from the raw material remaining after the deposition of pulsed discharge. With the raw material of amorphous B, at the temperature over 1000°C[280], amorphous powder which has not yet reacted with Ti while being heated may form β-rhombohedral. In addition, a peak at 28.4° was also detected, however, did not belong to any possible phases. An X-ray diffraction measurement with a low scan speed (1 deg/minute) of only Si holder without any powder revealed a peak at diffraction angle 28.4°, which is corresponding to (*hkl*) indices of 111 of Si. As a result, the peak at 28.4° is considered as a part of the background.

Figure 3.29(a) shows a bright-field TEM image of the as-synthesized powder obtained using crystalline B micron-sized powder as the raw material. All of the observed particles are in a nearly spherical morphology and smaller than 100 nm. EDS analysis was employed to identify the composition of a single nanoparticle or a small area including a few nanoparticles. In order to do that, the electron beam was focused to a spot size of 10 nm. For the convenience of detection of X-ray, the specimen was tilted 15° with respect to the electron incident axis. Figure 3.29(b) shows the results of the EDS analysis of the nanoparticles shown in Fig. 3.29(a). In Fig. 3.29(b), from bottom to top, spectra (1) to (6) show the composition of nanoparticles of the corresponding positions marked in Fig. 3.29(a). The top EDS spectrum shows the composition of all nanoparticles in the overall area. According to the EDS analysis, B, C, Ti, O, Fe, Cu, and Cr were detected in the analyzed area. The presence of B and Ti, which are elemental components of the main phase determined by XRD as $TiB_2$, is explainable. By considering the intensity of the peaks of B and Ti in the EDS spectrum of an overall area, due to the fact that B is more difficult to be detected with X-ray than Ti because B is a much lighter element, the intensity of the B peak is relatively high compared with that of the Ti peak despite Ti being easier to detect by EDS. In similar experiments described in section3.3.1, where although a Cu peak was clearly observed by EDS, quantitative measurement by an analysis of standard samples using XRD showed a Cu content of only 4.8% by mass. In this case, with a similar way of consideration, despite the weak peaks of B in Fig. 3.28, it is speculated that B was not only present in $TiB_2$ but was also present in excess. Additionally, the presence of oxygen detected by EDS might indicate the presence of a passivation oxide layer on the nanoparticles. This passivation oxide layer is usually observed with nanoparticles with large specific surface area and plays a role to protect the nanoparticles from further oxidation. C originated from the melted carbon-made heat-shrinkable tube due to the high temperature of electrical pulsed discharge. Moreover, the detection of Fe and Cr can be explained as the unexpected impurities stemming from the stainless steel nuts and electrodes. Finally, Cu peaks in the EDS spectra were because of using of copper TEM microgrid.

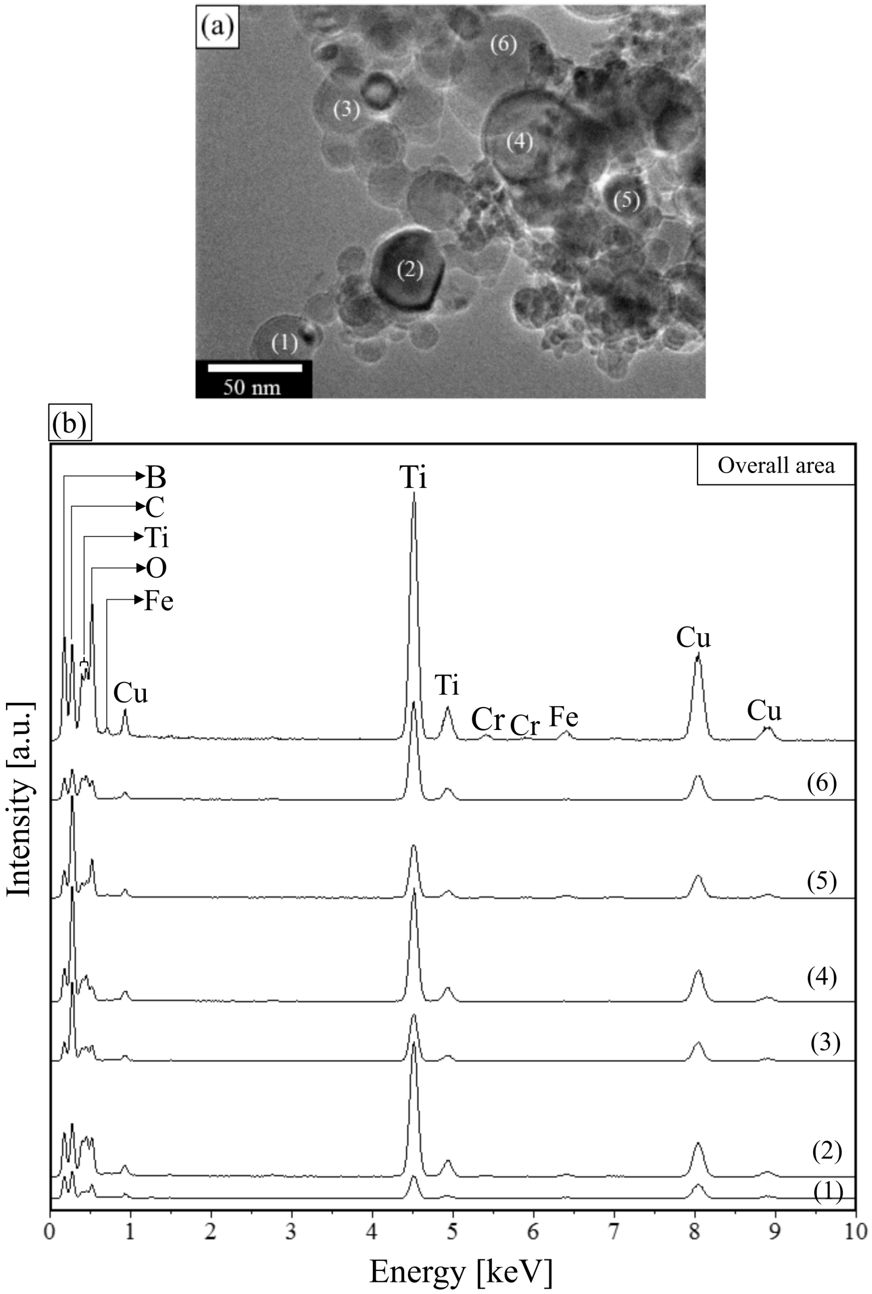

Figure 3.29: (a) Bright-field TEM image of nanoparticles prepared by the pulsed discharge of crystalline B micron-sized powder with Ti rods and (b) EDS spectra of the overall area and corresponding positions marked in (a) from (1) to (6).

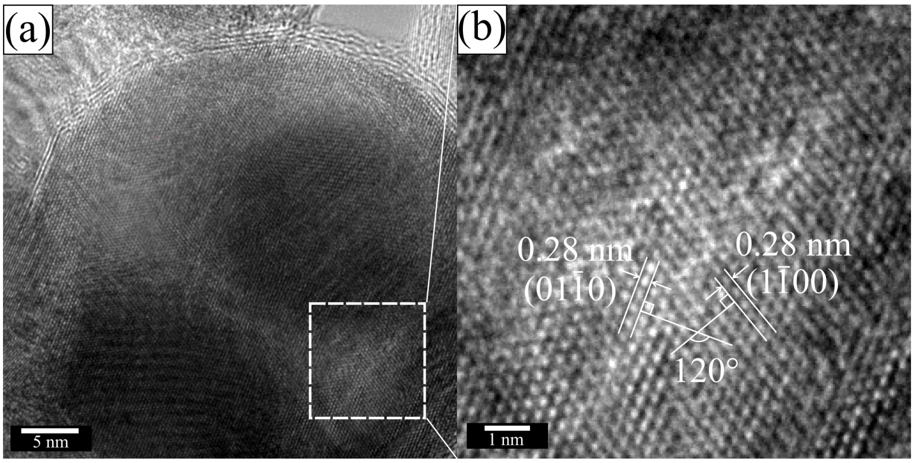

Figure 3.30: (a) TEM lattice image of a TiB$_2$ nanoparticle and (b) enlarged image of (a). An angle of 120° between planes with interplanar distances of 0.28 nm and 0.28 nm correspond to that between two planes with (*hkil*) indices of $\{10\bar{1}0\}$, which are $(01\bar{1}0)$ and $(1\bar{1}00)$ of TiB$_2$, respectively.

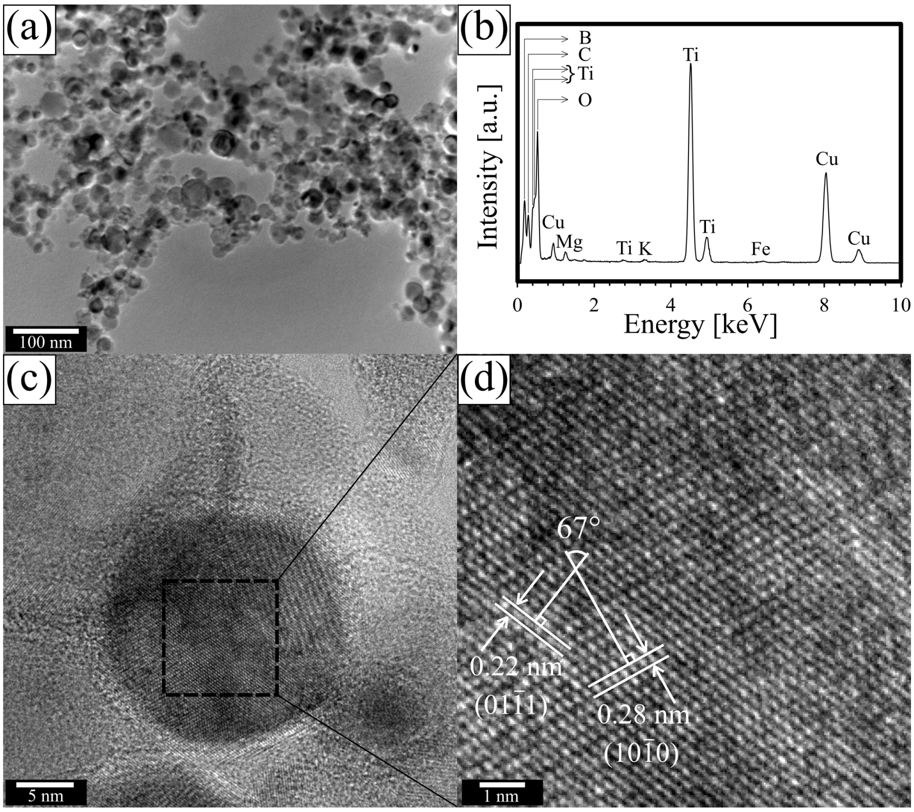

Figure 3.31: (a) Bright-field TEM image of nanoparticles prepared by the pulsed discharge of amorphous B powder with Ti rods; (b) EDS spectrum of the overall area observed in (a). (c) TEM lattice image of a TiB$_2$ nanoparticle; (d) an enlarged and cropped image of (c), showing an angle of 67° between planes with interplanar distances of 0.22 nm and 0.28 nm, corresponding to planes $(01\bar{1}1)$ and $(10\bar{1}0)$ of TiB$_2$, respectively.

Figure 3.30 shows TEM lattice images of a nanoparticle identified as TiB$_2$ from the sample prepared using crystalline B micron-sized powder. In Fig. 3.30(b) enlarged image of (a), an angle of 120° between planes with interplanar distances of 0.28 nm and 0.28 nm corresponds to that between two planes with (*hkil*) indices of $\{10\bar{1}0\}$, which are possibly $(01\bar{1}0)$ and $(1\bar{1}00)$ of $TiB_2$, because $TiB_2$ has a hexagonal unit cell, with two $\{10\bar{1}0\}$ planes creating an angle of 60°, 120°, or 180°. The $TiB_2$ nanoparticles with such lattice fringes were observed in many areas of the TEM specimen. Therefore, from the results of XRD patterns, EDS spectra, and the lattice images, it can be concluded that $TiB_2$ nanoparticles were generated by the pulsed discharge of crystalline B micron-sized powder and represented a large proportion of the sample.

Figure 3.31(a) shows a bright-field TEM image of the as-synthesized nanoparticles using amorphous B powder as a raw material. Similar to the case of using crystalline B powder as raw material, these nanoparticles are also smaller than 100 nm and in a spherical shape. Figure 3.31(b) shows the EDS spectrum corresponding to the nanoparticles in Fig. 3.31(a). From the EDS results, it can be seen that Ti, B, C, O, Mg, K, and Fe are present in these nanoparticles. Among that, Ti and B were target elements; C originated from the heat-shrinkable tube and O originated from the passivation layer on the surface of the nanoparticles, similar to the case of the crystalline B micron-sized powder. Additionally, Mg and K were also detected by EDS. Since these elements did not involve in any parts of the experiment, they were likely coming from the raw material. Amorphous B powder was subjected to analysis by TEM, the results are shown in Fig. 3.32. According to the EDS quantitative analysis, the amount of Mg and K was 0.74 wt.% and 0.31 wt.%, respectively. Moreover, from the EDS result of Fig. 3.31(b), the amount of Fe, which was an unexpected impurity, was determined to be 0.23 wt.%. This Fe might come partially from the Fe pole pieces of the magnetic lens inside the TEM. In Fig. 3.31 (d), which is a high magnification of a lattice image shown in (c), an angle of 67° between planes with interplanar distances of 0.22 nm and 0.28 nm, corresponding to planes $(01\bar{1}1)$ and $(10\bar{1}0)$ of $TiB_2$, confirmed the presence of $TiB_2$ nanoparticles in the sample.

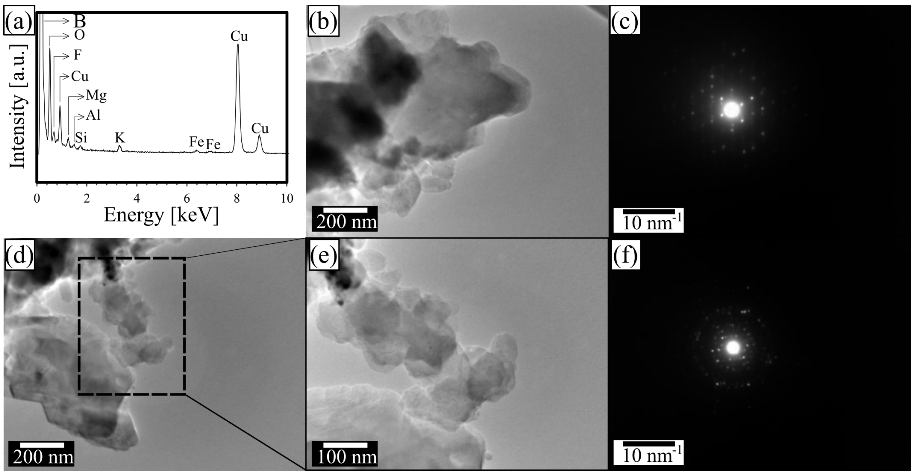

Figure 3.32: (a) EDS spectrum of amorphous B powder. (b), (d), and (e) are bright-field TEM images of amorphous B. (b) shows relatively large B particles whose diffraction image is shown in (c). (e) is an enlargement of (d) and shows small B particles whose diffraction image is shown in (f)

Figure 3.32 shows (a) EDS spectrum of amorphous B powder, (b), (d), and (e) bright-field TEM images of amorphous B. Figure 3.32 (c) and (f) are diffraction images of (b) and (d), respectively. A quantitative measurement using EDS results in Fig. 3.32(a) indicated that Mg, Al, Si, K, and Fe are present in concentrations of 0.37, 0.1, 0.08, 0.51, and 0.35 wt.%, respectively. Figure 3.4(b) shows a group of submicron-sized particles whose diffraction image shown in Fig. 3.32 exhibits a diffraction pattern of crystalline particles. On the other hand, Fig. 3.32(e) shows a group of submicron-sized particles with a smaller size than those shown in (b). These submicron-sized particles have diffraction images shown in Fig. 3.32(f) indicating a diffraction pattern of polycrystalline particles which are different from particles shown in (b).

#### 3.3.2.2 Molybdenum boride nanoparticles

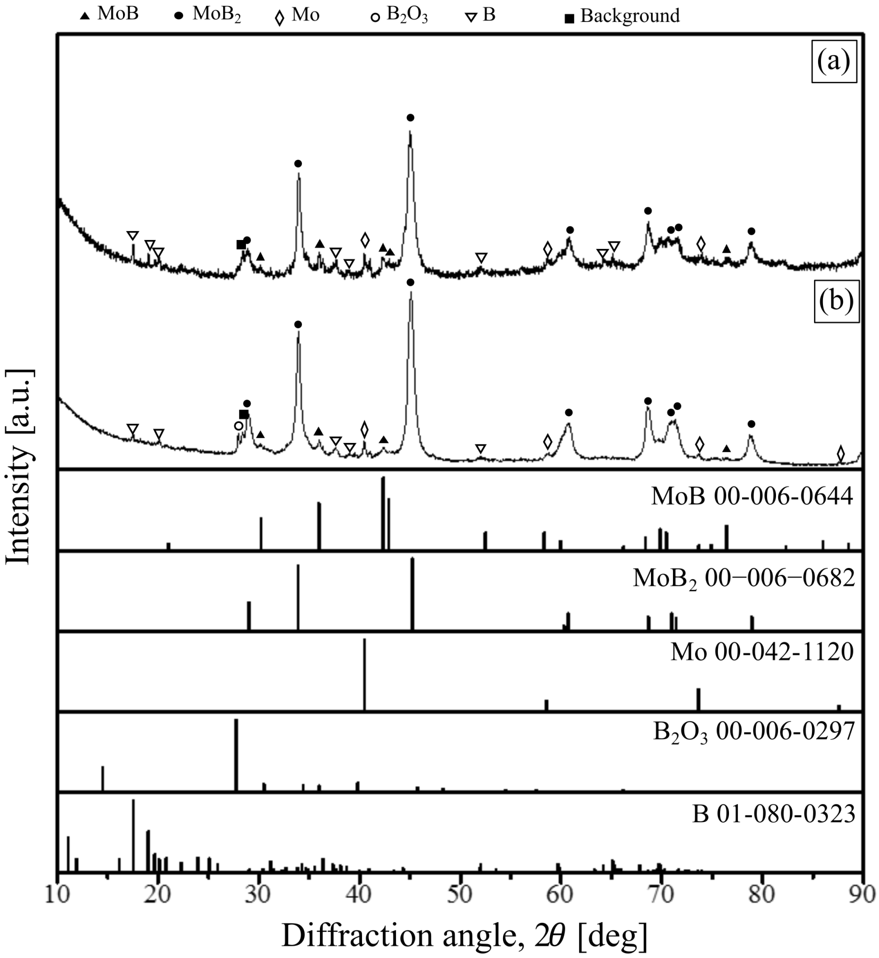

Figure 3.33: XRD pattern of the as-prepared powder obtained by the pulsed discharge of (a) crystalline and (b) amorphous B micron-sized powder with Mo rods.

Figure 3.33 shows XRD patterns of the powders obtained by the pulsed discharge of (a) crystalline and (b) amorphous B micron-sized powder with Mo rods. As shown in the XRD patterns, the as-synthesized powder in both cases (a) and (b) consisted of MoB, $MoB_2$, Mo, and B. Among those, $MoB_2$ was considered the main phase in both cases (a) and (b) because peaks of $MoB_2$ were the most clearly observed. Besides, MoB whose peaks were very low compared to those of $MoB_2$ was considered as a minor phase of the reactions between Mo and B. The presence of B and $B_2O_3$ indicates the amount of residual B and its oxide phase after the deposition of the pulsed discharge. Furthermore, a peak at 28.4°, which appeared in both cases (a) and (b), was confirmed as a background peak, as mentioned in section3.3.2.1.

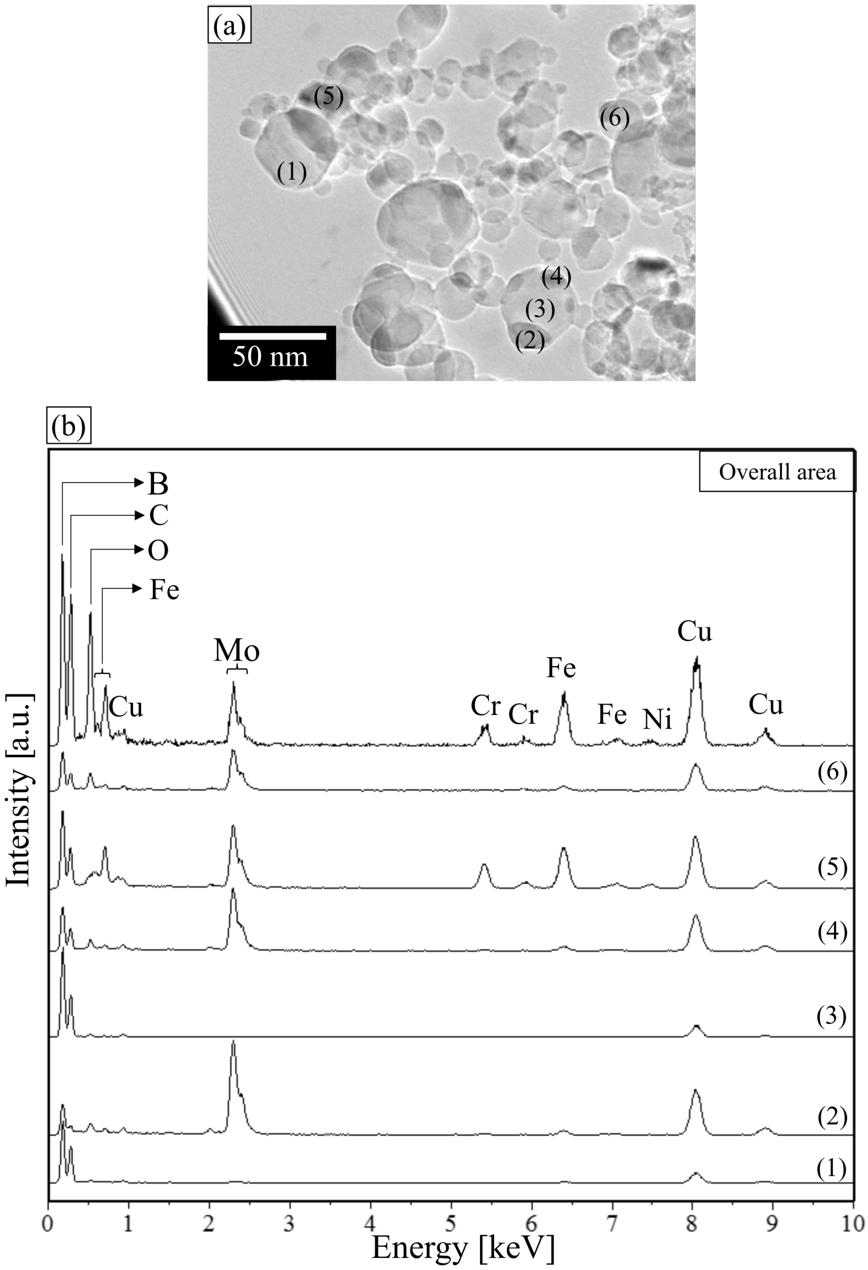

Figure 3.34: (a) Bright-field TEM image of nanoparticles prepared by the pulsed discharge of crystalline B micron-sized powder with Mo rods and (b) EDS spectra of the overall area and the corresponding positions labeled as (1) to (6) in (a).

Figure 3.34(a) shows a bright-field TEM image of nanoparticles prepared by the pulsed discharge of crystalline B micron-sized powder and Fig. 3.34(b), from bottom to top, shows EDS spectra corresponding to the six numbered positions in (a) and to nanoparticles in the overall area. According to the bright-field TEM image, the as-synthesized particles are smaller than 100 nm and in a nearly spherical shape. The EDS result in the overall area shows that Mo, B, C, O, Fe, Cr, Ni, and Cu were present in the sample. Among those, in the EDS result of an overall area, the intensity B peak is even higher than that of Mo, indicating that the B might be more abundant in the sample than in the Ti–B samples. It was noted that, at positions (1) and (3), almost no Mo was detected. If the diffraction contrast is negligible, based on the contrast of the positions (1) and (3) in the TEM images, it can be considered that there was a high concentration of B in these positions, which is consistent with the EDS spectra. This is because the greater the atomic mass, the shallower the electron beam can penetrate the sample, which means that fewer electrons reach the fluorescent screen and the shadows become darker. Additionally, C is an impurity coming from heated and vaporized heat-shrinkable tubes. Fe, Cr, and Ni are impurities originating from the stainless steel electrodes, and Cu was not from the sample but detected due to the scattering of electrons on the Cu TEM microgrid.

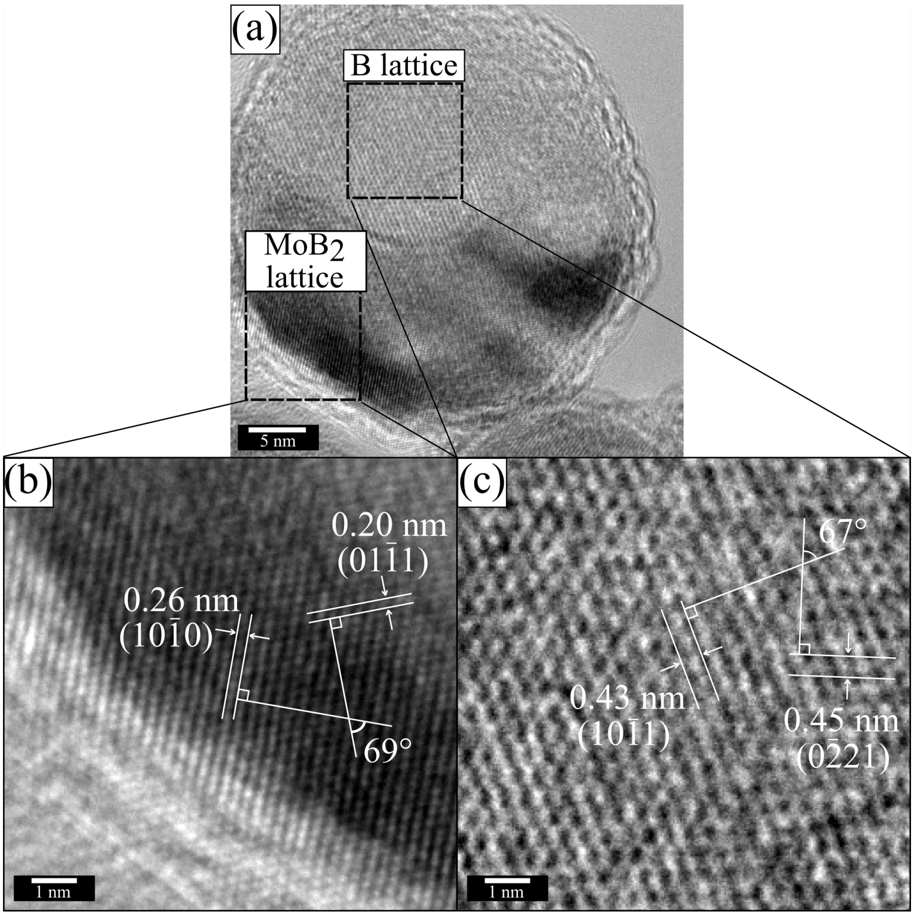

Figure 3.35: (a) TEM lattice image of a $MoB_2$ nanoparticle. In (b), which is an enlargement of (a), an angle of 69° between planes with interplanar distances of 0.26 nm and 0.20 nm is observed. These planes correspond to two planes $(10\bar{1}0)$ and $(01\bar{1}1)$ of $MoB_2$, respectively. (c) an angle of 67° between planes with interplanar distances of 0.43 nm and 0.45 nm corresponding to two planes $(10\bar{1}1)$ and $(0\bar{2}21)$ of B, respectively.

Figure 3.35(a) shows a TEM micrograph of a single nanoparticle in the sample. Figures 3.35(b) and (c) are high magnification of (a) and show lattices identified as $MoB_2$ and B, respectively. In the lattices shown in (b), an angle of 69° is observed between planes with interplanar distances of 0.26 nm and 0.20 nm. These planes correspond to the two planes with (*hkil*) indices of $\{10\bar{1}0\}$ and $\{10\bar{1}1\}$, which are $(10\bar{1}0)$ and $(01\bar{1}1)$ of $MoB_2$, respectively. At (c), an angle of 67° between planes with interplanar distances of 0.43 nm and 0.45 nm corresponds to the $(10\bar{1}1)$ and $(0\bar{2}21)$ planes of B, respectively. Basing on these lattice images and the EDS spectra in Fig. 3.34(b), it can be concluded that the synthesized nanoparticles mainly comprise crystallites of $MoB_2$ and B. From these results, it is also possible to explain the presence of excess B in XRD results.

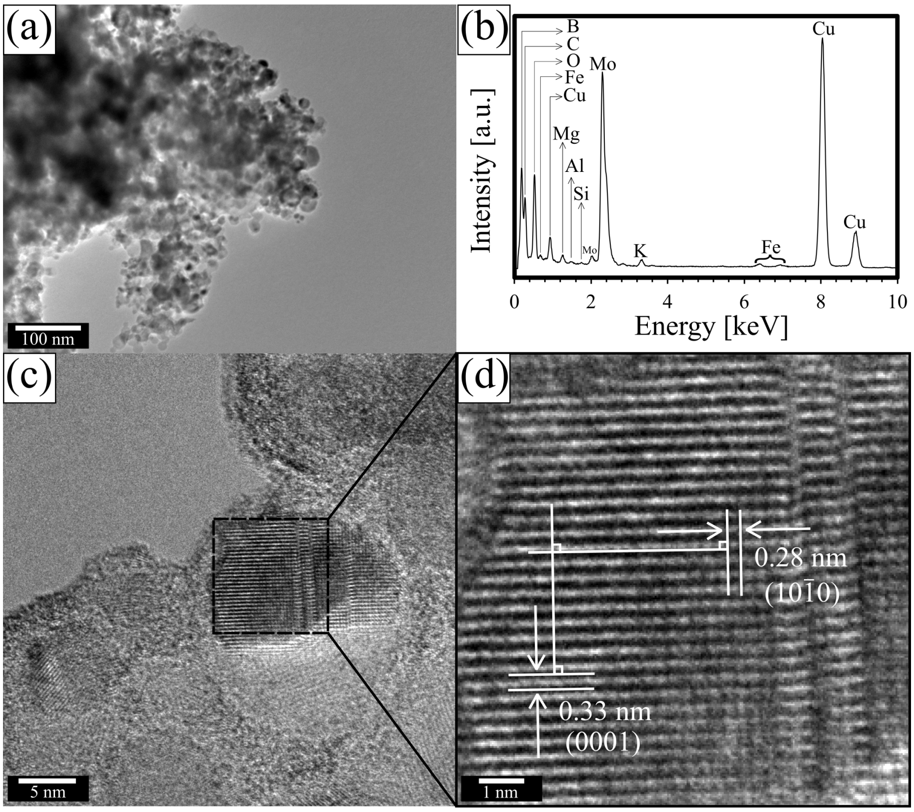

Figure 3.36: (a) Bright-field TEM image of nanoparticles prepared by the pulsed discharge of amorphous B powder with Mo rods and (b) EDS spectrum of the overall area observed in (a). (c) TEM lattice image of a MoB$_2$ nanoparticle, (d) enlarged and cropped image of (c) shows a right angle between planes with interplanar distances of 0.33 nm and 0.28 nm, corresponding to planes (0001) and $(10\bar{1}0)$ of MoB$_2$, respectively.

Figure 3.36(a) shows a bright-field TEM image of nanoparticles prepared by the pulsed discharge of amorphous B powder with Mo rods. Figure 3.36(b) shows the EDS spectrum of the nanoparticles observed in Fig. 3.36(a). According to the EDS result, besides Mo and B are target elements, C, O, Mg, Al, Si, K, and Fe are also present in the as-synthesized nanoparticles. The presence of Mo, B, C, and O can be explained for the same reasons mentioned in section 3.3.2.1, while Mg, Al, Si, and K are originally present in the amorphous B powder itself as explained by the EDS results obtained from Fig. 3.32(a). Figures 3.36(c) and (d) show lattice images of a nanoparticle. In Fig. 3.36(d), a right angle between planes with interplanar distances of 0.33 nm and 0.28 nm corresponding to planes (0001) and $(10\bar{1}0)$ of MoB$_2$, respectively, was confirmed. The results of bright-field TEM image, EDS spectra, and lattice images in Fig. 3.36 show that with the raw material of amorphous B powder, it was also possible to synthesize MoB$_2$ powder similar to the case of using crystalline B powder.

#### 3.3.2.3 Tungsten boride nanoparticles

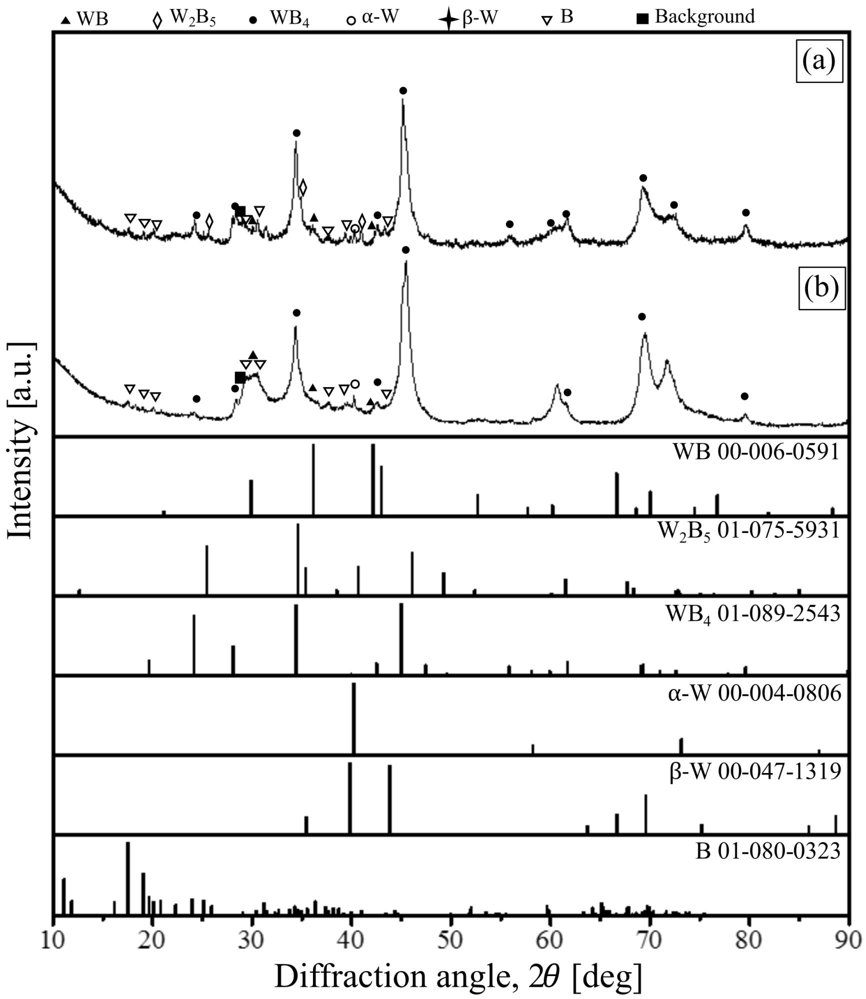

Figure 3.37: XRD pattern of the as-prepared powder obtained by the pulsed discharge of (a) crystalline and (b) amorphous B micron-sized powder with W rods.

Figure 3.37 shows the XRD patterns of as-synthesized powder obtained by the pulsed discharge of (a) crystalline and (b) amorphous B micron-sized powder with W rods. In both Figs. 3.37(a) and (b), two strong peaks at $\sim 34°$ and $\sim 45°$ and a group of several peaks between 55° and 80° are very close to the peak positions listed in the ICDD database for $WB_4$. However, because of the difference in relative intensity of these peaks in the two XRD patterns compared with the peaks in the ICDD database for $WB_4$, it is hard to conclude that this phase is $WB_4$. Due to the similarity between the results and the ICDD data for $WB_4$, it is speculated that this phase is a tungsten boride whose crystal structure is similar to $WB_4$ but probably different in the number of B atoms per stoichiometric formula. Additionally, the phase $W_2B_5$ (R-3m) referred to in Fig. 3.37 was already reported by Wu et al.[278]. According to Wu et al.[278], this phase was formed due to the decomposition of $WB_4$ at temperatures greater than 1200°C because $WB_4$ is an unstable phase. Therefore, it is understandable that phase $W_2B_5$ (R-3m) was present in the sample. Furthermore, WB, $\alpha$-W, $\beta$-W, and B were confirmed in both (a) and (b) and considered as minor phases due to the low relative intensity. Among those, $\alpha$-W originated from the phase transition of $\beta$-W at temperatures greater than 700°C[281], which was likely to occur in the pulsed electrical discharge.

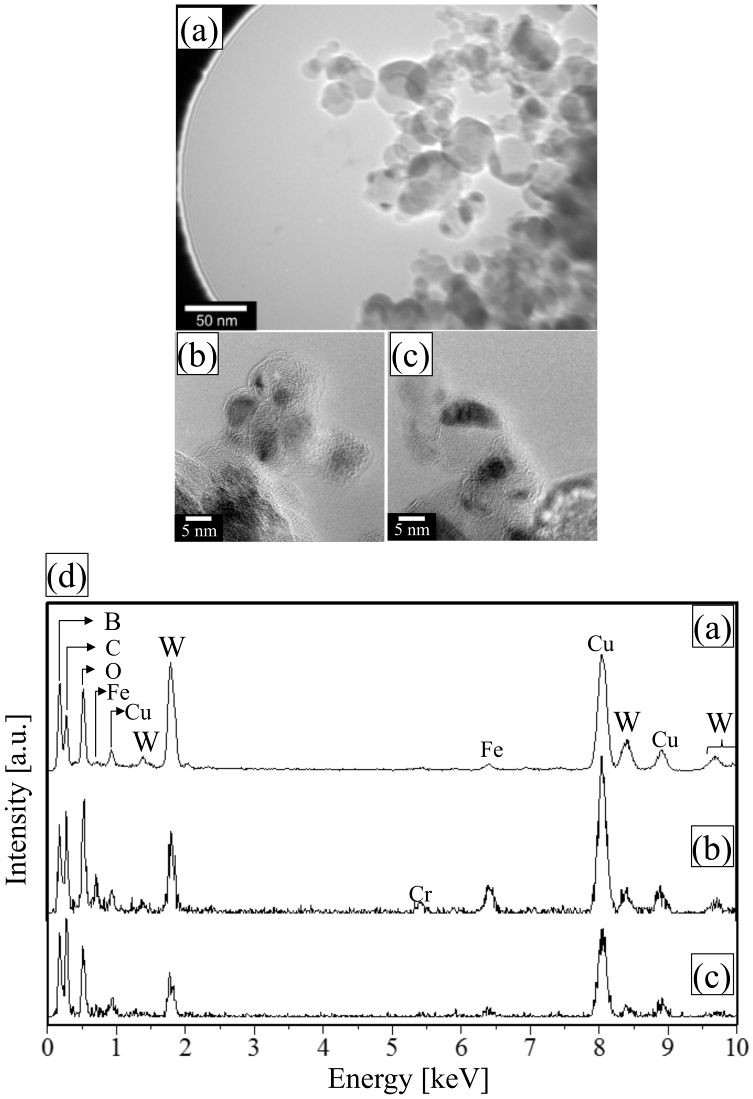

Figure 3.38: (a), (b), (c) Bright-field TEM images of nanoparticles prepared by the pulsed discharge of crystalline B micron-sized powder with W rods and (d) EDS spectra of the overall area and corresponding positions in (a), (b), and (c).

Figures 3.38(a), (b), and (c) show TEM images of nanoparticles synthesized by the pulsed discharge of crystalline B micron-sized powder with W rods. Figure 3.38(d) shows the corresponding EDS spectra of the nanoparticles observed in Figs. 3.38. The TEM images show that these as-synthesized nanoparticles are smaller than 100 nm and have a nearly spherical shape. The EDS spectra show that B and W were present in high concentrations in all three positions. Additionally, C from the heat-shrinkable tube and Fe and Cr from the stainless-steel electrodes were detected. Besides, O originated from the oxidized surface of nanoparticles. Cu was not from the sample but from the Cu TEM microgrid. Basing on the TEM images, the relative intensity of B and W in all three EDS spectra, and the hypothesis that B was excess, the darker regions in the TEM images are likely tungsten boride and the lighter parts are likely B. In order to make clear this assumption, some lattice images were analyzed and shown in Fig. 3.39 below.

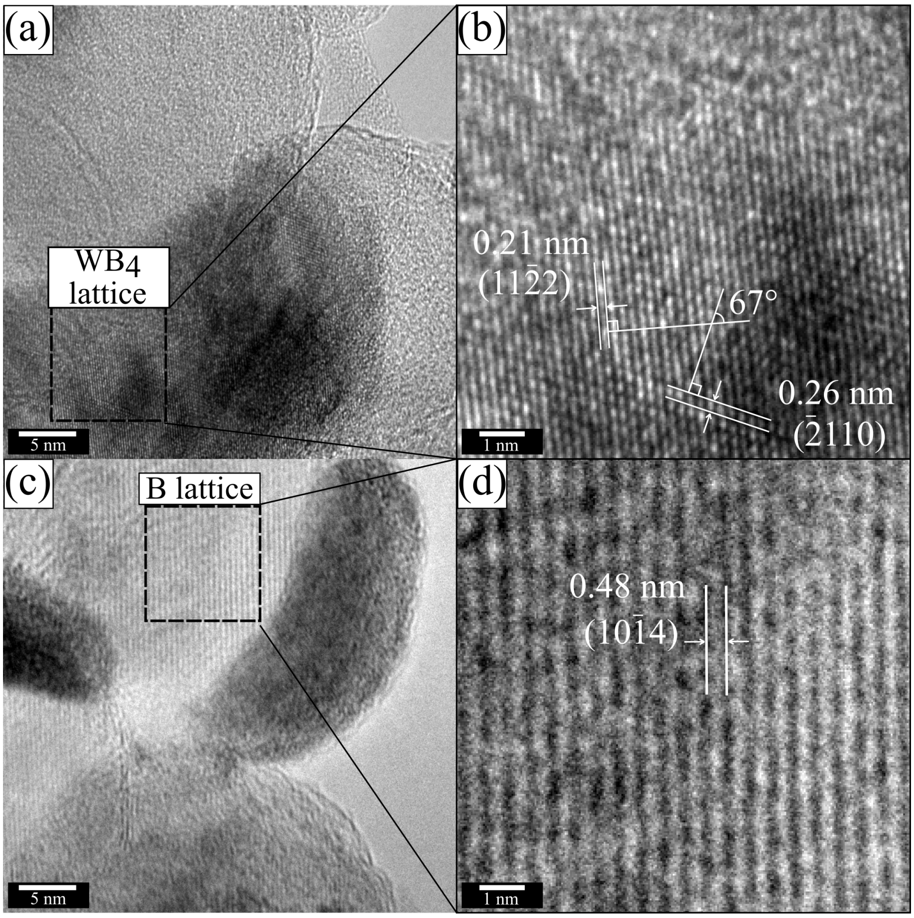

Figure 3.39: TEM lattice images of "approximately $WB_4$" nanoparticles. In (b)-enlargement of (a), an angle of 67° between planes with interplanar distances of 0.21 nm and 0.26 nm is observed. These planes correspond to two planes, $(11\bar{2}2)$ and $(\bar{2}110)$, of $WB_4$, respectively. In (d)-enlargement of (c), a distance of 0.48 nm corresponds to planes with (*hkil*) indices of $\{10\bar{1}4\}$ of B.

Figure 3.39 shows lattice images of "approximately $WB_4$" nanoparticles (the quote marks indicate the difference of XRD patterns of as-synthesized powder and the ICDD card, which was mentioned in the XRD result). In (b), which is a high-magnification image of the regions shown in (a), an angle of 67° is observed between planes with interplanar distances of 0.21 nm and 0.26 nm. These planes correspond to the $(11\bar{2}2)$ and $(\bar{2}110)$ planes of $WB_4$, respectively. In Fig. 3.39 (c), a particle is comprised of two parts: a dark part on the right and a light part on the left which are likely grains of $WB_4$ and B, respectively. By analyzing Fig. 3.39 (d)-the enlarged image of (c), it was understood that the light part exhibited an interplanar distance of 0.48 nm and corresponds to the plane of B with (*hkil*) indices of $\{10\bar{1}4\}$. Despite the error of 0.02 nm compared with the reference data (B ICDD 01-080-0323), since no other possible phases had a spacing similar to 0.48 nm, this lattice was identified as B.

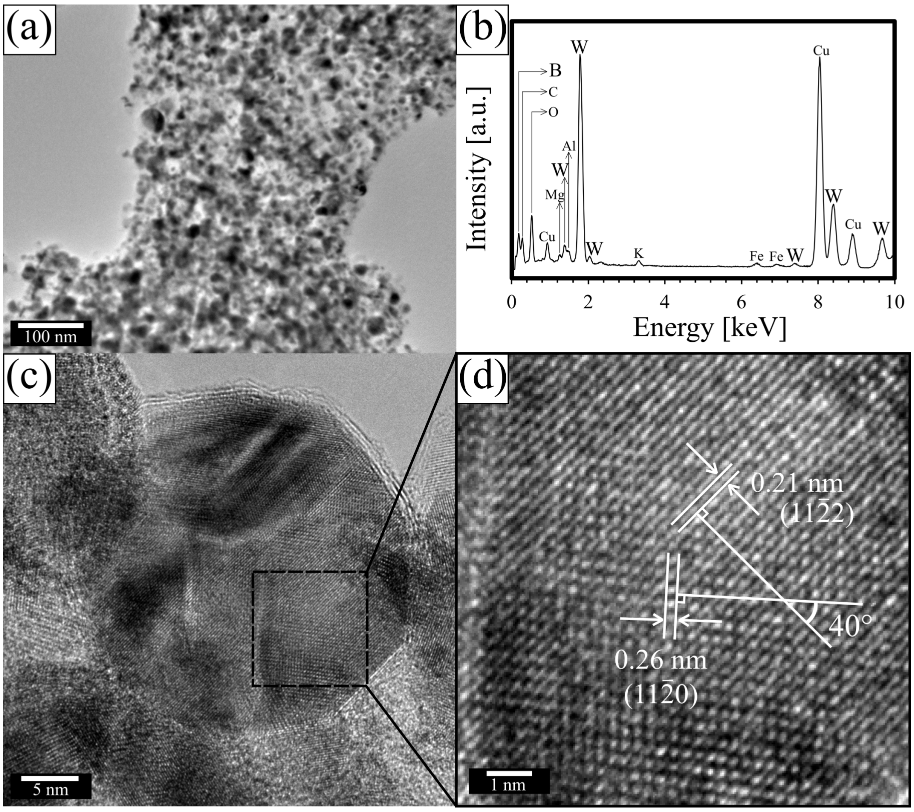

Figure 3.40: (a) Bright-field TEM image of nanoparticles prepared by the pulsed discharge of amorphous B powder with W rods. (b) EDS spectrum of the overall area observed in (a). (c) TEM lattice image of an "approximately $WB_4$" nanoparticle. (d) Enlarged and cropped image of (c) showing an angle of 40° between planes with interplanar distances of 0.26 nm and 0.21 nm, corresponding to planes (11$\bar{2}$0) and (11$\bar{2}$2) of $WB_4$, respectively.

Basing on the results obtained with Ti-B and Mo-B experiments as well as the XRD patterns shown in Fig. 3.37, the composition analyses of nanoparticles synthesized with W rods and amorphous B powder were expected to be similar to those synthesized with W rods and crystalline one. Figure 3.40(a) shows a bright-field TEM image of nanoparticles prepared by the pulsed discharge of amorphous B powder with W rods. Figure 3.40(b) shows the EDS spectrum of the nanoparticles observed in Fig. 3.40(a). According to the EDS results, besides W and B are target elements, B, C, O, Mg, Al, K, and Fe are also present in the sample. Quantitative analysis by EDS shows that the contents of Mg, Al, K, and Fe are 0.58, 1.00, 0.76, and 0.81 wt.%, respectively. Figure 3.40(c) shows a TEM lattice image of an "approximately $WB_4$" nanoparticle, and Fig. 3.40(d) shows a higher-magnification and cropped image of (c). In Fig. 3.40(d), an angle of 40° is observed between planes with interplanar distances of 0.26 nm and 0.21 nm, corresponding to planes (11$\bar{2}$0) and (11$\bar{2}$2) of $WB_4$, respectively.

### 3.3.2.4 Zirconium boride nanoparticles

When nanoparticles of borides were synthesized using the original experimental setup shown in Fig. 2.1(c), unexpected impurities from the stainless steel electrodes were usually incorporated into the samples. To suppress the occurrence of these impurities, another experimental setup was developed. Instead of the rods being held by stainless steel nuts, holes were drilled through the stainless-steel electrodes, through which the metal rods were inserted; this arrangement lowered the contact resistance, decreasing the likelihood of the stainless steel electrodes melting and contaminating the sample. This modified experimental setup was used with crystalline B micron-sized powder as a raw material.

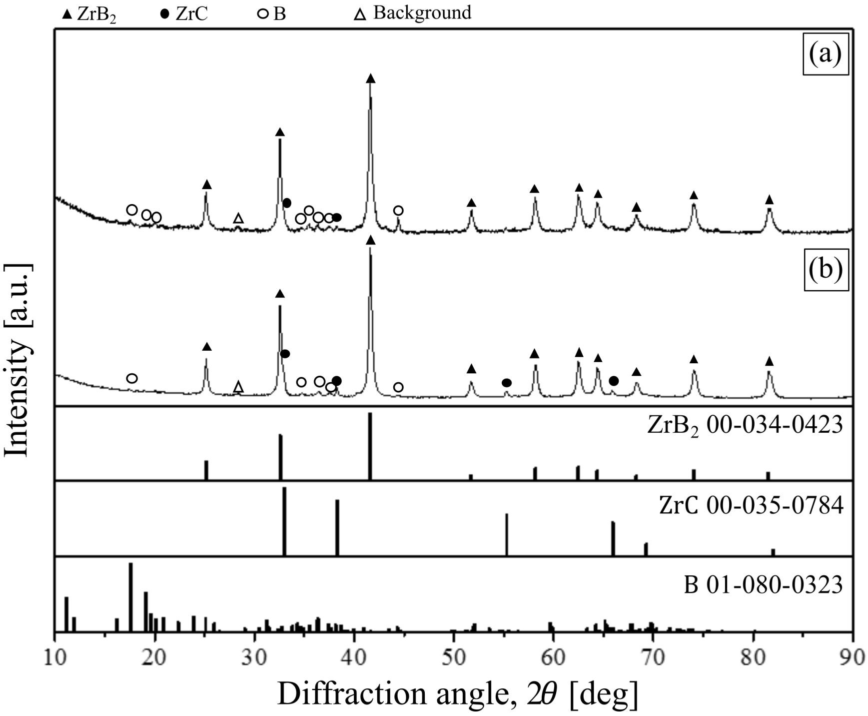

Figure 3.41: XRD pattern of as-prepared powder obtained by the pulsed discharge of (a) crystalline and (b) amorphous B micron-sized powder with Zr rods.

Figure 3.41 shows XRD patterns of the as-synthesized powder obtained by pulsed discharge of (a) crystalline and (b) amorphous B micron-sized powders with Zr rods. According to the XRD patterns, the main phase was determined to be $ZrB_2$ basing on the relative intensity of the XRD peaks. Additionally, ZrC was identified as a minor phase. The formation of ZrC is considered to occur by the high temperature of Zr rods and the C-based heat-shrinkable tubes during the pulsed electrical discharge. The relative content of ZrC compared to that of $ZrB_2$ was calculated by the reference intensity ratio (RIR) method. In this calculation, $ZrB_2$ was assumed as the standard sample. Weight fraction of ZrC ($X_{ZrC}$) was calculated by below formula:

$$X_{ZrC} = \frac{(I/I_c)_{ZrB_2}}{(I/I_c)_{ZrC}} \frac{I_{ZrC}}{I_{ZrB_2}} X_{ZrB_2}, \tag{3.1}$$

where $I_{ZrC}$ and $I_{ZrB_2}$ are intensities of the strongest peaks of ZrC and $ZrB_2$, respectively, obtained from the XRD patterns in Fig. 3.41. The weight fractions of ZrC with respect to $ZrB_2$ in samples prepared using crystalline and amorphous B powder were calculated to be 10.0 wt.% and 12.3 wt.%, respectively. Similar to the previously synthesized boride nanoparticles, these synthesized zirconium boride nanoparticles likely contained excess B.

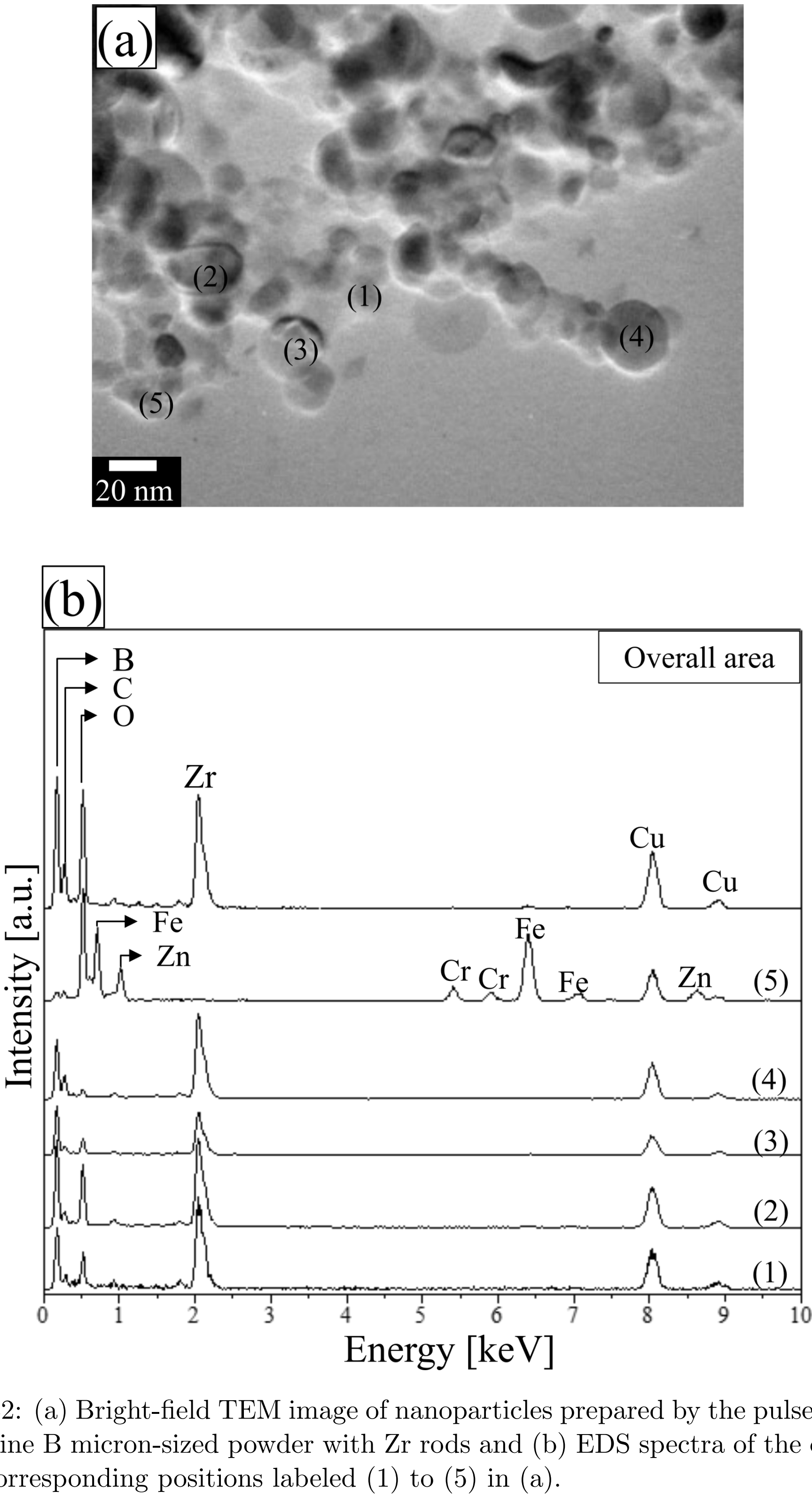

Figure 3.42: (a) Bright-field TEM image of nanoparticles prepared by the pulsed discharge of crystalline B micron-sized powder with Zr rods and (b) EDS spectra of the overall area and the corresponding positions labeled (1) to (5) in (a).

Figures 3.42(a) and (b) show a bright-field TEM image and the EDS spectra of the overall area and the numbered positions in (a), respectively. As shown in the TEM image, nanoparticles prepared by the pulsed discharge of crystalline B micron-sized powder with

Zr rods are smaller than 100 nm and spherical in morphology. The EDS spectrum of the overall area shows that B, Zr, C, and O were present in the sample. Cu from the Cu TEM microgrid was also detected. In particular, comparing to the original experimental setup, the amount of impurities from the stainless steel electrodes was substantially lower. Only a very low peak of Fe at a dispersive energy of $\sim 6.4$ keV was observed in the spectrum of the overall area. Due to the low intensity of this peak, it might be a signal coming from the pole piece of the magnetic lens of the TEM. No impurities from the stainless steel electrodes were visible in the spectra corresponding to positions (1) through (4). Fe, Cr, and Zn were detected at position (5), whereas Zr and B were hardly detected here. As a result, it is speculated that, at position (5), a small piece of stainless steel may be mixed with the sample. In contrast, with the samples prepared using the original experimental setup, either Fe or other components of stainless steel were detected at almost all of the positions, which means melting/vaporization occurred at the contacts between the stainless steel electrodes and the Ti/Mo/W rods during the experiments and were mixed into the sample. Therefore, based on the EDS spectra, the new experiment setup could effectively suppress the impurity formation from the stainless steel electrodes.

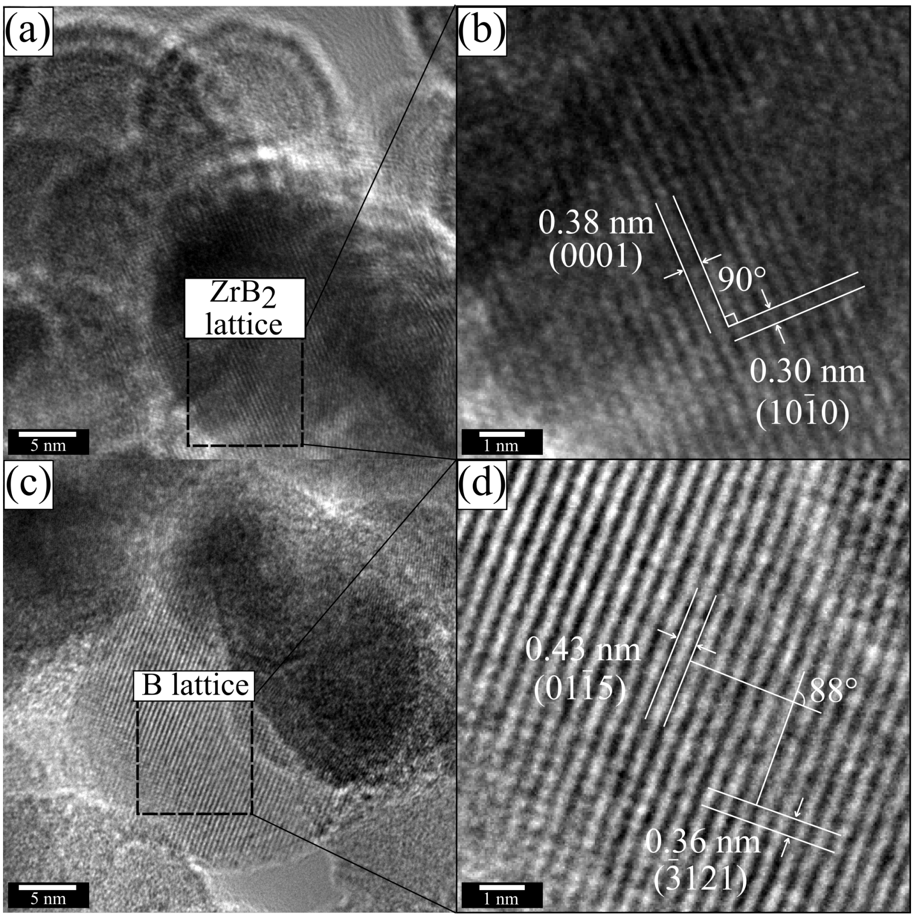

Figure 3.43: TEM lattice images of $ZrB_2$ nanoparticles. In (b), which is an enlargement of (a), an angle of 90° between interplanar distances of 0.38 nm and 0.30 nm is observed. These planes correspond to two planes, (0001) and (10$\bar{1}$0) of $ZrB_2$, respectively. Also, in (d), which is an enlargement of (c), an angle of 88° is observed between interplanar distances of 0.43 nm and 0.36 nm. These planes correspond to planes (01$\bar{1}$5) and ($\bar{3}$121) of B, respectively.

Figure 3.43(a) shows the lattice images of $ZrB_2$ nanoparticles. Figure 3.43(b) shows an enlarged image of the particles in (a), exhibiting a right angle between planes with interplanar distances of 0.38 nm and 0.30 nm. These planes correspond to the planes (0001) and $(10\bar{1}0)$ of ZrB$_2$, respectively. Other nanoparticles are shown in Fig. 3.43(c). In (d), which is the high-magnification of (c), an angle of 88° is observed between planes with interplanar distances of 0.43 nm and 0.36 nm, which correspond to the planes $(01\bar{1}5)$ and $(\bar{3}121)$ of B, respectively. Comparing these results to those described in the synthesis of borides of Ti, Mo, and W, the obtained nanoparticles of borides also comprised of two parts: zirconium diboride and excess boron, which might be the common point of nanoparticles of transition metal boride synthesized by the pulsed discharge of compacted powder.

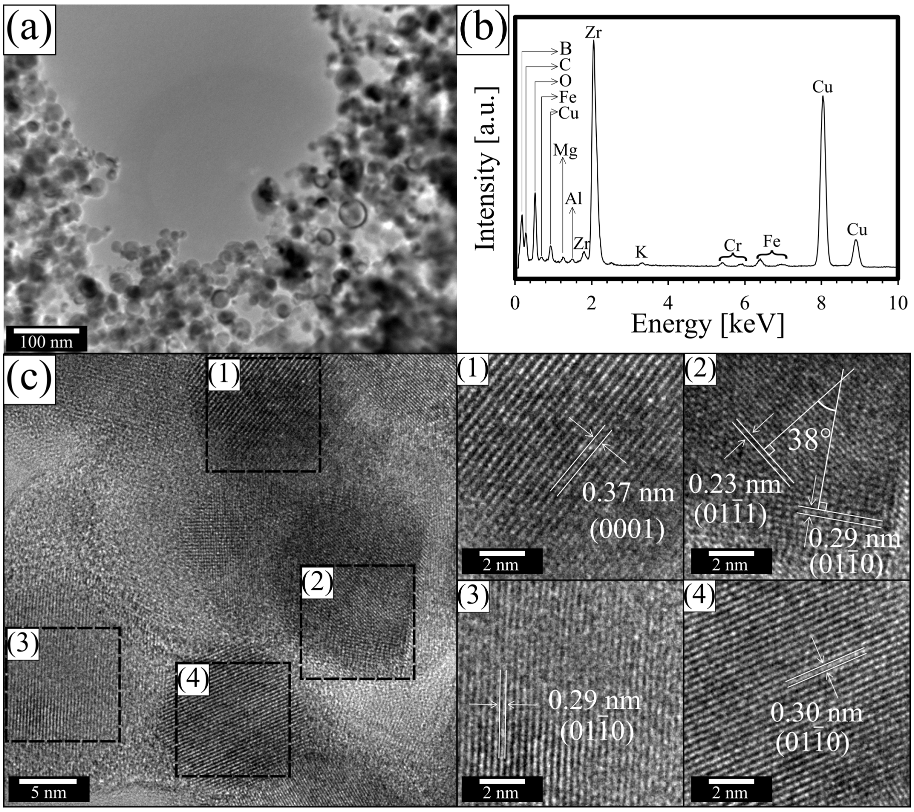

Figure 3.44: (a) Bright-field TEM image of nanoparticles prepared by the pulsed discharge of amorphous B powder with Zr rods. (b) EDS spectrum of the overall area observed in (a). (c) TEM lattice image of several ZrB$_2$ nanoparticles; (1), (2), (3), and (4) are enlarged and cropped images of the corresponding regions in (c). In regions (1), (3), and (4), distances of 0.37 nm, 0.29 nm, and 0.30 nm, correspond to (0001), $(01\bar{1}0)$, and $(01\bar{1}0)$, respectively, of ZrB2. In (2), an angle of 38° is observed between planes with interplanar distances of 0.23 nm and 0.29 nm, corresponding to $(01\bar{1}1)$ and $(01\bar{1}0)$ of ZrB$_2$, respectively.

Figure 3.44(a) shows a bright-field TEM image of nanoparticles synthesized by the pulsed discharge of amorphous B powder with Zr rods. Figure 3.44(b) shows the EDS analysis results for the nanoparticles observed in (a). The EDS result shows that besides Zr and B are target elements, C, O, Mg, Al, K, Cr, and Fe are present in the sample. Quantitative analysis by EDS provided the weight fractions of Mg, Al, K, Cr, and Fe were 0.36, 0.27, 0.23, 0.53, and 1.18 wt.%, respectively. Figure 3.44(c) and the numbered (1) to (4) of the enlarged and cropped images of the nanoparticles in (c) provide the lattice fringes of the synthesized nanoparticles. In detail, the lattices at the positions (1), (3), and (4) show distances of 0.37 nm, 0.29 nm, and 0.30 nm, corresponding to the (0001),

$(01\bar{1}0)$, and $(01\bar{1}0)$ planes of $ZrB_2$, respectively, were confirmed. At position (2), an angle of 38° between planes with interplanar distances of 0.23 nm and 0.29 nm, corresponding to $(01\bar{1}1)$ and $(01\bar{1}0)$ of $ZrB_2$, respectively, was also observed.

#### 3.3.2.5 Discussion on the synthesis of nanoparticles of transition metal borides.

The phase composition of nanoparticles of transition metal borides synthesized by the pulsed discharge of powder can be explained by comparing the phases of the synthesized nanoparticles with the phase diagrams. In the process of nanoparticle synthesis, with the decrease in temperature during cooling, phases began to form from the liquid state. However, although the amount of B in all of the experiments was excessive, the ratio of metal and B was not the same at every position inside the arc discharge. Based on these conditions, phase diagrams of Ti-B, Mo-B, W-B, and Zr-B systems were referred.

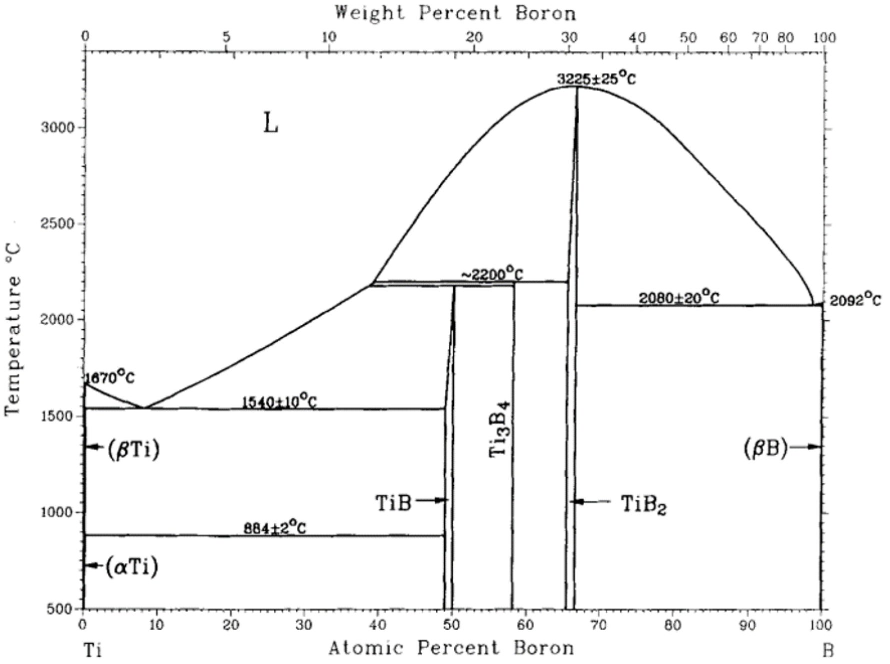

Figure 3.45: Phase diagram of Ti-B system [282](Reproduced with permission from Springer Nature).

Ti-B phase diagram in Fig. 3.45 shows that phase $TiB_2$ could be formed by a mixture of greater than 39 at.% B. In the range between 39 and 66.7 at.% B, TiB, and Ti could be formed via a peritectic reaction[282]. According to the phase diagram, TiB was likely present in the sample; however, the concentration of TiB was probably too small to be detected by XRD. Additionally, the body-centered cubic (bcc) β-Ti beta phase might be formed and then either reacted with residual oxygen to form titanium dioxide at high temperatures or remained in the sample, as detected in the XRD pattern (Fig. 3.28(a)). Basing on the phase diagram, it is possible to explain the reason $TiB_2$ was obtained as the main phase of the synthesized titanium boride nanoparticles.

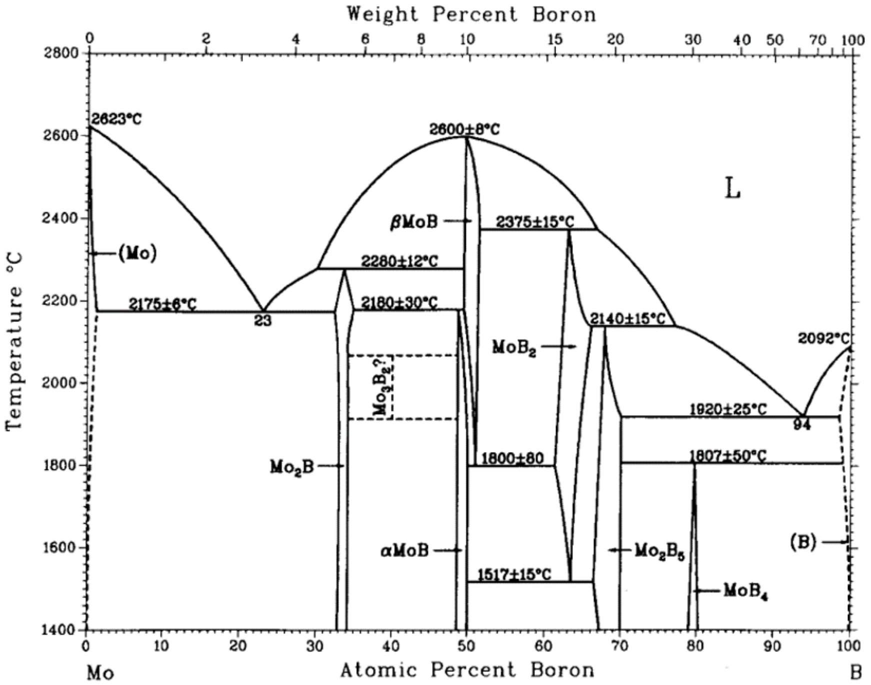

Figure 3.46: Phase diagram of Mo-B system [283](Reproduced with permission from Springer Nature).

In the Mo-B system shown in Fig. 3.46, as described in the last section, the main phase was identified as $MoB_2$ by XRD patterns (Fig. 3.33). According to the phase diagram[283], β-MoB was first formed for Mo-30-67 at.% B liquid. However, from the liquid with 50–77 at.% B, $MoB_2$ formed via a peritectic reaction of the liquid phase and solid phase of β-MoB during the cooling process. By using this phase diagram, it is possible to explain the formation of phases of the synthesized nanoparticles of molybdenum boride as well as the structure of boride-boron nanoparticles. According to the phase diagram, although the highest B content of molybdenum boride is identified as $MoB_4$, nanoparticles of molybdenum boride synthesized by pulsed discharge of compacted powder could only yield the $MoB_2$ phase.

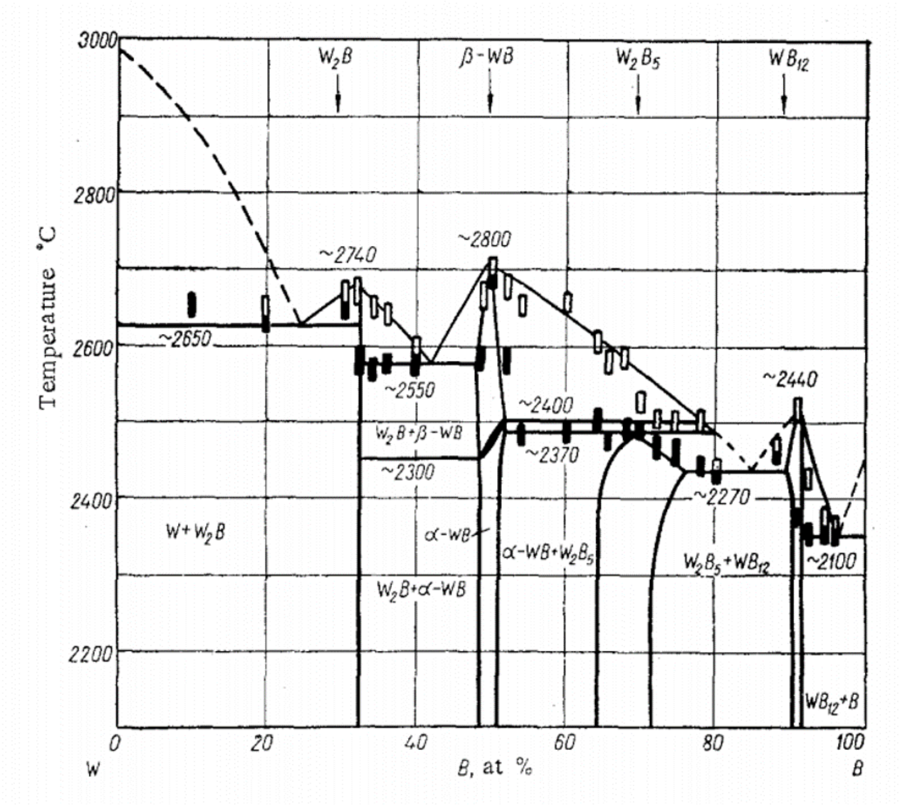

Figure 3.47: Phase diagram of W-B system [284](Reproduced with permission from Springer Nature).

Phase diagrams for the W–B system have been reported in several studies. The phase diagram reported by Portnoi et al.[284] and Rudy et al.[285] did not mention the $WB_4$ phase; instead, $WB_{12}$ phase was suggested as the highest B content. On the other hand, Bodrova et al., Itoh et al., and Romans et al.[276, 277, 264] reported tungsten boride compound with the highest boron content was $WB_4$. The XRD results in the present study shown in Fig.3.37 are similar to those reported in refs. [276] and [264], in which $WB_4$ was confirmed with a hexagonal unit cell with lattice parameters a = 0.52004 nm, c = 0.63348 nm[276] and a = 0.5200 nm, c = 0.6340 nm[264], respectively. Besides the main phase was determined as "approximately $WB_4$", XRD patterns showed that the synthesized phases of nanoparticles of tungsten boride also contained WB, $W_2B_5$ (or $WB_2$[286]). Due to the uneven metal: boron content in different places in the plasma vapor, the presence of minor phases is understandable. However, generally, because B powder was used in excess, according to the phase diagram, the predominance of phase "approximately $WB_4$" in the sample is reasonable.

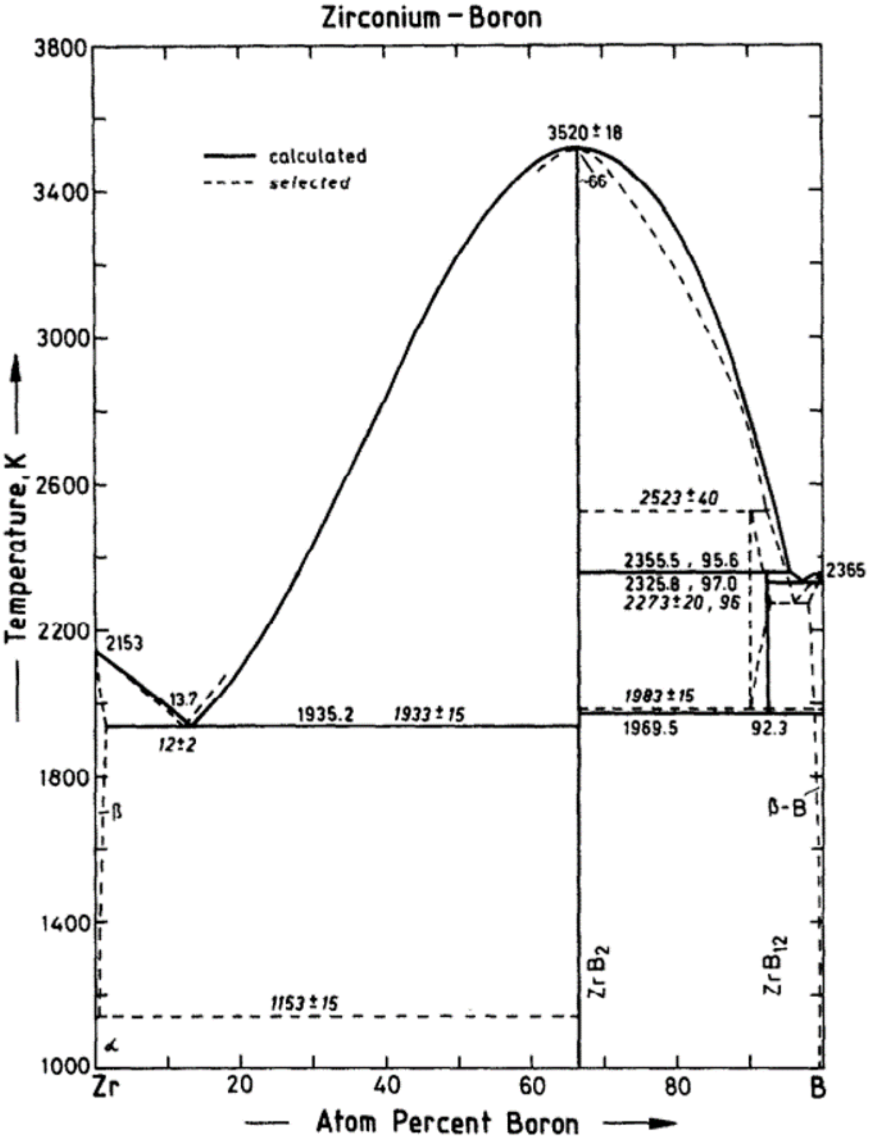

Figure 3.48: Phase diagram of Zr-B system [287](Reproduced with permission from Elsevier).

The phase diagram of Zr-B system shown in Fig. 3.48 looks quite similar to that of Ti-B system. It is likely that these two elements are in the same group in the periodic table. According to the Zr-B phase diagram, it can be seen that $ZrB_2$ is the most likely to form when the mixture of Zr and B vapors cooling from temperatures that are higher than the melting temperature of $ZrB_2$. As a result, the main phase obtained by discharging B powders with Zr rods was $ZrB_2$.

According to the XRD results of synthesized nanoparticles in the present study, Zr was the only transition metal that reacted with the C in the heat-shrinkable tube to form zirconium carbide. In order to clarify this, Gibbs's free energy of reactions was calculated. First, by using the formulas proposed by Shatynski et al.[288], the Gibbs free energy of the reaction between C and Ti, Zr, Mo, and W at 1200 K was calculated as $-171$, $-173$, $-58$, and $-33$ kJ/mol, respectively. By these values, it can be seen that it is easier for the reactions between Ti, Zr, and C to occur than those between Mo, W, and C. Furthermore, at 1200 K, the Gibbs free energy of reactions between Ti, Zr, and B has been reported to be −262[289] and −275[290] kJ/mol, respectively. At the same temperature, the Gibbs free energy of the reaction between W and B has been calculated as −309 kJ/mol[291]. Due to the scarce of information, it was not possible to calculate the Gibbs free energy of the reaction between Mo and B, however, because Mo is in the same periodic group as W, it was speculated that the reaction between Mo and B would be as thermodynamically favorable as that between W and B. Therefore, with the presence of B and C, although Ti and Zr tend to react with B to form boride compounds rather than reacting with C to form carbides, it is easier for carbides of Ti or Zr to form than Mo and W. However, the fact that only ZrC was detected by XRD analysis can be explained as the melting temperature of ZrC is higher than that of $ZrB_2$ (∼3540°C vs ∼3240°C, respectively), while the melting temperature of TiC is lower than that of $TiB_2$ (∼3160°C vs ∼3230°C, respectively). As a result, during the quenching process from the liquid phase, Zr first reacted with C to form ZrC; however, when the temperature was as low as the melting temperature of $ZrB_2$, Zr was more likely to react with B to form $ZrB_2$. On the other hand, TiC had less chance to form than $TiB_2$ since the melting temperature of TiC is less than that of $TiB_2$. The low content of ZrC in the product also supports this explanation.

Basing on the EDS analyses, it was seen that the unexpected impurities such as Fe, Cr, or Ni could be limited to less than 2 wt.% without using the improved experimental setup by keeping the contact between the SUS nuts and metal rods sufficiently tight. On the other hand, the presence of Fe, Cr, and Ni may have a good effect on the solidification of boride ceramics. This can be explained by the difficulty to solidify due to the refractory property of transition metal borides. One of the most used solutions is to employ a metallic additive that forms a liquid phase at the sintering temperature. Several studies have been reported using Fe, Cr, or Ni as a low-concentration additive[292, 293, 294, 295, 296]. Therefore, although these metal traces are treated as unexpected impurities in the present study, they may be useful for facilitating the solidification of the transition-metal borides. On the other hand, these metallic impurities also can be suppressed by using the improved experimental setup described in the case of crystalline B micron-sized powder and Zr rods. Finally, the content of O could be decreased by improving the vacuum degree of the synthesis chamber.

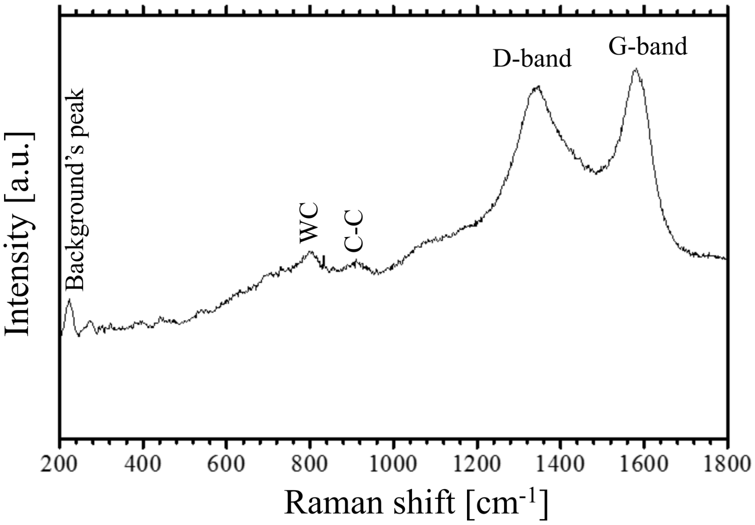

Figure 3.49: Raman spectrum of nanopowder synthesized from amorphous B powder and W rods.

In order to further clarify the presence of C detected by EDS, Raman spectroscopy was employed. The Raman spectroscopy result is shown in Fig. 3.49. It can be seen that the D-band (between 1300 and 1440 $\mathrm{cm}^{-1}$) and the G-band (between 1500 and 1640 $\mathrm{cm}^{-1}$) in the Raman spectra of tungsten borides synthesized from amorphous B powder confirmed the presence of an amorphous C phase[297]. Additionally, bonding between the W and C was also observed. As a result, WC may be present in the sample, however, because the content was probably lower than the detection limit of the X-ray diffractometer, no peak of WC was detected in the XRD patterns. By avoiding using the heat-shrinkable tube and using lightly sintered B powder, it is expected to eliminate the C content in the products.

## 3.4 Preparation of NPs of light elements (Al and Mg) by PWD

### 3.4.1 Aluminum nanoparticles

Although Al nanoparticles have been extensively prepared by PWD in previous studies [67, 298], for the purpose of synthesizing various light elements by PWD, Al nanoparticles were prepared again by PWD in this study with the same experimental setup to compare the particle size distributions of other metal NPs. The experimental setup for Al nanoparticle preparation by PWD is shown in Fig. 2.1(a).

The conditions of preparation of Al nanoparticles by PWD are shown in Table 3.6,

Table 3.6: Experimental conditions for preparation of Al nanoparticles by PWD

| | | | | |
|---|---|---|---|---|
| | Material | Al | | |
| Wire | Diameter, $d$ [mm] | 0.1 | | |
| | Length, $l$ [mm] | 25 | | |
| Vaporization energy, $E_{\mathrm{v}}$ [J] | | 7.5 | | |
| Charging voltage, $V_{\mathrm{c}}$ [kV] | | 2 | 4 | 6 |
| Capacitance, $C$ [µF] | | 30 | | |
| Charging energy, $E_{\mathrm{c}}$ [J] | | 60 | 240 | 540 |
| Relative energy, $K$ | | 8 | 31.9 | 71.7 |
| Gas species | | Ar | | |
| Pressure, $P$ [kPa] | | 50, 100 | | |

Al wires with a small diameter (0.1 mm) yielded a very small amount of Al nanopowder every discharge, especially at low-pressure conditions due to the small dielectric breakdown voltage of Ar gas. As a result, for the purpose of comparison, 6 experimental conditions at pressure 50 and 100 kPa, along with relative energy ($K$) 8, 31.9, 71.7 were carried out. Figure 3.50shows V-I waveforms of the experiment.

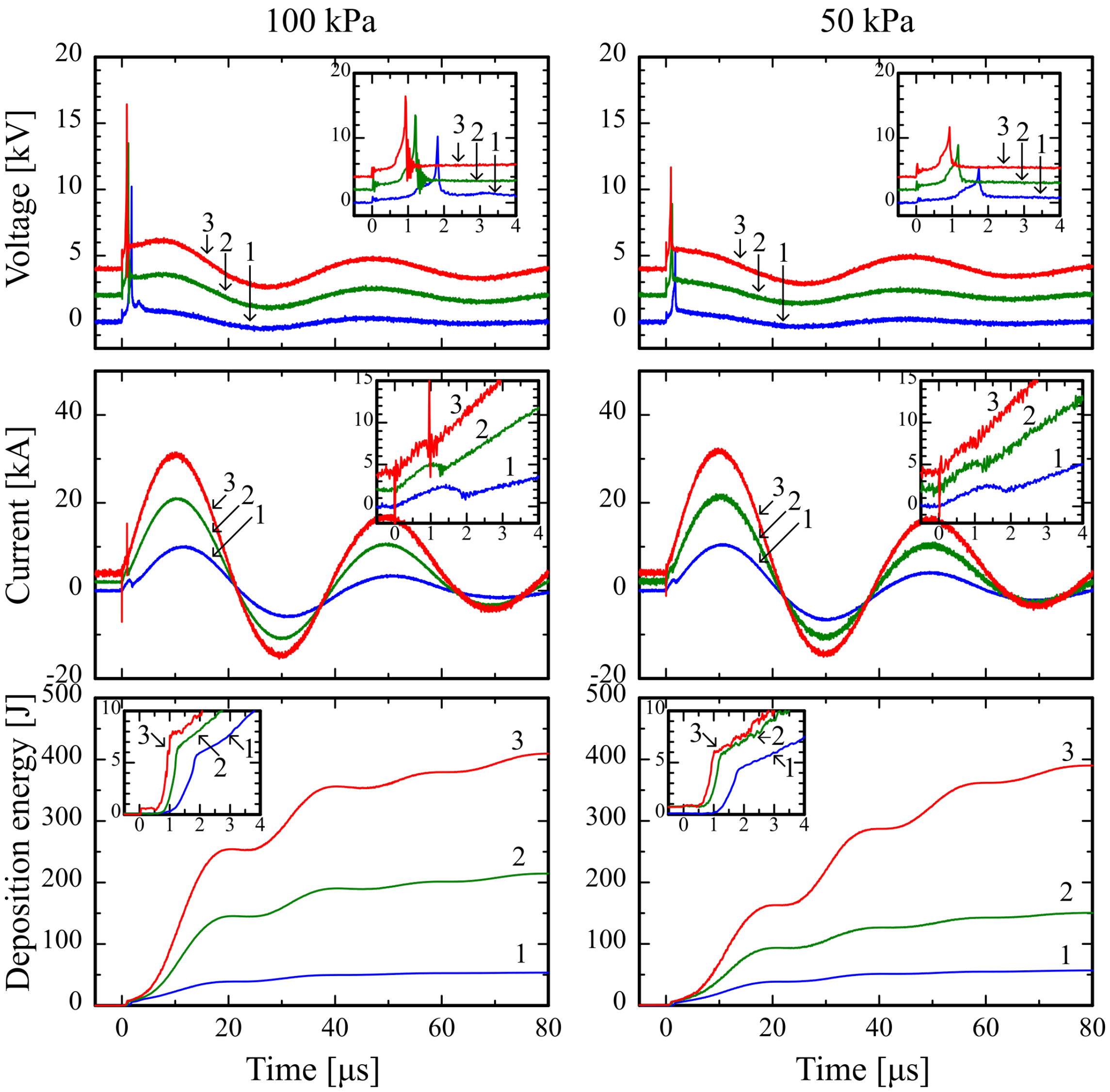

Figure 3.50: Waveforms of $V(t)$, $I(t)$, and $E(t)$ of PWD of Al wires at 100 kPa (left) and 50 kPa (right) and various $K$. $K$ is #1:8, #2:31.9, #3:71.7. Voltage and current waveforms are offset 2 kV and 2 kA, respectively, for readability.

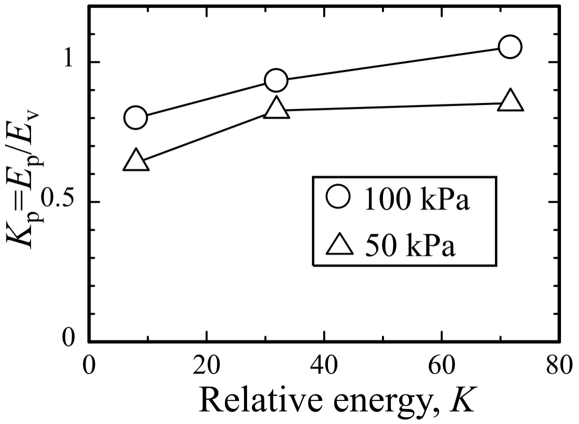

Figure 3.51: The relationship between $K_\mathrm{p}$ and $K$ of PWD of Al wires at 100 kPa and 50 kPa at various $K$.

From Fig. 3.50, it can be seen that the current waveforms are much like the case in Fig. 1.2(A), which means that there was no dwell time happening and arc discharge appeared soon after the wire evaporation. It might happen due to the low dielectric breakdown voltage of Ar gas, high charging voltage, and relatively short wire. However, energy deposited into the wire up to the end of the wire heating stage ($E_\mathrm{p}$) was nearly equal to vaporization energy of the Al wire ($E_\mathrm{v}$=7.5 J) in the case of 100 kPa. At 50 kPa, $E_\mathrm{p}$ is approximately 0.7-0.8 times of $E_\mathrm{v}$. Also, $E_\mathrm{p}$ increased with increasing $K$ in both 100 kPa and 50 kPa, however, this difference of $E_\mathrm{p}$ is as significant as the difference in the deposition energy during the arc discharge stage. As a result, it can be concluded that the increase in $K$ is effective on the increment of deposition energy after the wire was vaporized.

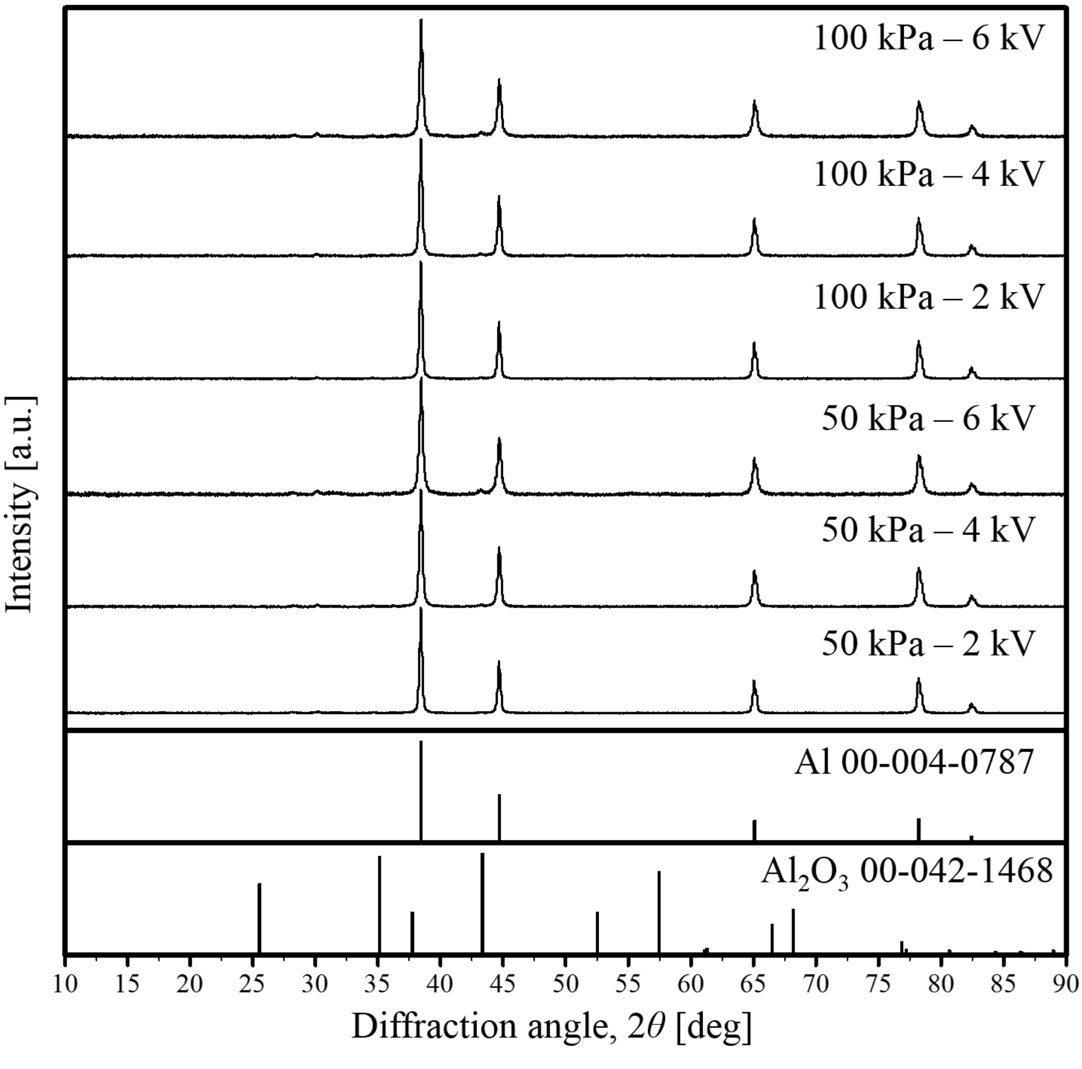

Figure 3.52: XRD patterns of as-prepared Al nanoparticles by PWD at various $P$ and $K$.

Figure 3.52 shows that XRD patterns of all samples prepared with conditions in Table 3.6, the as-prepared nanopowders are single-phase Al and a few amount of $Al_2O_3$. The presence of $Al_2O_3$ might originate from the reaction of Al nanoparticles and residual oxygen amount inside the chamber. The very small intensity of peaks of phase $Al_2O_3$ indicates that $Al_2O_3$ is probably present on the surface of Al nanoparticles. This layer of $Al_2O_3$ is considered to act as a passivation layer to prevent further oxidation of nanoparticles.

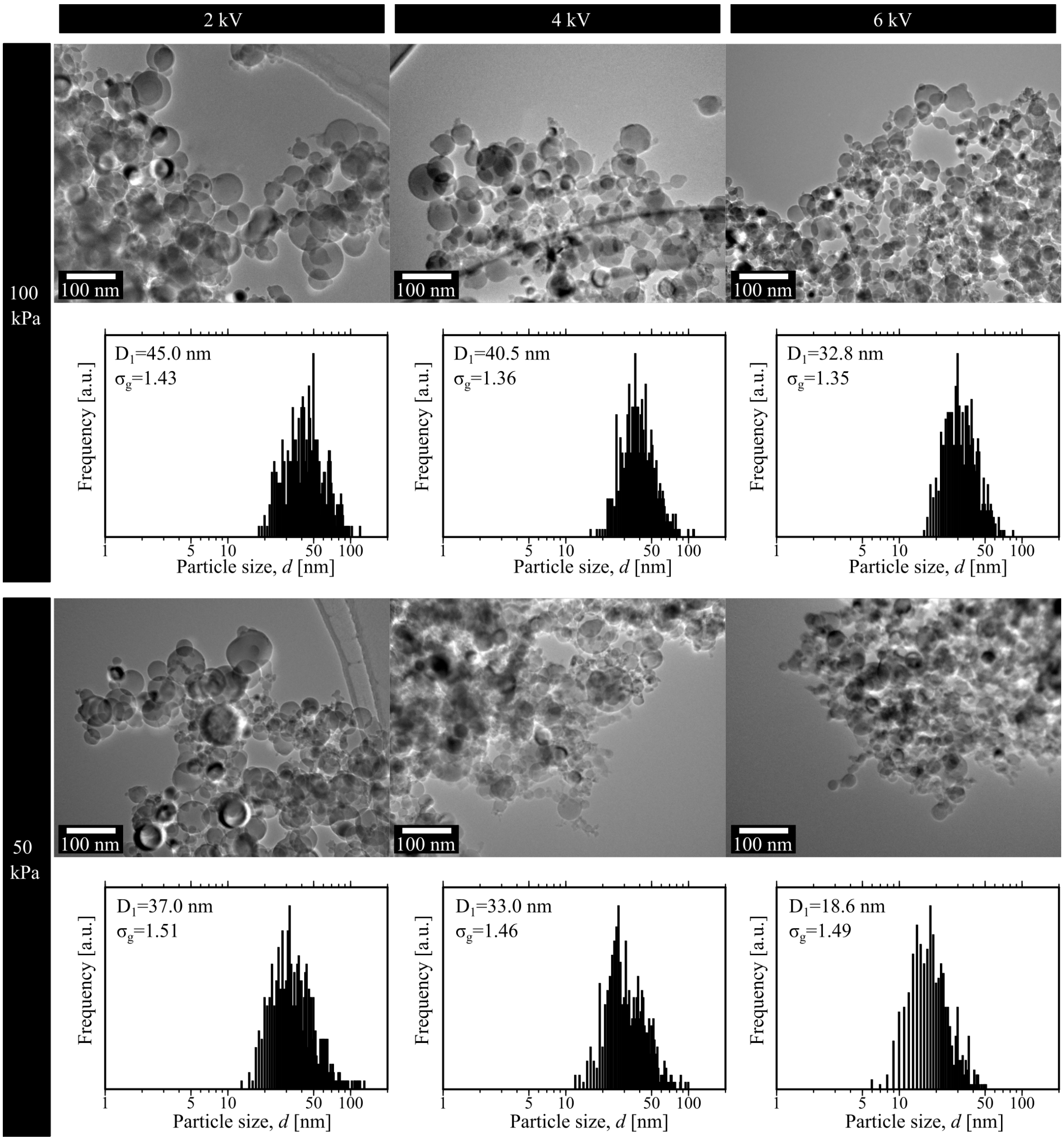

Figure 3.53: Bright-field TEM images of Al nanoparticles prepared by PWD (upper half) and corresponding particles size distribution (lower half) at various $P$ and $K$.

Bright-field TEM images are shown in Fig.3.53. The morphology of Al nanoparticles prepared by PWD in all experimental conditions is nearly spherical. In addition, by the results of geometric mean diameter, it is apparent that the size of nanoparticles decreases with increasing $K$ and decreasing $P$. This result agrees with most of the results of previous studies of various materials[112, 113, 114, 172]. Particle size distribution results show that sizes of particles follow a log-normal distribution with geometric standard deviations is in the range of 1.35-1.5. These values of geometric standard deviations are also in agreement with the theoretical value mentioned in Refs. [114, 299] and in Chapter 1 for coagulation without chemical reactions. Additionally, at both 100 kPa and 50 kPa, with increasing $K$, geometric standard deviations decrease, which can be explained by the reduction of the amount of liquid droplets during PWD process[109] and the increment of $E_\mathrm{p}$ as mentioned in Fig 3.50.

For the summary of this section, single-phase Al nanoparticles with thin $Al_2O_3$ passivation layer were successfully prepared by PWD in Ar gas. The reduction in geometric mean particle size with decreasing $P$ and increasing $K$ was confirmed and was in good agreement with previous studies.

### 3.4.2 Magnesium submicron particles

Preparation of Mg submicron particles in Ar gas ambient has been reported by Suematsu et al.[182]. Since Mg is highly reactive with oxygen, oxidation prevention of Mg particles prepared by PWD was investigated by pulsed discharging Mg wire in mineral oil[300] or 1,2-epoxydodecane[176]. Although preparation of Mg particles by PWD in Ar could lead to the oxidation on the surface of particles, for the purpose of comparison with other materials, Ar gas was used as the ambient medium of the experiment.

The experimental setup can be referred to in Fig. 2.1(a). Experimental conditions are shown in Table 3.7 below. Despite the low dielectric breakdown voltage of Ar gas, due to the possibility that nitride of magnesium ($Mg_3N_2$) could be formed when discharging Mg wire in $N_2$ ambient gas, Ar gas was chosen to do PWD experiments of Mg wires.

Table 3.7: Experimental conditions for preparation of Mg nanoparticles by PWD

| | | | | | |
|---|---|---|---|---|---|
| Wire | Material | Mg | | | |
| | Diameter, $d$ [mm] | 0.1 | | | |
| | Length, $l$ [mm] | 23 | | | |
| Vaporization energy, $E_v$ [J] | | 2.2 | | | |
| Charging voltage, $V_c$ [kV] | | 1.9 | 2.7 | 3.8 | 4.7 |
| Capacitance, $C$ [µF] | | 10 | | | |
| Charging energy, $E_c$ [J] | | 18.1 | 36.5 | 72.2 | 110.5 |
| Relative energy, $K$ | | 8 | 16 | 32 | 50 |
| Gas species | | Ar | | | |
| Pressure, $P$ [kPa] | | 10, 50, 100 | | | |

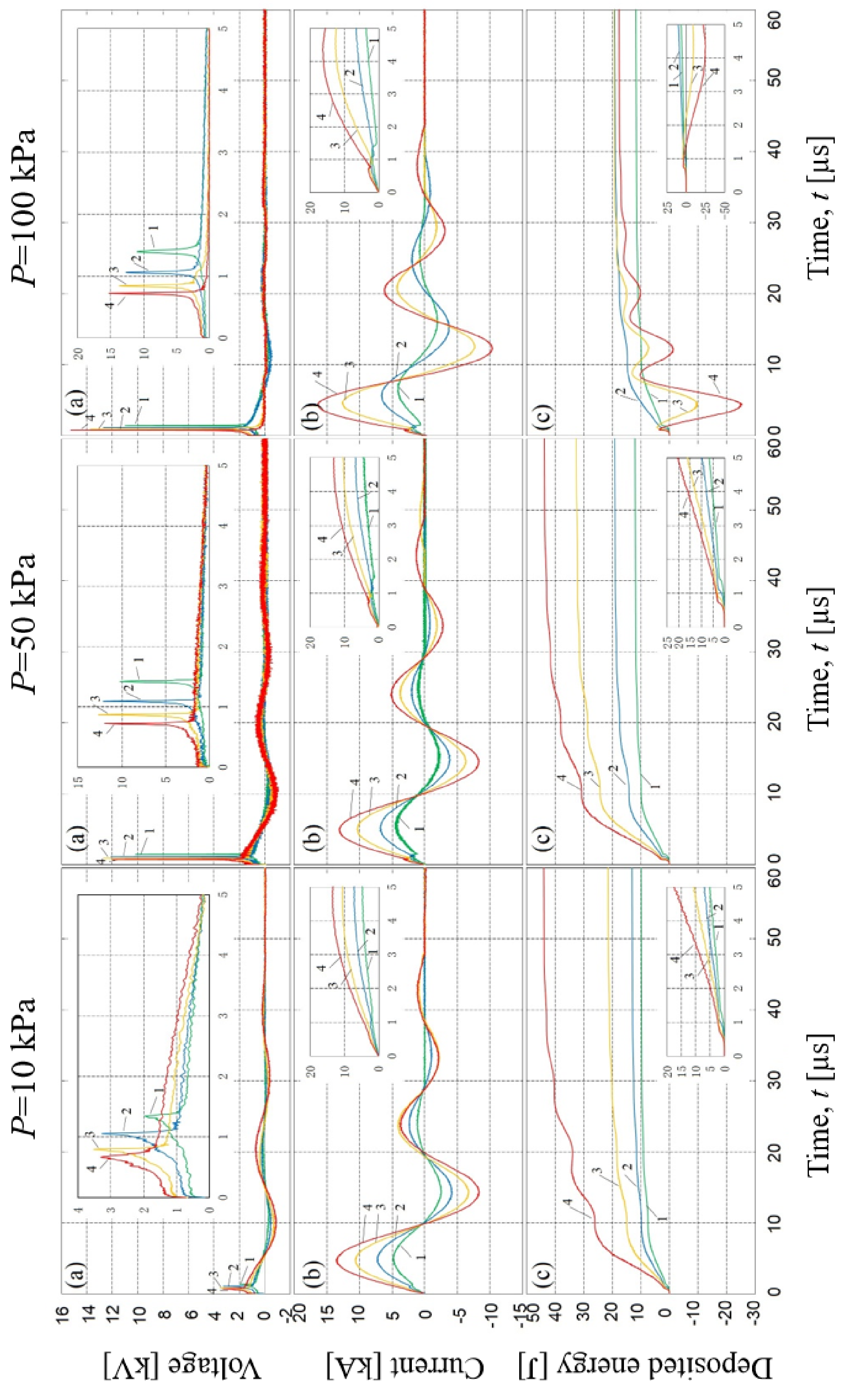

Figure 3.54: Waveforms of $V(t)$, $I(t)$, and $E(t)$ of PWD of Mg wires at 10, 50, and 100 kPa at various $K$. $K$ is #1:8, #2:16, #3:32, and #4:50.

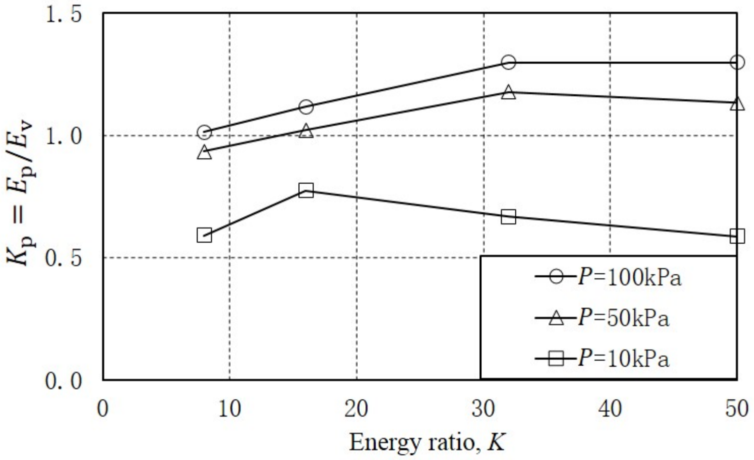

Figure 3.55: The relationship between $K_{\mathrm{p}}$ and $K$ of PWD of Mg wires at various $P$ and $K$ values.

Figure 3.54 shows waveforms of $V(t)$, $I(t)$, and $E(t)$ obtained by PWD experiments of Mg wires at various values of $P$ and $K$. It can be seen that the current waveforms are similar to those obtained by discharging with Al wires in the previous experiment. There was no dwell time and the arc discharge stage happened immediately after the first peak of current waveforms. Arc discharge even happened earlier with large $K$, which is quite understandable. By voltage waveforms, at the same Ar gas pressure, the time for arc discharge to occur became shorter with increasing $K$. This can be considered that with higher $K$, the current rising rate also increased and accelerated the heating rate of wire. Deposition energy waveforms ($E(t)$) show that energy can be well deposited into the wire. The relationship of $K_{\mathrm{p}}$ and $K$ at various $P$ and $K$ is shown in Fig. 3.55. It can be seen that at 50 and 100 kPa, $K_{\mathrm{p}}$ is equal or larger than 1, which implies that at 50 and 100 kPa, the electrical current could heat Mg wires effectively. At 10 kPa, due to the uneven heating at low ambient pressure, $K_{\mathrm{p}}$ is smaller than 1. Additionally, at 10 kPa and high $K$ (32, 50), $K_{\mathrm{p}}$, contrary to the tendency at 50 and 100 kPa, decreased. This is probably attributed to the early breakdown which terminated the wire heating stage. Particularly, at 100 kPa and $K = 32$ and $K = 50$, there was an unusual decrease of the period in the waveforms. The decrease of the period in an RLC circuit may attribute to the change in R, L, or C values, however, there was no possibility that C could change, in addition, apart from the wire, all other components were unchanged during the experiment, hence, it is anticipated that during the discharge, the inductance and/or resistance of the wire were probably varied peculiarly, which is quite different from other conditions.

Figure 3.56 shows XRD patterns of as-prepared Mg powders by PWD of Mg wires at various $P$ and $K$. It is visible that the as-prepared Mg powders include single-phase Mg and a small amount of MgO. The highest peak of MgO as referred to in XRD card ICDD 00-045-0946 was detected in most of the samples at diffraction angle $2\theta = 43°$. The presence of the oxide phase is predictable for the high reactivity of Mg to oxygen. The distribution of Mg and MgO in the sample is further characterized by other analytical instruments.

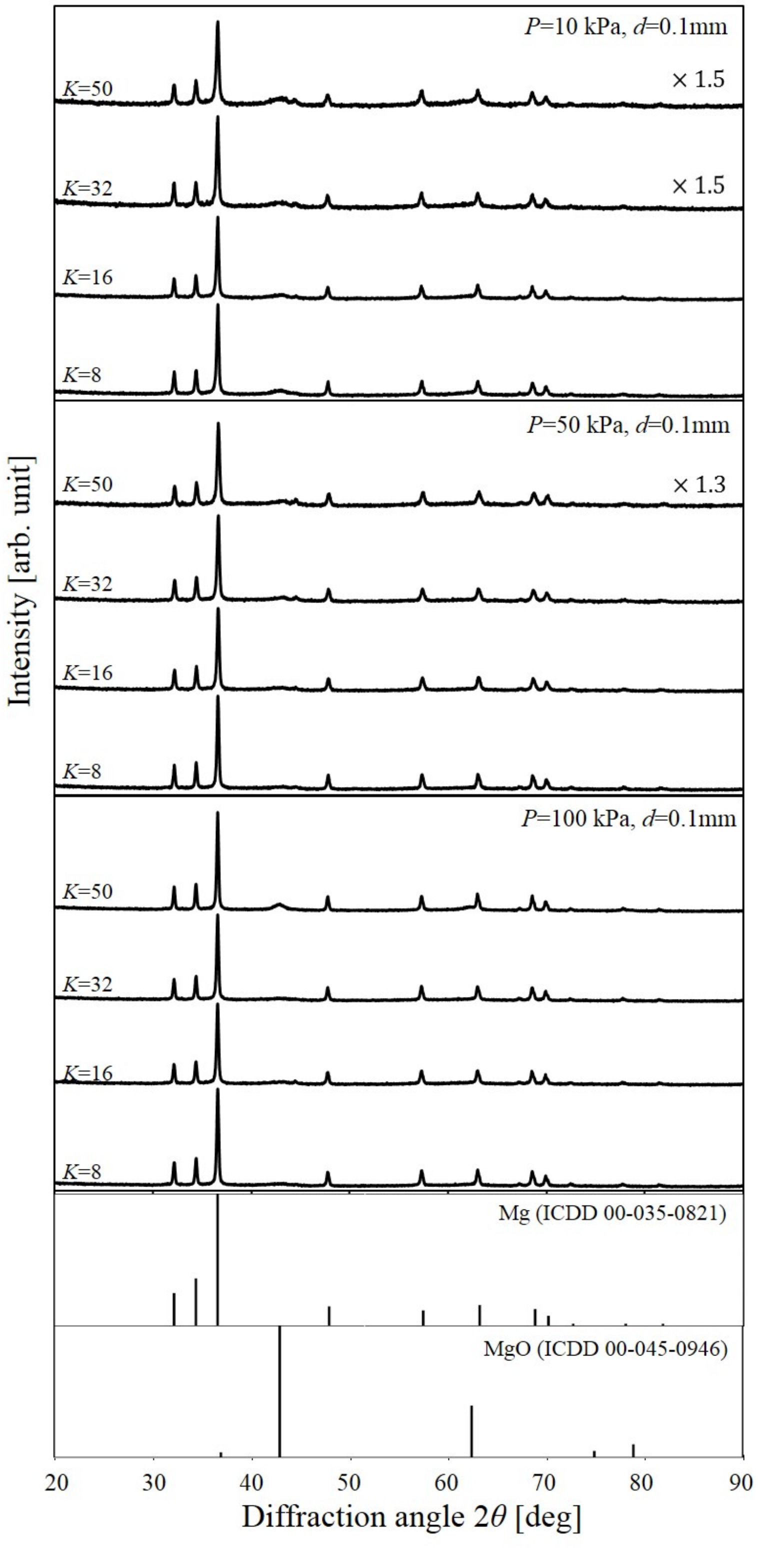

Figure 3.56: XRD patterns of as-prepared Mg submicron particles by PWD of Mg wires at various $P$ and $K$ values.

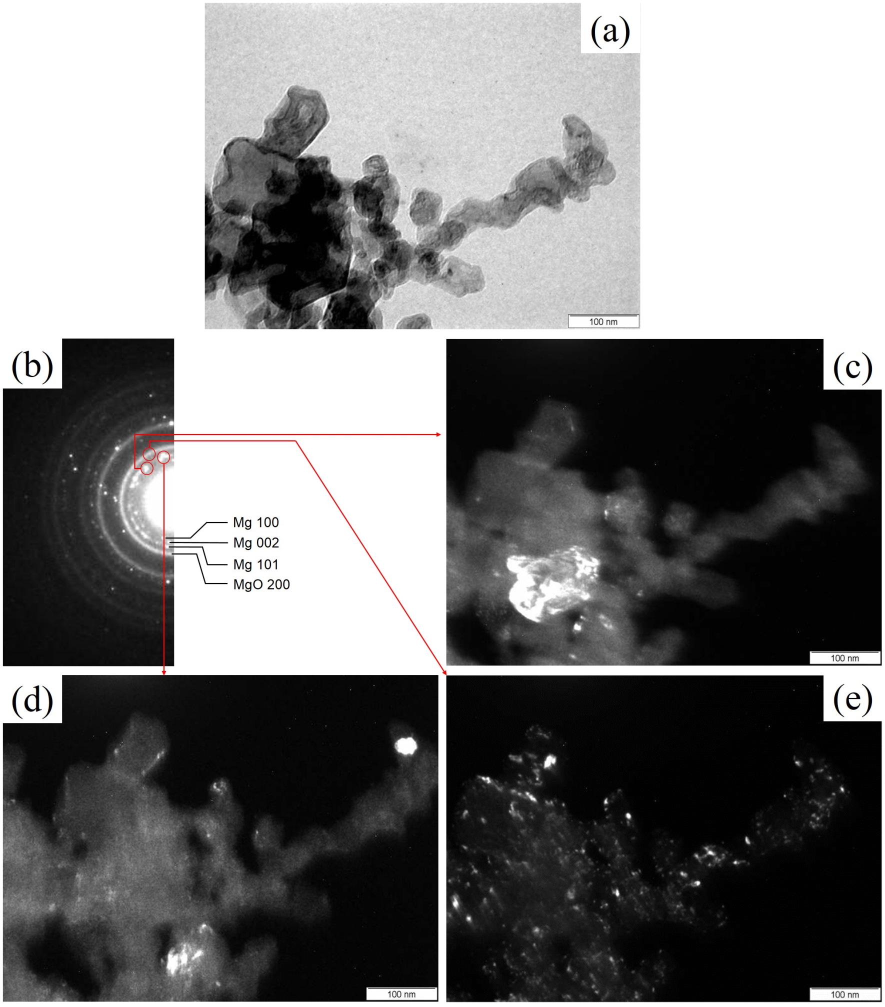

Figure 3.57: (a) Bright-field TEM image, (b) SAD profile and (c)-(e) dark-field TEM images of the same area of a powder sample prepared by PWD of Mg wire.

Figure 3.57 shows a bright-field TEM image, selected-area diffraction (SAD) profile, and dark-field TEM images of a selected area of an Mg submicron powder sample. In Fig. 3.57(b), the SAD profile shows that the Mg particles are large and scattered, which are shown by many bright and scattered spots. On the other hand, the MgO particles are small and more numerous than Mg particles, which could be found as a continuous concentric ring. To visualize the positions of Mg and MgO particles, dark-field TEM images were taken. First, large Mg particles were identified by choosing the spots in the SAD profile that corresponding to Mg. By this, particles that were identified as Mg became brighter. Therefore, Figs 3.57(c) and (d) show Mg particles. Next, by choosing an optional position in the SAD profile that corresponding to MgO, it was possible to visualize the positions of MgO particles. Fig. 3.57(e) shows how the MgO particles were present in Fig. 3.57(a). By this result, it is possible to say that MgO particles are very small particles (smaller than 10 nm in diameter) compared to Mg particles (few tens of nm) and MgO particles are considered to adhere to the surfaces of Mg particles. Therefore, it is possible to distinguish Mg and MgO particles by their sizes.

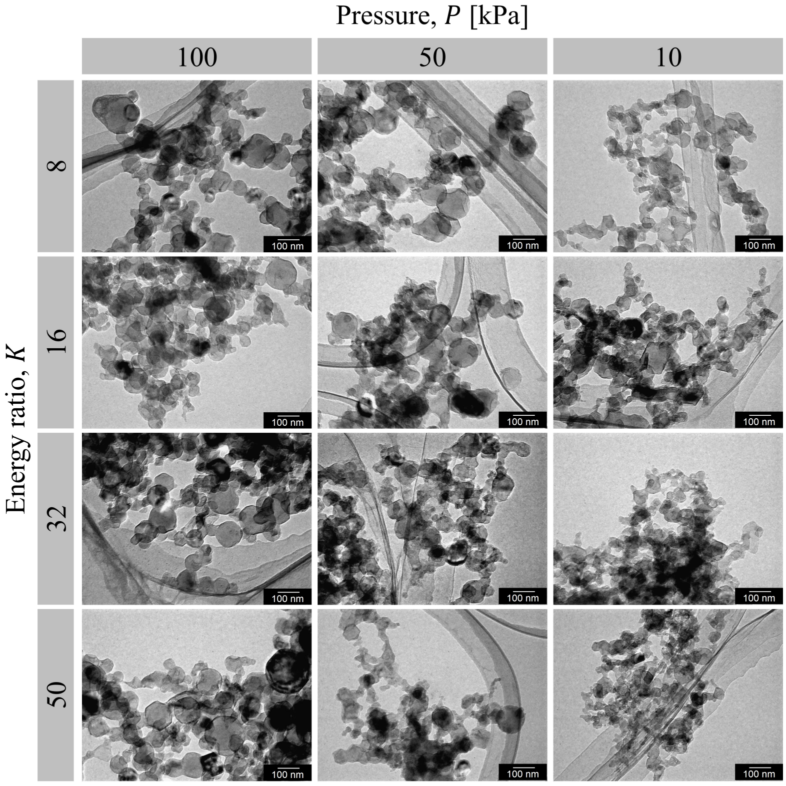

Figure 3.58: Bright-field TEM images of as-prepared Mg submicron particles by PWD of Mg wires at various $P$ and $K$ values.

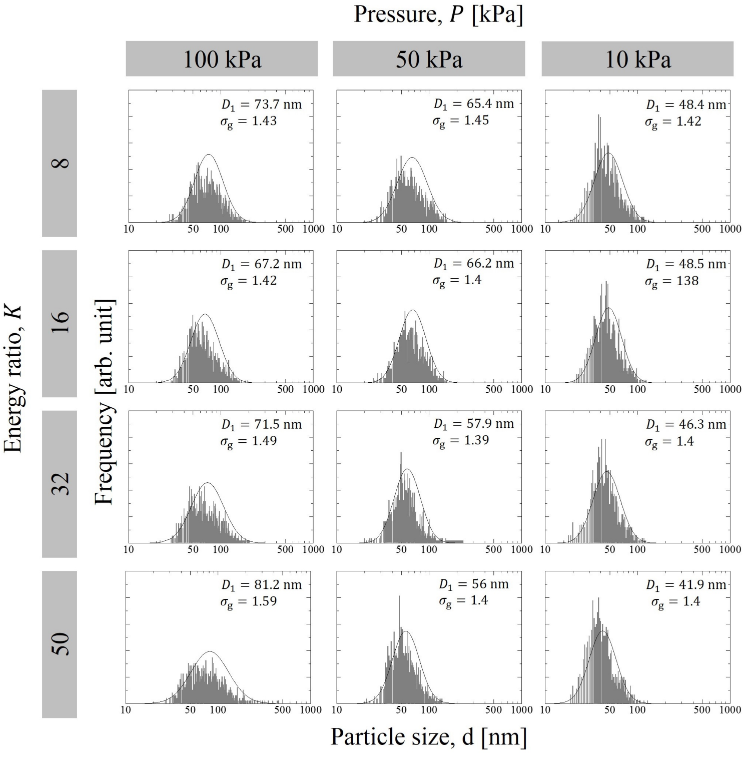

Figure 3.59: Particle size distribution of as-prepared Mg submicron particles by PWD of Mg wires at various $P$ and $K$ values.

Figure 3.58 shows bright-field TEM images of as-prepared Mg submicron particles by PWD of Mg wires at various $P$ and $K$. From TEM images, it is apparent that these Mg submicron particles are in nearly spherical shape at pressure 50 kPa and 100 kPa. At 10 kPa the morphology of particles becomes more irregular with increasing $K$. It is noted that in PWD, the condition of high $K$ and low $P$ induce the low plasma density, however, small particles with irregular shapes were formed. In PWD, particles are formed by nucleation in the vapor phase, this is different from the nucleation in the liquid phase, in which highly supersaturated concentration leads to the generation of small particles with irregular shapes. Also, it is visible that the particles were in agglomeration form.

Figure 3.59 shows the particle size distribution of as-prepared Mg submicron particles by PWD at various $P$ and $K$ values. The values of geometric mean diameter, $D_1$ and standard deviation, $\sigma_{\mathrm{g}}$ were calculated by using equations (2.13) and (2.12). Similar to the particle size distribution of Al nanoparticles mentioned in section3.4.1, the particle size distribution of Mg submicron the particles are in agreement with the log-normal distribution induced by Brownian coagulation[204]. The smooth lines show the log-normal distribution curves fitted to the particle size distribution of the particles prepared by PWD. The log-normal distribution curves are defined by equation (2.11). Additionally, the geometric mean diameter, $D_1$ decreases with decreasing Ar gas pressure and increasing $K$, which agrees with the tendency of other materials' nanoparticles prepared by PWD[112, 67, 172]. Values of geometric standard deviation are in the range between 1.4 and 1.6, which is also consistent with the results of particles prepared by other physical vapor methods[299].

For the summary of this section, by increasing relative energy $K$ and decreasing ambient pressure $P$, it is possible to reduce the particle size of Mg submicron particles prepared PWD. On the surfaces of Mg submicron particles, MgO is present and considered to act as a passivation layer to prevent Mg submicron particles from further being oxidized, which is similar to the case of Al nanoparticles.

## 3.5 Particle size determining equation

Particle size control has been mentioned in section 1.3.2.3. For the purpose of controlling the size of nanoparticles prepared by PWD, Tokoi et al. proposed a particle size determining equation[112]. This equation was modified by Sato et al. with considerations of the effectiveness of the wire heating stage by adding the $K_\mathrm{p}$ in $D_\mathrm{th}$ (equation (1.5)). By the studies of Tokoi et al. and Sato et al., the size determining equation of nanoparticles by PWD was defined as followings,

$$D_1 = 3.8\left[106\left(\frac{mPK_\mathrm{p}}{E_\mathrm{c}}\right)^{0.6}\right]^{0.4}. \tag{3.2}$$

In the present study, experimental results of Al and Mg submicron/nanoparticles are applied in Eq. (3.2) to investigate the validity of this equation on light metals like Al and Mg.

### 3.5.1 The inconsistency of Mg and Al nanoparticles by PWD in Tokoi's equation

By applying the Eq. (1.5) on the data obtained in the present study, a graph describing the relationship between the geometric mean diameter, $D_1$ and the experimental plasma/density, $D_\mathrm{exp}$ were plotted below.

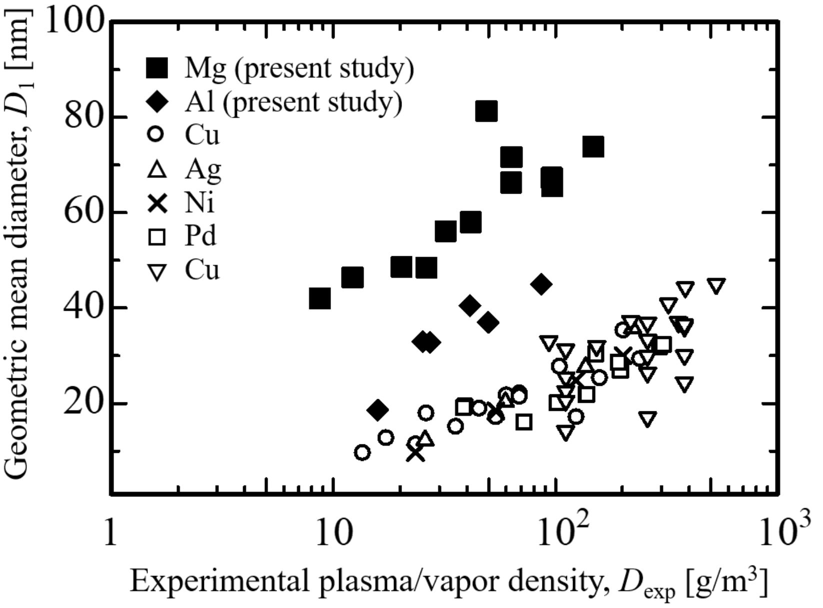

Figure 3.60: The relationship between the geometric mean diameter, $D_1$ and the experimental plasma/density, $D_\mathrm{exp}$ of various metallic nanoparticles prepared by PWD.

From Fig. 3.60, it is visible that data of the size of Al and Mg nanoparticles prepared in this study are not fitting well with those of other materials such as Cu[112, 113], Ag[197], Ni[197], and Pd[172] reported in previous studies. However, while data of Al nanoparticles are quite close to those of the remaining materials, data of Mg nanoparticles are quite far from them. In particular, with the same experimental plasma/vapor density, sizes of Al nanoparticles are approximately 10 nm larger than those of other materials apart from Mg, sizes of Mg nanoparticles are at least 2 times larger than those of those materials.

There are two conceivable hypotheses on the inconsistency of Al and Mg nanoparticle size.

- First, both Al and Mg are considerably light compared to other considering metals. As a result, by using Eq. (1.5) to define the density of plasma/vapor with dimension g/m$^3$, obviously, the density of plasma/vapor of light metals like Al and Mg are relatively smaller than those of the remaining considering metals, which may cause the inconsistency shown if Fig. 3.60.

- Second, when proposing the particle size determining equation, Tokoi et al. only considered the Brownian coagulation in the particle formation process[112]. However, the particle formation process is known to start by nucleation, followed by particle growth by Brownian coagulation and further agglomeration. In particular, the critical size depends on the temperature and the supersaturation of the metal vapor, which may affect the number density of nuclei and the growth speed of NPs. Therefore, it is understandable that nucleation should contribute to the formation of particles and may be responsible for considering inconsistency.

### 3.5.2 Homogeneous nucleation theory and critical size calculation

The nucleation process for metallic nanoparticle formation in an inert gas by PWD is considered to be homogeneous nucleation from the vapor phase. By considering a droplet model for vapor condensation of classical nucleation theory, one can think about the interaction between a cluster and a single molecule. Assuming that $A_1$ is the single-molecule and $A_{\text{i-1}}$ the cluster consisting of $(i-1)$ molecules, we have the rise to a cluster consisting of i molecules $A_{\text{i}}$ as followings,

$$A_1 + A_{\text{i-1}} \rightarrow A_{\text{i}}. \tag{3.3}$$

Also, the cluster $A_{\text{i}}$ may be created by the loss of a molecule from a cluster consisting of $(i+1)$ molecules $A_{\text{i+1}}$ as follows,

$$A_{\text{i+1}} \rightarrow A_{\text{i}} + A_1. \tag{3.4}$$

At the same time, a cluster with i molecules $A_{\text{i}}$ may decompose into a cluster with $(i-1)$ $A_{\text{i-1}}$ and a molecule or grow into $A_{\text{i+1}}$ by addition of a molecule. In this way, if a molecule interacts with all other molecules in the cluster, a potential energy $U$ can be derived.

By considering thermodynamics of the vapor-droplet system, droplet is treated as a new phase called phase $\alpha$ formed inside the vapor phase. The phase $\alpha$ can be thermodynamically characterized by its entropy $S_\alpha$, volume $V_\alpha$, and composition. The composition is described by the quantities $n_{\alpha,\text{i}}$ of various chemical species that constitute the phase. The potential energy $U_\alpha$ can be defined as followings,

$$dU_\alpha = TdS_\alpha - PdV_\alpha + \sum_i \left(\frac{\partial U_\alpha}{\partial n_{\alpha,\text{i}}}\right) dn_{\alpha,\text{i}} \tag{3.5}$$

$$= TdS_\alpha - PdV_\alpha + \sum_i \mu_{\alpha,\text{i}} dn_{\alpha,\text{i}}, \tag{3.6}$$

where $T$ and $P$ are the temperature and pressure, respectively and

$$\mu_{\alpha,\text{i}} = \left(\frac{\partial U_\alpha}{\partial n_{\alpha,\text{i}}}\right)_{\text{S}_\alpha \text{V}_\alpha \text{n}_{\text{j},\alpha}} \qquad (j \neq i) \tag{3.7}$$

is the chemical potential of species $i$ in the phase $\alpha$. However, in practical, Gibbs free energy $G_\alpha$ is used. Gibbs free energy is defined by:

$$dG_\alpha = -S_\alpha dT + V_\alpha dP + \sum_i \mu_{\alpha,\text{i}} dn_{\alpha,\text{i}} \tag{3.8}$$

The condition that a new homogeneous phase can transform into another homogeneous phase is

$$\Delta G = G_{\text{new}} - G_{\text{old}} < 0. \tag{3.9}$$

By calling the unit building block of the new phase a monomer and assuming the transformation involves $M$ monomers, the relation between Gibbs free energies and chemical potentials of the old and new phases is

$$\frac{\Delta G}{M} = \frac{G_{\text{new}} - G_{\text{old}}}{M} = \mu_{\text{new}} - \mu_{\text{old}} = \Delta\mu < 0. \tag{3.10}$$

Here, $\Delta\mu$ is defined as supersaturation. Supersaturation drives the phase transformation, the larger the supersaturation (the more negative ) is, the more favorable the phase transformation will be. For the transformation from the old phase to the new phase, the system actually has to proceed through a succession of intermediate states. These states are less stable than the old phase, thus, $\mu_{\text{intermediate}} > \mu_{\text{old}}$ (i.e. $G_{\text{intermediate}} > G_{\text{old}}$). The relationship of Gibbs free energies of states is described below,

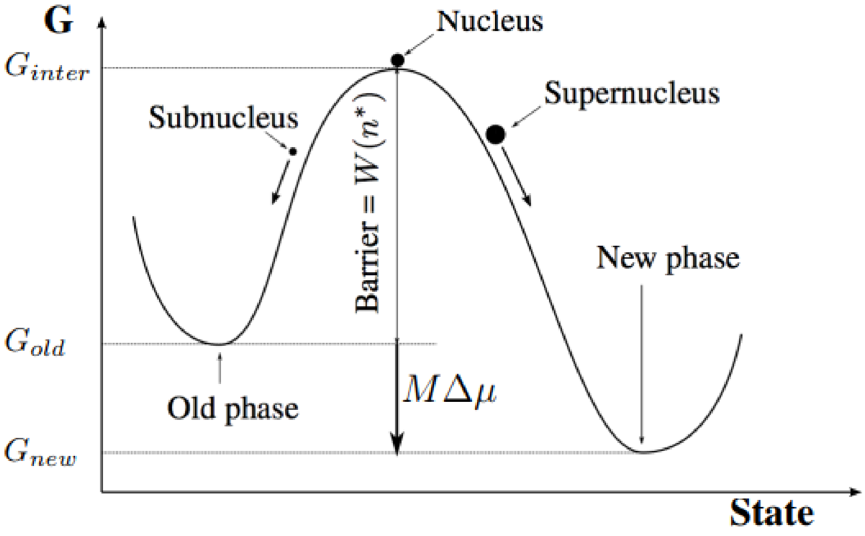

Figure 3.61: Illustration of the transition from an old phase into a new phase based on homogeneous nucleation theory[301].

From Fig. 3.61, it is understandable that for an old phase to transform into a new phase, it is essential for the system to overcome an energetic barrier. This energetic barrier is $M\Delta\mu$ as described in Fig. 3.61. To overcome this energetic barrier, it is impossible to involve M monomers at once. For an alternative way, by considering a number of $n$ monomers where $n$ is very small compared to $M$, it is much easier for the system to overcome this energetic barrier. As a result, there is a minimum value of $n$ that the transformation can occur, and a cluster containing such $n$ monomers has a specific size called *critical size* or *critical radius*. Clusters with sizes equal to or larger than this critical size continue to grow into larger components of the new phase called nuclei, otherwise decompose into the old phase.

The critical size of nucleus formed by nucleation in vapor phase is defined by[302],

$$r_{\text{cr}} = \frac{2\sigma\nu}{RTlnS}, \tag{3.11}$$

where, $r_{\text{cr}}$ is the critical size, $\sigma$ is the surface tension, $\nu$ is the molar volume, $R$ is the gas constant in [J.mol$^{-1}$.K$^{-1}$], $T$ is temperature in [K], and $S$ is the supersaturation. Here, supersaturation is defined by $S = P_{\mathrm{v}}/P_{\mathrm{ve}}$, in which $P_{\mathrm{v}}$ is the actual vapor pressure and $P_{\mathrm{ve}}$ is the equilibrium vapor pressure[302]. Looking at equation (3.11), by considering $T$ is the variable, one can see that it is essential to identify $\sigma$, $\nu$, and $S$ to calculate critical size $r_{\mathrm{cr}}$. These parameters are identified as following,

- Surface tension ($\sigma$) and molar volume ($\nu$) are identified as follows,

$$\sigma = \sigma_0 + (T - T_0)(d\sigma/dT), \tag{3.12}$$

$$\nu = \frac{M}{D_0 + (T - T_0)(dD/dT)}, \tag{3.13}$$

  where $T_0$ is the melting temperature, $M$ is the molar mass, $\sigma_0$ and $\nu_0$ are the surface tension and density of liquid metal at its melting temperature, respectively[303].

- In PWD, after the wire is heated by the pulsed current, obviously since the whole wire is not completely vaporized, a mixture of plasma/vapor and liquid droplets may concurrently exist. During the expansion of these plasma/vapor state, it is very difficult to identify the actual vapor pressure. However, when the expansion of plasma/vapor attains its maximum volume (i.e. the energy deposited in the plasma/vapor is not sufficient anymore for the plasma/vapor to expand), the pressure of actual vapor is considered to balance with the ambient gas pressure which is controlled by the experimental conditions. In present study, let us consider the condition of plasma/vapor at this time. Equilibrium vapor pressure $P_{\mathrm{ve}}$ is calculated as

$$logP_{\mathrm{ve}} = -\frac{\mathrm{A}}{T} + \mathrm{B} + \mathrm{C}logT + 10^{-3}\mathrm{D}T, \tag{3.14}$$

  where A, B, C, and D of Mg, Cu, Ag, Ni, Pd, and Al are referred from Ref. [303] and shown in Table 3.8.

Table 3.8: Values of A, B, C, and D of various metals for calculation of equilibrium vapor pressure[303]

| Element | A | B | C | D | Temp. range [K] |
|---|---|---|---|---|---|
| Mg | 7780 | 11.41 | −0.855 | 0 | 298 − m.p. |
| | 7550 | 12.79 | −1.41 | 0 | m.p. − b.p. |
| Al | 16450 | 12.36 | −1.023 | 0 | 1200 − 2800 |
| Cu | 17870 | 10.63 | −0.236 | −0.16 | 298 − 1356 |
| | 17650 | 13.39 | −1.273 | 0 | 1356 − 2870 |
| Ag | 14710 | 11.66 | −0.755 | 0 | 298 − 1234 |
| | 14260 | 12.23 | −1.055 | 0 | 1234 − 2400 |
| Ni | 22500 | 13.6 | −0.96 | 0 | 298 − m.p. |
| | 22400 | 16.95 | −2.01 | 0 | m.p. − b.p. |
| Pd | 19800 | 11.82 | −0.755 | 0 | 298 − m.p. |
| | 17500 | 4.81 | 1 | 0 | m.p. − b.p. |

By using Eq. (3.14)the values shown in Table 3.8, the equilibrium vapor pressure of various metals can be calculated. Figure 3.62 shows the relationship between equilibrium vapor pressure and temperature of various metals.

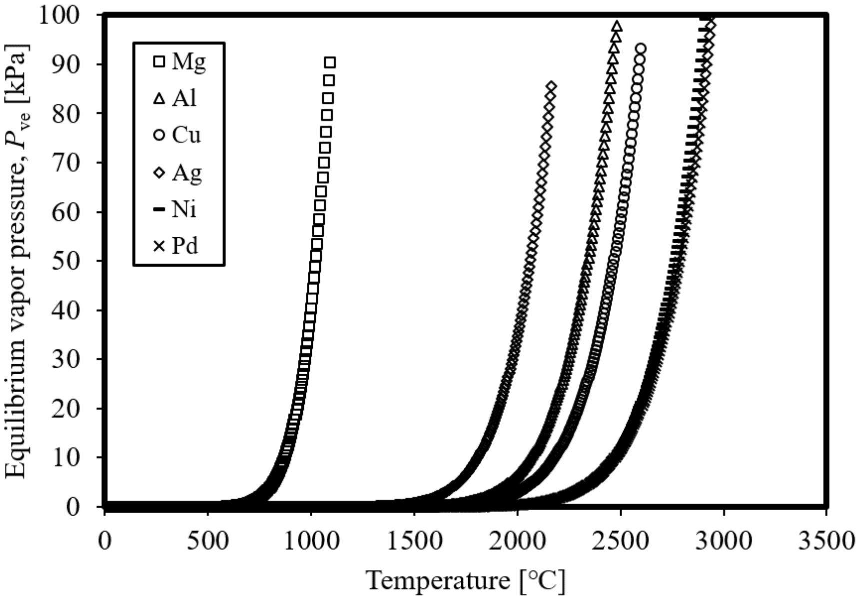

Figure 3.62: Relationship between equilibrium vapor pressure and temperature of various metals.

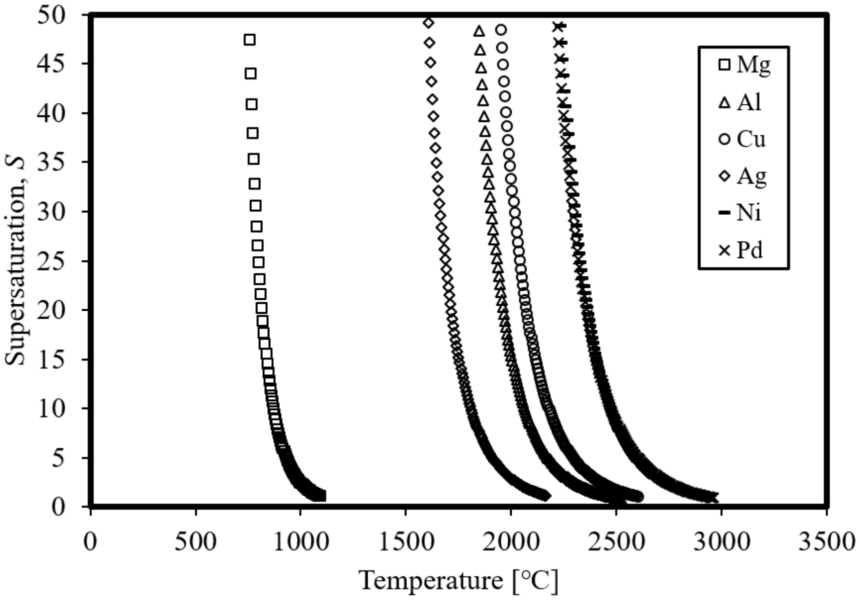

Figure 3.63: Relationship between supersaturation and temperature of various metals at 100 kPa.

By Fig. 3.62, it can be understood that equilibrium vapor pressure of all metals increases with increasing temperature, however, increase significantly after the melting temperature of each metal. At equilibrium vapor pressure is equal to 100 kPa, metals attain their normal boiling temperature ($T_{\mathrm{b}}$). In the PWD process, plasma/vapor is cooled very quickly from the extremely high temperature of plasma through boiling temperature to room temperature. At every value of temperature, equilibrium vapor pressure defines the value of vapor pressure at which vapor is saturated. During the cooling process of plasma/vapor, the vapor pressure of metal is considered to be larger than this equilibrium vapor pressure, as a result, supersaturation occurs. Supersaturation is different in various metals. By adopting the relation $S = P/P_{\mathrm{ve}}$, assuming the actual vapor pressure $P$ is 100 kPa, supersaturation can be calculated. Figure 3.63 shows the relationship between supersaturation and temperature of various metals.

Since $S$ is inversely proportional to $P_{\mathrm{ve}}$, it is clear that the tendency of Fig. 3.63 is inverse of Fig. 3.62. The more it is cooled down, the more temperature decreases and the larger the supersaturation becomes. By adopting Eqs. (3.11-3.14), it is possible to calculate critical size. Figure 3.64 shows the relationship between the critical size and the temperature of various metals at 100 kPa.

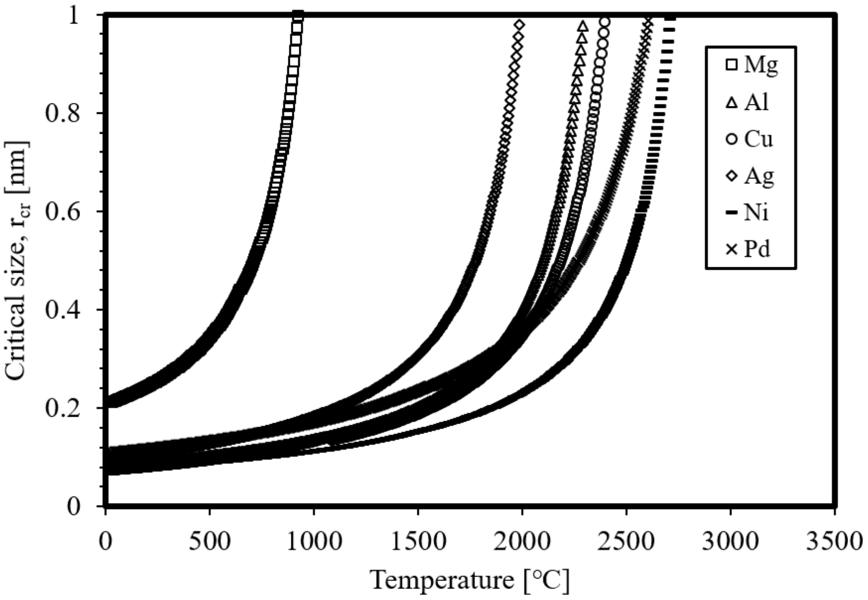

Figure 3.64: Relationship between critical size and temperature of various metals at 100 kPa.

From Fig.3.64, it is easy to realize that at 100kPa, at the same temperature, the critical size of Mg is considerably larger than those of other metals. However, it would be inappropriate to compare like that since there is a large difference in the boiling temperature of Mg and other metals of interest. This result supports the hypothesis that a larger critical size may lead to a larger geometric mean diameter.

On the other hand, the values of critical size are also dependent on the actual vapor pressure, in this case, is the pressure of ambient gas inside the chamber. The relationship between the critical size and the temperature at 100, 50, and 10 kPa of Mg was calculated and shown in Fig.3.65.

From Fig. 3.65, one can see that at the same temperature, at lower ambient gas pressure, the critical size is larger. This factor may also contribute to the final size of particles prepared by PWD.

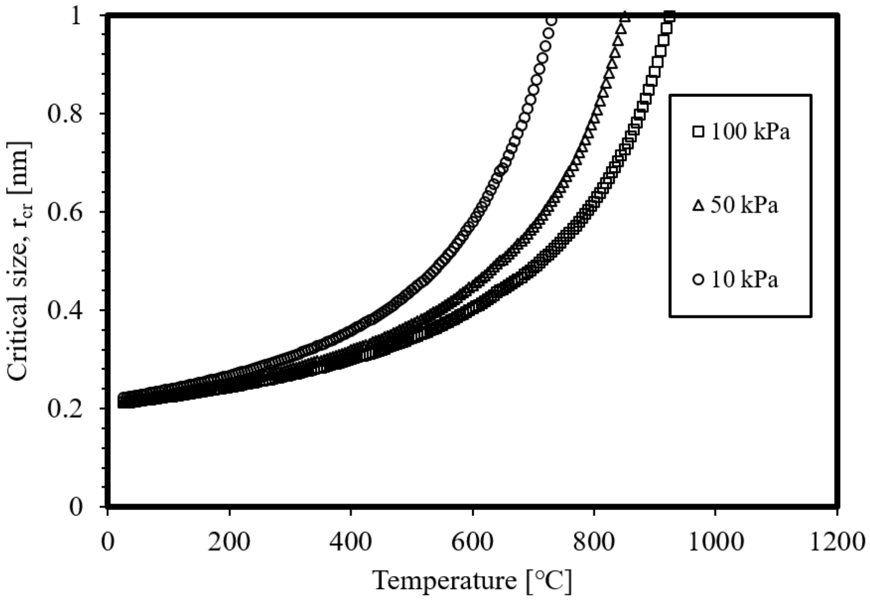

Figure 3.65: Relationship between critical size and temperature at 100, 50, and 10 kPa of Mg.

### 3.5.3 Proposal of a new equation for particle size prediction by PWD

#### 3.5.3.1 Theory

In the present study, it is considered that with various metals, the difference in critical size may lead to the difference in the final size of the particles after the growth process. In vapor with the same number of molecules, with a larger critical size (i.e. larger nucleus) the number of nuclei is smaller, thus, the number density is smaller. According to Brownian coagulation, particles are grown by colliding with each other. Assuming a similar gas medium, with a smaller initial number density, the coagulation time identified by the Smoluchowski diffusion model[199] increases. Coagulation time or also known as the characteristic aggregation time can be considered as the average time for the particle concentration to reduce to half of the initial value. Coagulation time is given by:

$$\tau = \frac{1}{k_{\mathrm{a}} n_0}, \tag{3.15}$$

where $\tau$ is coagulation time, $k_{\mathrm{a}}$ is aggregation rate constant and dependent on the condition, $n_0$ is initial particle concentration. Assuming that the number of coagulation time (period) is similar for various metals in PWD, it is possible to consider that metal with a larger critical size after Brownian coagulation has a larger geometric mean diameter. Therefore, the critical size must be a crucial factor regarding the nucleation process.

Basing on the hypotheses mentioned in section 3.5.1, a modification was considered. First, instead of using the parameter of the density of mass (g/m$^3$), the parameter of the density of number (m$^{-3}$) should be more suitable to apply for light elements like Al and Mg. In addition, since the critical size has an effect on the geometric mean diameter, in detail, proportional to geometric mean diameter, the volume of a nucleus with the critical size should be added. Therefore, the parameter named as relative nucleus number ($N_{\mathrm{r}}$) was proposed as follows,

$$N_{\mathrm{r}} = \frac{D_{\mathrm{th}}}{A} V_{\mathrm{cr}} = \frac{mPV_{\mathrm{p}}V_{\mathrm{cr}}}{E_{\mathrm{c}}A}, \tag{3.16}$$

where, $A$ is the atomic mass, $V_{\mathrm{cr}} = {r_{\mathrm{cr}}}^3$ is the volume of nucleus with critical size $r_{\mathrm{cr}}$. Because $N_{\mathrm{r}}$ is the substitution for $D_{\mathrm{th}}$, there must be a parameter that can substitute $D_{\mathrm{exp}}$. Basing on the work of Tokoi et al.[112], an experimental parameter is considered. Since the process does not change, the relationship between the experimental and theoretical parameters, in this case, should be similar as in the work of Tokoi et al., therefore, the experimental relative nucleus number should be determined as follows,

$$N_{\mathrm{r\_exp}} = 106{N_{\mathrm{r}}}^{0.6}. \tag{3.17}$$

From the results of the previous section, it is seen clearly that critical size is dependent on ambient gas pressure, temperature, and materials. In addition, the density of plasma/vapor in the PWD experiment does not distribute uniformly, hence, the temperature may vary spatially. However, in order to identify the relative nucleus number $N_{\mathrm{r}}$, it is essential to identify a single value of critical size $r_{\mathrm{cr}}$ of each metal. An attempt to approach experimentally and semi-empirically was carried out.

For the experimental approach, a PWD experiment on Mg and Cu wires to observe time evolution of plasma/vapor size and deposition energy was conducted. Discharge conditions of Mg wires were set similar to those in section 3.4.2. Discharge conditions of Cu wires were determined so that results can be comparable to those of Mg wires. Then, a numerical calculation was carried out to estimate the temperature in the plasma/vapor.

Finally, from these results, the temperature and the supersaturation were estimated to calculate $V_{\mathrm{cr}}$ and $N_{\mathrm{r}}$.

#### 3.5.3.2 PWD experiments to observe expanding plasma/vapor

Experimental conditions are shown in Table 3.9.

Table 3.9: Experimental conditions for comparison of Mg and Cu wires.

| | Mg | Cu |
|---|---|---|
| Wire | l = 25 mm, $\phi$ = 0.1 mm | |
| Evaporation energy, $E_{\mathrm{v}}$ [J] | 2.4 | 10.5 |
| Charging voltage, $V_{\mathrm{c}}$ [kV] | 4.7 | 6 |
| Capacitance, C [µF] | 10 | 30 |
| Charging energy, $E_{\mathrm{c}} = 0.5CV_{\mathrm{c}}{}^2$[J] | 110.5 | 540 |
| Relative energy, $K = E_{\mathrm{c}}/E_{\mathrm{v}}$ | 50 | 51 |
| Ambient gas | Ar | |
| Ambient gas pressure [kPa] | 10, 50, and 100 | |

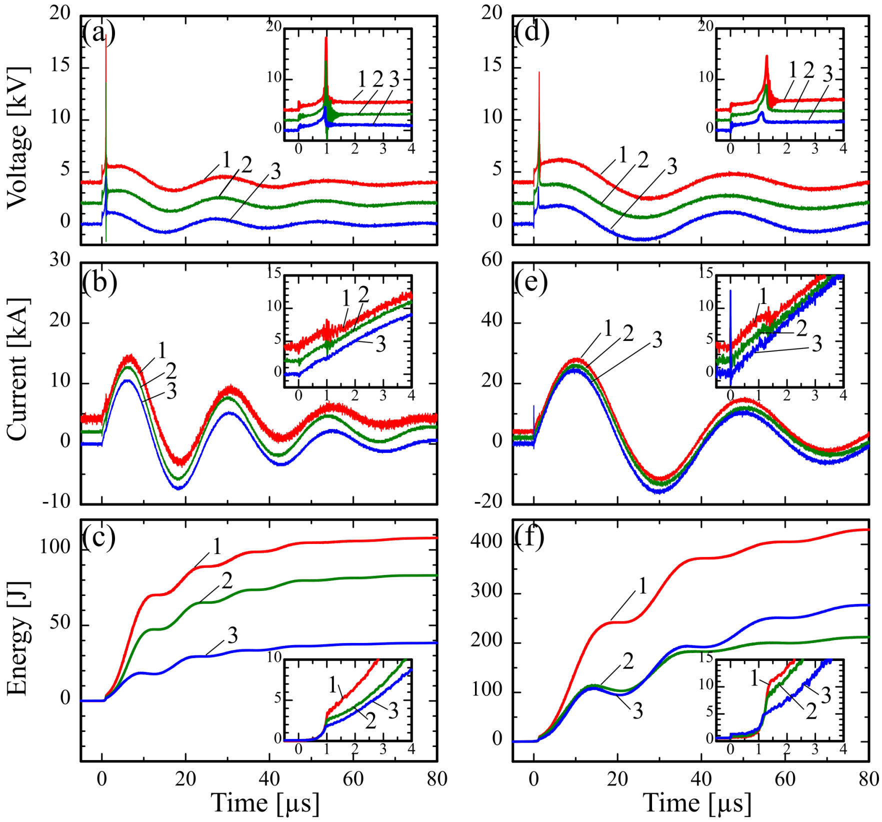

Figure 3.66: Voltage-current waveforms and deposition energies of Mg (a)−(c) and Cu (d)−(f), respectively at various Ar gas pressures (#1:100 kPa, #2: 50 kPa, and #3: 10 kPa). Insets are enlargements of corresponding graphs in the range of 0−4 µs. Current and voltage waveforms have been offset by 2 kV and 2 kA per waveform for readability.

The experiments were conducted to observe the time evolution of the expansion of plasma/vapor by a high-speed camera. The experimental setup was shown in Fig. 2.1. Details about the experimental procedure can be found in section 2.5. In this experiment, the high-speed camera was set with a frame rate of 150000 fps and the interval between two continuous frames is approximately 6.7 µs. The experiments were repeated 5 times at each condition for reproducibility. During the experiment, voltage-current waveforms were obtained to calculate deposition energy. Deposition energy can be calculated using Eqs. (2.8),(2.9),(2.10).

Voltage and current waveforms shown in Figs. 3.66(a), (b), (d), (e) indicate that there was no dwell time during the discharge. Dwell time is more easily observed when discharge voltage is low, pressure is high, and increases with increasing wire length[304, 305]. Moreover, gas species also have an effect on the appearance of dwell time[306]. Here, due to employing Ar gas, high-voltages, and relatively short wires, it is understandable that it is difficult for dwell time to happen. Figure 3.66(c) shows that energies deposited into Mg wires at the end of the wire heating stage are sufficient to vaporize the wire completely with all Ar gas pressures. However, in Fig. 3.66(f), only at 100 kPa, the deposition energy was sufficient for vaporizing Cu wires. At 50 kPa, the deposition energy was nearly sufficient while at 10 kPa, only about half of vaporization energy was supplied. The reason might be attributed to the usage of Ar gas with a low dielectric breakdown voltage[172]. The high-speed images were recorded at the same time as the PWD experiments. These results are shown in Fig. 3.67.

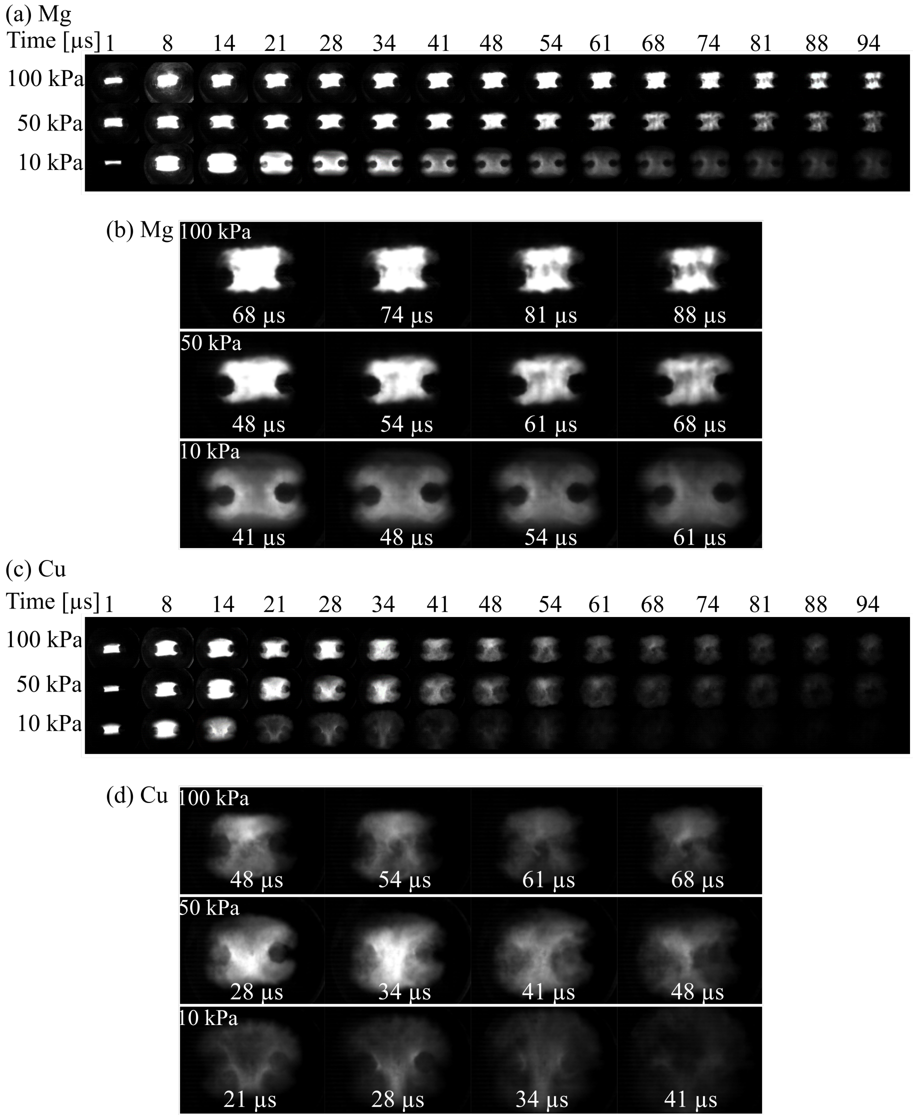

Figure 3.67: High-speed photographs at various ambient Ar gas pressures ((a) and (c)), and enlargement images at times of interest((b) and (d)) of Mg and Cu, respectively.

By Fig. 3.67, it is apparent that with both cases Mg and Cu, the volume of expanding plasma/vapor increased with decreasing ambient gas pressure. This phenomenon was reported by several pieces of literature regarding PWD [307, 112]. In order to explain this, one should consider shock waves generated at the beginning of the wire explosion. At the moment the wire is vaporized and the metallic vapor starts to expand outward, due to extremely high temperature and pressure, the vaporized wire expands at a velocity higher than the speed of sound in ambient gas. This facilitates cylindrical shock waves propagating radially outward. The propagation of shock waves following with metallic vapor from vaporized wire has been comprehensively investigated and visualized by means of Kerr cell schlieren photography[308], rotating-mirror streak camera[309, 310], and microwave Doppler measurements[311]. In particular, based on Taylor's analysis of the intense spherical explosion[312], Lin et al. extended to the cylindrical case and numerically derived an expression of the radius of shock waves in terms of time in the air as follows: $R = 1.009(E/\rho_0)^{1/4}t^{1/2}$, where $E$ is the energy released per unit length, $\rho_0$ is the density of the atmosphere, $t$ is time[313]. The factor of 1.009 is due to the numerical calculation result with the ambiance is air and varies with different gas species [313]. According to this relationship, the radius of the propagating shock waves is inversely proportional to the power of 0.25 of the density of the ambiance, as a result, with decreasing ambient gas pressure,i.e. decreasing the density of ambient gas, the radius of shock waves in terms of time should increase. As the presence of shock waves makes it possible to the metallic vapor to expand outward, with decreasing ambient gas pressure it is explainable that the volume of plasma/vapor increases. Furthermore, according to Muller et al., the radius of expansion of plasma/vapor keeps unchanged after increasing to a certain value[308]. Therefore, the result of high-speed images of the expansion of plasma/vapor shown in Fig. 3.67 is in good agreement with observations of the phenomenon by a different method.

The enlargements of high-speed images shown at Figs. 3.67(b) and (d) show images of plasma/vapor at the time it attains the maximum volume of Mg and Cu, respectively. By the hypotheses stated in section 3.5.2, it was considered that at this time, the pressure of plasma/vapor is equivalent to that of ambient gas pressure, the value of supersaturation is greater than 1, and the nucleation starts to happen. Next section provides the result numerical calculation and radius of expanding plasma/vapor by solving hydrodynamic conventional equations for further investigation.

#### 3.5.3.3 Numerical calculation of temperature and radius of expanding plasma/vapor

By using the calculated deposition energy as the input to the hydrodynamic behavior calculation, the temperature during the process of PWD of Cu and Mg wires under various conditions was simulated. These calculations employed Eqs. (2.17-2.19) in section 2.7. After that, by using the obtained temperature profiles, corresponding temporal equilibrium vapor pressures of Cu and Mg vapor/plasma in terms of radial direction were determined by Eq. (3.14). These temperature and equilibrium vapor pressure profiles are shown below Figs. 3.68 and 3.69.

Figures 3.68 and 3.69 show the time-evolution of temperature distributing radially at the midpoint of Mg and Cu wire during the pulsed discharge calculated using energy inputs from Figs. 3.66(c) and (f) and corresponding equilibrium vapor pressures.

For the temperature profiles, when the volume of plasma/vapor expanded too large, the conditions deviated from the fluid approximation and the calculation was automatically terminated. As a result, with decreasing Ar gas pressure, simulation time decreased. Moreover, by comparing Mg and Cu wires at similar discharge conditions, Cu wires attained higher temperatures but reached the limit of calculation more quickly than Mg wires did. Therefore, it was possible that Cu wires were quenched faster than Mg wire was, which might induce the formation of smaller nanoparticles.

In addition, in temperature profiles of Figs. 3.68 and 3.69, darker areas are present among lighter areas, which indicates the decrease, then increase of temperature. When the plasma/vapor expanded adiabatically, work was done on the ambient Ar gas by the plasma/vapor, however, there were some intervals when energy was not deposited on as seen in Fig. 3.66 due to the oscillation of voltage and current. Consequently, the decrease of temperature of plasma/vapor in these intervals is understandable.

In each condition of Ar ambient gas pressure, from the equilibrium vapor pressure profiles, it is possible to roughly identify the time that the radially distributed values of equilibrium vapor pressure were equivalent to the Ar ambient gas pressure. These times are intentionally shown by the distinguishable red rectangles where the color changes from yellow-orange-red in Figs. 3.68 and 3.69. As mentioned in section 3.5.2, it is very difficult to know the actual vapor pressure of the plasma/vapor of Mg and Cu, therefore, an assumption that the pressure of metallic plasma/vapor is equivalent to that of the Ar ambient gas when the plasma/vapor state has attained its maximum volume has been made. This assumption was verified by the high-speed images shown in Figs. 3.67(b) and (d) of Mg and Cu wires, respectively. According to these high-speed images, it is seen that in these ranges of time, almost no further expansion of plasma/vapor state is visible. As a result, it can be considered that during this range of time, the actual vapor pressure of metallic plasma/vapor is equivalent to Ar gas ambient gas pressure. In addition, the times identified before by using profiles of equilibrium vapor pressure in Figs. 3.68 and 3.69 are all in this time of ranges. Therefore, it can be considered that nucleation started to happen after these times. Let us call these times nucleation times and summarize in Table 3.10.

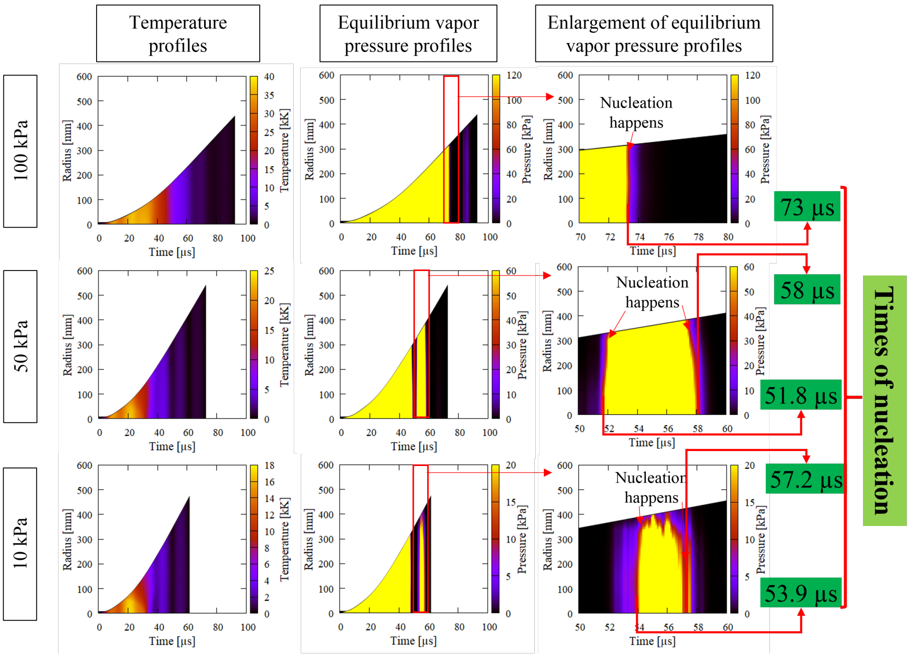

Figure 3.68: Temperature, equilibrium vapor pressure, and enlargement of equilibrium vapor pressure profiles of Mg wires in PWD experiment at various Ar gas pressures.

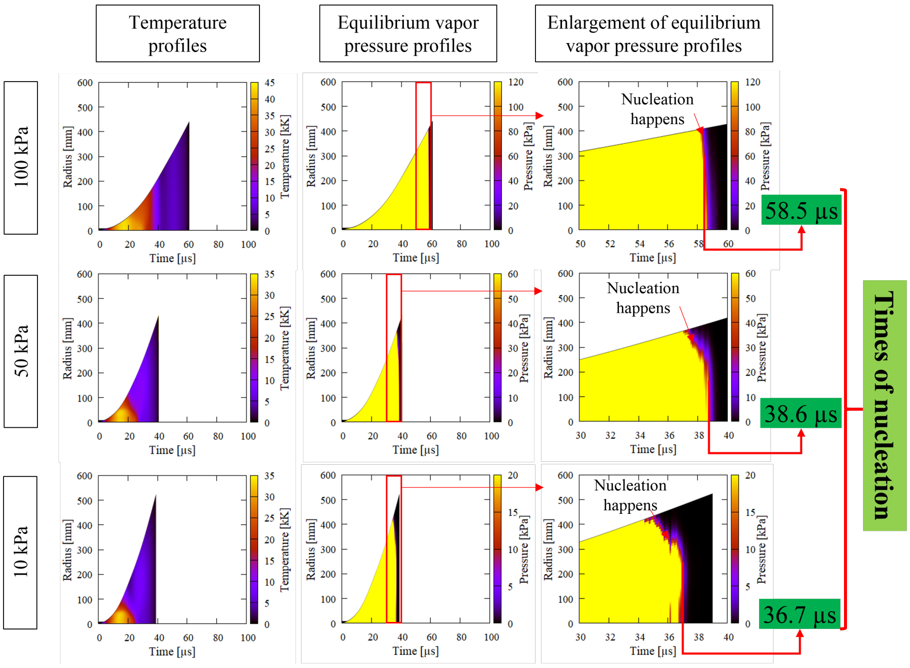

Figure 3.69: Temperature, equilibrium vapor pressure, and enlargement of equilibrium vapor pressure profiles of Cu wires in PWD experiment at various Ar gas pressures.

Table 3.10: Nucleation time of Mg and Cu wires in PWD experiment.

| Pressure | 100 kPa | 50 kPa | 10 kPa |
|---|---|---|---|
| Mg | 73 µs | 51.8 and 58 µs | 53.9 and 57.2 µs |
| Cu | 58.5 µs | 38.6 µs | 36.7 µs |

#### 3.5.3.4 Estimation of temperature of nucleation

From the temperature profiles of Mg and Cu wires by PWD obtained in Figs. 3.68 and 3.69, by calculating the average values of temperature along the radial direction, it is possible to plot graphs of the average temperature of Mg and Cu wires by PWD in terms of time. These graphs are shown in Figs. 3.70 (a) and (b). From the high-speed images of the phenomenon shown in Fig. 3.67, it can be seen that although the delay of the trigger signal for the high-speed camera was supposed to be maximum 50 ns, due to the fact that at the first frame, the expansion of exploding wire has been already observed, it is estimated that this frame might be recorded at around 1 µs after the starting of the phenomenon. By using Figs. 3.70(a) and (b) and the values of nucleation times shown in Table 3.10, it is possible to identify the values of average temperature at the nucleation time under each condition. These values are shown in Table 3.11.

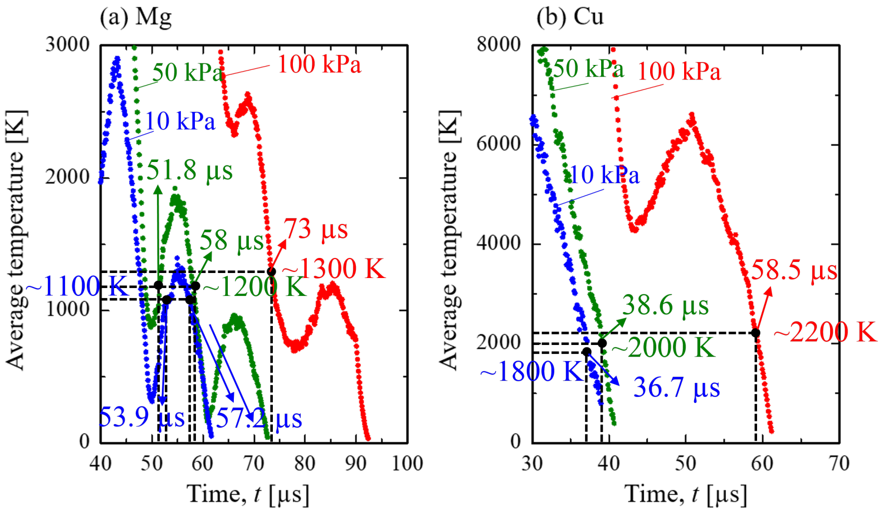

Figure 3.70: Time evolution of average temperature calculated from simulated data in Figs. 3.68 and 3.69 of (a) Mg and (b) Cu, respectively.

Table 3.11: Estimated nucleation temperature of Mg and Cu wires in PWD experiment.

| Pressure | 100 kPa | 50 kPa | 10 kPa |
|---|---|---|---|
| Mg | ∼1300 K | ∼1200 K | ∼1100 K |
| Cu | ∼2200 K | ∼2000 K | ∼1800 K |

It can be seen that these values are also different from each other under different conditions of ambient Ar gas pressure. However, for the convenience of calculation, the average temperature for each material was taken. As a result, the average temperature for nucleation to happen with Mg and Cu are 1200 K and 2000 K, respectively. On the other hand, it has been known that the empirical values of measured temperature are 80% to 90% of calculated values (T. Sasaki, private communication, June 2, 2021). In the present study, let us consider that the actual values of temperature comprise 80% of calculated values. Therefore, we can determine the average temperatures under which nucleation happened with Mg and Cu are ∼ 960 K and ∼ 1600 K, respectively.

It is worth noticing that Tokoi et al. suggested the parameter of experimental plasma/vapor density by estimating the volume of plasma/vapor expansion[112]. As a result, investigating the critical size of nuclei in this way is consistent with the idea suggested by Tokoi et al.

It is also found that 960 K and 1600 K are equivalent to 0.7 and 0.56 times of the normal boiling temperature of Mg and Cu, respectively. This means that the nucleation temperature is lower than the normal boiling point of each material, which can be explained.

By ref. [314], when dealing with the nucleation from the liquid phase, at the melting temperatures, the probability for the stable nuclei to form is extremely small and the solidification does not begin until the temperature decreases below the melting temperature. The difference between the actual temperature of the liquid and the normal melting temperature is called undercooling. Also, according to similar references, typical undercooling for homogeneous nucleation is larger for metals with larger heat of fusion. By applying for the present issue, the finding that the nucleation temperature of Mg and Cu vapor is lower than the normal boiling temperatures is reasonable. In addition, the latent heat of vaporization of Mg is lower than that of Cu (127.7 kJ/mol vs. 304.8 kJ/mol)[303]. Therefore, it is reasonable that the nucleation temperature of Mg and Cu vapor are 0.7 and 0.56 times the normal boiling temperatures of Mg and Cu, respectively.

#### 3.5.3.5 Particle size determining equation in PWD

By the above consideration, it can be speculated that the nucleation temperature of Ag, Ni, and Pd in PWD is equal to 0.56 times the normal boiling temperature of each metal, respectively. Additionally, J.Bai et al. has reported that Al nucleated from the vapor phase by PWD in the temperature range between 1773 K and 1540 K by means of numerical investigation[117]. Basing on this numerical result, let us assume the representative temperature at which Al vapors nucleate to be the average temperature in this range, which is 1656.5 K or 0.59 times the normal boiling temperature of Al. Basing on these considerations, the critical size of Mg, Cu, Al, Ag, Ni, and Pd have been calculated and shown in Table 3.12.

Table 3.12: Critical sizes of various metals at $T$

| Metals | $T_{\mathrm{b}}$ [K] | $T$ [K] | $r_{\mathrm{cr}}$ at 10 kPa [nm] | $r_{\mathrm{cr}}$ at 50 kPa [nm] | $r_{\mathrm{cr}}$ at 100 kPa [nm] |
|---|---|---|---|---|---|
| Mg | 1363 | 954.1 | 0.77 | 0.49 | 0.42 |
| Al | 2792 | 1647.3 | 0.22 | 0.18 | 0.17 |
| Cu | 2833 | 1313.5 | 0.18 | 0.15 | 0.14 |
| Ag | 2435 | 1363.6 | 0.23 | 0.19 | 0.18 |
| Ni | 3186 | 1784.2 | 0.19 | 0.16 | 0.15 |
| Pd | 3236 | 1812.2 | 0.26 | 0.21 | 0.2 |

By substituting the results calculated in Table 3.12 in Eqs. (3.16) and (3.17), a graph expressing the dependence of geometric mean diameter $D_1$ on experimental relative nucleus number $N_{\mathrm{r}}$ is plotted below. After applying for the new parameter, all data of various metallic nanoparticles fall in a curve as shown in Fig. 3.71. Therefore, the validity of the newly proposed relative nucleus number was confirmed.

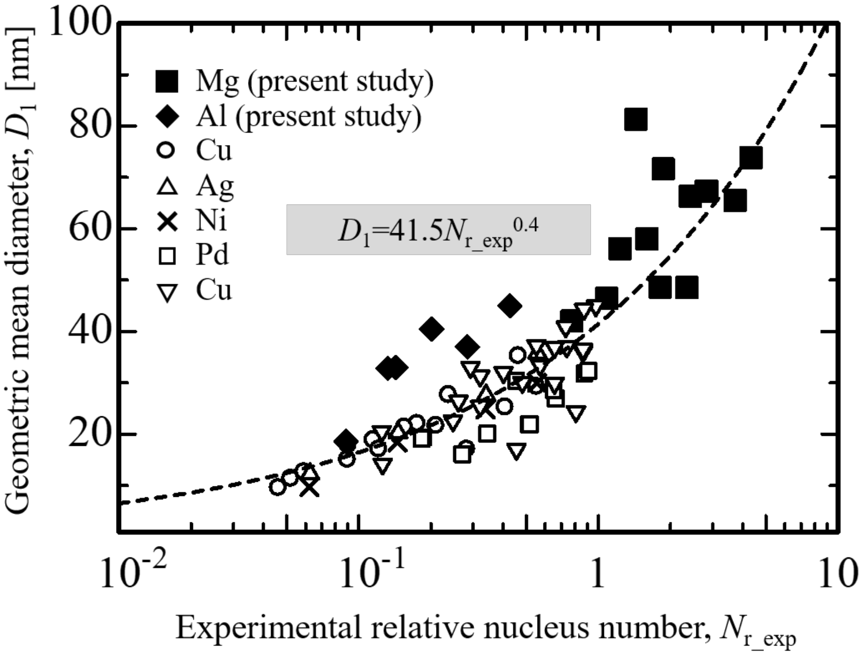

Figure 3.71: The relationship between geometric mean diameter, $D_1$ and experimental relative nucleus number, $N_{\mathrm{r\_exp}}$ of nanoparticles prepared by PWD.

The equation of the fitting curve of all the experimental data represents the equation to predict the particle size of nanoparticles of various metals prepared by PWD. This equation is shown in Fig. 3.71 as follows,

$$D_1 = 41.5 N_{\mathrm{r\_exp}}{}^{0.4}. \tag{3.18}$$

It should be noted that the form of Eq.(3.18) is similar to Eq.(1.18) because of the same power of 0.4. This means that the obtained experimental results are in good agreement with the average size expected by a log-normal distribution of particles undergoing Brownian coagulation in the free molecule regime[204, 112].

From this result, it is apparent that identifying the temperature at which nucleation happens in PWD is important. However, it is difficult to identify the temperature of every metal without investigating the experiments and simulations so that the equation to determine the particle size of nanoparticles by PWD can be used. Nevertheless, this result also suggested a feasible way to predict the appropriate nucleation temperatures basing on the latent heat of vaporization. The values of latent heat of vaporization of Mg, Al, Cu, Ag, Ni, and Pd are shown in the below table[303].

Table 3.13: Latent heat of vaporization of various metals at normal boiling temperature

| Metals | Latent heat of vaporization [kJ/mol] |
|---|---|
| Mg | 127.7 |
| Al | 290.9 |
| Cu | 304.8 |
| Ag | 257.8 |
| Ni | 374.3 |
| Pd | 361.7 |

From Table 3.13, it can be seen that the latent heat of vaporization of Mg is significantly smaller than those of the remaining metals of interest. As a result, it can be considered that the value of latent heat of vaporization may correlate with the nucleation temperature. Basing on this consideration, accompanying with Mg, Zn is speculated to have nucleation temperature as high as 0.7 times of normal boiling point. Obviously, it is necessary to investigate by doing experiments, however, the value of latent heat of vaporization is one of the factors which are useful for predicting the particle size of nanoparticles prepared by PWD without doing experiments.

In summary, a new particle size prediction equation of various light and heavy metallic nanoparticles was proposed as follows,

$$D_1 = 41.5 \left[ 106 \left( \frac{mPK_{\mathrm{p}}V_{\mathrm{cr}}}{E_{\mathrm{c}}A} \right)^{0.6} \right]^{0.4} \tag{3.19}$$

with newly proposed factors: atomic mass and critical size, the size prediction equation is able to be applied for various metals. To determine critical sizes of nuclei, basing on the homogeneous nucleation theory, homogeneous nucleation in the vapor phase was considered. Critical sizes of nuclei of Mg at $T = 0.7T_{\mathrm{b}}$, Al at $T = 0.59T_{\mathrm{b}}$, and Cu, Ag, Ni, Pd at $T = 0.56T_{\mathrm{b}}$ were selected for particle size determining equation. PWD experiments of Mg and Cu wires were conducted to investigate the appropriateness of the temperature at which nucleation happened. Although it is difficult to give a clear conclusion about the temperature of the non-equilibrium plasma/vapor generated in PWD experiments and further studies are necessary to be done, the simulation of temperature by solving hydrodynamic conventional equations with empirically obtained V-I waveforms from the discharge, along with the high-speed photographs gave reasonable evidence to estimate the hypothesis of proposing new size prediction equation of nanoparticles prepared by PWD.

#### 3.5.3.6 Discussion on the proposal of new particle size determining equation

As mentioned in section 1.3.2.4, Eq.(1.18) indicates that by assuming size distribution by Brownian coagulation following log-normal distribution, average particle size is proportional to the power of 0.4 of initial number concentration of particle multiplying with geometric mean of initial particle volume. In PWD, it was considered that the initial number concentration of particles is equivalent to experimental plasma/vapor density $D_{\mathrm{exp}}$. Furthermore, the geometric mean of initial particle volume can be considered to be equivalent to the volume of the nucleus with critical size. As a result, the term $v_{\mathrm{g}0}N_0$ in Eq.(1.18) must be comparable to experimental relative nucleus number in Eq.(3.18). Therefore, it is plausible that the newly proposed equation is in good agreement with particle size expected using a log-normal distribution by considering Brownian coagulation in the free-molecule regime.

In the present study, submicron/nano-sized particles of Mg and Al have been prepared by PWD and particle size distributions of them have been characterized. The failure of the previously proposed size determining equation of metallic nanoparticles prepared by PWD to apply for Mg and Al particles gave a chance to complement the equation. By using approaches of experiment and numerical calculation, nucleation temperatures have been roughly estimated based on the hypothesis that nucleation starts to happen at the time pressure of plasma/vapor is equivalent to ambient gas pressure. It may be criticized that whether it is rational to consider only a very short range of time in the process. It is known that equilibrium vapor pressure is dependent on temperature. During the quenching process, with decreasing temperature, the equilibrium vapor pressure also decreases. However, the criterion for the nucleation to happen is the supersaturation must be equal or greater than 1, in other words, the equilibrium vapor pressure must be equal or smaller than actual vapor pressure. As a result, only from a certain time that the nuclei form then grow into particles by Brownian coagulation should be considered. The temperature at this time is the most important factor to determine the critical size. The validity of estimated nucleation temperature was mentioned and discussed in the previous section.

Besides the validity of estimated nucleation temperature with respect to time, due to the distribution of plasma/vapor with respect to radial position, distribution of density and temperature should also be discussed. First, with experimental conditions employed in the present study, the skin depth of Mg and Cu wires was calculated as $\sim 0.206$ mm and $\sim 0.165$ mm, respectively. These values are all greater than the diameter of any wires, as a result, the skin effect could be negligible in the present study. Based on this fact, the input energy was assumed to deposit uniformly throughout the whole wire in the numerical calculation by solving conventional hydrodynamic equations. Temperature profiles shown in Figs. 3.68 and 3.69 indicate that at the beginning of the discharge (0∼30μs) the radial temperature gradient is easily seen, however, at the end of the discharge (plasma/vapor was cooled and condensed) the distribution of temperature became much more uniform. This is also evidence for the validity of average temperature calculated and shown in Fig. 3.70. Additionally, during the expansion, it was shown in a recent numerical investigation that the density of the metallic vapor behind the shock front is almost uniform, which is consistent with current assumption on the uniformity of the temperature of plasma/vapor[315]. In particular, an experimental study of the density distribution of W wire in the air using a two-wavelength interferometry method was reported[316]. According to the result of this study, the electrical exploding W wire in the air has a two-layer structure: a dense core occupied with neutral atoms (W atoms), and a surrounding layer containing plasma and compressed air. It was described that the dense core has a consistent density distribution with the tube-like structure. As a result, although in practice the temperature obviously distributes to some extent due to the irregularity of wire's resistance, the assumption that temperature distribution is roughly uniform inside the expanding metallic vapor is not irrational. Consequently, in the present study, for the purpose of establishing an approximation curve for the prediction of the size of various materials' nanoparticles, an assumption to simplify the calculation was necessary. Further demand for the accuracy of the approximation curve should be investigated in the future.

Considering the parameters in the bracket of Eq.(3.19), the value of $E_c$ is dependent on the value of the capacitor and charging voltage. However, it is known that the value of the capacitor affects the wire heating rate. With the experimental apparatus employed in the present study, it is possible to generate a pulsed current with a period of several tens of microseconds. As a result, the effect of a pulsed current with a longer or shorter period should be considered. With the same amount of energy, the power decreases with increasing the energy release time. For example, let us consider a pulsed current with a period of millisecond-order with a similar dimension of wire. If a millisecond-order pulsed current was used, the wire heating rate would decrease remarkably. Concurrently, due to heat dissipation, it would be harder to vaporize the wire. By this consideration, by keeping charging energy constant, the power of pulsed current would decrease approximately 1000 times compared to using a microsecond-order pulsed current. With this considerable decrease, it can be predicted that the wire could only be melted and broken or partially vaporized, as a result, no powder or only a small amount of large particles by droplet formation would probably be obtained. Reversely, if a pulsed current with a shorter period was used, for example, a nanosecond-order pulsed current, the value of the capacitor should be decreased greatly. The considerable decrease of capacity reduces the charging energy, as a result, with keeping the wire's diameter and length constant, the charging energy is not sufficient to vaporize the wire. There are two feasible ways to vaporize the wire, which are to increase charging voltage and to decrease the wire's diameter and/or length. The former way faces the risk of dielectric breakdown, by which, the energy is not deposited into the wire because the current passes through the surrounding ambiance between electrodes. Hence, this is considered to be not a reasonable way. The latter way is feasible, however, the wire would be too small for the purpose of nanopowders production. Without considering the obtained amount of nanoparticles, by decreasing diameter and/or length, the mass of the wire also decreases. Considering the parameter of relative nucleus number $\frac{mPK_\mathrm{p}V_\mathrm{cr}}{E_\mathrm{c}A}$, with simultaneously decreasing $E_\mathrm{c}$ and $m$, there would be no change compared to the case of using microsecond-order pulsed current which were used in the present study. In summary, although the equation was established by employing experimental apparatus which can only generate microsecond pulsed current, an extension for applying in pulsed current with different periods is expected to be feasible, however, the criterion that the wire must be vaporized properly should be fulfilled, i.e. the heating rate should be considered.

# Chapter 4

# Conclusions

In general, the present study dealt with the synthesis of nanoparticles by a pulsed discharge. The energy of the pulsed discharge was transferred to metallic wire or compacted powder via Joule heating.

- In the case of using the pulsed current to heat a metallic wire, we have pulsed wire discharge method which is comprehensively investigated in several decades. It has been widely known that the particle size of nanoparticles prepared by PWD decreases with increasing charging voltage and decreasing ambient gas pressure. However, a method to determine the particle size by previously known parameters has not been built until such a proposal was reported by Tokoi et al.[112]. The proposed particle size determining equation by Tokoi et al. has successfully determined the particle size of Cu, Ag, and Ni nanoparticles prepared by PWD with known parameters. Nevertheless, this equation has failed to predict the size of Mg and Al particles. The key issue was investigated to be the difference in the critical size of nuclei which was determined by nucleation temperature. Furthermore, it was found that nucleation temperature could be estimated based on the normal boiling temperature and the latent heat of vaporization which are known properties. The originality of the present study is the solution to this issue by considering the nucleation process, which contributes to the whole process of particle formation by PWD. By this, the particle size determining equation for metallic nanoparticles prepared by PWD becomes applicable for various materials without doing experiments, which is considered to be practically meaningful for mass production of metallic nanoparticles by PWD.

- In the case of using the pulsed current to heat compacted powder, Si nanoparticles have been the first example of nanoparticles prepared by this means of discharge[165]. Basing on this study, in the present work, crystalline nanoparticles of B have been prepared. Furthermore, the novelty of this work lies in the synthesis of nanoparticles of transition metal borides by a pulsed discharge, which has never been reported before. This result may provide knowledge about a one-step, low-cost, high production-rate, and energy-efficient method to synthesize raw nano-sized material for sintering ceramics with high hardness.

The pulsed discharge method with its advantages compared to other methods for the synthesis of nanoparticles made it meaningful to carry out the present study. With the results of the present study, the author expects that it will contribute to the development of the method in the aspect of both theory and practice.

There were four main purposes of this study. The conclusions for those purposes are as follows,

**Purpose 1:** Discussing the effects of different sizes of starting powder on the monolithic transition metal boride and reactive transition metal boride sintering.

**Conclusion 1:** Size of starting powder significantly influences the consolidation of monolithic $TiB_2$ pellets and nano−sized W and B powder are expected to decrease sintering temperature in order to obtain dense and high-concentration $WB_4$ pellets.

For monolithic $TiB_2$ sintering experiment, it was found that:

1. By using the spark plasma sintering method, with starting powder with a grain size of ∼1.87µm, dense pellets of monolithic $TiB_2$ were able to be sintered under conditions of 1600°C, 60 MPa, 5 minute keeping time. The relative density of pellets fabricated at these conditions was 96.7%. The highest relative density was 98.2% obtained at conditions 1900°C, 60 MPa, 5 minute keeping time. Vickers hardness of these samples was approximately 46 GPa at 500 g load.

2. By using starting powder with a grain size of ∼10µm, it was not able to obtain dense pellet with the highest relative density of 74.6% at 1900°C.

3. By mixing ∼1.87µm powder with ∼10µm powder with ratios of 30 wt.% and 70 wt.%, it was possible to obtain dense $TiB_2$ pellets with the relative density of 97.1% and 96.7%, respectively. However, the measurement of Vickers hardness yielded only roughly 32 GPa, which was lower than that of pellet using 100% small powder.

4. The reason for the degradation of Vickers hardness was discussed to be the formation of $Ti_2O_3$ due to the mixing of $ZrO_2$ from zirconia ball of ball milling.

For the tungsten boride sintering experiments, by varying the compositions, sintering temperatures, and pressures, it was able to find the conditions to obtain relatively dense $WB_4$ pellets by SPS. It was found that:

1. The excess of B amount in the compound has an effect of maintaining the presence of $WB_4$ phase when increasing sintering temperature and pressure.

2. With increasing temperature from 1300°C to 1600°C, with compositions of W:B=1:8 and 1:12, $WB_4$ phase was maintained in the range of 1300-1500°C, while at 1600°C, $WB_4$ was decomposed to hex-$WB_2$.

3. With increasing temperature from 1300°C to 1600°C, with the composition of W: B=1:4.5, almost $WB_2$ phase was formed with a very small amount of $WB_4$, however, this $WB_4$ also decomposed with increasing temperature.

4. Keeping pressure constant at 50 MPa with increasing temperature from 1300°C to 1600°C only yielded relatively dense pellet at 1600°C.

5. Pressure played a crucial role to obtain a dense pellet of tungsten boride. At 1500°C, the density of pellets increased with increasing pressure in all compositions.

6. Pressure also promoted the decomposition of $WB_4$ into $WB_2$ at a composition of W:B=1:8.

7. A Pellet with single-phase $WB_4$ (and excess B) and highest density 3.82 g/cm$^3$ was obtained at conditions of W: B=1:12, 1500°C, 90 MPa and 5 min keeping time. Therefore, using nano-sized starting material is expected to obtain dense single-phase $WB_4$ pellets by SPS.

**Purpose 2:** Synthesis of NPs of transition metal boride by a one-step, cost-effective method.

**Conclusion 2:** It was possible to synthesize NPs of transition metal boride and B by using pulsed discharge of compacted powder. Pulsed discharge of compacted powder was basically similar to PWD, but instead of using wire as the raw material, here, the powder was compacted inside a heat-shrinkable tube and between two metallic rods. It was found that:

1. By discharging B wire with diameter 0.1 mm with charging voltage 6 kV and capacitance 30 µF in Ar and $N_2$ gases, it was not possible to prepare NPs of B. It was very difficult to heating wire and B wires were always broken into fragments and fell on the bottom of the experiment chamber.

2. By discharging through 10 mg of micron-sized crystalline B powder (∼40 µm) compacted by Cu rods with $\phi$=2 mm at a voltage of 6.2 kV and capacitance of 30µF, it was possible to prepare NPs of B. These NPs have spherical shape and size less than 100 nm. The product also contained micron-sized particles (few µm), a small amount of Cu from Cu rods (occupying 4.8 wt.%), and C from the heat-shrinkable tube. Impurity of carbon can be avoided by using a slightly sintering B pellet instead of using the heat-shrinkable tube.

3. By discharging through 5 mg of micron-sized crystalline B powder and 1.5 mg of micron-sized amorphous B powder using Ti, Mo, Zr, and W rods at a voltage of 6 kV and capacitance of 30µF, it was possible to synthesize NPs of $TiB_2$, $MoB_2$, $ZrB_2$, and $WB_4$, respectively by using a combination of XRD, bright-field TEM images, EDS spectra, and lattice images. These NPs were spherical in shape and smaller than 100 nm. In addition, minor phases MoB, WB, and $W_2B_5$, small amount metals, and excess B were formed due to the unevenness of ratio metal: boron. A small amount of impurities of Fe/Cr (less than 2wt.%) and C was detected by EDS, however, these impurities can be suppressed by improving the experiment setup and using a slightly sintering B pellet instead of a heat-shrinkable tube, respectively.

4. The main phases of NPs of transition metal borides can be explained using phase diagrams with consideration of the simultaneous cooling of metals and boron from temperatures above the melting temperature of each transition metal boride.

5. These NPs are expected to be used for raw material of sintering transition metal borides ceramics for the purpose of reducing sintering temperature.

**Purpose 3:** Clarifying the particle formation of light elements (Mg and Al) by PWD

**Conclusion 3:** NPs/submicron-sized particles of light elements (Al and Mg) were prepared using PWD of Al and Mg wires, respectively, in Ar gas. By characterizing NPs/submicron-sized particles of Al and Mg, analyzing discharge waveforms, and calculating of deposition energy, it was found that:

1. By XRD, NPs/submicron-sized particles of Al and Mg were almost single-phase

metallic phase. A small amount of MgO was detected by a broad peak at a diffraction angle of 43°. These MgO crystallites are observed to be very small (<10 nm) and decorating on the surface of Mg particles.

2. By observing TEM images, it was found that Al NPs and Mg submicron-sized particles were in a spherical shape. However, Mg submicron-sized particles became more irregular with low $P$ and high $K$ due to the small plasma/vapor density.

3. Particle size distribution of Al NPs and Mg submicron-sized particles followed log-normal distribution. Geometric mean particle size decreased with increasing $K$ and decreasing $P$. Values of geometric standard deviation were in the range of 1.3 and 1.6, which is in the agreement of numerical simulation of gas-phase NPs synthesis in a free molecular regime with the conditions of only coagulation or coagulation with moderate reaction.

4. Since the pulsed discharge was carried out in Ar gas, in the voltage and current waveforms, dwell time was not seen in all conditions of Al and Mg wires, which meant the arc-discharge stage occurred when the wire heating stage had not been completed yet due to the low dielectric breakdown voltage of Ar gas.

5. Due to the incomplete heating of wires, $E_\mathrm{p}$ was sometimes lower than $E_\mathrm{v}$, especially at low $P$.

6. In general, in the aspect of morphology, Al NPs, and Mg submicron-sized particles are similar to other metals belonging to class 1 and class 2 by PWD classification. In addition, the tendency of decreasing particle size with increasing $K$ and decreasing $P$ is also consistent with NPs of other metals by PWD.

**Purpose 4:** By applying the case of Mg and Al in the particle size determining equation by Tokoi et al. and considering a nucleation process in the particle size determining equation, confirming the validity of the equation and proposing a modification if necessary.

**Conclusion 4:** By applying the case of Mg and Al in particle size determining equation by Tokoi et al. and considering the relationship between geometric mean diameter and experimental plasma/vapor density, it was found that with the same experimental plasma/vapor density, while Al was quite close to other metals, Mg submicron-sized particles were at least two times larger than other metals. This lead to the conclusion that the particle size determining equation by Tokoi el al. was not applicable for the case of Mg.

Two hypotheses were stated so that the particle size determining equation could be modified and applicable for Mg and Al cases:

1. The current particle size determining equation described the theoretical plasma/vapor density as the parameter regarding to controllable values $D_\mathrm{th} = mPE_\mathrm{c}{}^{-1}K_\mathrm{p}$ with the dimension [g/m$^3$]. However, in the case of various metals, it was considered that instead of mass density, number density should be more reasonable.

2. When proposing the particle size determining equation, only Brownian coagulation was considered, however, in the particle formation process, nucleation was also thought to contribute to the final particle size of NPs by PWD. By considering similar plasma/vapor density, nuclei with larger critical size have less number density, which leads to a slower growth rate, as a result, grow to larger particles.

Basing on the above hypotheses, a new parameter named as relative nucleus number was proposed as

$$N_{\mathrm{r}} = \frac{D_{\mathrm{th}}}{A} V_{\mathrm{cr}} = \frac{mPK_{\mathrm{p}}V_{\mathrm{cr}}}{E_{\mathrm{c}}A}, \tag{4.1}$$

where $N_{\mathrm{r}}$ is relative nucleus number, $V_{\mathrm{cr}}$ is the volume of nucleus with critical size $r_{\mathrm{cr}}$.

By considering the time when pressure plasma/vapor was balance with ambient gas pressure, the critical sizes of various metals such as Mg, Al, Cu, Ag, Ni, Pd were calculated. Since the critical size is dependent on the temperature and pressure of the plasma/vapor, it was necessary to find the appropriate value to substitute into the newly proposed parameter. By a combination of PWD experiments and simulation of temperature profiles during PWD using hydrodynamic behavior calculations, it was found that critical sizes calculated at the temperature between $T = 0.7T_{\mathrm{b}}$ and $T = 0.56T_{\mathrm{b}}$ for Mg, Al, Cu, Ag, Ni, and Pd would be the appropriate values. The appropriate values of nucleation temperature for the calculation of the critical size of each metal may be predicted based on the value of latent heat of vaporization. According to that consideration, metals such as Cu, Ag, Ni, Pd, and Al with the high latent heat of vaporization may have nucleation temperature around $0.56T_{\mathrm{b}}$ to $0.59T_{\mathrm{b}}$, while metals such as Mg, Zn with the low latent heat of vaporization may have nucleation temperature around $0.7T_{\mathrm{b}}$. After substituting values of critical sizes into the relative nucleus number, the geometric median diameter of various light and heavy metals fell in a curve, which confirmed the validity of the newly proposed relative nucleus number. Consequently, the new particle size determining equation became

$$D_1 = 41.5 \left[ 106 \left( \frac{mPK_{\mathrm{p}}V_{\mathrm{cr}}}{E_{\mathrm{c}}A} \right)^{0.6} \right]^{0.4}. \tag{4.2}$$

The above equation is expected to be applicable for prediction of size of various metallic nanoparticles prepared by PWD. However, the parameter of charging energy $E_{\mathrm{c}}$ could be further discussed in terms of time, in other words, considering parameter of power is speculated to shed a new light for the particle size determining equation. The reason is, as mentioned before, there are two stages in the process of pulsed wire discharge: wire heating and arc discharge. Although the effect of power on the wire heating stage was mentioned in section 3.5.3.6, that on the arc discharge stage has not been clearly understood. After vaporizing and expanding outward, the metallic vapor/plasma is continuously heated by the current from the capacitors. This heating process is considered to be varied with different values of power (i.e. heating rate). The formation of nanoparticles by PWD is significantly dependent on the heating and cooling process of this stage. As a result, the investigation about this topic is considered to be interesting and necessary to carry out in the future.

# Bibliography

[1] C.C. Koch. The synthesis and structure of nanocrystalline materials produced by mechanical attrition: A review. *Nanostructured Materials*, 2(2):109–129, 1993.

[2] E Hellstern and HJ Fecht. C. garland und wl. johnson. In *Mat. Res. Soc. Symp. Proc*, volume 132, page 137, 1989.

[3] E Hellstern, Ho J Fecht, Z Fu, and WL Johnson. Structural and thermodynamic properties of heavily mechanically deformed Ru and AlRu. *Journal of applied physics*, 65(1):305–310, 1989.

[4] D Maurice and TH Courtney. Modeling of the mechanical alloying process. *JOM*, 44(8):10–14, 1992.

[5] HJ Fecht, E Hellstern, Z Fu, and WL Johnson. Nanocrystalline metals prepared by high-energy ball milling. *Metallurgical Transactions A*, 21(9):2333–2337, 1990.

[6] Kenjiro Yamada and Carl C Koch. The influence of mill energy and temperature on the structure of the TiNi intermetallic after mechanical attrition. *Journal of materials research*, 8(6):1317–1326, 1993.

[7] J Eckert, JC Holzer, CE Krill, and WL Johnson. Reversible grain size changes in ball-milled nanocrystalline Fe–Cu alloys. *Journal of materials research*, 7(8):1980–1983, 1992.

[8] Cury Suryanarayana. Mechanical alloying and milling. *Progress in materials science*, 46(1-2):1–184, 2001.

[9] NG Semaltianos. Nanoparticles by laser ablation. *Critical reviews in solid state and materials sciences*, 35(2):105–124, 2010.

[10] Takaaki Orii, Makoto Hirasawa, and Takafumi Seto. Effect of in situ annealing on structure and optical properties of ZnTe nanoparticles produced by pulsed laser ablation. In *Journal of Physics: Conference Series*, volume 59, page 152. IOP Publishing, 2007.

[11] Takeshi Tsuji, Kenzo Iryo, Norihisa Watanabe, and Masaharu Tsuji. Preparation of silver nanoparticles by laser ablation in solution: influence of laser wavelength on particle size. *Applied Surface Science*, 202(1-2):80–85, 2002.

[12] NG Semaltianos, S Logothetidis, W Perrie, S Romani, RJ Potter, SP Edwardson, P French, M Sharp, G Dearden, and KG Watkins. Silicon nanoparticles generated by femtosecond laser ablation in a liquid environment. *Journal of Nanoparticle*

*Research*, 12(2):573–580, 2010.

[13] Fumitaka Mafuné, Jun-ya Kohno, Yoshihiro Takeda, Tamotsu Kondow, and Hisahiro Sawabe. Formation and size control of silver nanoparticles by laser ablation in aqueous solution. *The Journal of Physical Chemistry B*, 104(39):9111–9117, 2000.

[14] Fumitaka Mafuné, Jun-ya Kohno, Yoshihiro Takeda, and Tamotsu Kondow. Full physical preparation of size-selected gold nanoparticles in solution: laser ablation and laser-induced size control. *The Journal of Physical Chemistry B*, 106(31):7575–7577, 2002.

[15] Sumio Iijima. Helical microtubules of graphitic carbon. *nature*, 354(6348):56–58, 1991.

[16] Michael Keidar. Factors affecting synthesis of single wall carbon nanotubes in arc discharge. *Journal of Physics D: Applied Physics*, 40(8):2388, 2007.

[17] Xinluo Zhao, Takenori Kadoya, Takuya Ikeda, Tomoko Suzuki, Sakae Inoue, Masato Ohkohchi, Yuji Takimoto, and Yoshinori Ando. Development of Fe-doped carbon electrode for mass-producing high-yield single-wall carbon nanotubes. *Diamond and related materials*, 16(4-7):1101–1105, 2007.

[18] Yoshinori Ando and Xinluo Zhao. Synthesis of carbon nanotubes by arc-discharge method. *New diamond and frontier carbon technology*, 16(3):123–138, 2006.

[19] Wei-Tang Yao, Shu-Hong Yu, Yong Zhou, Jun Jiang, Qing-Song Wu, Lin Zhang, and Jie Jiang. Formation of uniform CuO nanorods by spontaneous aggregation: Selective synthesis of CuO, $Cu_2O$, and Cu nanoparticles by a solid- liquid phase arc discharge process. *The Journal of Physical Chemistry B*, 109(29):14011–14016, 2005.

[20] AA Ashkarran, MM Ahadian, SA Mahdavi Ardakani, et al. Synthesis and photocatalytic activity of $WO_3$ nanoparticles prepared by the arc discharge method in deionized water. *Nanotechnology*, 19(19):195709, 2008.

[21] AA Ashkarran, MM Ahadian, MR Hormozi Nezhad, et al. Stability, size and optical properties of colloidal silver nanoparticles prepared by electrical arc discharge in water. *The European Physical Journal Applied Physics*, 48(1):10601, 2009.

[22] Der-Chi Tien, Kuo-Hsiung Tseng, Chih-Yu Liao, Jen-Chuen Huang, and Tsing-Tshih Tsung. Discovery of ionic silver in silver nanoparticle suspension fabricated by arc discharge method. *Journal of alloys and compounds*, 463(1-2):408–411, 2008.

[23] Ali Akbar Ashkarran, Seyed Mohammad Mahdavi, Mohammad Mahdi Ahadian, Mohammad Reza Hormozi Nezhad, et al. Rapid and efficient synthesis of colloidal gold nanoparticles by arc discharge method. *Applied Physics A*, 96(2):423–428, 2009.

[24] Jen-Kuang Lung, Jen-Chuen Huang, Der-Chi Tien, Chih-Yu Liao, Kuo-Hsiung Tseng, Tsing-Tshin Tsung, Wen-Shiow Kao, Teh-Hua Tsai, Ching-Song Jwo, Hong-Ming Lin, et al. Preparation of gold nanoparticles by arc discharge in water. *Journal of alloys and compounds*, 434:655–658, 2007.

[25] I Alexandrou, N Sano, A Burrows, RR Meyer, H Wang, AI Kirkland, CJ Kiely, and GAJ Amaratunga. Structural investigation of $MoS_2$ core–shell nanoparticles formed

by an arc discharge in water. *Nanotechnology*, 14(8):913, 2003.

[26] N Parkansky, L Glikman, II Beilis, B Alterkop, RL Boxman, and D Gindin. W–C electrode erosion in a pulsed arc submerged in liquid. *Plasma Chemistry and Plasma Processing*, 27(6):789–797, 2007.

[27] Donald M Mattox. *Handbook of physical vapor deposition (PVD) processing*. William Andrew, 2010.

[28] YC Kong, DP Yu, B Zhang, W Fang, and SQ Feng. Ultraviolet-emitting ZnO nanowires synthesized by a physical vapor deposition approach. *Applied physics letters*, 78(4):407–409, 2001.

[29] Lisheng Wang, Xiaozhong Zhang, Songqing Zhao, Guoyuan Zhou, Yueliang Zhou, and Junjie Qi. Synthesis of well-aligned ZnO nanowires by simple physical vapor deposition on c-oriented ZnO thin films without catalysts or additives. *Applied Physics Letters*, 86(2):024108, 2005.

[30] Seung Chul Lyu, Ye Zhang, Cheol Jin Lee, Hyun Ruh, and Hwack Joo Lee. Low-temperature growth of ZnO nanowire array by a simple physical vapor-deposition method. *Chemistry of materials*, 15(17):3294–3299, 2003.

[31] Christopher Muratore, JJ Hu, Baoming Wang, M Amanul Haque, John E Bultman, Michael L Jespersen, PJ Shamberger, ME McConney, RD Naguy, and AA Voevodin. Continuous ultra-thin $MoS_2$ films grown by low-temperature physical vapor deposition. *Applied Physics Letters*, 104(26):261604, 2014.

[32] Xiao Lin Li and Ya Dong Li. Formation of mos2 inorganic fullerenes (IFs) by the reaction of $MoO_3$ nanobelts and S. *Chemistry–A European Journal*, 9(12):2726–2731, 2003.

[33] Sivacarendran Balendhran, Jian Zhen Ou, Madhu Bhaskaran, Sharath Sriram, Samuel Ippolito, Zoran Vasic, Eugene Kats, Suresh Bhargava, Serge Zhuiykov, and Kourosh Kalantar-Zadeh. Atomically thin layers of $MoS_2$ via a two step thermal evaporation–exfoliation method. *Nanoscale*, 4(2):461–466, 2012.

[34] Yi-Hsien Lee, Xin-Quan Zhang, Wenjing Zhang, Mu-Tung Chang, Cheng-Te Lin, Kai-Di Chang, Ya-Chu Yu, Jacob Tse-Wei Wang, Chia-Seng Chang, Lain-Jong Li, et al. Synthesis of large-area $MoS_2$ atomic layers with chemical vapor deposition. *Advanced materials*, 24(17):2320–2325, 2012.

[35] Alfonso Reina, Xiaoting Jia, John Ho, Daniel Nezich, Hyungbin Son, Vladimir Bulovic, Mildred S Dresselhaus, and Jing Kong. Large area, few-layer graphene films on arbitrary substrates by chemical vapor deposition. *Nano letters*, 9(1):30–35, 2009.

[36] J-F Colomer, C Stephan, Serge Lefrant, Gustaaf Van Tendeloo, Isabelle Willems, Z Konya, Antonio Fonseca, Ch Laurent, and Janos B Nagy. Large-scale synthesis of single-wall carbon nanotubes by catalytic chemical vapor deposition (CCVD) method. *Chemical Physics Letters*, 317(1-2):83–89, 2000.

[37] Dongjin Byun, Yongki Jin, Bumjoon Kim, Joong Kee Lee, and Dalkeun Park. Photocatalytic $TiO_2$ deposition by chemical vapor deposition. *Journal of hazardous materials*, 73(2):199–206, 2000.

[38] J-J Wu and S-C Liu. Low-temperature growth of well-aligned ZnO nanorods by chemical vapor deposition. *Advanced materials*, 14(3):215–218, 2002.

[39] Bernard S Meyerson. Low-temperature silicon epitaxy by ultrahigh vacuum/chemical vapor deposition. *Applied Physics Letters*, 48(12):797–799, 1986.

[40] Larry L Hench and Jon K West. The sol-gel process. *Chemical reviews*, 90(1):33–72, 1990.

[41] Della M Roy and Rustum Roy. An experimental study of the formation and properties of synthetic serpentines and related layer silicate minerals. *American Mineralogist: Journal of Earth and Planetary Materials*, 39(11-12):957–975, 1954.

[42] Rustum Roy. Aids in hydrothermal experimentation: Ii, methods of making mixtures for both "dry" and "wet" phase equilibrium studies. *Journal of the American Ceramic Society*, 39(4):145–146, 1956.

[43] Rustum Roy. Gel route to homogeneous glass preparation. *Journal of the American Ceramic Society*, 52(6):344–344, 1969.

[44] GREGORY J McCARTHY, Rustum Roy, and JOYCE M McKAY. Preliminary study of low-temperature "glass" fabrication from noncrystalline silicas. *Journal of the American Ceramic Society*, 54(12):637–638, 1971.

[45] Werner Stöber, Arthur Fink, and Ernst Bohn. Controlled growth of monodisperse silica spheres in the micron size range. *Journal of colloid and interface science*, 26(1):62–69, 1968.

[46] Egon Matijević, Michael Budnik, and Louis Meites. Preparation and mechanism of formation of titanium dioxide hydrosols of narrow size distribution. *Journal of Colloid and Interface Science*, 61(2):302–311, 1977.

[47] Larry L Hench. Ultrastructural processing of ceramics, glasses and composites. Technical report, FLORIDA UNIV GAINESVILLE DEPT OF MATERIALS SCIENCE AND ENGINEERING, 1984.

[48] Wey Yang Teoh, Rose Amal, and Lutz Mädler. Flame spray pyrolysis: An enabling technology for nanoparticles design and fabrication. *Nanoscale*, 2(8):1324–1347, 2010.

[49] Luis F Hakim, Julie L Portman, Michelle D Casper, and Alan W Weimer. Conformal coating of nanoparticles using atomic layer deposition in a fluidized bed reactor. In *AIChE Annual Meeting, Conference Proceedings*, pages 6543–6563, 2004.

[50] MFPSJP Formenti, F Juillet, P Meriaudeau, SJ Teichner, and P Vergnon. Preparation in a hydrogen-oxygen flame of ultrafine metal oxide particles. oxidative properties toward hydrocarbons in the presence of ultraviolet radiation. *Journal of colloid and interface science*, 39(1):79–89, 1972.

[51] Hendrik K Kammler and Sotiris E Pratsinis. Carbon-coated titania nanostructred particles: Continuous, one-step flame-synthesis. *Journal of materials research*, 18(11):2670–2676, 2003.

[52] Tue Johannessen and Sotiris Koutsopoulos. One-step flame synthesis of an active

$Pt/TiO_2$ catalyst for $SO_2$ oxidation—a possible alternative to traditional methods for parallel screening. *Journal of Catalysis*, 205(2):404–408, 2002.

[53] Bjoern Schimmoeller, Heiko Schulz, Sotiris E Pratsinis, Anika Bareiss, Andreas Reitzmann, and Bettina Kraushaar-Czarnetzki. Ceramic foams directly-coated with flame-made $V_2O_5/TiO_2$ for synthesis of phthalic anhydride. *Journal of Catalysis*, 243(1):82–92, 2006.

[54] Bjoern Schimmoeller, Heiko Schulz, Anika Ritter, Andreas Reitzmann, Bettina Kraushaar-Czarnetzki, Alfons Baiker, and Sotiris E Pratsinis. Structure of flame-made vanadia/titania and catalytic behavior in the partial oxidation of o-xylene. *Journal of Catalysis*, 256(1):74–83, 2008.

[55] Richard Kydd, Wey Yang Teoh, Kenneth Wong, Yong Wang, Jason Scott, Qing-Hua Zeng, Ai-Bing Yu, Jin Zou, and Rose Amal. Flame-synthesized ceria-supported copper dimers for preferential oxidation of CO. *Advanced Functional Materials*, 19(3):369–377, 2009.

[56] Runduo Zhang, Wey Yang Teoh, Rose Amal, Biaohua Chen, and Serge Kaliaguine. Catalytic reduction of NO by CO over $Cu/Ce_xZr_{1-x}O_2$ prepared by flame synthesis. *Journal of Catalysis*, 272(2):210–219, 2010.

[57] Clint R Bickmore, Kurt F Waldner, David R Treadwell, and Richard M Laine. Ultrafine spinel powders by flame spray pyrolysis of a magnesium aluminum double alkoxide. 1996.

[58] TR Hinklin and RM Laine. Synthesis of metastable phases in the magnesium spinel-alumina system. *Chemistry of Materials*, 20(2):553–558, 2008.

[59] Gian Luca Chiarello, Ilenia Rossetti, and Lucio Forni. Flame-spray pyrolysis preparation of perovskites for methane catalytic combustion. *Journal of catalysis*, 236(2):251–261, 2005.

[60] Gian Luca Chiarello, Jan-Dierk Grunwaldt, Davide Ferri, Frank Krumeich, Cesare Oliva, Lucio Forni, and Alfons Baiker. Flame-synthesized $LaCoO_3$-supported pd: 1. structure, thermal stability and reducibility. *Journal of Catalysis*, 252(2):127–136, 2007.

[61] Evagelos K Athanassiou, Robert N Grass, and Wendelin J Stark. Large-scale production of carbon-coated copper nanoparticles for sensor applications. *Nanotechnology*, 17(6):1668, 2006.

[62] Evagelos K Athanassiou, Christian Mensing, and Wendelin J Stark. Insulator coated metal nanoparticles with a core/shell geometry exhibit a temperature sensitivity similar to advanced spinels. *Sensors and Actuators A: Physical*, 138(1):120–129, 2007.

[63] Robert N Grass and Wendelin J Stark. Gas phase synthesis of fcc-cobalt nanoparticles. *Journal of Materials Chemistry*, 16(19):1825–1830, 2006.

[64] EK Athanassiou, P Grossmann, RN Grass, and Wendelin J Stark. Template free, large scale synthesis of cobalt nanowires using magnetic fields for alignment. *Nanotechnology*, 18(16):165606, 2007.

[65] Robert N Grass and Wendelin J Stark. Flame spray synthesis under a non-oxidizing atmosphere: Preparation of metallic bismuth nanoparticles and nanocrystalline bulk bismuth metal. *Journal of Nanoparticle Research*, 8(5):729–736, 2006.

[66] Sotiris E Pratsinis. Flame aerosol synthesis of ceramic powders. *Progress in Energy and Combustion Science*, 24(3):197–219, 1998.

[67] Weihua Jiang and K. Yatsui. Pulsed wire discharge for nanosize powder synthesis. *IEEE Transactions on Plasma Science*, 26(5):1498–1501, 1998.

[68] Edward Nairne. Vii. electrical experiments by mr. edward nairne, of london, mathematical instrument-maker, made with a machine of his own workmanship, a description of which is prefixed. *Philosophical Transactions of the Royal Society of London*, (64):79–89, 1774.

[69] Michael Faraday. X. the bakerian lecture.—experimental relations of gold (and other metals) to light. *Philosophical Transactions of the Royal Society of London*, (147):145–181, 1857.

[70] JA Anderson. Spectra of explosions. *Proceedings of the National Academy of Sciences of the United States of America*, 6(1):42, 1920.

[71] John Augustus Anderson. The spectrum of electrically exploded wires. *The Astrophysical Journal*, 51:37, 1920.

[72] JA Anderson. The spectral energy distribution and opacity of wire explosion vapors. *Proceedings of the National Academy of Sciences of the United States of America*, 8(7):231, 1922.

[73] Hantaro NAGAOKA, Tetsugoro FUTAGAMI, and Toshio MACHIDA. Electric explosion of wires and threads. *Proceedings of the Imperial Academy*, 2(7):328–331, 1926.

[74] Hantaro NAGAOKA and Tetsugoro FUTAGAMI. Instantaneous photographs of electrically exploded wires. *Proceedings of the Imperial Academy*, 2(8):387–389, 1926.

[75] Hantaro NAGAOKA and Tetsugoro FUTAGAMI. Cinematographic sketch of electrically exploded wires. *Proceedings of the Imperial Academy*, 4(5):198–200, 1928.

[76] W Kleen. Passage of electricity through fine metallic filaments. *Ann. Physik*, 11:579–605, 1931.

[77] Joachim Wrana. Vorgänge beim schmelzen und verdampfen von drähten mit sehr hohen stromdichten. *Archiv für Elektrotechnik*, 33(10):656–672, 1939.

[78] B. Eiselt. Über den ablauf von drahtexplosionen. (the course of wire explosions). *Z. Physik*, 132:54–71, 1952.

[79] WM Conn. Studien zum mechanismus von elektrischen drahtexplosionen. *Z. angew. Phys.*, 7:539–554, 1955.

[80] IF Kvartskhava, VV Bondarenko, RD Meladze, and KV Suladze. Electrical explosion of wires in vacuum. *SOVIET PHYSICS JETP-USSR*, 4(5):637–644, 1957.

[81] IF Kvartskhava, VV Bondarenko, PD MELADZE, and KV Suladze. Electric explosion of spiral wires in vacuum. *SOVIET PHYSICS JETP-USSR*, 8(4):634–638, 1959.

[82] SV Lebedev and SE Khaikin. Some anomalies in the behavior of metals heated up with high-density current pulses. *Zh. Tekh. Fiz.*, 26(5):629, 1954.

[83] William George Chace. *A bibliography of the electrically exploded wire phenomenon*, volume 58. Thermal Radiation Laboratory, Geophysics Research Directorate, Air Force ..., 1958.

[84] W. Chace. A brief survey of exploding wire research. 1959.

[85] W.G. Chace, H.K. Moore, Air Force Cambridge Research Laboratories (U.S.). Geophysics Research Directorate, and Lowell Technological Institute Research Foundation. *Exploding Wires: Proceedings*. Number v. 1. Plenum Press, 1959.

[86] W.G. Chace, H.K. Moore, Air Force Cambridge Research Laboratories (U.S.). Geophysics Research Directorate, and Lowell Technological Institute Research Foundation. *Exploding Wires: Proceedings*. Number v. 3. Plenum Press, 1964.

[87] W.G. Chace, H.K. Moore, Air Force Cambridge Research Laboratories (U.S.). Geophysics Research Directorate, and Lowell Technological Institute Research Foundation. *Exploding Wires: Proceedings*. Number v. 4. Plenum Press, 1968.

[88] W.G. Chace and H.K. Moore. *Exploding Wires: Volume 2 Proceedings of the Second Conference on the Exploding Wire Phenomenon, Held at Boston, November 13–15, 1961, under the Sponsorship of the Geophysics Research Directorate, Air Force Cambridge Research Laboratories, Office of Aerospace Research, with the Cooperation of the Lowell Technological Institute Research Foundation.* Springer US, 2012.

[89] RJ Reithel, JH Blackburn, GE Seay, and S Skolnick. The current pause in an exploding wire. *Exploding Wires*, 1(S 19):32, 1959.

[90] William G Chace, Robert L Morgan, and Kauko R Saari. Conductivity during the 'dwell-time'of a wire explosion. In *Exploding Wires*, volume 1, pages 59–72. Plenum Press, 1959.

[91] Robert C Good Jr. Resistance variation of exploding wires. Technical report, GENERAL ELECTRIC CO PHILADELPHIA PA MISSILE AND SPACE DIV, 1964.

[92] EARLE B MAYFIELD. Radiometric temperature measurements of short duration events. Technical report, NAVAL ORDNANCE TEST STATION CHINA LAKE CA, 1961.

[93] RC Maninger. Preburst resistance and temperature of exploding wires. Technical report, California. Univ., Livermore. Lawrence Radiation Lab., 1964.

[94] T Korneff, JL Bohn, and FH Nadig. Exploding wire phenomena at reduced pressures. *Exploding Wires*, 1:104–114, 1959.

[95] Akira Sakurai, T Takao, and T Taira. Effect of applied magnetic field on the exploding wire phenomenon-ii. In *Exploding Wires*, pages 63–69. Springer, 1968.

[96] David P Ross and OH Zinke. High-temperature plasmas produced by exploding wires. In *Exploding Wires*, pages 147–160. Springer, 1968.

[97] RA Marcus. Technique in photochemistry. *Exploding Wires*, 1:307, 1959.

[98] WL Starr. Exploding wire plasma accelerator. In *Exploding Wires*. Plenum Press Inc., 1959.

[99] Louis Baker and Raymond L Warchal. Studies of metal—water reactions by the exploding wire technique. In *Exploding Wires*, pages 207–223. Springer, 1962.

[100] JA Kersavage. Pressure environments created by wires exploded in water. In *Exploding wires*, pages 225–233. Springer, 1962.

[101] G Sargent Janes and H Koritz. High-power pulse steepening by means of exploding wires. *Review of Scientific Instruments*, 30(11):1032–1037, 1959.

[102] H Bruce McFarlane. *A High-voltage, Quick-acting Fuse to Protect Capacitor Banks.* University of California Radiation Laboratory, 1956.

[103] Victor E Scherrer. An exploding wire hypervelocity projector. In *Exploding Wires*, pages 235–244. Springer, 1962.

[104] H Jäger and W Lochte-Holtgreven. Exploding wires as a light source for quantitative spectroscopy. In *Exploding Wires*, pages 41–50. Springer, 1968.

[105] FG Karioris, BR Fish, and GW Royster. Aerosols from exploding wires. In *Exploding Wires*, pages 299–311. Springer, 1962.

[106] MJ Joncich and DG Ren. Synthesis of inorganic binary compounds using exploding wire techniques in exploding wires. Plenum Press/dited by WG Chace, HK Moore.—NY—1964, 1964.

[107] Micheal J Joncich, Joe W Vaughn, and Byron F Knutsen. Preparation of metal nitrides by the exploding wire technique. *Canadian Journal of Chemistry*, 44(2):137–142, 1966.

[108] Yu A Kotov. Electric explosion of wires as a method for preparation of nanopowders. *Journal of Nanoparticle Research*, 5(5):539–550, 2003.

[109] Chuhyun Cho, Keiichi Murai, Tsuneo Suzuki, Hisayuki Suematsu, Weihua Jiang, and Kiyoshi Yatsui. Enhancement of energy deposition in pulsed wire discharge for synthesis of nanosized powders. *IEEE transactions on plasma science*, 32(5):2062–2067, 2004.

[110] Keiichi Murai, Hisayuki Suematsu, Weihua Jiang, Kiyoshi Yastui, and Koichi Niihara. Determination of submicrometer particle content in copper powder prepared by pulsed wire discharge. *Japanese Journal of Applied Physics*, 47(1S):605, 2008.

[111] Francis H Webb, Henry H Hilton, Paul H Levine, and Alvin V Tollestrup. The electrical and optical properties of rapidly exploded wires. In *Exploding wires*, pages 37–75. Springer, 1962.

[112] Yoshinori Tokoi, Hong-Baek Cho, Tsuneo Suzuki, Tadachika Nakayama, Hisayuki

Suematsu, and Koichi Niihara. Particle size determining equation in metallic nanopowder preparation by pulsed wire discharge. *Japanese Journal of Applied Physics*, 52(5R):055001, 2013.

[113] Keiichi Murai, Yoshinori Tokoi, Hisayuki Suematsu, Weihua Jiang, Kiyoshi Yatsui, and Koichi Niihara. Particle size controllability of ambient gas species for copper nanoparticles prepared by pulsed wire discharge. *Japanese Journal of Applied Physics*, 47(5R):3726, 2008.

[114] Kinemuchi Yoshiaki, Sato Kimiyasu, Koji Watari, Chuhyun Cho, Keiichi Murai, Suematsu Hisayuki, Weihua Jiang, and Kiyoshi Yatsui. Particle size distribution of $SnO_2$ nano-particles synthesized by pulsed wire discharge. *Journal of the Ceramic Society of Japan*, 112(1307):355–362, 2004.

[115] L Santhosh Kumar, SR Chakravarthi, R Sarathi, and R Jayaganthan. Thermodynamic modeling and characterizations of Al nanoparticles produced by electrical wire explosion process. *Journal of Materials Research*, 32(4):897, 2017.

[116] P Ranjan, DH Nguyen, L Chen, I Cotton, H Suematsu, SR Chakravarthy, R Jayaganthan, and R Sarathi. Dynamical aspects of nanoparticle formation by wire explosion process. *Nano Express*, 1(1):010049, 2020.

[117] Jun Bai, Zongqian Shi, and Shenli Jia. Numerical investigation on the growth process and size distribution of nanoparticles obtained through electrical explosion of aluminum wire. *Journal of Physics D: Applied Physics*, 50(7):075301, 2017.

[118] N. Svarovskaya, O Bakina, Alexander Pervikov, Konstantin Rubtsov, and Marat Lerner. Electrical explosion of wires for manufacturing bimetallic antibacterial Ti–Ag and Fe–Ag nanoparticles. *Russian Physics Journal*, 62:1580–1586, 01 2020.

[119] A.S. Lozhkomoev, S.O. Kazantsev, A.M. Kondranova, A.N. Fomenko, A.V. Pervikov, N.G. Rodkevich, and O.V. Bakina. Design of antimicrobial composite nanoparticles $Zn_xMe_{100\text{-}x}/o$ by electrical explosion of two wires in the oxygen-containing atmosphere. *Materials Design*, 183:108099, 2019.

[120] A. Lozhkomoev, Alexander Pervikov, S Kazantsev, Aliya Sharipova, Nikolay Rodkevich, Nikita Toropkov, Konstantin Suliz, N. Svarovskaya, Anastasiya Kondranova, and Marat Lerner. Synthesis of $Fe/Fe_3O_4$ core-shell nanoparticles by electrical explosion of the iron wire in an oxygen-containing atmosphere. *Journal of Nanoparticle Research*, 23:73, 03 2021.

[121] Kyungsun Song, Wonbaek Kim, Chang-Yul Suh, Dongbok Shin, Kyung-Seok Ko, and Kyoochul Ha. Magnetic iron oxide nanoparticles prepared by electrical wire explosion for arsenic removal. *Powder Technology*, 246:572–574, 09 2013.

[122] Young Il Song. Characterization and dispersion stabilities of multi-layer graphene-coated copper prepared by electrical wire-explosion method. 04 2016.

[123] Elseddik Abdelkader, Paul Jelliss, and Steven Buckner. Metal and metal carbide nanoparticle synthesis using electrical explosion of wires coupled with epoxide polymerization capping. *Inorganic chemistry*, 54, 05 2015.

[124] AV Bushman, VS Vorob'ev, VN Korobenko, AD Rakhel, AI Savvatimskii, and VE Fortov. Diamond production as a result of electrical explosions of graphite-

containing samples. *International journal of thermophysics*, 14(3):565–572, 1993.

[125] VG Ivanov, SN Leonov, OV Gavrilyuk, and VN Gerasimova. Self-propagating high-temperature synthesis of ultradisperse molybdenum disulfide. *Combustion, Explosion and Shock Waves*, 30(5):621–625, 1994.

[126] Yu A Kotov, IV Beketov, AM Murzakaev, OM Samatov, R Boehme, and G Schumacher. Synthesis of $Al_2O_3$, $TiO_2$ and $ZrO_2$ nanopowders by electrical explosion of wires. In *Materials Science Forum*, volume 225, pages 913–916. Trans Tech Publications Ltd., 1996.

[127] Alexander Petrovich Il'in, Olga Bronislavovna Nazarenko, and V Ya Ushakov. Formation of chemical compounds in the electrical explosion of metal wires in liquids. *Russian Physics Journal*, 39(6):510–513, 1996.

[128] Yu A Kotov, EI Azarkevich, IV Beketov, TM Demina, and AM Murzakaev. Producing Al and $Al_2O_3$ nanopowders by electrical explosion of wire. *Key Engineering Materials*, pages 173–176, 1997.

[129] VV Valevich and VS Sedoi. Producing highly disperse powder in fast electrical explosion. *Russian physics journal*, 41(6):569–574, 1998.

[130] Frederick Tepper. Metallic nanopowders produced by the electro-exploding wire process. *International journal of powder metallurgy (1986)*, 35(7):39–44, 1999.

[131] Yu A Kotov and OM Samatov. Production of nanometer-sized AlN powders by the exploding wire method. *Nanostructured materials*, 12(1-4):119–122, 1999.

[132] Qun Wang, Hai-Bin Yang, Wei-Li Guo, and Guang-Tian Zou. Characterization of Cu-Zn alloy nanocrystalline powders prepared by wire electrical explosion. *Chinese Physics Letters*, 17(2):145, 2000.

[133] Qun Wang, Haibin Yang, Jianlin Shi, and Guangtian Zou. One-step synthesis of the nanometer particles of $\gamma$-$Fe_2O_3$ by wire electrical explosion method. *Materials research bulletin*, 36(3-4):503–509, 2001.

[134] Yoshiaki Kinemuchi, Tadashi Ikeuchi, Tsuneo Suzuki, Hisayuki Suematsu, Weihua Jiang, and Kiyoshi Yatsui. Synthesis of nanosize PZT powders by pulsed wire discharge. *IEEE transactions on plasma science*, 30(5):1858–1862, 2002.

[135] Yoshiaki Kinemuchi, Kazuhiro Ishizaka, Hisayuki Suematsu, Weihua Jiang, and Kiyoshi Yatsui. Magnetic properties of nanosize $NiFe_2O_4$ particles synthesized by pulsed wire discharge. *Thin solid films*, 407(1-2):109–113, 2002.

[136] Yoshiaki Kinemuchi, Hiroshi Mouri, Tsuneo Suzuki, Hisayuki Suematsu, Weihua Jiang, and Kiyoshi Yatsui. Increase in phase transition temperature of activated alumina with nano-zirconia synthesized by pulsed wire discharge. *Journal of the American Ceramic Society*, 86(9):1522–1526, 2003.

[137] Yoshiaki Kinemuchi, Keiichi Murai, Channalong Sangurai, Chu-Hyun Cho, Hisayuki Suematsu, Weihua Jiang, and Kiyoshi Yatsui. Nanosize powders of aluminum nitride synthesized by pulsed wire discharge. *Journal of the American Ceramic Society*, 86(3):420–424, 2003.

[138] Hisayuki Suematsu, Chihiro Minami, Ryota Kobayashi, Yoshiaki Kinemuchi, Takamichi Hirata, Rikizo Hatakeyama, Sung-Chae Yang, Weihua Jiang, and Kiyoshi Yatsui. Preparation of fullerene by pulsed wire discharge. *Japanese journal of applied physics*, 42(8B):L1028, 2003.

[139] Young Soon Kwon, Alexander A Gromov, Alexander P Ilyin, Alexander A Ditts, Ji Soon Kim, Sang Ha Park, and Moon Hee Hong. Features of passivation, oxidation and combustion of tungsten nanopowders by air. *International Journal of Refractory Metals and Hard Materials*, 22(6):235–241, 2004.

[140] Yu A Kotov, AV Bagazeev, IV Beketov, AM Murzakaev, OM Samatov, AI Medvedev, NI Moskalenko, OR Timoshenkova, TM Demina, and AK Shtol'ts. Characteristics of nickel oxide nanopowders prepared by electrical explosion of a wire. *Glass Physics and Chemistry*, 31(4):477–481, 2005.

[141] Ryouta Kobayashi, Seigo Nishimura, Tsuneo Suzuki, Hisayuki Suematsu, Weihua Jiang, and Kiyoshi Yatsui. Synthesis of single-walled carbon nanotubes by pulsed wire discharge. *Japanese journal of applied physics*, 44(1S):742, 2005.

[142] Koji Suwa, Tsuneo Suzuki, Hisayuki Suematsu, Weihua Jiang, and Kiyoshi Yatsui. Synthesis of Fe-N nanosized powders by pulsed wire discharge. *Japanese journal of applied physics*, 44(1S):745, 2005.

[143] PY Lee, H Suematsu, W Jiang, and K Yatsui. Novel method to synthesize nanosized $ZnFe_2O_4$ powders. *Journal of the Ceramic Society of Japan*, 113(1322):663–665, 2005.

[144] Alexander Alexandrovich Gromov, Ulrich Förter-Barth, and Ulrich Teipel. Aluminum nanopowders produced by electrical explosion of wires and passivated by non-inert coatings: Characterisation and reactivity with air and water. *Powder technology*, 164(2):111–115, 2006.

[145] PY Lee, Hisayuki Suematsu, Weihua Jiang, Kiyoshi Yatsui, and Koichi Niihara. Synthesis of $Al_2O_3$–$ZrO_2$ nanocomposite powders by pulsed wire discharge. *IEEE transactions on plasma science*, 34(4):1190–1194, 2006.

[146] Wonbaek Kim, Je-shin Park, Chang-yul Suh, Jae-chun Lee, Junghwan Kim, and Yong-Jun Oh. A new method for the production of alloy nanoparticles by electrical wire explosion. *Materials transactions*, pages 0706180017–0706180017, 2007.

[147] YS Kwon, AP Ilyin, Dmitry Vladimirovich Tikhonov, GV Yablunovsky, and Vladimir Vilorievich An. Characteristics of nanopowders produced by wire electrical explosion of tinned copper conductor in argon. *Materials Letters*, 62(17-18):3143–3145, 2008.

[148] Wonbaek Kim, Je-shin Park, Chang-yul Suh, Jong-Gwan Ahn, and Jae-chun Lee. Cu–Ni–P alloy nanoparticles prepared by electrical wire explosion. *Journal of alloys and compounds*, 465(1-2):L4–L6, 2008.

[149] Yoshinori Tokoi, Tsuneo Suzuki, Tadachika Nakayama, Hisayuki Suematsu, Weihua Jiang, and Koichi Niihara. Synthesis of $TiO_2$ nanosized powder by pulsed wire discharge. *Japanese journal of applied physics*, 47(1S):760, 2008.

[150] Koji Suwa, Tadachika Nakayama, Tsuneo Suzuki, Hisayuki Suematsu, Weihua Jiang,

and Koichi Niihara. Synthesis of Ni–Cu nanoparticles by pulsed wire discharge and their compositional distribution. *Japanese Journal of Applied Physics*, 47(1S):775, 2008.

[151] Qi Qi, Tong Zhang, Yi Zeng, and Haibin Yang. Humidity sensing properties of KCl-doped cu–Zn/CuO–ZnO nanoparticles. *Sensors and Actuators B: Chemical*, 137(1):21–26, 2009.

[152] Yu A Kotov, IV Beketov, AI Medvedev, and OR Timoshenkova. Synthesizing aluminum nanoparticles in an oxide shell. *Nanotechnologies in Russia*, 4(5):354–358, 2009.

[153] Wonbaek Kim, Je-shin Park, Chang-yul Suh, Sung-wook Cho, and Sujeong Lee. Ti-Cr nanoparticles prepared by electrical wire explosion. *Materials transactions*, 50(9):2344–2346, 2009.

[154] Wonbaek Kim, Je-shin Park, Chang-yul Suh, Sung-wook Cho, Sujeong Lee, and In-Jin Shon. Synthesis of TiN nanoparticles by explosion of Ti wire in nitrogen gas. *Materials transactions*, 50(12):2897–2899, 2009.

[155] WH Goo, LH Bac, EJ Park, JS Kim, JC Kim, HS Jung, and HD Lee. Synthesis and characterization of nano-sized Zn powder by electrical explosion of wire in liquid. *Modern Physics Letters B*, 23(31n32):3903–3909, 2009.

[156] Forming a carbide coating on the surface of aluminum nanoparticles and producing nanopowders from Al-$Al_4C_3$ using the method of electric explosion of wire, author=Kotov, Yu A and Beketov, IV and Medvedev, AI and Murzakaev, AM and Timoshenkova, OP and Demina, TM, journal=Nanotechnologies in Russia, volume=5, number=11, pages=831–836, year=2010, publisher=Springer.

[157] Yoshinori Tokoi, Tsuneo Suzuki, Tadachika Nakayama, Hisayuki Suematsu, Futao Kaneko, and Koichi Niihara. Preparation of titanium nanopowders covered with organics by pulsed wire discharge. *Scripta Materialia*, 63(9):937–940, 2010.

[158] Yoshinori Tokoi, Tsuneo Suzuki, Tadachika Nakayama, Hisayuki Suematsu, Futao Kaneko, and Koichi Niihara. Synthesis of aluminum nitride nanopowder with particle size less than 10 nm by pulsed wire discharge in nitrogen gas. *Japanese Journal of Applied Physics*, 49(11R):116201, 2010.

[159] Eun Ju Park, Seung Won Lee, In Cheol Bang, and Hyung Wook Park. Optimal synthesis and characterization of Ag nanofluids by electrical explosion of wires in liquids. *Nanoscale research letters*, 6(1):1–10, 2011.

[160] Bac Luong, B.K. Kim, Ji Soon Kim, and J.C. Kim. Characteristics of Fe-Ni nanopowders prepared by electrical explosion of wire in water and ethanol. *Journal of Magnetics*, 1616435:435–439, 11 2011.

[161] Bac Luong, G Yun, Ji Soon Kim, Hanshin Choi, and J Kim. Preparation and stability of gold colloid by electrical explosion of wire in various media. *Journal of nanoscience and nanotechnology*, 11:1730–3, 02 2011.

[162] Aijie Liu, Bac Luong, Jin-Chun Kim, and Lizhu Liu. Preparation and characterization of polymer -copper composites by electrical explosion of wire. *Proceedings of the 6th International Forum on Strategic Technology, IFOST 2011*, 1, 08 2011.

[163] Yoshinori Tokoi, Takuya Orikawa, Tsuneo Suzuki, Tadachika Nakayama, Hisayuki Suematsu, and Koichi Niihara. Phase control of Ti–Fe nanoparticles prepared by pulsed wire discharge. *Japanese Journal of Applied Physics*, 50:01BJ06, 01 2011.

[164] A.P. Ilyin, O.B. Nazarenko, and D.V. Tikhonov. Synthesis and characterization of metal carbides nanoparticles produced by electrical explosion of wires. *Journal of Nanoscience and Nanotechnology*, 12(10):8137–8142, 2012. cited By 9.

[165] Satoru Ishihara, Tetsuya Koishi, Takuya Orikawa, Hisayuki Suematsu, Tadachika Nakayama, Tsuneo Suzuki, and Koichi Niihara. Synthesis of intermetallic NiAl compound nanoparticles by pulsed wire discharge of twisted Ni and Al wires. *Intermetallics*, 23:134–142, 04 2012.

[166] Dong-Woo Joh, Taek-Kyun Jung, Hyo-Soo Lee, and Do Hyang Kim. Synthesis of nanoparticles using electrical explosion of Ni wire in Pt solution. *Journal of nanoscience and nanotechnology*, 13:6092–4, 09 2013.

[167] Gyoung-Ja Lee, Chang-Kyu Kim, Lee Min Gu, and Chang Kyu Rhee. Facile synthesis of surface oxide free copper nanoparticles by in-situ coating with oleic acid. *Powder Technology*, 261:143–146, 07 2014.

[168] G. V. Kurlyandskaya, I. Madinabeitia, A. M. Murzakaev, M. B. Sanchez-Ilarduya, V. Beketov, A. I. Medvedev, A. Larrañaga, A. P. Safronov, and N. N. Schegoleva. Core-shell fine structure of feni magnetic nanoparticles produced by electrical explosion of wire. *IEEE Transactions on Magnetics*, 50(11):1–4, 2014.

[169] Lingfeng He, J. Shirahata, H. Suematsu, Tadachika Nakayama, Tomohiko Suzuki, Winnie Jiang, and Koichi Niihara. Synthesis of BN nanosheet/nanotube-Fe nanocomposites by pulsed wire discharge and high-temperature annealing. *Materials Letters*, 117:120–123, 02 2014.

[170] Elseddik M. Abdelkader, Paul A. Jelliss, and Steven W. Buckner. Synthesis of organically-capped metallic zinc nanoparticles using electrical explosion of wires (EEW) coupled with PIERMEN. *Materials Chemistry and Physics*, 149-150:238–245, 2015.

[171] Go Kawamura, Samuel Alvarez, Ian Stewart, Matthew Catenacci, Zuofeng Chen, and Yoon-Cheol Ha. Production of oxidation-resistant Cu-based nanoparticles by wire explosion. *Scientific reports*, 5:18333, 12 2015.

[172] Yasunobu Sato, Hisayuki Suematsu, R. Sarathi, Takashi Kikuchi, Toru Sasaki, Yoshinori Tokoi, Tsuneo Suzuki, Tadachika Nakayama, and Koichi Niihara. Preparation of palladium nanoparticles and a grain-size determining equation of pulsed wire discharge in $N_2$ , Ar, and He ambient gasses. *Japanese Journal of Applied Physics*, 54:045002, 04 2015.

[173] Marat Lerner, Alexander Pervikov, Elena Glazkova, N. Svarovskaya, A. Lozhkomoev, and Sergey Psakhie. Structures of binary metallic nanoparticles produced by electrical explosion of two wires from immiscible elements. *Powder Technology*, 288:371–378, 01 2016.

[174] M. Shoushtari, C. Nezhad, and Kobra Omidfar. Fabrication and optical properties of Ag-Au alloy nanoparticles. *Indian Journal of Science and Technology*, 9, 03 2016.

[175] Q. Wang, M. Guo, and Chunlong Li. Rapid fabrication and characterization of spherical mumetal nanoparticles by an electrical wire explosion process. *Integrated Ferroelectrics*, 172:49 – 58, 2016.

[176] Elseddik Abdelkader, Paul Jelliss, and Steven Buckner. Main group nanoparticle synthesis using electrical explosion of wires. *Nano-Structures Nano-Objects*, 7:23–31, 07 2016.

[177] Xin Gao, Peng Chen, Xiao Wang, Chun Xu, Qiu Song, and Hao Yin. Production of AlN nanopowders by electrical wire explosion in liquid nitrogen. *Materials Science Forum*, 910:46–51, 01 2018.

[178] Kenta Sugashima, Kazuma Suzuki, Tomohiko Suzuki, Tadachika Nakayama, Hisayuki Suematsu, and Koichi Niihara. Synthesis of zirconium carbide nanosized powders by pursed wire discharge in oleic acid. *Journal of the Korean Physical Society*, 68:345–350, 01 2016.

[179] Jong Kim, Dae Kim, Hisayuki Suematsu, and Bong Ryu. Synthesis of three-component nanoparticles using Sn–58Bi and Cu wires by the pulsed wire discharge method. *Japanese Journal of Applied Physics*, 55:116203, 11 2016.

[180] Bakina, Elena Glazkova, N. Svarovskaya, Marat Lerner, Matvei Korovin, and Alla Fomenko. Synthesis and characterization of electro-explosive magnetic nanoparticles for biomedical applications. volume 1882, page 020004, 09 2017.

[181] Seyed Mojtaba Seyedi, Hesamoddin Rabiee, Seyed Mahdi Seyed Shahabadi, and Seyed Mehdi Borghei. Synthesis of zero-valent iron nanoparticles via electrical wire explosion for efficient removal of heavy metals. *CLEAN – Soil, Air, Water*, 45(3):1600139, 2017.

[182] Hisayuki Suematsu, Kenta Tanaka, Kenta Sugashima, Tsuneo Suzuki, Tadachika Nakayama, and Koichi Niihara. Preparation of mg submicron particles by pulsed wire discharge. *Journal of the Society of Powder Technology, Japan*, 54(8):514–518, 2017.

[183] Do Van Lam, Hisayuki Suematsu, and Toru Ogawa. Characterization of ZrN, $ZrO_2$ and $\beta$–$Zr_7O_{11}N_2$ nanoparticles synthesized by pulsed wire discharge. *Journal of the American Ceramic Society*, 100(10):4884–4892, 2017.

[184] A. Lozhkomoev, Alexander Pervikov, Bakina Olga, Kazantsev Sergey, and Gotman Irena. Synthesis of antimicrobial AlOOH–Ag composite nanostructures by water oxidation of bimetallic Al–Ag nanoparticles. *RSC Advances*, 8:36239–36244, 10 2018.

[185] E. A. Glazkova, A. V. Pervikov, N. G. Rodkevich, A. S. Apkaryan, and S. Yu. Muzhetskaya. Sintering of W-Ni-Fe powders produced by electrical explosion of wires. *AIP Conference Proceedings*, 2053(1):040027, 2018.

[186] Xin Gao, Naoaki Yokota, Hayato Oda, Shigeru Tanaka, Kazuyuki Hokamoto, and Pengwan Chen. One step preparation of Fe–FeO–Graphene nanocomposite through pulsed wire discharge. *Crystals*, 8(2), 2018.

[187] A. Pervikov, A. Lozhkomoev, O. Bakina, and M. Lerner. Synthesis of core-shell and janus-like nanoparticles by non-synchronous electrical explosion of two intertwined wires from immiscible metals. *Solid State Sciences*, 87:146–149, 2019.

[188] Alexander Pervikov, A. Lozhkomoev, Edgar Dvilis, Mark Kalashnikov, Vladimir Paygin, Oleg Khasanov, and Marat Lerner. Synthesis of W-Cu composite nanoparticles by the electrical explosion of two wires and their consolidation by spark plasma sintering. *Materials Research Express*, 6:1265i9, 02 2020.

[189] Bakina, Elena Glazkova, N. Svarovskaya, Nikolay Rodkevich, and Marat Lerner. ≪janus≫-like Cu-Fe bimetallic nanoparticles with high antibacterial activity. *Materials Letters*, 242, 05 2019.

[190] Neelmani, Jayaganthan Rengaswamy, Chakravarthi Satyanarayanan Raghuraman, Suematsu Hisayuki, and Sarathi Ramanujam. Enhancement of hydrogen generation using nanoaluminum particles produced by a wire explosion process. *IEEJ Transactions on Electrical and Electronic Engineering*, 14(6):810–818, 2019.

[191] Anastasiya Kondranova, A. Lozhkomoev, S. Kazantsev, Alexander Pervikov, Alla Fomenko, and Bakina. Production and properties of composite nanoparticles ($Cu_xMe_{1-x}$)o. volume 2167, page 020168, 11 2019.

[192] Prem Ranjan, Duy Nguyen, Kenta Tanaka, H. Suematsu, Jayaganthan Rengaswamy, and R. Sarathi. Synthesis, characterisation and formation mechanism of Sn-0.75 Cu solder nanoparticles by pulsed wire discharge. *Applied Nanoscience*, 9, 11 2018.

[193] Chu Ngo, Hieu Nguyen, Dzung Do, Ramanujam Sarathi, Tadachika Nakayama, and Hisayuki Suematsu. Synthesis of molybdenum carbide nanoparticles using pulsed wire discharge in mixed atmosphere of kerosene and argon. *Journal of the American Ceramic Society*, 102, 06 2019.

[194] L.Santhosh Kumar, S.R. Chakravarthy, Raviraj Verma, R. Jayaganthan, R. Sarathi, and A. Srinivasan. Synthesis of multiphase binary eutectic Al–Mg alloy-nanoparticles by electrical wire explosion technique for high-energy applications, its characterisation and size-dependent thermodynamic and kinetic study. *Journal of Alloys and Compounds*, 838:155630, 2020.

[195] Ngo Chu, Nguyen Hieu, Dung Do, Tadachika Nakayama, Koichi Niihara, and Hisayuki Suematsu. Synthesis of metastable monoclinic beta molybdenum trioxide nanoparticles by pulsed wire discharge. *Japanese Journal of Applied Physics*, 59:SCCC02, 02 2020.

[196] Xin Gao, Kun Huang, Zhen Tan, Bi Wang, Qiuzhi Song, Qi Chen, and Pengwan Chen. Formation of nanodiamond by pulsed discharge of carbon fiber wires. *Applied Physics Letters*, 117(8):081902, 2020.

[197] Yoshinori Tokoi, Tsuneo Suzuki, Tadachika Nakayama, Hisayuki Suematsu, Weihua Jiang, and Koichi Niihara. Effect of wire diameter on particle size of metal nanosized powder prepared by pulsed wire discharge. *Journal of the Japan Society of Powder and Powder Metallurgy*, 55(3):192–197, 2008.

[198] A Meesters and MH Ernst. Numerical evaluation of self-preserving spectra in Smoluchowski's coagulation theory. *Journal of colloid and interface science*, 119(2):576–587, 1987.

[199] Menachem Elimelech, John Gregory, and Xiadong Jia. *Particle deposition and aggregation: measurement, modelling and simulation.* Butterworth-Heinemann, 2013.

[200] David L Swift and S_K_ Friedlander. The coagulation of hydrosols by Brownian motion and laminar shear flow. *Journal of colloid science*, 19(7):621–647, 1964.

[201] KW Lee. Change of particle size distribution during Brownian coagulation. *Journal of Colloid and Interface Science*, 92(2):315–325, 1983.

[202] KW Lee. Conservation of particle size distribution parameters during Brownian coagulation. *Journal of colloid and interface science*, 108(1):199–206, 1985.

[203] SK Friedlander and CS Wang. The self-preserving particle size distribution for coagulation by Brownian motion. *Journal of Colloid and interface Science*, 22(2):126–132, 1966.

[204] KW Lee, LA Curtis, and H Chen. An analytic solution to free molecule aerosol coagulation. *Aerosol science and technology*, 12(2):457–462, 1990.

[205] Tianran Zhang, Zhanliang Tao, and Jun Chen. Magnesium–air batteries: from principle to application. *Materials Horizons*, 1(2):196–206, 2014.

[206] Liwen F Wan, Yi-Sheng Liu, Eun Seon Cho, Jason D Forster, Sohee Jeong, Hsiao-Tsu Wang, Jeffrey J Urban, Jinghua Guo, and David Prendergast. Atomically thin interfacial suboxide key to hydrogen storage performance enhancements of magnesium nanoparticles encapsulated in reduced graphene oxide. *Nano letters*, 17(9):5540–5545, 2017.

[207] Ming Chen, Xiubo Xie, Peng Liu, and Tong Liu. Facile fabrication of ultrathin carbon layer encapsulated air-stable Mg nanoparticles with enhanced hydrogen storage properties. *Chemical Engineering Journal*, 337:161–168, 2018.

[208] Luca Pasquini, Elsa Callini, Emanuela Piscopiello, Amelia Montone, Torben René Jensen, Marco Vittori Antisari, and Ennio Bonetti. Hydrogen sorption in magnesium nanoparticles: Size-and surface-related phenomena. *MRS Online Proceedings Library Archive*, 1216, 2009.

[209] Taishi Fujimoto, Satoshi Ogawa, Tomomi Kanai, Naoki Uchiyama, Tomoko Yoshida, and Shinya Yagi. Hydrogen storage property of materials composed of Mg nanoparticles and Ni nanoparticles fabricated by gas evaporation method. *International Journal of Hydrogen Energy*, 40(35):11890–11894, 2015.

[210] Yana Liu, Jinglian Zhu, Zhibing Liu, Yunfeng Zhu, Jiguang Zhang, and Liquan Li. Magnesium nanoparticles with Pd decoration for hydrogen storage. *Frontiers in chemistry*, 7:949, 2020.

[211] Xiubo Xie, Xiujuan Ma, Peng Liu, Jiaxiang Shang, Xingguo Li, and Tong Liu. Formation of multiple-phase catalysts for the hydrogen storage of Mg nanoparticles by adding flowerlike NiS. *ACS applied materials & interfaces*, 9(7):5937–5946, 2017.

[212] John S Biggins, Sadegh Yazdi, and Emilie Ringe. Magnesium nanoparticle plasmonics. *Nano letters*, 18(6):3752–3758, 2018.

[213] Emilie Ringe. Shapes, plasmonic properties, and reactivity of magnesium nanoparticles. *The Journal of Physical Chemistry C*, 124(29):15665–15679, 2020.

[214] Masahiro Uda, Hideo Okuyama, Tohru S Suzuki, and Yoshio Sakka. Hydrogen gen-

eration from water using mg nanopowder produced by arc plasma method. *Science and Technology of Advanced Materials*, 2012.

[215] Xianguo Liu, Niandu Wu, Caiyun Cui, Yongtao Li, Pingping Zhou, and Nannan Bi. Facile preparation of carbon-coated Mg nanocapsules as light microwave absorber. *Materials Letters*, 149:12–14, 2015.

[216] Gang Ho Lee and Jeong-Tae Kim. *Ultrasmall lanthanide oxide nanoparticles for biomedical imaging and therapy.* Woodhead Publishing, 2014.

[217] Bung Uk Yoo, Hayk H Nersisyan, Hong Youl Ryu, Jin Seok Lee, and Jong Hyeon Lee. Structural and thermal properties of boron nanoparticles synthesized from $B_2O_3$+ 3Mg+ kNaCl mixture. *Combustion and flame*, 161(12):3222–3228, 2014.

[218] Hayk H Nersisyan, Sin Hyong Joo, Bung Uk Yoo, Young Hee Cho, Hong Moule Kim, and Jong-Hyeon Lee. Melt-assisted solid flame synthesis approach to amorphous boron nanoparticles. *Combustion and Flame*, 162(9):3316–3323, 2015.

[219] Meijie Du and Gang Li. Preparation of silane-capped boron nanoparticles with enhanced dispersibility in hydrocarbon fuels. *Fuel*, 194:75–82, 2017.

[220] Fateme Sadat Shariatmadar and Shahram Ghanbari Pakdehi. Synthesis and characterization of aviation turbine kerosene nanofluid fuel containing boron nanoparticles. *Energy & Fuels*, 30(9):7755–7762, 2016.

[221] Wazir Akbar, Mohamed Radzi Noor, Katarzyna Kowal, Tofail Syed, Tewfik Soulimane, and G Bahar Basim. Characterization and antibacterial properties of nanoboron powders and nanoboron powder coated textiles. *Advanced Powder Technology*, 28(2):596–610, 2017.

[222] Prodromos Chatzispyroglou, Joseph L Keddie, and Paul J Sellin. Boron-loaded polymeric sensor for the direct detection of thermal neutrons. *ACS Applied Materials & Interfaces*, 12(29):33050–33057, 2020.

[223] SA Uspenskii, PA Khaptakhanova, AA Zaboronok, TS Kurkin, O Yu Volkova, LV Mechetina, AV Taranin, VV Kanygin, Matsumura Akira, and S Yu Taskaev. Elemental boron nanoparticles: Production by ultrasonication in aqueous medium and application in boron neutron capture therapy. In *Doklady Chemistry*, volume 491, pages 45–48. Springer, 2020.

[224] L Liu, Y Tanoue, T Nonaka, M Tanaka, and T Watanabe. Synthesis of transition metal boride nanoparticles by induction thermal plasma.

[225] Jinhua Zhang, Si Xiong, Jingran Wang, Yue'e Ni, and Changming Ke. Silicothermic synthesis of phase-pure $HfB_2$ fine powder. *Journal of the American Ceramic Society*, 104(2):785–792, 2021.

[226] Jeong-Hwan Oh, Minseok Kim, Yong Hee Lee, Seung-Hyun Hong, Sung Sil Park, Tae-Hee Kim, and Sooseok Choi. Synthesis of cobalt boride nanoparticles and h-BN nanocage encapsulation by thermal plasma. *Ceramics International*, 46(18):28792–28799, 2020.

[227] Gregory Young, Haiyang Wang, and Michael R Zachariah. Application of nano-aluminum/nitrocellulose mesoparticles in composite solid rocket propellants. *Pro-*

*pellants, Explosives, Pyrotechnics*, 40(3):413–418, 2015.

[228] Jiang Yu, Tonya N Jensen, William K Lewis, Christopher E Bunker, Steven P Kelley, Robin D Rogers, Owen M Pryor, Steven D Chambreau, Ghanshyam L Vaghjiani, and Scott L Anderson. Combustion behavior of high energy density borane–aluminum nanoparticles in hypergolic ionic liquids. *Energy & Fuels*, 32(7):7898–7908, 2018.

[229] Chengdong Kong, Qiang Yao, Dan Yu, and Shuiqing Li. Combustion characteristics of well-dispersed aluminum nanoparticle streams in post flame environment. *Proceedings of the Combustion Institute*, 35(2):2479–2486, 2015.

[230] Yong Tang, Chengdong Kong, Yichen Zong, Shuiqing Li, Jiankun Zhuo, and Qiang Yao. Combustion of aluminum nanoparticle agglomerates: From mild oxidation to microexplosion. *Proceedings of the Combustion Institute*, 36(2):2325–2332, 2017.

[231] Miles C Rehwoldt, Haiyang Wang, Dylan J Kline, Tao Wu, Noah Eckman, Peng Wang, Niti R Agrawal, and Michael R Zachariah. Ignition and combustion analysis of direct write fabricated aluminum/metal oxide/PVDF films. *Combustion and Flame*, 211:260–269, 2020.

[232] Florin Saceleanu, John Z Wen, Mahmoud Idir, and Nabiha Chaumeix. Laser-assisted ignition and combustion characteristics of consolidated aluminum nanoparticles. *Journal of Nanoparticle Research*, 18(11):1–15, 2016.

[233] Vladimir B Storozhev and Alexander N Yermakov. Activation of aluminum nanopowder combustion in water vapor by $O_2$ additions. *Combustion and Flame*, 200:82–84, 2019.

[234] Xiangrui Zou, Ningfei Wang, Junlong Wang, Ying Feng, and Baolu Shi. A numerical investigation on heterogeneous combustion of aluminum nanoparticle clouds. *Aerospace Science and Technology*, 112:106604, 2021.

[235] Junais Habeeb Mokkath. Ultraviolet plasmon resonance in transition-metal doped aluminum nanoparticle arrays. *Journal of Materials Chemistry C*, 6(9):2225–2228, 2018.

[236] Y Ekinci, HH Solak, and Jörg F Löffler. Plasmon resonances of aluminum nanoparticles and nanorods. *Journal of Applied Physics*, 104(8):083107, 2008.

[237] Xinyuan Chong, Naibo Jiang, Zhili Zhang, Sukesh Roy, and James R Gord. Plasmonic resonance-enhanced local photothermal energy deposition by aluminum nanoparticles. *Journal of nanoparticle research*, 15(6):1–10, 2013.

[238] Jiang Yu, Brandon W McMahon, Jerry A Boatz, and Scott L Anderson. Aluminum nanoparticle production by acetonitrile-assisted milling: effects of liquid-vs vapor-phase milling and of milling method on particle size and surface chemistry. *The Journal of Physical Chemistry C*, 120(35):19613–19629, 2016.

[239] Abazar Hajnorouzi and Reza Afzalzadeh. A novel technique to generate aluminum nanoparticles utilizing ultrasound ablation. *Ultrasonics sonochemistry*, 58:104655, 2019.

[240] Vyacheslav V Kim, Dmitry S Ivanov, Rashid A Ganeev, Mottamchetty Venkatesh, Ganjaboy S Boltaev, Martin E Garcia, Baerbel Rethfeld, and Chunlei Guo. Alu-

minum nanoparticle plasma formation for high-order harmonic generation. *Journal of Physics B: Atomic, Molecular and Optical Physics*, 52(24):245601, 2019.

[241] Anaram Shahravan, Tapan Desai, and Themis Matsoukas. Passivation of aluminum nanoparticles by plasma-enhanced chemical vapor deposition for energetic nanomaterials. *ACS applied materials & interfaces*, 6(10):7942–7947, 2014.

[242] RM More, KH Warren, DA Young, and GB Zimmerman. A new quotidian equation of state (QEOS) for hot dense matter. *The Physics of fluids*, 31(10):3059–3078, 1988.

[243] ASM International. Handbook Committee. *Engineered Materials Handbook: Ceramics and glasses*, volume 4. CRC, 1991.

[244] B Basu, GB Raju, and AK Suri. Processing and properties of monolithic $TiB_2$ based materials. *International materials reviews*, 51(6):352–374, 2006.

[245] TSR Ch Murthy, R Balasubramaniam, B Basu, AK Suri, and MN Mungole. Oxidation of monolithic $TiB_2$ and $TiB_2$–20 wt.% $MoSi_2$ composite at 850° C. *Journal of the European Ceramic Society*, 26(1-2):187–192, 2006.

[246] Ronald G Munro. Material properties of titanium diboride. *Journal of Research of the National institute of standards and Technology*, 105(5):709, 2000.

[247] TSR Ch Murthy, B Basu, R Balasubramaniam, AK Suri, C Subramanian, and RK Fotedar. Processing and properties of $TiB_2$ with $MoSi_2$ sinter-additive: a first report. *Journal of the American Ceramic Society*, 89(1):131–138, 2006.

[248] Weimin Wang, Zhengyi Fu, Hao Wang, and Runzhang Yuan. Influence of hot pressing sintering temperature and time on microstructure and mechanical properties of $TiB_2$ ceramics. *Journal of the European Ceramic Society*, 22(7):1045–1049, 2002.

[249] Asit Kumar Khanra, Mahadev Malhar Godkhindi, and Lokesh Chandra Pathak. Comparative studies on sintering behavior of self-propagating high-temperature synthesized ultra-fine titanium diboride powder. *Journal of the American Ceramic Society*, 88(6):1619–1621, 2005.

[250] A Rabiezadeh, AM Hadian, and A Ataie. Synthesis and sintering of $TiB_2$ nanoparticles. *Ceramics International*, 40(10):15775–15782, 2014.

[251] CTSR Subramanian, TSR Ch Murthy, and AK Suri. Synthesis and consolidation of titanium diboride. *International Journal of Refractory Metals and Hard Materials*, 25(4):345–350, 2007.

[252] Amartya Mukhopadhyay, GB Raju, Bikramjit Basu, and AK Suri. Correlation between phase evolution, mechanical properties and instrumented indentation response of $TiB_2$-based ceramics. *Journal of the European Ceramic Society*, 29(3):505–516, 2009.

[253] ZH Zhang, XB Shen, FC Wang, SK Lee, and L Wang. Densification behavior and mechanical properties of the spark plasma sintered monolithic $TiB_2$ ceramics. *Materials Science and Engineering: A*, 527(21-22):5947–5951, 2010.

[254] Mettaya Kitiwan, Akihiko Ito, and Takashi Goto. Densification and microstructure

of monolithic TiN and $TiB_2$ fabricated by spark plasma sintering. In *Key Engineering Materials*, volume 508, pages 38–41. Trans Tech Publ, 2012.

[255] Ahmet Turan, Filiz Cinar Sahin, Gultekin Goller, and Onuralp Yucel. Spark plasma sintering of monolithic $TiB_2$ ceramics. *J. Ceram. Process. Res*, 15(6):464–468, 2014.

[256] D Demirskyi, J Cheng, D Agrawal, and A Ragulya. Densification and grain growth during microwave sintering of titanium diboride. *Scripta Materialia*, 69(8):610–613, 2013.

[257] Özge Balcı, Ulrich Burkhardt, Marcus Schmidt, Jürgen Hennicke, M Barış Yağcı, and Mehmet Somer. Densification, microstructure and properties of $TiB_2$ ceramics fabricated by spark plasma sintering. *Materials Characterization*, 145:435–443, 2018.

[258] Amartya Mukhopadhyay, T Venkateswaran, and Bikramjit Basu. Spark plasma sintering may lead to phase instability and inferior mechanical properties: a case study with $TiB_2$. *Scripta Materialia*, 69(2):159–164, 2013.

[259] Edoardo Giorgi, Salvatore Grasso, Eugenio Zapata-Solvas, and William Edward Lee. Reactive carbothermal reduction of zrc and zroc using spark plasma sintering. *Advances in Applied Ceramics*, 117(sup1):s34–s47, 2018.

[260] H Okamoto. O-ti (oxygen-titanium). *Journal of Phase Equilibria and Diffusion*, 32(5):473–474, 2011.

[261] Richard B Kaner, John J Gilman, and Sarah H Tolbert. Designing superhard materials. *Science*, 308(5726):1268–1269, 2005.

[262] Reza Mohammadi, Andrew T Lech, Miao Xie, Beth E Weaver, Michael T Yeung, Sarah H Tolbert, and Richard B Kaner. Tungsten tetraboride, an inexpensive superhard material. *Proceedings of the National Academy of Sciences*, 108(27):10958–10962, 2011.

[263] A Chretien and Helgorsk. J. Sur les borures de molybdene et de tungstene $MoB_4$ et $WB_4$, composes nouveaux. *COMPTES RENDUS HEBDOMADAIRES DES SEANCES DE L ACADEMIE DES SCIENCES*, 252(5):742, 1961.

[264] PA Romans and MP Krug. Composition and crystallographic data for the highest boride of tungsten. *Acta Crystallographica*, 20(2):313–315, 1966.

[265] X-Y Cheng, X-Q Chen, D-Z Li, and Y-Y Li. Computational materials discovery: the case of the W–B system. *Acta Crystallographica Section C: Structural Chemistry*, 70(2):85–103, 2014.

[266] Andrew T Lech, Christopher L Turner, Reza Mohammadi, Sarah H Tolbert, and Richard B Kaner. Structure of superhard tungsten tetraboride: A missing link between $MB_2$ and $MB_{12}$ higher borides. *Proceedings of the National Academy of Sciences*, 112(11):3223–3228, 2015.

[267] Alexander G Kvashnin, Dmitry V Rybkovskiy, Vladimir P Filonenko, Vasilii I Bugakov, Igor P Zibrov, Vadim V Brazhkin, Artem R Oganov, Andrey A Osiptsov, and Artem Ya Zakirov. $WB_{5\text{-}x}$: Synthesis, properties, and crystal structure—new insights into the long-debated compound. *Advanced Science*, 7(16):2000775, 2020.

[268] Georgiy Akopov, Michael T Yeung, Christopher L Turner, Reza Mohammadi, and Richard B Kaner. Extrinsic hardening of superhard tungsten tetraboride alloys with group 4 transition metals. *Journal of the American Chemical Society*, 138(17):5714–5721, 2016.

[269] Elizabeth M Carnicom, Judyta Strychalska-Nowak, Piotr Wiśniewski, Dariusz Kaczorowski, Weiwei Xie, Tomasz Klimczuk, and Robert J Cava. Superconductivity in the superhard boride $WB_{4.2}$. *Superconductor Science and Technology*, 31(11):115005, 2018.

[270] Qiang Tao, Dafang Zheng, Xueping Zhao, Yanli Chen, Quan Li, Qian Li, Changchun Wang, Tian Cui, Yanming Ma, Xin Wang, et al. Exploring hardness and the distorted sp2 hybridization of B–B bonds in $WB_3$. *Chemistry of Materials*, 26(18):5297–5302, 2014.

[271] Ke Ma, Xiaozhou Cao, He Yang, and Xiangxin Xue. Formation of metastable tungsten tetraboride by reactive hot-pressing. *Ceramics International*, 43(12):8551–8555, 2017.

[272] Ke Ma, Xiaozhou Cao, Tao Jiang, He Yang, and Xiangxin Xue. In situ synthesis, mechanical properties, and microstructure of reactively hot pressed $WB_4$ ceramic with Ni as a sintering additive. *Ceramics International*, 44(16):19442–19450, 2018.

[273] Ying Long, Zong Wu, Xin Zheng, Hua-Tay Lin, and Fenglin Zhang. Mechanochemical synthesis and annealing of tungsten di-and tetra-boride. *Journal of the American Ceramic Society*, 103(2):831–838, 2020.

[274] Dariusz Garbiec, Maria Wiśniewska, Rafał Psiuk, Piotr Denis, Neonila Levintant-Zayonts, Volf Leshchynsky, Rafał Rubach, and Tomasz Mościcki. Zirconium alloyed tungsten borides synthesized by spark plasma sintering. *Archives of Civil and Mechanical Engineering*, 21(1):1–15, 2021.

[275] T Moscicki, Joanna Radziejewska, Jacek Hoffman, Justyna Chrzanowska, Neonila Levintant-Zayonts, Dariusz Garbiec, and Z Szymanski. $WB_2$ to $WB_3$ phase change during reactive spark plasma sintering and pulsed laser ablation/deposition processes. *Ceramics International*, 41(7):8273–8281, 2015.

[276] LG Bodrova, MS Koval'Chenko, and TI Serebryakova. Preparation of tungsten tetraboride. *Soviet Powder Metallurgy and Metal Ceramics*, 13(1):1–3, 1974.

[277] H Itoh, T Matsudaira, S Naka, H Hamamoto, and M Obayashi. Formation process of tungsten borides by solid state reaction between tungsten and amorphous boron. *Journal of materials science*, 22(8):2811–2815, 1987.

[278] Zong Wu, Ying Long, Hua-Tay Lin, and Fenglin Zhang. Effect of tantalum on phase transition and thermal stability of metastable tungsten tetra-boride. *Ceramics International*, 46(11):17217–17223, 2020.

[279] J Zemann. Crystal structures, vol. 1 by RWG Wyckoff. *Acta Crystallographica*, 18(1):139–139, 1965.

[280] JS Gillespie Jr. Crystallization of massive amorphous boron. *Journal of the American Chemical Society*, 88(11):2423–2425, 1966.

[281] Akira Katagiri, Minoru Suzuki, and Zen-ichiro Takehara. Electrodeposition of tungsten in $ZnBr_2$-NaBr and $ZnCl_2$-NaCl melts. *Journal of The Electrochemical Society*, 138(3):767, 1991.

[282] JL Murray, PK Liao, and KE Spear. The B-Ti (boron-titanium) system. *Bulletin of Alloy Phase Diagrams*, 7(6):550–555, 1986.

[283] KE Spear and PK Liao. The B-Mo (boron-molybdenum) system. *Bulletin of Alloy Phase Diagrams*, 9(4):457–466, 1988.

[284] KI Portnoi, VM Romashov, Yu V Levinskii, and IV Romanovich. Phase diagram of the system tungsten-boron. *Soviet Powder Metallurgy and Metal Ceramics*, 6(5):398–402, 1967.

[285] E Rudy. Ternary phase equilibria in transition metal-boron-carbon-silicon systems. part i. related binary systems. volume 8. systems Mo-B and W-B. Technical report, AEROJET-GENERAL CORP SACRAMENTO CA MATERIALS RESEARCH LAB, 1966.

[286] Michael Frotscher, Wilhelm Klein, Joseph Bauer, Chang-Ming Fang, Jean-Franois Halet, Anatoliy Senyshyn, Carsten Baehtz, and Barbara Albert. $M_2B_5$ or $m_2b_4$? a reinvestigation of the Mo/B and W/B system. *Zeitschrift für anorganische und allgemeine Chemie*, 633(15):2626–2630, 2007.

[287] P Rogl and PE Potter. A critical review and thermodynamic calculation of the binary system: Zirconium-boron. *Calphad*, 12(2):191–204, 1988.

[288] Stephen R Shatynski. The thermochemistry of transition metal carbides. *Oxidation of Metals*, 13(2):105–118, 1979.

[289] Yan-feng Li, Hui Xu, Qing-lin Xia, and Xiao-liang Liu. First-principles calculation of structural and thermodynamic properties of titanium boride. *Journal of Central South University of Technology*, 18(6):1773–1779, 2011.

[290] Wei-Ming Guo, Li-Xiang Wu, Yang You, Hua-Tay Lin, and Guo-Jun Zhang. Three-step reactive hot pressing of $B_4C$-$ZrB_2$ ceramics. *Journal of the European Ceramic Society*, 36(4):951–957, 2016.

[291] H Duschanek and Po Rogl. Critical assessment and thermodynamic calculation of the binary system boron-tungsten (BW). *Journal of phase equilibria*, 16(2):150–161, 1995.

[292] Mari-Ann Einarsrud, Eirik Hagen, Gunnar Pettersen, and Tor Grande. Pressureless sintering of titanium diboride with nickel, nickel boride, and iron additives. *Journal of the American Ceramic Society*, 80(12):3013–3020, 1997.

[293] Hamed Heidari, Houshang Alamdari, Dominique Dubé, and Robert Schulz. Interaction of molten aluminum with porous $TiB_2$-based ceramics containing Ti-Fe additives. *Journal of the European Ceramic Society*, 32(4):937–945, 2012.

[294] Ning Wu, Fengdan Xue, Qiumin Yang, Hailin Yang, and Jianming Ruan. Microstructure and mechanical properties of $TiB_2$-based composites with high volume fraction of Fe-Ni additives prepared by vacuum pressureless sintering. *Ceramics International*, 43(1):1394–1401, 2017.

[295] AK Khanra and MM Godkhindi. Effect of Ni additives on pressureless sintering of SHS $ZrB_2$. *Advances in applied ceramics*, 104(6):273–276, 2005.

[296] Suman Kumari Mishra, Swapan Kumar Das, Ajoy Kumar Ray, and P Ramachandrarao. Effect of Fe and Cr addition on the sintering behavior of $ZrB_2$ produced by self-propagating high-temperature synthesis. *Journal of the American Ceramic Society*, 85(11):2846–2848, 2002.

[297] Anna Dychalska, Piotr Popielarski, Wojciech Franków, Kazimierz Fabisiak, Kazimierz Paprocki, and Mirosław Szybowicz. Study of CVD diamond layers with amorphous carbon admixture by Raman scattering spectroscopy. *Materials Science-Poland*, 33(4):799–805, 2015.

[298] R Sarathi, TK Sindhu, and SR Chakravarthy. Generation of nano aluminium powder through wire explosion process and its characterization. *Materials Characterization*, 58(2):148–155, 2007.

[299] James D Landgrebe and Sotiris E Pratsinis. Gas-phase manufacture of particulates: interplay of chemical reaction and aerosol coagulation in the free-molecular regime. *Industrial & engineering chemistry research*, 28(10):1474–1481, 1989.

[300] Kenta Tanaka, Nguyen Duy Hieu, Tsuneo Suzuki, Tadachika Nakayama, Hisayuki Suematsu, and Koichi Niihara. Preparation of Mg nanoparticles by pulsed wire discharge in mineral oil. *Nanoscience and Nanotechnology Letters*, 10(5-6):858–861, 2018.

[301] Paul-Henri Haumesser. *Nucleation and growth of metals: from thin films to nanoparticles.* Elsevier, 2016.

[302] Barbara E Wyslouzil and Judith Wölk. Overview: Homogeneous nucleation from the vapor phase—the experimental science. *The Journal of chemical physics*, 145(21):211702, 2016.

[303] Eric A Brandes and GB Brook. *Smithells metals reference book.* Elsevier, 2013.

[304] Antonios E Vlastós. Current pause in exploding-wire discharges. *Journal of Applied Physics*, 38(13):4993–4998, 1967.

[305] Antonios E Vlastós. Restrike mechanisms of exploding wire discharges. *Journal of Applied Physics*, 39(7):3081–3087, 1968.

[306] CS Wong, B Bora, SL Yap, YS Lee, H Bhuyan, and M Favre. Effect of ambient gas species on the formation of Cu nanoparticles in wire explosion process. *Current Applied Physics*, 12(5):1345–1348, 2012.

[307] Tsuneo Suzuki, Komson Keawchai, Weihua Jiang, and Kiyoshi Yatsui. Nanosize al2o3 powder production by pulsed wire discharge. *Japanese Journal of Applied Physics*, 40(2S):1073, 2001.

[308] W Muller. Studies of exploding wire phenomenon by use of kerr cell shlieren photography. *Exploding Wires*, 1:186–193, 1959.

[309] FD Bennett. Flow fields produced by exploding wires. Technical report, ARMY BALLISTIC RESEARCH LAB ABERDEEN PROVING GROUND MD, 1959.

[310] FREDERICK D Bennett. Cylindrical shock waves from exploding wires. *The Physics of Fluids*, 1(4):347–352, 1958.

[311] Donald L Jones and Roger M Gallet. Microwave doppler measurements of the ionization front in cylindrical shock waves from exploding wires. In *Exploding Wires*, pages 127–144. Springer, 1962.

[312] Geoffrey Ingram Taylor. The formation of a blast wave by a very intense explosion i. theoretical discussion. *Proceedings of the Royal Society of London. Series A. Mathematical and Physical Sciences*, 201(1065):159–174, 1950.

[313] Shao-Chi Lin. Cylindrical shock waves produced by instantaneous energy release. *Journal of Applied Physics*, 25(1):54–57, 1954.

[314] Donald R Askeland, Pradeep Prabhakar Phulé, Wendelin J Wright, and DK Bhattacharya. The science and engineering of materials. 2003.

[315] Ali Kadivar, Kaveh Niayesh, N Sasaki Støa-Aanensen, and F Abid. Metal vapor content of an electric arc initiated by exploding wire in a model n2 circuit breaker: Simulation and experiment. *Journal of Physics D: Applied Physics*, 54(5):055203, 2020.

[316] Yihan Lu, Jian Wu, Huantong Shi, Daoyuan Zhang, Xingwen Li, Shenli Jia, and Aici Qiu. Study of density distribution of electrical exploding tungsten wire in air. *Physics of Plasmas*, 25(7):072709, 2018.

# List of Literatures Regarding This Study

1. **Nguyen Duy Hieu**, Yoshinori Tokoi, Kenta Tanaka, Toru Sasaki, Tsuneo Suzuki, Tadachika Nakayama, Hisayuki Suematsu, and Koichi Niihara, " Size reduction of submicron magnesium particles prepared by pulsed wire discharge", Jpn. J. Appl. Phys., No. 57, 02CC04 (2017).

2. Hisayuki Suematsu, Yu Shikoda, **Duy Hieu Nguyen**, Thi Mai Dung Do, Yoshinori Tokoi, Tadachika Nakayama, and Koichi Niihara,"Preparation of Nanosized Powders by Pulsed Wire Discharge", Journal of the Institute of Electrostatics Japan, Vol. 43, No. 3, (2019).

3. **Nguyen Duy Hieu**, Ngo Minh Chu, Yoshinori Tokoi, Thi-Mai-Dung Do, Tadachika Nakayama, Hisayuki Suematsu, and Koichi Niihara, "Preparation of boron nanoparticles by pulsed discharge of compacted powder", Jpn. J. Appl. Phys., No. 59, SCCC05 (2020).

4. **Nguyen Duy Hieu**, Ngo Minh Chu, Yoshinori Tokoi, Thi-Mai-Dung Do, Tadachika Nakayama, Hisayuki Suematsu, and Koichi Niihara, "Nanoparticle synthesis of transition metal borides by pulsed discharge of compacted powder", J. Am. Ceram. Soc. (in press).

5. **Hieu Duy Nguyen**, Toru Sasaki, Chu Minh Ngo, Yoshinori Tokoi, Thi-Mai-Dung Do, Tadachika Nakayama, Hisayuki Suematsu, and Koichi Niihara, "Particle size determining equation of various light and heavy metallic nanoparticles prepared by pulsed wire discharge" (to be submitted to).

# List of Conference Proceedings and Abstracts

1. **Nguyen Duy Hieu**, Yoshinori Tokoi, Kenta Tanaka, Tsuneo Suzuki, Tadachika Nakayama, Hisayuki Suematsu, and Koichi Niihara, "Size control of Magnesium Submicron Particles Prepared by Pulsed Wire Discharge", The 6th International Symposium on Organic and Inorganic Electronics Materials and Related Nanotechnology, Fukui, Japan (2017/6).

2. **Nguyen Duy Hieu**, Yoshinori Tokoi, Kenta Tanaka, Tsuneo Suzuki, Tadachika Nakayama, Hisayuki Suematsu, and Koichi Niihara, "Size Control of Magnesium Submicron Particles Prepared by Pulsed Wire Discharge", 42th International Conference and Exposition on Advanced Ceramics and Composites, Daytona Beach, Florida, USA (2018/1).

3. **Nguyen Duy Hieu**, Yoshinori Tokoi, Kenta Tanaka, Sasaki Toru, Tadachika Nakayama, Hisayuki Suematsu, and Koichi Niihara, "Particle Size Determining Equation in Submicron Magnesium Particles Preparation by Pulsed Wire Discharge", The 79th JSAP Autumn Meeting, Nagoya, Japan (2018/9).

4. **Nguyen Duy Hieu**, Ngo Minh Chu, Yoshinori Tokoi, Thi-Mai-Dung Do, Tadachika Nakayama, Hisayuki Suematsu, and Koichi Niihara, "Preparation of Boron Nanoparticles by Pulsed Discharge of Compacted Powder", The 7th International Symposium on Organic and Inorganic Electronics Materials and Related Nanotechnology, Nagano, Japan (2019/6).

5. **Nguyen Duy Hieu**, Ngo Minh Chu, Yoshinori Tokoi, Thi-Mai-Dung Do, Tadachika Nakayama, Hisayuki Suematsu, and Koichi Niihara, "Pulsed discharging of compacted B powder for B nanoparticle preparation", The 80th JSAP Autumn Meeting, Sapporo, Japan (2019/9).

6. **Nguyen Duy Hieu**, Ngo Minh Chu, Yoshinori Tokoi, Thi-Mai-Dung Do, Tadachika Nakayama, Hisayuki Suematsu, and Koichi Niihara, "Nanoparticle synthesis of borides by pulsed discharge of compacted powder", 44th International Conference and Exposition on Advanced Ceramics and Composites, Daytona Beach, Florida, USA (2020/1).

7. **Nguyen Duy Hieu**, Ngo Minh Chu, Yoshinori Tokoi, Thi-Mai-Dung Do, Tadachika Nakayama, Hisayuki Suematsu, and Koichi Niihara, "B and B-W nanoparticle preparation by pulsed discharge of compacted powder", 44th International Conference and Exposition on Advanced Ceramics and Composites, Daytona Beach, Florida, USA (2020/1).

8. **Nguyen Duy Hieu**, Ngo Minh Chu, Yoshinori Tokoi, Thi-Mai-Dung Do, Tadachika Nakayama, Hisayuki Suematsu, and Koichi Niihara, "Pulsed discharging of com-

pacted B powder for $ZrB_2$ nanoparticle preparation", The 67th JSAP Spring Meeting, Nagoya, Japan (2020/3).

9. **Nguyen Duy Hieu**, Ngo Minh Chu, Yoshinori Tokoi, Thi-Mai-Dung Do, Tadachika Nakayama, Hisayuki Suematsu, and Koichi Niihara, "Tungsten boride nanoparticle synthesis by pulsed discharge of compacted B powder", The 81th JSAP Autumn Meeting, Online (2020/9).

10. **Nguyen Duy Hieu**, Ngo Minh Chu, Yoshinori Tokoi, Thi-Mai-Dung Do, Tadachika Nakayama, Hisayuki Suematsu, and Koichi Niihara, "Understanding Particle Formation in Pulsed Wire Discharge by Colored High-speed Photographs", 45th International Conference and Exposition on Advanced Ceramics and Composites, Daytona Beach, Florida, USA (2021/2).

11. **Nguyen Duy Hieu**, Matsui Yoshio, Do Thi-Mai-Dung, Nakayama Tadachika, Suematsu Hisayuki, "Synthesis of tungsten boride nanoparticles by pulsed discharge of powder", The 77th Annual Meeting of the Japanese Society of Microscopy, Tsukuba, Japan (2021/6).